



HAL
open science

Study of Polycomb target genes architecture in *Drosophila* using multiplexed optical microscopy

Julián Roberto Gurgo

► **To cite this version:**

Julián Roberto Gurgo. Study of Polycomb target genes architecture in *Drosophila* using multiplexed optical microscopy. Molecular biology. Université Montpellier, 2021. English. NNT : 2021MONTT080 . tel-03637496

HAL Id: tel-03637496

<https://theses.hal.science/tel-03637496>

Submitted on 11 Apr 2022

HAL is a multi-disciplinary open access archive for the deposit and dissemination of scientific research documents, whether they are published or not. The documents may come from teaching and research institutions in France or abroad, or from public or private research centers.

L'archive ouverte pluridisciplinaire **HAL**, est destinée au dépôt et à la diffusion de documents scientifiques de niveau recherche, publiés ou non, émanant des établissements d'enseignement et de recherche français ou étrangers, des laboratoires publics ou privés.

THÈSE POUR OBTENIR LE GRADE DE DOCTEUR DE L'UNIVERSITÉ DE MONTPELLIER

En Biologie Santé

École doctorale Sciences Chimiques et Biologiques pour la Santé, CBS2

Unité de recherche Centre de Biochimie Structurale (CBS), INSERM U1054

Study of Polycomb target genes architecture in *Drosophila* using multiplexed optical microscopy

Présentée par Julián Roberto GURGO

Le 08 Décembre 2021

Sous la direction de Frédéric BANTIGNIES
et Marcelo NOLLMANN

Devant le jury composé de

Cédric VAILLANT, Directeur de Recherche, ENS, Lyon

Chiara LANZUOLO, Directrice de Recherche, INGM, Milan

Reini LUCO, Chargée de Recherche, IGH, Montpellier

Guillermo ORSI, Chargé de Recherche, IAB, Grenoble

Frédéric BANTIGNIES, Directeur de Recherche, IGH, Montpellier

Marcelo NOLLMANN, Directeur de Recherche, CBS, Montpellier

Président du Jury, Rapporteur

Rapporteur

Examinatrice

Examineur

Directeur de thèse

Directeur de thèse



UNIVERSITÉ
DE MONTPELLIER

Acknowledgments

First of all I would like to thank my thesis supervisor, Dr. Marcelo Nollmann. He has been incredibly supportive, and always offered his guidance, both scientifically and career-wise. He gave me the opportunity to join a very dynamic, cutting-edge scientific environment, and I'm grateful for that. I would like to thank my thesis co-supervisor, Dr. Frédéric Bantignies. He was always available to discuss and to offer his guidance. They were always kind enough to take all the time needed to make sure that I had everything to advance on the project. One can not wish for kinder and more involved Ph.D. supervisors.

Thanks a lot to our collaborator Dr Jean Charles Walter, for his work, availability and helpful conversations. Collaborating with him has been very enriching. Thanks to Dr. Giacomo Cavalli for all of his useful suggestions.

I'm also grateful to the members of my thesis committee, Dr. Mounia Lagha and Dr. Cédric Vaillant. They gave crucial insights into my work, and they have given me great advice to develop my skills.

I would like to thank the rapporteurs, Dr. Chiara Lanzuolo and Dr. Cédric Vaillant for accepting to read my work, and for all the time and effort invested. I would also like to thank the examiners, Dr. Reini Luco and Dr. Guillermo Orsi.

When doing a PhD abroad, far away from family and old friends, a lot of mixed emotions are involved. I'm grateful to all the people that have been there. I would like to thank my family, they have always been present. A loving thought and all my gratitude to my grandparents. I would like to thank Ale, Juani, Rocio, Mari, Franco, Vale, Sergi and Angeles. Despite the distance, and seeing each other unfrequently, they managed to be very close, and I'm honored to be a part of their lives. I'm really thankful to Oriane for her support. Thank you for making every moment special.

I've spent most of these last 4 years in the lab. I'm grateful to have worked with great people that are not only colleagues, but friends. With them we shared lots of great moments and discussions, both scientifically and personally. That's why I would also like to thank Christophe, Olivier, Jean-Bernard, Antoine, Sara, Marion, Marie, Sergio, Hernan, Markus. Thanks to all of them for making the lab a friendly, dynamic, supportive and fun environment.

I would like to thank friends that are/were part of the CBS, as well as the people I met in these years outside of the lab. Their friendship is invaluable, and I'm grateful for all that we shared: Angéline, Jacqueline, Constance, Thales, Mathieu, Amelie, Oscar, Anthony, Viviana, Vanessa, Peter, Ana, Amandine. Thanks to Anny for all the time we shared, even though we are far away. Thanks to Elodie for being there and for the fun trips. I'm grateful for all we shared with Sébastien, Guilhem, Thierry, and many others. Thank you for your friendship.

To all those that were there, thank you.

Resumé de la thèse

L'organisation de la chromatine est liée à de nombreux processus biologiques. Les techniques de capture de conformation des chromosomes ont révélé que la chromatine est organisée en domaines enrichis en interactions chromatiniennes, appelés Topologically Associating Domains (TADs). Chez la drosophile, les TADs coïncident avec les marques chromatiniennes actives et réprimées, et sont classés en fonction de leurs états épigénétiques. L'un de ces types de TAD, connu sous le nom de TADs Polycomb, est lié aux protéines du groupe Polycomb (protéines PcG), une famille de facteurs conservés dans la plupart des organismes eucaryotes, et cruciaux pour la régulation de la répression des gènes. Des preuves issues de la microscopie et des techniques de capture de la conformation des chromosomes montrent que les cibles PcG ont tendance à interagir préférentiellement les unes avec les autres, ce qui suggère qu'elles forment des compartiments de répression. Cependant, on sait peu de choses sur la nature de ces interactions, ou si plusieurs gènes PcG sont associés en 3D pour former des compartiments.

Dans ce travail, nous étudions le rôle des protéines du groupe Polycomb dans la formation de compartiments répressifs au cours du développement de la drosophile en appliquant Hi-M, une nouvelle méthode basée sur l'imagerie qui permet la reconstruction de la conformation de la chromatine tout en préservant l'information spatiale. Nous avons d'abord étendu Hi-M pour permettre l'imagerie d'échantillons épais et multicouches en combinant un robot de manipulation fluide à un microscope confocal et en adaptant les pipelines d'analyse existants. Ensuite, nous avons appliqué cette méthode pour étudier l'organisation chromosomique des gènes cibles de Polycomb dans différents segments d'un embryon de drosophile en développement. Nous montrons que la co-localisation spatiale de cibles Polycomb intra-chromosomiques distantes est peu fréquente, et que ces interactions sont principalement par paires. Nous observons également que les interactions à longue portée sont acquises après l'émergence des TADs à NC14, de façon concomitante avec l'enrichissement des foyers de PcG. Ces résultats ont été soutenus par la modélisation du polymère montrant qu'un polymère séparé en microphase dans le régime des globules capture le comportement expérimental des domaines Polycomb. Nos expériences et simulations suggèrent que les compartiments répressifs Polycomb se forment par des associations par paires peu fréquentes de domaines Polycomb. Enfin, nous montrons que les fréquences d'interaction entre les cibles Polycomb sont modulées à la fois par la répression et l'activation transcriptionnelle. Dans l'ensemble, nos résultats éclairent l'organisation des gènes cibles de Pc à l'échelle du chromosome, et contraignent les futurs modèles de formation des compartiments de Pc.

Abstract

Chromatin organization is related to many biological processes. Chromosome conformation capture techniques revealed that chromatin is organized in domains enriched in chromatin interactions, called Topologically Associating Domains (TADs). In *Drosophila*, TADs coincide with active and repressed chromatin marks, and are classified according to their epigenetic states. One of these TAD types, known as Polycomb TADs, are bound by Polycomb group proteins (PcG proteins), a family of factors conserved in most eukaryotic organisms, and crucial for the regulation of gene repression. Evidence from microscopy and chromosome conformation capture techniques shows that PcG targets tend to preferentially interact with each other, suggesting that they form repressive compartments. However, little is known about the nature of these interactions, or if several PcG genes are associated in 3D to form compartments.

In this work, we investigate the role of Polycomb group proteins in the formation of repressive compartments during *Drosophila* development by applying Hi-M, a novel imaging-based method that enables the reconstruction of chromatin conformation while preserving spatial information. We first extended Hi-M to enable imaging of thick, multi-layered samples by combining a fluidics handling robot to a confocal microscope and adapting existing analysis pipelines. Next, we applied this method to the study the chromosome-wide organization of Polycomb target genes in different segments of a developing *Drosophila* embryo. We show that spatial co-localization of distant intrachromosomal Polycomb targets is infrequent, and that these interactions are predominantly pairwise. We also observe that long-range interactions are acquired after the emergence of TADs at NC14, concomitantly with the enrichment of PcG foci. These results were supported by polymer modelling showing that a microphase-separated polymer in the globule regime captures the experimental behaviour of Polycomb domains. Our experiments and simulations suggest that Polycomb repressive compartments form by infrequent pairwise associations of Polycomb domains. Finally, we show that interaction frequencies between Polycomb targets are modulated by both transcriptional repression and activation. Overall our results shed light into the chromosome-wide organization of Pc target genes, and constrain future models for the formation of Pc compartments.

Contents

1	Introduction	11
1.1	Historical perspectives	11
1.2	From nucleosomes to chromosome territories: Different scales of organization	12
1.2.1	The chromatin fiber	12
1.2.2	Higher order chromatin structures at sub-chromosomal level and chromosome territories	13
1.2.3	Topologically associating domains (TADs)	15
1.3	Polycomb group proteins and their role in shaping chromatin structure: gene repression at multiple scales	17
1.3.1	PcG proteins diversity	18
1.3.2	Recruitment of PcG proteins to DNA	19
1.3.3	PcG proteins and 3D architecture	20
1.4	Chromatin architecture during early development	21
1.5	Techniques to dissect chromatin organization: chromosome conformation capture techniques	22
1.5.1	3C	23
1.5.2	4C	24
1.5.3	5C	24
1.5.4	Hi-C	25
1.5.5	Micro-C	25
1.5.6	Other sequencing-based techniques	26
1.6	Techniques to dissect chromatin organization: Microscopy techniques	26
1.6.1	DNA FISH	26
1.6.2	Conventional Wide-field microscopy approaches	27
1.6.3	Super-resolution microscopy	28
1.6.4	Structured illumination microscopy	28
1.6.5	Single-Molecule Localization Microscopy	29
1.6.6	Hi-M	30
1.7	Polymer modeling of chromatin	32
1.7.1	Early models: Fractal globule and Loop models	32
1.7.2	Strings and Binders Switch Model (SBS)	33
1.7.3	Block Copolymer models	34
1.8	Objective of this work	36
2	Results	37
3	Discussion	73
4	Materials and Methods	77
4.1	Domain selection and Library design	77
4.2	Library synthesis and amplification	78
4.3	Adaptor oligos	84
4.4	Embryo collection and fixation	85
4.5	Hybridization of Hi-M library	86
4.5.1	Optional: Immunostaining	88

4.6	Attachment of embryos to coverslip and mounting into microfluidics chamber	89
4.7	Fiducial mark and DAPI staining	90
4.8	Microscope setup	91
4.9	Image acquisition	92
4.10	Data analysis	94
5	Appendix	96
5.1	TADs are 3D structural units of higher-order chromosome organization in <i>Drosophila</i>	96
5.2	Microscopy-Based Chromosome Conformation Capture Enables Simultaneous Visualization of Genome Organization and Transcription in Intact Organisms	111
5.3	Direct and simultaneous observation of transcription and chromosome architecture in single cells with Hi-M	129
	References	169

1 Introduction

1.1 Historical perspectives

From early on, human curiosity oriented our efforts towards the understanding of nature and the world around us, including the study of living beings. Technological developments, like lenses (that were developed by the Greeks, around the 5th century BC) were crucial in the quest for knowledge, although we had to wait up to relatively recent years to see them in use in the life sciences. During the 17th century, the development of microscopes set in motion the study of microscopic life. One of the first accounts of microscopical observations comes from Robert Hooke, who used an early hand-crafted microscope. In his 1665 book *Micrographia* [, 1665], he describes the appearance of different organisms (figure 1). He coined the term cell, based on the resemblance of the structure he observed in plants and honeycomb cells. Roughly at the same time, the dutch scientist Anton van Leeuwenhoek observed motile objects, that we now know as protists, and bacteria. He called them "animalcules" (coming from a Latin expression that means "little animals") , and was one of the first persons to propose the existence of living microscopic organisms.

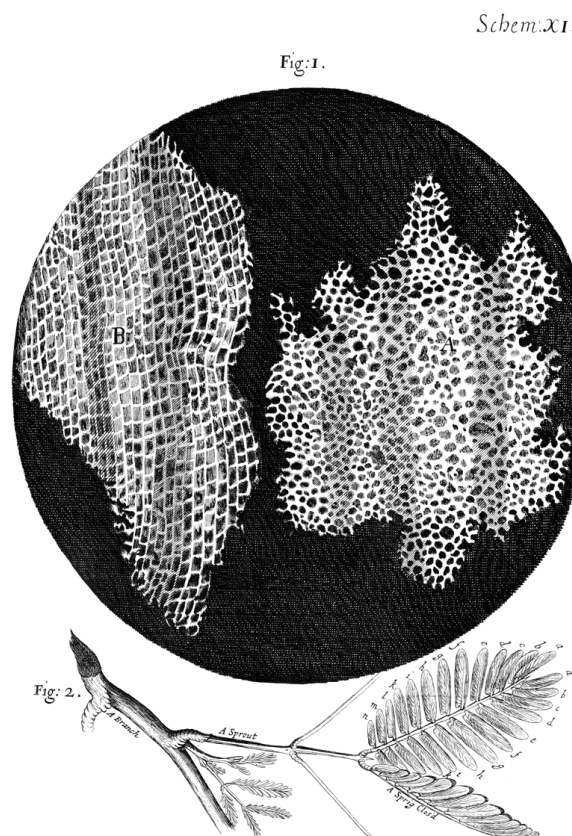


Figure 1: Robert Hooke's drawings of the cellular structure of cork and a branch of a plant from *Micrographia* (1665)

In 1839, based on microscopy images, the physiologist Theodor Schwann and the botanist Matthias Schleiden developed the cell theory. This was the starting point of cell biology. They stated that cells are the most basic unit of life, and that all living beings are composed of one or more cells. In 1831, Robert Brown identified an organelle in plant

cells which he called "nucleus". The work of several scientists, like Thomas Schleiden and Oscar Hertwig, suggested it was involved in heredity. Further developments in sample fixation and staining techniques allowed to identify structures within the nucleus. Walther Flemming discovered a stainable substance that he called "chromatin" (from the greek chromos, that means color), using an aniline based stain. He also described the process of mitosis. Around 1900, Walter Sutton and Theodor Boveri independently identified chromosomes as the carriers of genetic information, being the physical basis of Mendelian laws of heredity. The first studies of the spatial organization of chromosomes appeared in the same period, with the work of Carl Rabl and Boveri, who identified that chromosomes occupy defined positions in interphase nuclei, called chromosome territories (CT) [Cremer and Cremer, 2010]. In 1928, the geneticist Emil Heitz further described the structure of chromatin. By staining interphase chromosomes, he identified two different regions: one that was condensed, and other that remained decondensed. He called them heterochromatin and euchromatin respectively, and proposed that the differences in organization are related to gene activity [Passarge, 1979]. This was the first time that a relationship between chromatin architecture and gene expression was proposed. Around the same period, the American geneticist Hermann Muller describe the phenomenon of position-effect variegation, by which genes that are abnormally placed close to heterochromatin become silenced [Muller, 1930, Baker, 1968, Elgin and Reuter, 2013].

1.2 From nucleosomes to chromosome territories: Different scales of organization

1.2.1 The chromatin fiber

DNA (deoxyribonucleic acid) is the basic unit of genetic information, and forms a double helix structure first described in 1953 [Watson and Crick, 1953, Wilkins et al., 1953, Franklin and Gosling, 1953]. To fit in eukaryotic nuclei, DNA must be highly compacted. This is achieved via a hierarchical multi-level organization. The first organization level is the wrapping of the DNA double helix around histone proteins, to form the basic units of what is known as chromatin. This structure was first observed in vitro in 1974 [Olins and Olins, 1974, Kornberg, 1974, Woodcock et al., 1976, Maeshima et al., 2014], and consists in 147 base pairs (bp) wrapped around an octamer of histone proteins (a pair of each of H2A, H2B, H3 and H4). The association between the negatively charged DNA polymer and histone proteins forms a nucleosome, and shortens the length of chromosomes by 7-fold [Luger et al., 1997, Richmond and Davey, 2003, Fraser et al., 2015b]. Adjacent nucleosomes are connected by 20-80 bp linker DNA [Olins and Olins, 2003], forming the 11nm chromatin fiber [Ou et al., 2017]. This chromatin fiber has long been thought to fold into 30nm chromatin fibers, but recent electron microscopy tomography experiments show that chromatin arranges in disordered chains with 5-24nm diameters, that is packed with different 3D concentrations and distributions [Ou et al., 2017] (figure 2).

Histones possess N-terminal tails that extend out of the nucleosome that can be covalently modified. These enzyme-mediated modifications are known as post-translational modifications (PTMs), and directly affect the local compaction of chromatin. For example, acetylation leads to a de-condensation of chromatin, while deacetylation leads to condensation [Kouzarides, 2007]. Decondensed chromatin allows transcription factors and RNA polymerase to bind to regulatory regions associated with active genes, such as enhancers and promoters. Condensed chromatin, on the other hand, causes nucleo-

somes to be densely packed together, preventing RNA pol II binding, and its binding to repressed genes. Some PTMs lead to the recruitment of chromatin-binding proteins that can directly affect gene expression. For example, the H3K27me3 mark is deposited by Polycomb Repressive Complex 2 proteins (PRC2), and at a second stage bound by Polycomb Repressive Complex 1 (PRC1) proteins that can modify chromatin architecture and render it inaccessible to RNA pol II [Francis et al., 2004, Klemm et al., 2019].

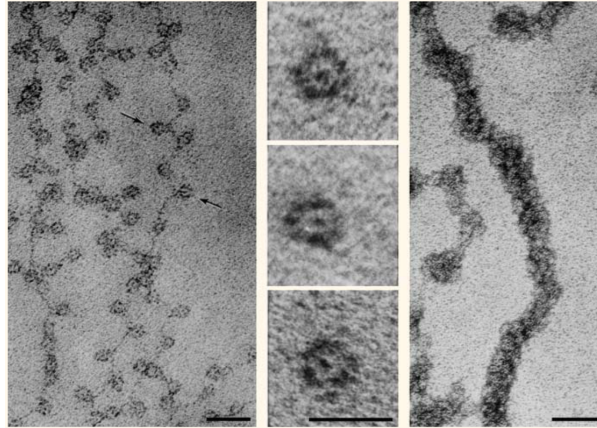


Figure 2: Electron microscopy images of chromatin. Left: typical image where we can observe the "beads on a string"; Scale bar = 30nm. Middle: images of isolated nucleosomes; Scale bar = 10nm. Right: Higher order chromatin fiber; Scale bar = 50 nm. Adapted from [Olins and Olins, 2003]

1.2.2 Higher order chromatin structures at sub-chromosomal level and chromosome territories

PMTs play a crucial role in processes like DNA replication, repair, and regulation of gene expression. But epigenetic state can also influence higher order chromatin organization. Traditionally, chromatin can be roughly divided into two broad categories: heterochromatin and euchromatin. Heterochromatin forms a more condensed structure, and is functionally related to gene regulation, chromosome integrity and nuclear structure [Grewal and Jia, 2007]. Euchromatin forms a lightly packed, gene-enriched form of chromatin, and mostly contains active genes. These two types of chromatin can be further subdivided according to combinations of histone modifications and associated factors [Filion et al., 2010]. Euchromatin or active chromatin is characterized by a high degree of acetylation, particularly H3K27ac, as well as H3K4me2/3 and H3K36me3. Deposition of these histone marks relies on the SET1/COMPASS and MLL COMPASS-like complexes (COMPASS coming from COMplex of Proteins ASSociated with Set1), which are also known as trithorax group proteins (TrxG) complexes. This group of proteins play a key role in transcriptional activation [Kennison and Tamkun, 1988, Piunti and Shilatifard, 2016, Schuettengruber et al., 2007]. Gene promoters are marked by H3K4me2/me3, transcriptional elongation at the gene body is characterized by H3K36me3, and enhancers are enriched in H3K4me1 and H3K27ac [Heintzman et al., 2007, Mikkelsen et al., 2007, Kharchenko et al., 2011, Filion et al., 2010]. In mammals and *Drosophila*, heterochromatin can be broadly classified as black chromatin, facultative heterochromatin, and constitutive heterochromatin. Black chromatin is the most prevalent type of repressive chromatin in the *Drosophila's* genome. It consists of gene-poor chromatin devoid of histone PMTs associated to heterochromatin. Some proteins are found enriched in black chromatin, like H1,

D1, IAL and SUUR [Filion et al., 2010, Kharchenko et al., 2011].

Constitutive heterochromatin is mostly present at pericentromeric regions and telomeres. It is gene-poor chromatin composed mainly of satellite repeats and transposable elements. It is characterized by H3K9me2/3 marks, and binding of HP1 [Maison and Almouzni, 2004, Lomberk et al., 2006, Ho et al., 2014]. It remains condensed throughout the cell cycle, and is crucial for the maintenance of chromosome integrity and proper chromosome segregation [Grewal and Jia, 2007].

Facultative heterochromatin, also known as Polycomb associated chromatin, can be found in developmentally regulated loci. Polycomb group proteins (PcG) are chromatin-associated factors that possess histone-modifying activity [Schuettengruber et al., 2017]. They are known to form discrete foci inside the nucleus, called Polycomb bodies or foci (PcG bodies or PcG foci) [Alkema et al., 1997, Buchenau et al., 1998, Saurin et al., 1998]. PcG foci contain Pc bound chromatin regions. PcG proteins associate to repress their target genes, via the deposition of H3K27me3 mark, and the modification of local chromatin architecture that renders chromatin inaccessible to the transcriptional machinery [Francis et al., 2004]. Euchromatin and heterochromatin tend to occupy different regions of the nucleus. Early evidence for a distinct organization came from imaging of human lymphocyte nuclei. Images of chromosome 18, a gene poor chromosome, and chromosome 19, the chromosome with the highest gene density [Croft et al., 1999] consistently showed that chromosome 19 was preferentially located in the nuclear interior, while chromosome 18 was located in the nuclear periphery. Later microscopy experiments completed and extended this picture, where imaging of all human chromosomes confirmed that euchromatic gene-rich chromatin tends to locate towards the center, while heterochromatic gene-poor chromatin tends to occupy the peripheral space, displaying a radial distribution of chromatin [Boyle et al., 2001, Bickmore, 2013]. Comparison of lymphoblastoid cells from various primate species showed that this nonrandom radial nuclear distribution has been evolutionary conserved despite major evolutionary chromosome rearrangements [Tanabe et al., 2002]. Interestingly, some regions of the genome that are located towards the nuclear periphery have been shown to associate with the nuclear lamina via the DamID technique [Pickersgill et al., 2006]. Briefly, a bacterial DNA adenine methyltransferase (Dam) is fused to a protein on the nuclear periphery, leading to a methylation of adenines in the genomic regions that are in contact with it. These regions have been termed Lamina Associated Domains (LADs) [Guelen et al., 2008]. LADs consist of gene poor regions, with low levels of expression. The nuclear lamina plays a role in gene repression, as it has been observed that genes that are artificially tethered to it are downregulated [Finlan et al., 2008, Reddy et al., 2008]. Nuclear lamina proteins can be also found in lower concentrations within the nucleoplasm [Hozák et al., 1995, Kolb et al., 2011]. These nucleoplasmic lamin A/C proteins of the nuclear lamina have been shown to interact with Polycomb proteins in mammals [Cesarini et al., 2015]. Lamina components are required for correct PcG protein compartmentalization inside the nucleus, and their knockdown leads to PcG bodies disruption, as well as ectopic PcG target activation [Cesarini et al., 2015].

At a higher level, chromosomes occupy preferential regions of the nucleus. Early microscopy experiments from Carl Rabl and Theodor Boveri showed that chromosomes are positioned in distinct positions inside the nucleus, called chromosome territories (CTs) [Cremer and Cremer, 2010]. In the 1970's, the work of several researchers [Stack et al., 1977, Cremer et al., 1982] resurfaced this concept, gathering compelling evidence supporting that chromosomes remain in different domains throughout interphase. Later imaging

developments, like Fluorescence in Situ Hybridization (FISH, see section 1.6.1), allowed to directly observe CTs [Manuelidis, 1985, Schardin et al., 1985]. Imaging of CTs shows that they're formed by structures of different shapes and sizes [Bolzer et al., 2005, Khalil et al., 2007, Küpper et al., 2007].

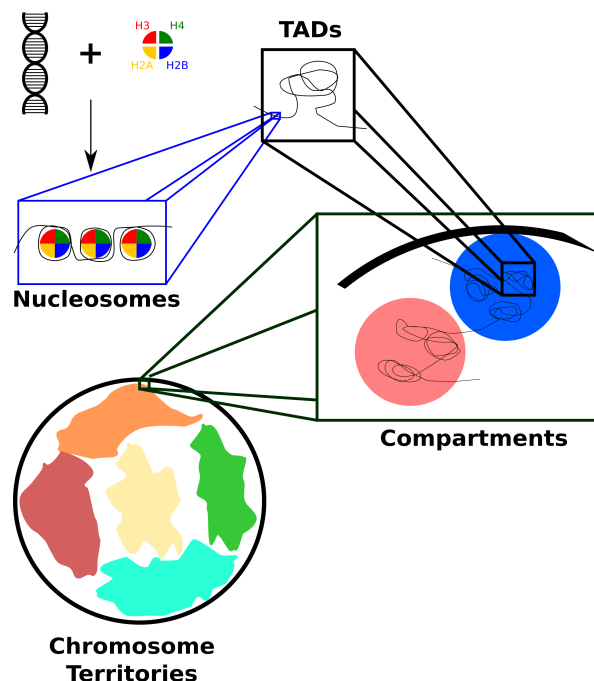


Figure 3: Schematic representation of the multiple scales of chromatin folding. 147 bp of DNA fold around histone octamers to form nucleosomes. Arrays of nucleosomes, together with DNA binding proteins form the chromatin fiber. The chromatin fiber folds into TADs, that associate into active and repressed compartments. Finally, chromosomes occupy discrete territories inside the cell nucleus.

1.2.3 Topologically associating domains (TADs)

We just saw how chromatin is organized at the sub-Kb level (chromatin fiber), and at the chromosome level (Mb). In between the Kb-Mb levels of organization, chromatin displays structures crucial to gene regulation. Hi-C and 5C methods (chromosome conformation capture techniques will be detailed in section 1.5 identified that A/B compartments are partitioned into smaller domains at the Kb-Mb level. These domains were called Topologically Associating Domains (TADs), and can be identified as "square blocks" on the diagonal of Hi-C matrices [Sexton et al., 2012, Nora et al., 2012, Dixon et al., 2012]. TADs are characterized by preferential intra-domain interactions, and are conserved across different tissues and species [Dixon et al., 2012, Vietri Rudan et al., 2015] (figure 4).

Given their implication in several biological processes, TADs are thought to define regulatory units. TAD borders correspond to replication domains [Pope et al., 2014], and genes within the same TAD tend to be co-regulated [Flavahan et al., 2016, Nora et al., 2012, Shen et al., 2012, Zhan et al., 2017]. Notably, reporter genes inserted in the genome are influenced by enhancers over regions that correlate with TADs [Symons et al., 2014]. TAD boundaries were observed to form loops, believed to reinforce insulation between domains [Hug et al., 2017, Rao et al., 2014]. In agreement with this hypothesis, disruption of TAD borders leads to ectopic gene expression [Flavahan et al.,

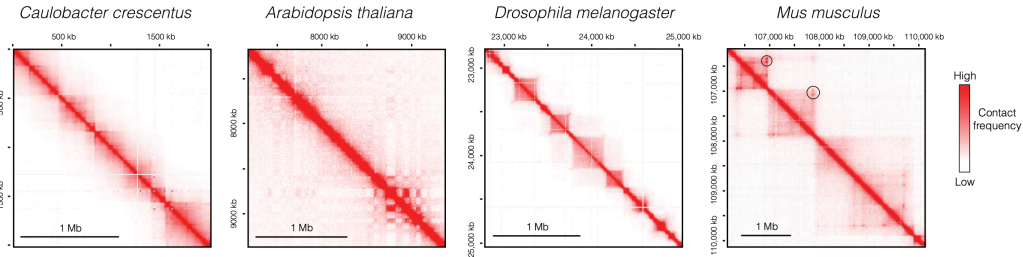


Figure 4: Hi-C maps of different species, showing genome partitioning. TADs are not easily defined in *A. thaliana*, but insulated-like genomic regions are appreciated. On mammals, loops between TAD borders (or corner peaks) are present (black circles). Adapted from [Szabo et al., 2019]

2016, Lupiáñez et al., 2015, Hnisz et al., 2016, Franke et al., 2016]. Furthermore, genome-wide enhancer-promoter contact analysis showed that these contacts occur predominantly within TADs [Bonev et al., 2017, Sun et al., 2019]. More recent studies, however, question the functional role of TADs in transcriptional regulation (see below).

In mammals, TADs have sizes in the order of Kb-Mb [Dixon et al., 2012, Nora et al., 2012]. Most TAD boundaries are enriched in CTCF [Vietri Rudan et al., 2015, Phillips-Cremins et al., 2013], and in cohesin. Moreover, TAD borders can interact to form CTCF border loops. TADs displaying CTCF-mediated corner loops are called looped domains, and represent 50% of all TADs. Border loops form from convergent CTCF sites, and are lost upon inversion or removal of a single CTCF site, shifting the border to the next CTCF site in the proper orientation [Sanborn et al., 2015, de Wit et al., 2015, Guo et al., 2015]. A linear tracking model known as "Loop-Extrusion Model" has been proposed to explain the formation of mammalian looped domains [Fudenberg et al., 2016, Vian et al., 2018, Fudenberg et al., 2017, Sanborn et al., 2015], in which chromatin is extruded by cohesin until it encounters two convergent CTCF sites.

In *Drosophila*, TADs correlate with epigenetic states, and are classified according to their specific epigenetic marks as active TADs (H3K4me3, H3K36me3), Polycomb repressed TADs (H3K27me3 and PcG proteins), black TADs (devoid of specific marks), and heterochromatin TADs (H3K9me2, HP1, Su(var)3-9) [Sexton et al., 2012, Filion et al., 2010]. *Drosophila* TAD boundaries display gene-dense, transcriptionally-active chromatin, that is accessible and decompacted. Several insulator proteins are enriched in TAD boundaries: BEAF-32, Chromator, CP190, M1BP and TFIIC. The number of insulator proteins bound to a TAD border directly correlates with its strength [Van Bortle et al., 2014]. Contrary to mammals, *drosophila* CTCF is not abundant at TAD borders. Since TADs correlate with epigenetic states, their compartmentalization strength correlates with the degree of transcriptional activity of regions located in between them [Luzhin et al., 2019], although inhibition of transcription does not impede boundary formation [Hug et al., 2017]. The transcription factor Zelda has been proposed to be a key player in the formation of boundaries in *Drosophila*, where TADs emerge early in development (nuclear cycles 13-14) [Hug et al., 2017, Ogiyama et al., 2018, Cardozo Gizzi et al., 2019].

Global run-on sequencing (GRO-seq) of *Drosophila* genome partitions the genome into active and inactive regions that correlate with TADs as observed by Hi-C [Rowley et al., 2017]. Furthermore, super-resolution imaging shows that chromatin is organized into condensed repressed TADs interspersed by active regions [Szabo et al., 2018, Boettiger et al., 2016]. In line with these findings, STORM imaging showed that immunolabeled H3K27me3 and H3K4me3 marks are spatially segregated in single cells [Cattoni et al.,

2017]. Hence, TADs in *Drosophila* may represent the physical segregation of active and repressed chromatin.

However, the role of TADs as functional units of chromosome organization is still a subject of intense debate. Large rearrangements in *Drosophila* chromosomes caused by deletions, duplications or inversions has been shown to affect gene expression only in selected chromatin regions [Ghavi-Helm et al., 2019]. This effect may be due, among other factors, to enhancer redundancy [Cannavò et al., 2016], a pervasive feature in *Drosophila*. In another study, engineered inversions were performed in testis-specific gene clusters in *Drosophila* [Meadows et al., 2010], and caused little effect in the expression of neighboring genes.

In mammals, the role of TADs as functional units is also under current debate. One study focused on the sonic hedgehog locus (*Shh*), involved in the growth and patterning of many tissues in mice [Williamson et al., 2019]. Internal deletions, deletion of CTCF sites, and deletions and inversions at the TAD border of the *Shh* locus were shown to have no effect on *Shh* expression pattern or level of expression, resulting in no detectable phenotypes (as long as enhancers were not deleted). In another study in mice, the removal of major CTCF sites in the *Sox9/Kcnj* loci resulted in the fusing of this two neighbouring TADs, without major changes of gene expression [Despang et al., 2019], suggesting that TAD structure is not essential for developmental gene regulation. However, gene misexpression is attained with inversions and insertions of boundaries, that cause a re-wiring of enhancer-promoter interactions [Despang et al., 2019]. Finally, another study focused in the *HoxD* locus, that lies between two TADs containing enhancers which control expression of different *Hoxd* genes in different tissues [Montavon et al., 2011, Andrey et al., 2013, Berlivet et al., 2013]. The TAD boundary is thought to prevent genes from responding to the wrong enhancers, ensuring correct limb development. However, deletions across the boundary did not affect the independent functioning of enhancers located at each side of the locus, even when performing a big 400 Kb deletion that fused the two TADs [Rodríguez-Carballo et al., 2017]

1.3 Polycomb group proteins and their role in shaping chromatin structure: gene repression at multiple scales

PcG proteins are evolutionary conserved chromatin-modifying factors that were originally identified as regulators of homeotic gene expression in *Drosophila*. They are now known to be involved in several processes such as X chromosome inactivation, cell fate choices, cell cycle control, cellular senescence, genomic imprinting, and cancer, among others [Mills, 2010, Pasini et al., 2008, Sparmann and van Lohuizen, 2006, Delaval and Feil, 2004, Heard, 2005, Schuettengruber et al., 2007]. PcG proteins locally modify chromatin, via their histone-modifying activities and their ability to change chromatin architecture. They can also mediate H3K27me3 deposition, that can directly block the deposition of antagonist marks like H3K27ac, and interfere with the recruitment of RNA Pol II. PcG protein activity is also known to prevent histone acetylation [Tie et al., 2016]. In the nucleus, some PcG proteins appear as microscopically visible foci, called Polycomb bodies [Alkema et al., 1997, Buchenau et al., 1998, Saurin et al., 1998]. They regulate the expression of developmental genes (e.g. *Hox* genes) by ensuring their efficient repression where they should not be active. Another protein complex, called Trithorax group complex (TrxG) plays an antagonistic role, acting as a transcriptional activator [Ingham, 1983, Ingham, 1985, Struhl and Akam, 1985, Kennison and Tamkun, 1988].

1.3.1 PcG proteins diversity

PcG proteins can be roughly divided into different complexes: Polycomb Repressive Complex 1 and 2 (PRC1 and PRC2 respectively, figure 5). PRC1 complexes can be further divided into canonical PRC1 (cPRC1) and noncanonical PRC1 (ncPRC1). In mammals, all proteins from the PRC1 complex share a conserved protein core that consists in two subunits: a Ring1 protein (RING1A-B), and one PcG Ring finger proteins (PCGF1-6). RING1A/B contains E3 ubiquitinating ligase activity that monoubiquitinates histone H2A on lysine 119, depositing the H2AK119ub mark [Napoletano et al., 2004, Wang et al., 2004]. PCGF proteins are thought to regulate RING1A/B ubiquitination activity. The difference between cPRC1 and ncPRC1 lies on the other proteins forming the complex. cPRC1 has one of the chromobox proteins (CBX2,4,6-8) that bind the H3K27me3 mark [Fischle et al., 2003, Min et al., 2003], and a homolog of Polyhomeotic (PH) protein that contains a sterile alpha motif (SAM) essential for PcG repression [Robinson et al., 2012]. ncPRC1 possesses YY1-binding protein (RYBP) or the homolog YAF2, that contribute to ubiquitination activity [Tavares et al., 2012, Basu et al., 2014, Wilkinson et al., 2010, Rose et al., 2016], that can associate with accessory proteins to define specific ncPRC1 subcomplexes. In *Drosophila*, cPRC1 contains the homologs of the mammalian proteins, that is dRING (homolog of RING1B), PSC (homolog of PCGF proteins), PC (homolog of CBX proteins) and PH [Beisel and Paro, 2011]. dRING and PSC are present in both cPRC1 and ncPRC1 in *Drosophila*, and they are responsible for the deposition of the H2AK118/119Ub marks. The ncPRC1 complex also contains the histone demethylase dKDM2, that demethylates H3K36me2 and stimulates H2A ubiquitylation by dRING [Lagarou et al., 2008]. Both in mammals and *Drosophila*, ncPRC1 complexes have a more enzymatic activity [Gao et al., 2012, Blackledge et al., 2014, Francis et al., 2004, King et al., 2005, Rose et al., 2016], while cPRC1 mediate chromatin compaction.

The PRC2 core complex is comprised by three proteins. In mammals it contains the SET histone methyltransferase enhancer of zeste (EZH2 or EZH1), embryonic ectoderm development (EED) and suppressor of zeste (SUZ12). Functionally, the core complex catalyzes mono-, di- and trimethylation of histone H3 on lysine 27 (H3K27me1/2/3) [Pasini et al., 2008, Müller et al., 2002, Cao and Zhang, 2004a]. The RbAp46/48 proteins are also part of PRC2, and they stabilize the complex [Ciferri et al., 2012, Satrimafitrah et al., 2016]. In *Drosophila*, PRC2 core complex contains E(z), ESC, SUZ(12) and NURF55 (also known as p55 or CAF-1). Other proteins associate with core PRC2. PHF finger protein 1 (PHF1) or its *Drosophila* homolog Polycomb-like (PCL) associate to PRC2, stimulating the trimethylation activity of EZH2 or E(z) respectively [Nekrasov et al., 2007, Sarma et al., 2008]. AEBP protein also associates to regulate enzymatic activity [Cao and Zhang, 2004b]. The protein family Jumonji (JARID2) also associates to PRC2, to stabilize PRC2 occupancy and regulate H3K27me3 deposition [Shen et al., 2009, Herz et al., 2012].

In *Drosophila*, genetic screens revealed further proteins that are not part of PRC1/2, but that form additional PcG complexes. One of these complexes is the Pho-Repressive complex. It comprises a zinc finger protein called Pleiohomeotic (PHO) and Scm-related gene containing four mbt domains (dSFMBT) that can bind to H3K9me1 and H3K20me2. Pho-repressive complex is thought to play a crucial role in the recruitment of PRC1 and PRC2. The Polycomb repressive deubiquitinase complex (PR-DUB) is also part of the PcG complex [Scheuermann et al., 2010], and is formed by two proteins: Calypso and Additional sex combs (Asx). PR-DUB has H2A-specific deubiquitinase activity, that

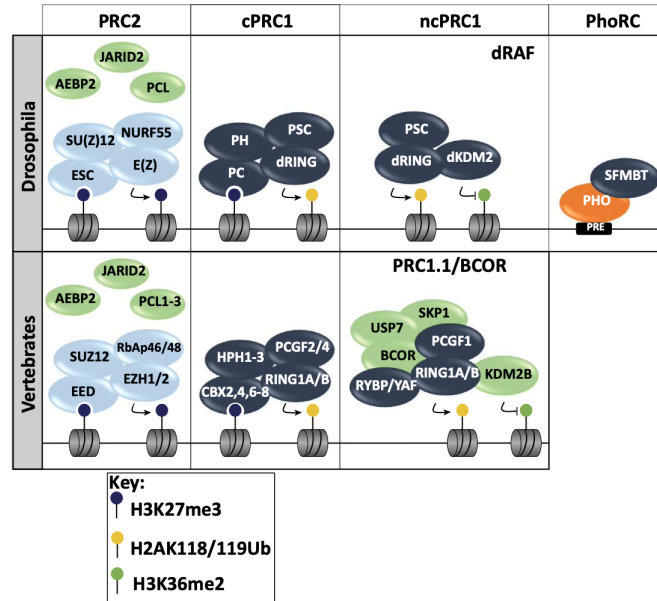


Figure 5: PcG proteins in *Drosophila* and mammals. They can be roughly divided in PRC1 and PRC2 complexes, with the PRC1 complex further subdivided in cPRC1 and ncPRC1. Each complex is defined by the interaction between core proteins (light and dark blue) and accessory proteins (green). Their enzymatic activity is also indicated. Image adapted from [Entrevan et al., 2016]

is paradoxically required for PcG repression, suggesting that a balance between H2A ubiquitination and deubiquitination is necessary for PcG-dependent silencing. There are additional PcG proteins that are required for homeotic gene silencing that are not yet assigned to a protein complex, like Sex combs on middle leg (Scm) [Kassis and Kennison, 2010] and Super sex combs (Sxc/Ogt) [Gambetta et al., 2009], that can associate with PRC1.

1.3.2 Recruitment of PcG proteins to DNA

In *Drosophila*, PcG proteins are recruited to specific DNA sequences, called Polycomb Response Elements (PREs), which also display binding sites for other DNA-binding proteins (like PHO, GAF, Zeste, Cg, among others) [Kassis and Brown, 2013, Fauvarque and Dura, 1993, Simon et al., 1993, Müller and Bienz, 1991]. These transcription factors are important to PcG recruitment, but none of them can recruit PcG independently. A hierarchical model of PcG recruitment was proposed, in which PHO recruits PRC2 via direct interaction involving the ESC and E(Z) subunits [Klymenko et al., 2006, Wang et al., 2004]. Subsequently, PRC2 component E(Z) deposits the H3K27me3 mark, that is later recognized by the chromodomain of the PC subunit of PRC1, enabling the binding of PRC1 to PREs. However, other studies question this model, suggesting that PRC1 can bind to some of its targets in absence of H3K27me3 [Loubiere et al., 2016, Kahn et al., 2016, Schaaf et al., 2013, Farcas et al., 2012, Tavares et al., 2012, Blackledge et al., 2014]. Furthermore, PRC1 recruitment was observed in absence of PRC2 binding [Kahn et al., 2016]. Besides, PRC1 can mediate H2A ubiquitination, creating a binding site for PRC2 that later deposits H3K27me3 [Kahn et al., 2016, Kalb et al., 2014, Blackledge et al., 2014, Cooper et al., 2014], inverting the canonical hierarchy of recruitment of PcG proteins in many PREs.

In mammals, genome-wide mapping of PcG proteins shows a strong correlation with

CpG hypomethylated regions (CGIs) [Boyer et al., 2006, Tanay et al., 2007]. Furthermore, an artificial CG enriched region devoid of TF binding sites has been shown to ectopically recruit PcG proteins, suggesting that CGIs represent mammalian PREs [Farcas et al., 2012, Mendenhall et al., 2010, Riising et al., 2014]. The transcription status at CGIs is also related to PcG recruitment, as global inhibition of transcription leads to ectopic recruitment of PcG proteins to silenced CGIs [Riising et al., 2014]. PcG proteins in mammals have also been found at transcriptional start sites of developmental regulators [Boyer et al., 2006, Lee et al., 2006]. Another factor related to regulation of PcG recruitment in mammals is long non-coding RNAs (lncRNAs). XIST RNA has been shown to be involved in the recruitment of PcG proteins to the inactivated X chromosome [Plath et al., 2003]. Other lncRNAs have been shown to recruit PcG proteins to Hox locus in humans and mouse [Rinn et al., 2007], or to be involved the targetting of PcG proteins to imprinted loci [Pandey et al., 2008].

1.3.3 PcG proteins and 3D architecture

PcG proteins act to repress their target genes at several levels. PRC1 complex proteins modify chromatin structure at the nucleosome level both in mammals and *Drosophila* [Shao et al., 1999, Francis et al., 2004, Francis et al., 2001, Yuan et al., 2012, Lau et al., 2017], causing nucleosome compaction that inhibits remodeling by TrxG group proteins and rendering chromatin inaccessible to transcriptional machinery [Shao et al., 1999]. In mammals, PRC2 components have been also shown to compact chromatin [Margueron et al., 2008, Terranova et al., 2008]. Furthermore, they deposit the H3K27me3 mark, that can block the deposition of antagonizing acetylation marks, interfering with the recruitment of RNA Pol II [Chopra et al., 2011]. In addition to modifying chromatin compaction, PRC2 can also bind H3K27me3 [Margueron et al., 2009], suggesting a cooperative state between PRC1 and PRC2 in chromatin condensation. At the TAD level, PcG bound domains display a more compact architecture with respect to active or black regions, both in *Drosophila* and mammals [Boettiger et al., 2016, Kundu et al., 2017]. At this level, PcG proteins are required to form specific topologies, such as looping interactions between specific elements [Lanzuolo et al., 2007, Comet et al., 2011, Tiwari et al., 2008]. In *Drosophila*, the first evidence of physical interactions between PREs came from the measurement of contacts between inserted transgenes containing PREs [Bantignies et al., 2003, Vazquez et al., 2006] and the study of long range interactions in the BX-C [Lanzuolo et al., 2007]. Other binding sites of PcG proteins undergo specific looping involving gene promoters, cis-regulatory elements, and PREs, and these interactions contribute to domain compaction and gene repression [Eagen et al., 2017, Ogiyama et al., 2018]. Mutation in PREs, or insertion of insulator elements between looping PREs can affect repression, without loss of PcG binding [Ogiyama et al., 2018], highlighting the link between structure and function. Furthermore, deletion of PRC1 components induces chromatin decompaction prior to ectopic gene expression at the Bithorax complex in *Drosophila* [Cheutin and Cavalli, 2018]. Interactions between PcG bound regions have also been observed within mammalian TADs, for example in Hox clusters or the GATA-4 locus [Ferraiuolo et al., 2010, Tiwari et al., 2008]. These interactions are dependent on EZH2, and the transcriptional status of the intervening genes. The architecture of PcG TADs in mammals has also been shown to be dependent on PRC1 components, particularly PH [Kundu et al., 2017]. The architecture of these domains changes during development, following the changes in PRC1 binding.

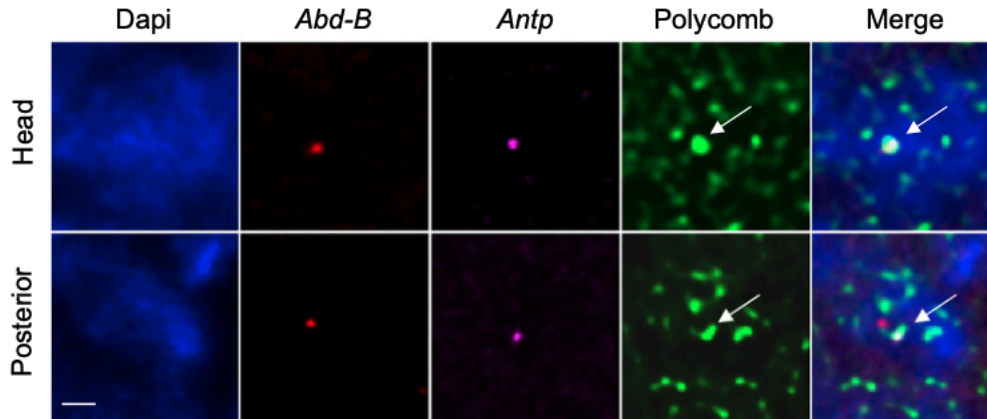


Figure 6: Long range looping between *Abd-B* (red spot) and *Antp* (magenta spot) genes in *Drosophila* S13-S14 embryos. In the head (Head, upper row on image), where they co-repress, these genes were observed to be spatially close in space, inside of PcG foci (green foci). In tissues where one of them is repressed, but not the other, the active gene loops out of PcG foci (see Posterior, lower row on image). Image adapted from [Bantignies et al., 2011]

At the chromosomal level, PcG domains have been observed to form long-range interactions between PcG foci in *Drosophila* embryos and in mouse [Bantignies et al., 2011, Schoenfelder et al., 2015, Bonev et al., 2017] (figure 6). This behaviour is believed to help reinforce repression of PcG targets, since the mutation of one of the interacting partners affects the repression state of the other [Bantignies et al., 2011]. PcG domains undergo Mb level interactions between Hox gene clusters [Bantignies et al., 2011, Tolhuis et al., 2011]. PcG proteins, in particular Pc and Ph, are required for the establishment of these interactions. In mammalian ESCs, PRC2 component Eed has been shown to be required for long range interactions between PcG targets separated by tens of Mb or in different chromosomes [Denholtz et al., 2013, Vieux-Rochas et al., 2015], including non-Hox and Hox genes. Finally, RING1B plays a major role in establishing long range interactions between promoters of PcG regulated genes in mESCs [Schoenfelder et al., 2015].

Given the evidence of inter-domain interactions, PcG domains were proposed to form repressive hubs represented by PcG foci [Delest et al., 2012, Bantignies and Cavalli, 2011, Isono et al., 2013]. Indeed, the disruption of the polymerization activity of Polycomb subunits in *Drosophila* leads to the loss of clustering between loci, both at the intra-TAD and the inter-TAD levels [Wani et al., 2016]. This phenomenon is also observed upon deletion of a single PcG subunit [Bantignies et al., 2011]. Recently, mammalian PcG-mediated long-range interactions were proposed to involve liquid-liquid phase separation (LLPS) [Plys et al., 2019, Tatavosian et al., 2019, Seif et al., 2020]. More research is needed to test this hypothesis.

1.4 Chromatin architecture during early development

All animals start their life as a single cell, the fertilized egg. This cell divides or cleaves to form smaller cells, that organize as an external layer, known as ectoderm (precursor of epidermis and nervous system). During development, cells move towards the interior of the embryo to form the endoderm (precursor of gut and internal organs). Other groups of cells occupy the space between the ectoderm and endoderm, forming the mesoderm (precursor of muscles, connective tissues and other components). The transformation of

a hollow body of cells, known as the blastula, into an organism with a gut is called gastrulation.

During the blastula phase, the embryo's development switches from being directed by maternally-deposited RNAs, to being controlled by the zygotic genome. This is known as Maternal to Zygotic transition, and is characterized both by Zygotic Gene Activation (ZGA), and degradation of maternal products.

These developmental processes are accompanied by changes in genome architecture. Hi-C data on mouse spermatozoa showed that TADs, loops and A/B compartments are similar to those in somatic cells [Battulin et al., 2015, Jung et al., 2017, Du et al., 2017, Ke et al., 2017]. The differences observed arise from differences in compaction (spermatozoa display a tighter packaging) and in cell-type specific looping [Battulin et al., 2015, Du et al., 2017, Ke et al., 2017]. TADs are present in early germinal oocytes (transcriptionally active), but they vanish in mature oocytes (transcriptionally inactive) [Ke et al., 2017, Flyamer et al., 2017, Du et al., 2017]. Mature oocytes also lack compartments, showing that the genome is largely unstructured before fertilization [Ke et al., 2017, Du et al., 2017]. After fertilization, there are two stages of domain formation at the 2-cell (major ZGA) stage and the 8-cell stage. At the 2-cell stage, both maternal and paternal genomes are organized in different manners, showing parentally-biased preformed domains [Collombet et al., 2020, Ke et al., 2017, Du et al., 2017]. Maternal genome displays most of the called domains at the 1-2 cell stages [Collombet et al., 2020], while paternal domains are present in lower numbers at 1-2 cell stages, and gradually appear as the embryo develops towards the 8-cell stage. However, compartmentalization of paternal domains is much stronger than maternal compartmentalization [Flyamer et al., 2017, Du et al., 2017, Ke et al., 2017]. These early parent-specific domains coincide with the detection of H3K27me3 histone marks, and with parentally biased gene expression. Later on development, TADs gradually appear from the 8-cell stage [Ke et al., 2017, Du et al., 2017].

In *Drosophila*, TADs appear at the ZGA step and seem to be independent of transcription [Hug et al., 2017]. Inhibition of transcription does, however, impact inter-TAD insulation. The transcription factor Zelda is required for locus-specific TAD insulation, showing a role of this factor in the establishment of chromatin architecture. At higher scales, long range contacts increase during development, and are mediated both by the GAF insulator and by PcG proteins [Ogiyama et al., 2018]. Compartmentalization of chromatin that shares the same epigenetic marks happens at different developmental times, and active and PcG repressed compartments are not well separated early in development [Ogiyama et al., 2018]. This was also observed before in human cells, where A-B compartmentalization varies during development, and may reflect a high degree of chromatin switching between compartments [Dixon et al., 2015]. Another factor involved in early establishment of compartments is HP1 [Zenk et al., 2021]. In early *Drosophila* embryos, reduced HP1 binding leads to loss of clustering and de-condensation of constitutive heterochromatin, affecting the Rab1 configuration of chromosomes and B-B compartmentalization.

1.5 Techniques to dissect chromatin organization: chromosome conformation capture techniques

The understanding of chromatin organization underwent a revolution in the last two decades, thanks to developments in molecular biology, sequencing, and microscopy. In

this section, I'll describe the most important techniques that were developed.

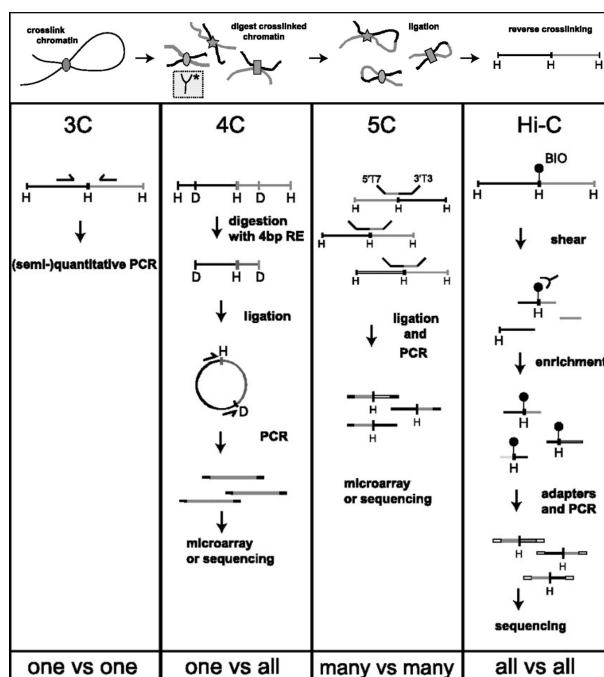


Figure 7: Chromosome conformation capture techniques. All of these techniques share the same first steps: crosslinking of chromatin interactions, DNA digestion using restriction enzymes, ligation of the fragments that are in close spatial proximity and reverse crosslinking. In 3C, the interacting regions are detected with specific primers over the region of interest. In 4C, a second round of digestion and ligation creates a circular DNA molecule, which is amplified by PCR using primers specific to the anchor sequence. The resulting PCR products are detected by microarray or sequencing. 5C consists in the detection of all pairwise interactions between several regions of interest. Ligation products are hybridized with oligos specific to the ligation site that are further amplified by PCR and sequenced. In Hi-C, the ends of the DNA fragments are filled with biotin, decrosslinked, DNA is sheared, and biotin is pulled down. The fragments are then sequenced. Image adapted from [Wit and Laat, 2012].

1.5.1 3C

Chromosome conformation capture (3C) is based on the cross-linking of pairs of genomic loci that are physically close, to obtain contact probabilities between them [Dekker et al., 2002]. The technique consists in the formaldehyde fixation of nuclei, which cross-links DNA and proteins. DNA fragments that are close are linked by their DNA-binding proteins. Then chromatin is digested using a restriction enzyme that cuts DNA at specific sites. The selected enzyme defines the resolution of the 3C experiment, because it determines the size of the fragments by the frequency of enzymatic sites. The cross-linked fragments are then diluted and ligated at low concentrations using a ligase (favouring intra-molecular ligation over inter-molecular ligation). The resulting DNA junctions are then quantified by qPCR [Hagège et al., 2007], using locus-specific primers. Genomic loci that are frequently close in space are detected at higher frequencies than loci that are far away. This technique was first used in 2002, to map chromatin interactions in yeast chromosome III [Dekker et al., 2002]. Then 3C allowed mapping interactions between functional elements, like the formation of active chromatin hubs [Tolhuis et al., 2002], enhancer-promoter interactions in vivo [Tolhuis et al., 2002, Vernimmen et al., 2007], interactions between gene promoters and PREs, and PRE-PRE interactions in Polycomb-bound domains [Lanzuolo et al., 2007], or interactions between insulator elements [Lanzuolo et al., 2007, Comet et al., 2011]. The 3C technique further increased

the evidence of correlations between chromatin conformation and gene regulation.

Long range interactions occur at low frequencies, making their detection difficult by 3C. Coupling 3C with microarrays, and later to next generation sequencing (NGS) led to the development of novel techniques known as 4C, 5C and Hi-C.

1.5.2 4C

4C allows to map contacts between one loci of interest and all other loci. Briefly, in 4C the ligated 3C molecules are cut with a second round of DNA digestion and ligated again to create small DNA circles. Some of them contain the 3C ligation junctions. These circles are then amplified by inverse PCR using specific primers for the desired anchor. The amplified products contain all sequences contacting this site of interest. They can then be analyzed by microarrays or high-throughput sequencing. Since it's development, 4C was used to obtain several important results. It was applied to get contact maps of the β -globin and Rad23 genes, which showed that active and inactive genes form both intra and inter chromosomal contacts with genes in the same transcriptional state [Simonis et al., 2006]; to the study of enhancer-promoter interactions [Lomvardas et al., 2006, Ghavi-Helm et al., 2014]; the detection of interaction networks of PcG repressed Hox genes in *Drosophila* or active mouse globin genes in erythroid tissues [Bantignies et al., 2011, Tolhuis et al., 2011, Schoenfelder et al., 2010]; to study the genomic environment of the HoxB1 gene during the induction of its expression, showing that it displays both intra and inter chromosomal contacts, and that inter chromosomal contacts become more frequent upon induction [Würtele and Chartrand, 2006]; the changes in Hox gene domain organization, showing that they're organized as single domains when repressed, but change into a bimodal 3D organization when parts of the locus become active, separating them from the region that is still repressed [Noordermeer et al., 2011, Andrey et al., 2013].

1.5.3 5C

Both 3C and 4C proved crucial to understand chromatin organization. However, they both measure interactions from a specific anchor. A technique that partially overcomes this limitation is 5C [Dostie et al., 2006], that allows to detect interactions between multiple sequences. First, a regular 3C library is obtained. This 3C template is hybridized to a mix of oligonucleotides, that are designed to overlap a different restriction site in the genomic region of interest. Each oligo carries one of two primer sequences at their 5' ends. Oligonucleotides that correspond to interacting fragments are ligated together after hybridization to the 3C library. Then, this ligated oligos can be simultaneously amplified via PCR, and read using microarrays or high-throughput sequencing. 5C does not only allow the detection of specific looping interactions, but also enables the construction of interaction matrices, where the contact frequencies of "many vs many" genomic loci can be assessed. 5C has been used to study the organization of Hox clusters in humans and mouse [Rousseau et al., 2014a, Wang et al., 2011], and to show that different classes of architectural proteins maintain constitutive and transient chromatin contacts in mouse embryonic stem cells and neural progenitor cells [Phillips-Cremins et al., 2013]. 5C was also used to identify TADs in the X chromosome [Nora et al., 2012], and helped understand the human HoxA locus conformation using a machine learning approach allowing the detection of different leukemia cell subtypes [Fraser et al., 2009, Rousseau et al., 2014b].

1.5.4 Hi-C

Next generation sequencing also led to the development of a genome-wide, "all vs all" technique called Hi-C [Lieberman-Aiden et al., 2009]. The 3C protocol is modified in the following manner. Before ligation, restriction sites are filled with biotin-labeled nucleotides. DNA is then purified, sheared, and a biotin pull-down is performed to ensure that only ligation products are kept for analysis. Using sequencing, reads are mapped back to the genome, and used to construct a matrix of ligation frequencies between all fragments in the genome. The first use of Hi-C confirmed the existence of chromosome territories in human cells, and the compartmentalization of chromatin into "A" gene-rich compartments, and "B" repressed chromatin compartments [Lieberman-Aiden et al., 2009]. Later work identified the existence of regions characterized by high frequencies of interaction called Topologically Associating Domains, or TADs. [Sexton et al., 2012, Nora et al., 2012, Dixon et al., 2012, Hou et al., 2012]. TADs were described in greater detail in section 1.2.3. Using a modified protocol in *Drosophila*, it was also shown that chromatin organization overlaps with epigenomic domains [Sexton et al., 2012], leading to the classification of TADs into four main types: active, Polycomb, heterochromatin and black (without any specific mark). Further developments of Hi-C allowed single-cell detection, which was used to reveal the heterogeneity of contacts in individual cells, reflecting a dynamic chromosome organization [Nagano et al., 2013, Stevens et al., 2017, Flyamer et al., 2017, Nagano et al., 2017, Tan et al., 2018]. Overall, these techniques provided further evidence of the relationship between gene activity and chromatin 3D organization. However, sequencing-based methods have a number of limitations: I) traditionally, they can only measure pairwise contacts and average conformations; II) They provide relative contact frequencies, making it difficult to know how often do interactions really occur; (III) They do not provide access to physical measurements, such as distances between loci, 3D shapes, or volumes; (IV) They do not provide information on nuclear localization. These limitations can be overcome by novel microscopy methods that we will explore in the following section.

1.5.5 Micro-C

Hi-C resolution is limited to around 1 Kb by the restriction enzymes used, and the sequencing depth. Resolution of C-based maps was improved by a novel technique called Micro-C [Hsieh et al., 2015], which fragments chromatin without restriction enzymes. Instead, a micrococcal nuclease is used, leading to chromatin fragmentation at the nucleosome level. Micro-C was used to obtain high resolution maps of chromatin folding in yeast [Hsieh et al., 2015], unveiling a tri- or tetra-nucleosome motif in chromatin fibers, the presence of self associating domains similar to those present in other species, but shorter than mammalian TADs, and that self associating domain boundaries occur at promoters of highly transcribed genes and regions of rapid nucleosome turnover. In human ESCs and fibroblasts, Micro-C revealed thousands of newly identified loops, many of which are localized along loop extrusion stripes, suggesting that their anchors are weak pausing sites that slow or stall structural maintenance of chromosomes (SMC, cohesin) proteins movement [Krietenstein et al., 2020]. This also suggest that TADs are a heterogeneous population of multiple transient loops. In mouse, Micro-C revealed that TADs are segregated into fine-scale structures, consistent with microscopy studies that show partitioning of TADs into nano-domains [Hsieh et al., 2020, Szabo et al., 2020]. Although Micro-C is a good technique to study local chromatin architecture, it is not as

efficient as Hi-C to capture long-distance and inter-chromosomal contacts [Akgol Oksuz et al., 2021]. Furthermore, it is still a method that is based on sequencing, so it keeps many of the limitations previously described.

1.5.6 Other sequencing-based techniques

C-based methods have been useful for understanding chromatin architecture. As we saw, they have some intrinsic limitations and bias. Other sequencing-based techniques have also been developed to overcome some of them, in particular to overcome the fact that C-methods: I) rely on formaldehyde crosslinking, that is limited when capturing interactions of proteins with short residence times, or with few aminoacids that can be crosslinked [Baranello et al., 2016, Gavrilov et al., 2015]; II) rely on ligation of fragments before sequencing, which is not always efficient; III) depends on paired-end sequencing, which does not capture multipartite interactions.

Genome Architecture Mapping (GAM) consists in the cryosection of nuclei, recovery of the DNA present in each section, and sequencing. These procedure generates contact maps based on the frequency at which DNA regions are found together in each of the cryosections of different nuclei [Beagrie et al., 2017]. The technique recovers features described by Hi-C, and also allows the detection of multi-way interactions between loci. Another sequencing-based technique that was recently developed is SPRITE [Quinodoz et al., 2018], where nuclei are crosslinked, isolated and fragmented; then crosslinked pieces of chromatin are uniquely barcoded; after high-throughput sequencing is performed, and reads carrying the same combination of barcodes represent genomic sites that are a part of the same crosslinked cluster.

As these techniques are sequencing based, they keep many of the limitations previously described. These limitations can be overcome with microscopy.

1.6 Techniques to dissect chromatin organization: Microscopy techniques

Imaging has been historically crucial to study cellular organization, from the nanometer scale of proteins, to the tens of micrometers occupied by entire cells.

1.6.1 DNA FISH

Fluorescent in Situ Hybridization, or FISH is a technique that started to be developed from the 1960s. The technique consists in the hybridization of probes that are complementary to a genomic region of interest. The first in-situ hybridization of DNA used radioactive labels to stain *Xenopus* cells [Gall and Pardue, 1969]. Soon after, fluorescent labels replaced the radioactive ones, since they were more stable, easy to use and to detect [Rudkin and Stollar, 1977, Bauman et al., 1980, Langer-Safer et al., 1982]. At that time, probes were synthesized from cloned sequences from bacterial artificial chromosome libraries or from polymerase chain reaction (PCR) on extracted genomic DNA. Fluorescent labels were added via the use of nick-translation probes with fluorescein-labeled bases [Wiegant et al., 1991]. In recent years, new tools opened the way for synthetic FISH probes that hybridize their targets with high coverage. Oligonucleotide libraries (or oligopaints) are one of the most used labeling tools, since they offer the possibility of detecting chromosomal regions from a few kilobases to full chromosomes [Beliveau

et al., 2012, Beliveau et al., 2015, Beliveau et al., 2018]). A conventional FISH protocol is described below. For a full description, see section 4.5 in Materials and methods. DNA-FISH comprise the following steps: First, samples are fixed with formaldehyde. Then, usually a permeabilization step is performed to facilitate the entry of FISH probes and thus increase the hybridization efficiency. After this, genomic DNA is denatured by placing the sample at 80°C for 15 minutes (although this depends on the cells or tissues being labeled). Finally, probes are added in a suitable buffer, and let at 37°C to hybridize to genomic DNA. Several wash steps follow to remove unbound probes.

Since its implementation, DNA-FISH allowed the imaging of chromatin at different scales. The simplest imaging method is the wide-field configuration. Diffraction of light within the optical system poses a limitation into the resolution with which point sources can be imaged. Theoretically, the image of a point source through an optical system is described by an Airy pattern. However, experimental aberrations modify this theoretical pattern. The real image of a point source through a microscope is called the point spread function (PSF), and PSFs that overlap can not be resolved. The resolution of an optical system is defined by the distance at which two point sources can be resolved in the image plane. For several applications, resolution may be a limitation, thus super-resolution methods have been developed to improve it, and obtain finer details on chromatin substructures. Importantly, multiplexed techniques have been recently introduced, allowing the detection of several loci at once. These implementations and the main applications will be discussed below.

1.6.2 Conventional Wide-field microscopy approaches

Conventional microscopy coupled to DNA-FISH demonstrated that CTs have a radial distribution, with gene-rich, active regions oriented towards the nuclear center, and gene-poor regions located towards the nuclear periphery [Croft et al., 1999, Boyle et al., 2001, Cremer et al., 2003, Bolzer et al., 2005, Murmann et al., 2005, Küpper et al., 2007, Goetze et al., 2007, Grasser et al., 2008]. Radial positioning can also depend on chromosome size, at least in human fibroblasts [Bolzer et al., 2005]. This distribution is not fixed, and changes during development and within a cell population [Mayer et al., 2005]. Furthermore, *Drosophila* chromosomes adopt a polarised orientation, called Rabl configuration, where centromeres and telomeres are located at opposite poles of the cell [Hochstrasser et al., 1986, Marshall et al., 1996]. Imaging of CTs showed structures of different shapes and sizes [Khalil et al., 2007, Küpper et al., 2007], while other studies identified Mb-Sized sub-CTs structures, based on imaging of replication foci [Schermelleh et al., 2001, Albiez et al., 2006, Malyavantham et al., 2008]. Use of DNA-FISH coupled to conventional microscopy approaches provided important evidence to support the existence of topologically associating domains [Nora et al., 2012, Dixon et al., 2012, Sexton et al., 2012].

Functional long range (LR) associations between distant foci have also been observed. Active regions have been observed to cluster into RNA pol II foci, forming "transcription factories" [Jackson et al., 1993, Iborra et al., 1996, Osborne et al., 2004]. Also other functional LR interactions were identified, notably between PcG loci that colocalize into PcG bodies, believed to reinforce repression [Bantignies et al., 2011]. Conventional microscopy has also been used to study homologue pairing. In *Drosophila*, homologous chromosomes remain paired during a large part of embryonic development. A DNA-FISH based, high-throughput screening technique as used to identify genes involved in homologous somatic

pairing [Joyce et al., 2012]. Identified genes were classified into "pairing-promoting genes" and "anti-pairing genes", showing that this process can be enhanced or antagonized.

Conventional microscopy is one of the most important techniques that help us understand chromatin organization. However, it has some limitations, mainly throughput and resolution. The number of colors that can be imaged simultaneously is limited to 3-4 due to overlapping emission spectra, limiting the number of loci that can be detected at once. The second limitation is resolution. Typically, the resolution limit of conventional microscopes ranges between 200 and 300nm, depending on imaging wavelength, numerical aperture of the microscope and the optical system itself. In the following subsection, I'll describe super-resolution techniques, that tackle this latter limitation.

1.6.3 Super-resolution microscopy

A huge challenge in microscopy has been to increase the resolution limit of conventional microscopy, developing new techniques collectively known as super-resolution microscopies (SRM). Here I'll focus in two SRM techniques, known as Structure illumination microscopy (SIM) and Single-Molecule localization microscopy (SMLM), and I'll describe relevant findings using these techniques.

1.6.4 Structured illumination microscopy

One way to improve the resolution limit is to use a widefield configuration, with a movable diffraction grating in the excitation path. Zero-order or first-order diffracted laser beams are let to reach the objective. These laser beams interfere with each other at the focal plane, creating sinusoidal alternating intensity maxima and minima of illumination. The overlap between the high frequency (physically close) organization of the sample and the high frequency of the illumination stripes creates a pattern of lower frequency which is well collected by the objective. This pattern is known as a Moiré pattern. By acquiring several raw images, each with a different orientation and phase of the excitation pattern, allows the reconstruction of a super-resolved image. SIM allows for a 2-fold increase in resolution in each axis, leading to a total 8-fold increase in 3D resolution with 3D-SIM, with respect to conventional microscopy [Gustafsson, 2000, Gustafsson, 2005, Gustafsson et al., 2008] (figure 8).

Using this technique, several interesting features have been observed. One of the first studies that used 3D-SIM imaged chromatin and nuclear pore complexes (NPC) at the same time, observing that chromatin forms a fibrous structure with heterochromatic condensed regions close to the nuclear envelope. But the novelty of super-resolution was to show that DNA is excluded from NPCs, creating chromatin-free channels underneath them [Schermelleh et al., 2008]. This is a feature that could not be observed with conventional techniques.

More recently, 3D-SIM was used to measure the contact frequencies between TADs borders in *Drosophila*, showing that genome organization is not formed by stable long-lived interactions, but rather by transient low-frequency contacts, modulated by different organization levels and cell types [Cattoni et al., 2017]. 3D SIM was also recently used to show that chromatin is organized in discrete nano-compartments in single cells that correspond to repressed TADs [Szabo et al., 2018], which are separated by active domains. These compartments interact preferentially with compartments of the same epigenetic type. Another application of the 3D-SIM revealed that mammalian TADs are divided

into small chromatin domains, termed chromatin nano-domains (CNDs) [Miron et al., 2020, Szabo et al., 2020].

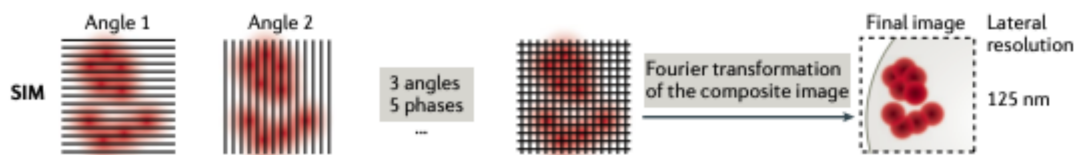


Figure 8: Scheme of SIM microscopy. The sample is illuminated with different illumination patterns. The obtained images are analysed by Fourier transformation to reconstruct the final image. Lateral and axial are improved by a factor of two in each axis, giving an 8-fold volumetric resolution increase. Image adapted from [Jerkovic´ and Cavalli, 2021]

1.6.5 Single-Molecule Localization Microscopy

As mentioned above diffraction within the microscope limits the spatial resolution achievable by conventional microscopes. Thus, fluorophores that are closer than the diffraction limit of light can not be resolved because their PSFs overlap. But if the emission from each fluorophore can be acquired at different times, then the position of each fluorophore could be determined by locating the center of the PSF of each fluorophore with high accuracy [Yildiz et al., 2003]. Several methods were developed where fluorophore photophysics are used to temporally separate the emission of fluorophores, including photoactivated localization microscopy (PALM, [Betzig et al., 2006]), and stochastic optical reconstruction microscopy (STORM, [Rust et al., 2006]). Super-resolution is achieved via photoactivatable proteins are reversibly/irreversibly turned on (PALM), or via the reversible stochastic photoswitching properties of organic dyes in the presence of a reducer in an oxygen-depleted medium. Other variations of these concepts were introduced since, but we will not review them here as it is not within the scope of this introduction. For simplicity, techniques relying on the principles highlighted above are called single-molecule localization microscopies (SMLM). In SMLM, images are acquired in widefield configuration and thousands of image frames are acquired, from where the positions of the fluorophores are determined. Single-molecule localizations are assembled into a single reconstructed image to obtain the final super-resolved image (figure 9). These techniques allow for a localization precision of 10-30 nm in XY and 10-75 nm in Z, that can be improved using brighter probes [Sydor et al., 2015].

SMLM techniques were used to study several features that were not accessible to conventional microscopies. Using 3D-STORM, chromatin of different epigenetic states was imaged [Boettiger et al., 2016]. This revealed different folding properties between active, inactive and PcG chromatin. Active chromatin was the more decondensed structure, while PcG repressed chromatin was the most condensed. Also, PcG repressed chromatin was shown to physically segregate from active chromatin. A second study used immunolabeling of active and repressed marks (H3K4me3 and H3K27me3 respectively) combined with dSTORM (direct STORM, which uses conventional fluorescent dyes), to show that epigenetic marks form discrete nano-compartments and that these active and repressed compartments are strictly segregated in single cells [Cattoni et al., 2017]. At smaller scales, nucleosomes were found to form heterogeneous clutches separated by nucleosome-depleted regions [Ricci et al., 2015]. PALM and STORM were also combined with live-cell imaging to understand the dynamics of DNA in vivo [Benke and Manley, 2012, Nozaki

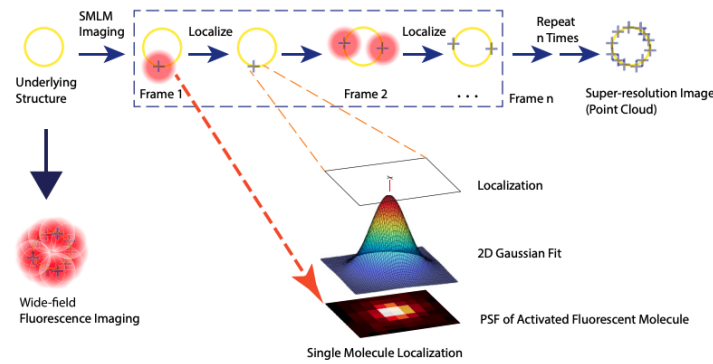


Figure 9: Basic scheme of SMLM microscopy principle. Imaging a biological structure (yellow circle) with a conventional diffraction-limited technique gives a blurred image. However, imaging the same structure in a time-separated manner where only a subset of the fluorophores is lightened up at each frame allows to obtain a high resolution image. Image adapted from [Khater et al., 2020]

et al., 2017]. Nucleosomes form compact domains of 160 nm diameter that move coherently. Consistent with other observations, heterochromatin moves less and is formed by more domains [Nozaki et al., 2017].

Super-resolution techniques proved useful to better understand chromatin organization. However, an important remaining limitation is the number of colors that can be imaged simultaneously (typically 2-3). This is an important issue, as it limits the number of genomic loci or epigenetic marks that can be imaged at any one time. In the following section, I'll describe a novel microscopy technique called Hi-M, that couples oligopaint technology with microfluidics, to overcome the limitation in the number of loci that can be imaged. During the first year of my thesis, I participated in the development of the technique in my host lab.

1.6.6 Hi-M

Visualization of several (more than two) genomic loci is necessary to better understand the relationship between chromatin architecture and gene expression. For instance, to see if specific promoter-enhancer configurations lead to active transcription. For this, we would need a microscopy technique that: (I) allows the localization of multiple genomic loci at the same time in single cells with genomic specificity (that is, knowing to which loci do detected spots correspond to); (II) maintains the spatial information of where each loci is within the nuclear volume and within the organism (e.g. embryo); (III) can be combined with RNA-FISH to monitor the transcriptional state of each cell being imaged so that chromosome architecture and transcriptional state can be linked in single cells. Recently, we developed Microscopy-based chromosome conformation capture, or Hi-M [Cardozo Gizzi et al., 2019, Cardozo Gizzi et al., 2020], an imaging method that uplifts these limitations (figure 10).

Hi-M uses Oligopaints-FISH to generate primary oligonucleotide libraries that target multiple genomic loci at once. Each oligonucleotide in a primary library contains two regions: a region of homology complementary to the genomic region being targeted; and a tail encoding several repeats of a locus-specific readout sequence. This sequence can be hybridized to a complementary, fluorescently-labeled oligonucleotide that is delivered with a microfluidics device and is used to image the 3D spatial location of the locus being

labeled. By performing this process sequentially, one can image the 3D location of as many loci as imaging rounds. Similar methods were also used by other groups [Wang et al., 2016, Bintu et al., 2018, Nir et al., 2018, Mateo et al., 2019]. These techniques are extremely useful because of their ability to image multiple (20-100), small (1kb) genomic loci with nanometer resolution. Furthermore, Hi-M can be combined with RNA-FISH, immunostaining, and imaging of chromatin marks to retrieve multi-omics datasets with spatial information.

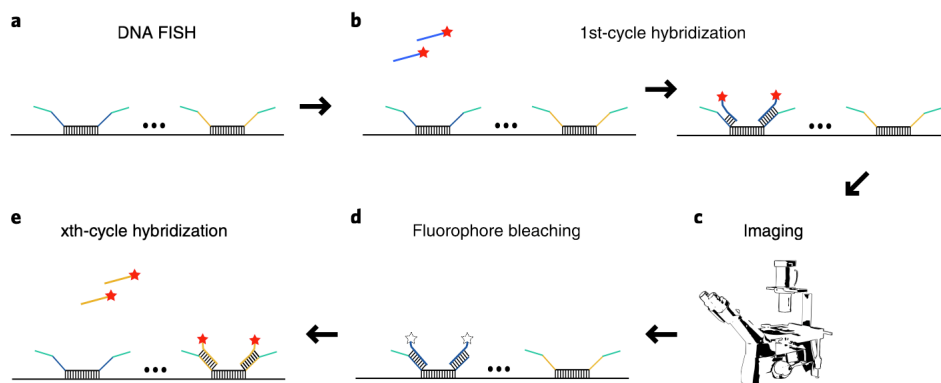


Figure 10: Scheme of Hi-M experiment. Briefly, oligonucleotide probes are hybridized to genomic DNA. The sample is placed onto a microfluidics chamber. Then, using a microfluidics device coupled to a microscope, a solution containing the imaging oligos is injected into the sample. The targeted locus is imaged, and then bleached. Then this process is repeated to image all loci of interest. Image adapted from [Cardozo Gizzi et al., 2020]

Sequential hybridization methods proved crucial in the study of chromatin structure. One of the first sequential hybridization techniques was called MERFISH (from Multiplexed Error-Robust FISH) [Chen et al., 2015]. MERFISH combined sequential hybridization with combinatorial encoding and was used to detect 100 to 1000 different RNAs, depending on the number of hybridization rounds and the type of encoding strategy. This allowed the single cell measurement of the spatial distribution of different RNA species and the identification of groups of co-varying genes that share common regulatory elements.

The technique was quickly adapted by us and others to probe DNA architecture. The first family of methods possessed low genomic resolution, was not able to detect DNA and RNA at once, and was applied to human cell cultures. Wang *et al* imaged the spatial organization of TAD centers in human cells at 100kb resolution, and showed that TADs are organized in a spatially polarized manner in single chromosomes, consistent with A/B compartmentalization of active and repressed chromatin [Wang et al., 2016]. A higher resolution version of this method was used to show that TAD-like structures are present in single cells and form spatially segregated globular structures [Bintu et al., 2018]. Domain boundaries displayed high cell to cell variability, and were preferentially located at CTCF and cohesin binding sites. This evidence supports the idea that TADs are physical structures present in single cells, although their borders display cell to cell variation. A variation of this method combined super-resolution microscopy with sequential imaging to image eight TADs in human chromosome 19 [Nir et al., 2018] and observed that homologous chromosomes are distinctly folded. Two very recent papers extended the capabilities of sequential imaging techniques, combining the detection of thousands of loci at the same time (both at the intra- and inter-chromosomal levels) with RNA transcript labeling and immunofluorescence-based approaches to label nuclear structures and histone

marks [Takei et al., 2021, Su et al., 2020]. These promising techniques allow to measure simultaneously chromatin architecture, transcription, nuclear structures and chromatin states.

However, these previous early works were performed in cultured cells. This experimental system suffers from intrinsic heterogeneities: (1) single cells are not executing the same transcriptional program, and (2) they are at different cell cycle stages. These intrinsic heterogeneities makes it difficult to correlate 3D chromosome structure and function (e.g. transcription). To further study how TAD structure changes in single cells and its relation to transcriptional activity in a tractable biological system, Hi-M (Microscopy-based Chromosome Conformation Capture) was developed (concomitantly with the development of Optical Reconstruction of Chromatin Architecture, or ORCA). The ability of Hi-M to detect both chromatin architecture and transcription is fundamental to be able to group together cells with similar, specific patterns of gene expression. Hi-M has been first used to study the relation between TAD structure and gene expression in full *Drosophila* embryos [Cardozo Gizzi et al., 2019]. Using simultaneous DNA and RNA labeling, we revealed that paired and unpaired chromosomes have equivalent architectures, but unpaired chromosomes have a more decompacted folding. This was also observed using haplotype-resolved Hi-C [Erceg et al., 2019]. In a second, more recent study, Espinola and Gotz [Espinola et al., 2020] studied interactions between cis-regulatory modules (CRMs), and their relation to transcriptional states. Using the dorsoventral patterning system of *Drosophila*, they applied high resolution Hi-M (3kb genomic resolution) to study a TAD containing three genes (*doc1-3*) displaying a similar dorsal pattern of expression. They found that most intra-TAD loops involve CRMs, but strikingly, they do not depend on transcriptional status [Espinola et al., 2020], suggesting that chromatin architecture plays a double role in activation or repression. CRM loops are established in early development, before the emergence of TADs and of transcriptional activation, and are dependent on the pioneering factor Zelda. Studies using ORCA investigated the structural changes in intra-TAD organization of the Bithorax Complex (BX-C) [Mateo et al., 2019]. This study observed that cells displaying different expression patterns show differential TAD organizations.

1.7 Polymer modeling of chromatin

DNA is a polymer, made of similar units or monomers (nucleotides) assembled together. FISH and Hi-C experiments revealed that the decay of contact probability with genomic distance follows a power law, and characteristic of polymers [Lieberman-Aiden et al., 2009, Sexton et al., 2012, Finn et al., 2019, Cattoni et al., 2017, Cardozo Gizzi et al., 2019]. To better understand the physics of chromatin folding, several modeling approaches have been developed in the last decade. Here, I'll briefly describe the most common modeling strategies used.

1.7.1 Early models: Fractal globule and Loop models

Early models considered chromatin as a homogeneous polymer, with identical monomers. The dynamics is mostly described by thermal forces, the non-overlapping of monomers, although other factors can be added to the model (for example, rigidity of the fiber or non-specific interactions between monomers) [Jost et al., 2017]. One of the first modelling strategies inspired by the power law decay of contact probability was the Fractal

Globule model (FG) [Grosberg et al., 1993]. In this model, the polymer folds into small globules that can in turn fold into larger globules. Chromatin then folds hierarchically without entanglement. Being un-knotted is an important requirement for models, since fast folding and unfolding is essential for biological processes [Mirny, 2011]. On top of these important characteristics (respecting power law for contact probability, being un-knotted, and folding in a hierarchical manner), there are other properties that make FG good candidates: (A) the lifetime of the FG conformation is long enough to remain stable through the cell cycle; (B) its fractal nature explains the formation of chromosome territories; (C) protein diffusion is faster for FGs than for other models, and (D) it facilitates the search of DNA binding proteins for their specific binding sites [Smrek and Grosberg, 2015]. However, the FG model does not describe accurately some known phenomena: it does not account for chromatin compartmentalization, and observed contact probabilities decay do not always follow the FG exponent (-1).

Another early model is known as Loop Model (LM) [Münkel and Langowski, 1998, Münkel et al., 1999]. This family of models consist in the cross-linking of the polymer chain into loops, and then into the arrangement of those loops into compartments. This model reproduces the organization of chromatin into chromosome territories, and the physical distances measured by FISH. Based on the detection of loops using 'C' technologies, several kinds of loop based models were developed [Bohn et al., 2007, Mateos-Langerak et al., 2009], that successfully predicted chromosome territories, the preference of inactive regions to locate near the nuclear envelope, TAD formation, and higher compaction of heterochromatin [Ganai et al., 2014, Kim et al., 2011, Bohn and Heermann, 2011]. However, the sizes of those loops are limited, thus they do not account for large scale compartmentalization.

1.7.2 Strings and Binders Switch Model (SBS)

More recently, a new family of models emerged. One example is the 'strings and binders' (SBS) model [Nicodemi and Prisco, 2009, Barbieri et al., 2012]. In this model, chromatin is considered as a self-avoiding polymer chain of beads (figure 11). The beads interact with diffusing molecules, called "binders", that are present in solution at a given concentration c . Binders can bridge pairs of beads and form loops, driving the folding of the chain. This interaction has an energy E_{int} . Different phases (conformations) exist, according to the values of these two degrees of freedom, E_{int} and c . Basically polymer conformations can be divided in a coil (open) conformation, and a globule (closed) conformation. Phase diagrams for the SBS model show both coil and globule conformations. A line separating those two states exists (that is, a line in the phase diagram separating two different phases, also known as θ line in the context of polymer physics), with stable conformations only arising above this threshold (in coil regime, the polymer is open and randomly folded). TAD formation was correctly reproduced by this model, and required two types of binding sites in the polymer [Barbieri et al., 2012, Barbieri et al., 2013, Chiariello et al., 2016].

In the SBS model, several parameters can be tuned, for example, the types of number of binding sites and binders, and the affinity between binders. Several studies exploited this degrees of freedom to explain experimentally-observed data. In one study, adding a third kind of binding sites correctly reflects the meta-TAD compartmentalization and inter-TAD contacts in mammals, while maintaining TAD structure [Fraser et al., 2015a]. Another study used a similar SBS model to study DNA architecture in the mouse alpha

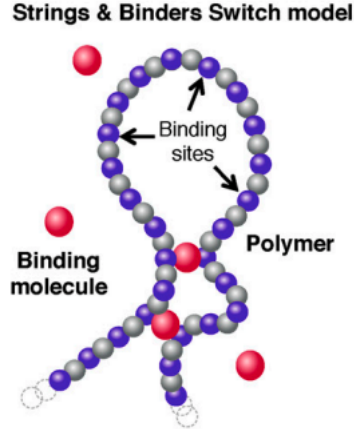


Figure 11: Schematic representation of the SBS model. Chromatin is represented by a self avoiding polymer, represented by n beads. A fraction of those beads can interact with binders, and are called binding sites. Molecules can bind to more than one binding site, forming loops. Image adapted from [Barbieri et al., 2012]

and β -globin locus [Brackley et al., 2016a]. By modeling interactions between proteins and locations of DNase1 hypersensitive sites (DHSs), CTCF binding sites, and H3K4me1 regions, they successfully reproduced Capture-C data for this locus. The authors also used a similar model with two kinds of binders interacting with euchromatin and heterochromatin, successfully reproducing Hi-C data for a 12Mb region of human chromosome 12 [Brackley et al., 2016b].

Another application of the SBS model was to consider active genes and polycomb-repressed genes in the mouse HoxB region [Barbieri et al., 2017], where the simulations correctly predicted that genes in the same activation state are spatially close, as observed via FISH experiments. They also explored the hypothesis that CTCF alone drives the locus organization. Modeling predictions with CTCF-driven folding were not compatible with their microscopy observations, suggesting that other factors are involved. These kind of models were also applied to study the effect of structural variants in genome topology [Chiariello et al., 2016, Bianco et al., 2018]. Deletions of TAD borders in the Xist locus are known to increase inter-TAD interactions [Nora et al., 2012]. SBS modeling of this region correctly recovers this behavior [Chiariello et al., 2016]. Furthermore, a model that predicts the effects of deletions, inversions and duplications was proposed [Bianco et al., 2018]. The accuracy of the model was confirmed using the Epha4 locus in mouse. Overall, the SBS model correctly predicts chromatin architecture at scales up to a few Mb. However, it still does not predict folding at larger scales, for example, reproducing compartment formation.

1.7.3 Block Copolymer models

In Block Copolymer models [Jost et al., 2014], chromatin is fragmented into "beads" of a certain size (figure 12). These beads can display attractive interactions between each other, based on the epigenetic signature that they represent. Thus, bead interaction depends on the local epigenetic state, and this introduces a non-mixing between monomers of different state. The dynamics is driven by epigenetic attractive interactions and bending stiffness of the chain.

An application of the model was done using 120 beads. Each bead represents 10Kb of chromatin, so the model describes regions of approximately 1Mb. The model considers

two types of interactions: (i) non-specific interactions with energy U_{ns} between every pair of monomers that accounts for compaction effects due to confinement into the nucleus; and (ii) specific attractive interactions with energy U_s between monomers having the same epigenetic state. Hence the total energy can be written as $E_{mn} = U_{ns} + \delta_{mn}U_s$ with $\delta_{mn} = 1$ if monomers m and n have the same epigenetic state, or $\delta_{mn} = 0$ if they have different epigenetic states.

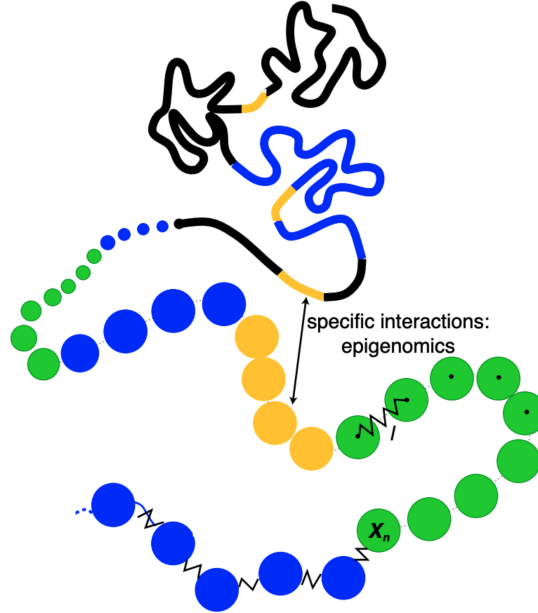


Figure 12: In Block Copolymer models, chromatin is modeled as a self-avoiding bead chain, each bead representing a portion of DNA (usually of some Kb in length). The polymer is divided in beads of different epigenetic states. In this picture, yellow represents active chromatin, green represents constitutive heterochromatin, blue represents PcG-bound chromatin, and black represents black chromatin. Image adapted from [Jost et al., 2014]

This model shows a phase diagram in which chromatin can exist in four different states. First, for weak interaction energies and low specificity, we have the coil regime, where the chain has an extended chain conformation. If interaction energy (compaction) is increased at low specificity, the chain undergoes a θ -collapse transition to a globule compact phase. For strong compaction and specificity, a checkerboard-like contact map is observed. This is characteristic of microphase separation where monomers of the same epigenetic state are packed into distinct separated domains. Microphase separation is a phenomenon generated by block copolymers composed of incompatible chemical components, where they tend to spontaneously form separated structures with microscopic length scales. Between coil and microphase separated regions there is a region of multi-stability, where the equations governing the system have multiple fixed points depending on initial conditions. These solutions represent intermediate configurations between the coil and micro-phase separated state. At this scale, multi-stable solutions represent a state in which epigenetic domains collapse internally, but are isolated from each other, forming TADs.

Another block copolymer model was established, in which no interactions were present between euchromatin, but only attractive interactions between heterochromatin were present [Ulianov et al., 2016]. In this case, a key role for euchromatin in the formation of TADs was found, in accordance with experimental data. Other models were proposed, with three different kinds of chromatin: euchromatin, heterochromatin and constitutive

heterochromatin [Falk et al., 2019]. Tuning the intensity of inter and intra block interactions, as well as interactions with the nuclear lamina, they were able to reproduce the architecture of different single cells observed by imaging techniques. In another example of modeling with block copolymers, chromatin was divided into two blocks of different flexibility and thickness that correspond to 10nm and 30nm fibers [Florescu et al., 2016]. The objective of this study was to quantify how heterogeneous chromatin fibers affect small and large scale structure. The authors showed limited effects of this chromatin compositions, below 10Kb scales, and in time-scales of the order of a few seconds. The block copolymer model was also used to simulate the folding of a region of 20 Mb, reproducing the formation of both TADs and compartments [Ghosh and Jost, 2018].

Another interesting model based on block copolymers is known as Living Chromatin (LC) model [Jost and Vaillant, 2018], where monomers can be in one of three epigenetic states: active, inactive or unmarked. Monomers can change their state from active to inactive (or vice-versa) passing through the intermediate unmarked state. This model takes into account the dynamical coupling between 1D epigenetic state and 3D folding. LC model describes the formation of domains of active and inactive chromatin, and describes the role of epigenetic features in the formation of TADs. In particular, an interesting prediction of the model is that spatial compaction of the polymer enhances domain epigenetic stability (which in turn enhances epigenetic state propagation, showing an interplay between structure and function). This is consistent with the increase of local concentrations of regulatory proteins (like PcG for example) due to physical proximity, allowing distal interactions between domains of the same type.

Overall, block copolymer models were able to reproduce chromatin architecture at different scales, being one of the most promising approaches to model chromatin folding.

1.8 Objective of this work

As discussed above, evidence suggest that PcG proteins associate together in single cells to form PcG foci [Delest et al., 2012, Bantignies and Cavalli, 2011, Isono et al., 2013]. These foci are thought to be physical sites where chromatin is repressed [Lanzuolo et al., 2007, Bantignies et al., 2011]. This suggests that genes within PcG TADs may associate in single cells, forming repressive compartments containing multiple interacting partners. The objective of my work is to test this hypothesis by studying the chromosome-wide architecture of PcG TADs during *Drosophila* embryogenesis, with a method that restores chromosome conformation while maintaining spatial information (thus enabling the study of PcG domain architecture in different embryonic segments). For this, we adapted and validated Hi-M to image multi-layered samples by resorting to a coupling of microfluidics and a confocal microscope setup. We also collaborated with theoretical physicists to implement polymer models and compared them to experimental data to understand the mechanisms behind PcG chromatin organization.

2 Results

In this chapter I present the results of our work, as a paper that is prepared for submission. For this work, the design and planning of experiments was done together with my thesis supervisors. I performed the library design, choosing the target regions. These selection was discussed with Frédéric Bantignies and Marcelo Nollmann. The oligos DNA sequence was generated by Marcelo Nollmann, using the oligopaints website (<https://oligopaints.hms.harvard.edu/>). They were mined using OligoArray [Rouillard et al., 2003]. Together with Christophe Houbron, we amplified the library. I performed *Drosophila* WT (NC14 and S15-S16) embryos recollection and fly handling. Together with Frédéric Bantignies, we performed the *PcXT109* mutant embryo collection. I performed all Hi-M experiments, from labeling embryos with the primary library, to data collection and deconvolution. The setup for confocal Hi-M imaging, as well as the wide-field Hi-M setup were built by Jean-Bernard Fiche. I performed image analysis using home-made MATLAB and Python software, coded by Marcelo Nollmann. Together with Marcelo Nollmann, we coded Python scripts to analyse the data. Polymer simulations were done by Jean-Charles Walter. Results were discussed by all authors. Figures were made with crucial input from Marcelo Nollmann and Frédéric Bantignies. Giacomo Cavalli gave important input for data analysis and interpretation. The paper was written together with Jean Charles Walter, Frédéric Bantignies and Marcelo Nollmann.

Chromosome tracing reveals that long-range, 3D clustering of *Drosophila* Polycomb genes predominantly involves pairwise coordination

Julian Gurgo¹, Jean-Charles Walter³, Jean-Bernard Fiche¹, Christophe Houbbron¹, Giacomo Cavalli², Frédéric Bantignies^{2,#}, Marcelo Nollmann^{1,#}

¹ *Centre de Biochimie Structurale, CNRS UMR 5048, INSERM U1054, Université de Montpellier, 60 rue de Navacelles, 34090, Montpellier, France*

² *Institut de Génétique Humaine, CNRS UMR 9002, Université de Montpellier, 141 rue de la Cardonille, 34396, Montpellier, France*

³ *Laboratoire Charles Coulomb (L2C), Univ. Montpellier, CNRS, Montpellier, France.*

corresponding authors: frederic.bantignies@igh.cnrs.fr, marcelo.nollmann@cbs.cnrs.fr

Abstract

Polycomb group (PcG) proteins are transcriptional regulators with key roles in cell identity and differentiation. PcG-bound chromatin regions are organized into repressive TADs, known as Polycomb domains. In the nucleus, they segregate in PcG foci, where PcG target genes colocalize when co-repressed. Evidence from microscopy and chromosome conformation capture techniques shows that PcG targets tend to preferentially interact with each other, suggesting that they form repressive compartments. However, little is known about the nature of these interactions, or if several PcG genes are associated in 3D to form compartments. Here, we investigate the role of Polycomb group proteins in the formation of repressive compartments during *Drosophila* development. We found that Polycomb domains undergo low frequency, mostly pairwise interactions. Furthermore, polymer modeling of chromatin shows that PcG domains behave as a microphase-separated polymer. Simulations are highly consistent with experimental data. Our results extend the current knowledge of Polycomb-mediated 3D chromatin organization.

Introduction

Chromatin is folded in a hierarchical, multi-level organization, ranging from nucleosomes to chromosome territories. Chromosome conformation capture techniques revealed that at an intermediate level, chromatin is organized in Topologically Associating Domains (TADs) (Dixon et al. 2012; Nora et al. 2012; Sexton et al. 2012; Hou et al. 2012). TADs can affect several biological processes, like gene regulation (Cavalli and Misteli 2013; Andrey and Mundlos 2017). In *Drosophila*, TADs are generally smaller than in mammals (median size of ~ 100 kb versus ~ 800 kb, respectively) and tend to correlate with active and repressed chromatin marks (Sexton et al. 2012; Szabo, Bantignies, and Cavalli 2019). *Drosophila* TADs are classified according to their epigenetic state into active (associated with H3K4me3 and H3K36me3), heterochromatic (enriched in H3K9me2, HP1, Su(var)), black (devoid of specific histone marks) and Polycomb repressed, enriched in H3K27me3 and bound by Polycomb group proteins (PcG proteins).

PcG proteins are conserved in most eukaryotic organisms. They mediate gene repression, and are classified into two main complexes, PRC1 and PRC2. In *Drosophila*, PcG proteins are recruited to specific sequences called Polycomb Response Elements (PREs) (Nègre et al. 2006) by a two-step process (Wang et al. 2004) involving the deposition of H3K27me3 marks by PRC2, followed by chromatin compaction by PRC1 (Francis, Kingston, and Woodcock 2004; Grau et al. 2011), a complex that contains the chromodomain protein Polycomb (PC), and Polyhomeotic (PH). PcG target genes are often contained within discrete PcG TADs (Sexton, 2012), which are characterized by a high degree of compaction and intermixing (Boettiger et al. 2016; Wani et al. 2016). In single cells, PcG TADs form discrete nano-compartments (Szabo et al. 2018) displaying a cell-type specific internal organization that responds to the transcriptional state of its PcG genes (Mateo et al. 2019). PcG proteins form discrete compartments (foci) in the nucleus, both in flies and mammals (Saurin et al. 1998; Buchenau et al. 1998; Bantignies et al. 2011). Genomically-distant PcG target genes can physically colocalize within PcG foci when co-repressed (Lanzuolo et al. 2007; Bantignies et al. 2011). Recent studies showed that mammalian PRC1 components can form phase-separated compartments (Plys et al. 2019), suggesting that PcG genes within PcG TADs may coalesce in 3D to form phase-separated condensates.

In *Drosophila*, PcG TADs tend to be spatially segregated from active domains (Boettiger et al. 2016; Szabo et al. 2018), consistent with the formation of active and repressive compartments (Sexton et al. 2012), and with the spatial separation of active and repressive marks in single cells (Boettiger et al. 2016; Cattoni et al. 2017). Taken together, this evidence suggests that multiple PcG TADs may often associate with each other in single cells to form PcG foci to reinforce gene repression.

Here, we tested this hypothesis by applying Hi-M, an imaging-based method that enables the capture of chromatin conformations in single cells while preserving the spatial information within the specimen (Cardozo Gizzi et al. 2019; 2020). We found that at the chromosomal scale the organization of PcG domains can be well described by a microphase-separated polymer. In addition, PcG domains rarely contacted each other, and most of these contacts involved only two PcG domains. Formation of hubs involving more than two PcG domains was highly infrequent. Interestingly, the interaction frequencies between PcG domains were enhanced in regions of the embryo where PcG target genes were co-repressed or co-expressed, indicating that 3D physical proximity between Polycomb domains may not only play a role at reinforcing repression but also in co-transcriptional activation.

Results

Chromosome-wide, simultaneous visualization of multiple Polycomb targets in single cells

To investigate the chromosome-wide organization of Polycomb targets, we focused on a ~15Mb region of chromosome 3R (chr3R) displaying most long-range Polycomb contacts (Sexton et al. 2012; Bantignies et al. 2011; Tolhuis et al. 2011). Within this region, we identified 19 genomic loci displaying binding of all PRC1 components (PC, PH and PSC) (Fig. 1A and S1A). This included PcG targets within the three large PcG TADs containing *Drosophila's* *hox* genes: Bithorax (BX-C), Antennapedia (ANT-C) and NK-C, in addition to 8 smaller non-*hox* PcG-regulated target genes (Fig. 1A). Next, we used Hi-M, an imaging-based technology that we and others recently developed to retrieve chromatin architecture in single cells while maintaining spatial context (Cardozo Gizzi et al. 2019; 2020; Mateo et al. 2019; Bintu et al. 2018; Takei et al. 2021; Su et al. 2020). Hi-M relies on the sequential imaging of tens of distinct genomic loci labeled by oligopaint-FISH (Beliveau et al. 2012) in intact *Drosophila* embryos (Cardozo Gizzi et al. 2019, 2020) (Fig. 1B, Fig. S2A). These methods were previously used in samples with single cell layers (e.g. cultured-cells, *Drosophila* embryos before gastrulation, or cryo-sections). Here, we coupled Hi-M to confocal imaging to be able to visualize the 3D localization of multiple Polycomb (Pc) target regions in multi-layered stage 15 - 16 (S15-S16, 12-16h of development) embryos without cryo-dissection (Fig. 1B).

The 19 Pc barcodes were sequentially hybridized to an oligopaint library, imaged, and bleached, as described elsewhere (Cardozo Gizzi et al. 2020; see Materials and Methods and Fig. S2 for more details). For each combination of barcodes, we built a pairwise distance distribution using the 3D barcode localizations detected in the same cells (Fig. S2E). From these distance distributions, we calculated the pairwise distance map and the proximity frequency map for wild-type S15-S16 embryos in a large number of cells (N=22243, 20 embryos, Fig. 1C, Materials and Methods). To validate the method, we first compared the Hi-M proximity frequency matrix for S15-S16 embryos (calculated with a contact threshold of T=250nm), with the publicly-available Hi-C contact matrix for S16 embryos (Ogiyama et al. 2018) (Fig. S2D). Both matrices display a similar organization, notably the presence of TADs and long-range interactions. To further test the robustness of the method, we calculated the Pearson correlation between Hi-M proximity frequencies and Hi-C contact frequencies as a function of proximity threshold and genomic distance (Fig. S2F). Hi-M and Hi-C data displayed a high correlation for all genomic distances ($p > 0.6$) for contact thresholds equal or higher than 200 nm, thus we chose a proximity threshold of 250 nm to calculate proximity frequencies. To further validate this choice, we calculated the Pearson correlation coefficient between Hi-M matrices obtained with different proximity thresholds (between 100-400 nm). In all cases, the correlation was high ($p > 0.9$) (Fig. S2G).

Barcodes within large PcG TADs (ANT-C, BX-C and NK-C) displayed high proximity frequencies and short pairwise distances (PWD) (Fig. 1C), consistent with previous observations in *hox* TADs (Lanzuolo et al. 2007; Sexton et al. 2012; Mateo et al. 2019; Cheutin and Cavalli 2018). In addition, we also observed long-range contacts between distant Hox TADs, such as BX-C and ANT-C), as expected from previous Hi-C and microscopy reports (Bantignies, 2011; Sexton et al. 2012). Interestingly, long-range interactions between other PcG targets were inhomogeneous, indicating that not all PcG targets have the same probability to interact with each other (Fig. 1C). Notably some targets display a similar mean pairwise distance, but different proximity frequencies (Fig. S2H).

Long-range contacts between Pc targets rely on PcG proteins (Bantignies, 2011). Thus, 3D proximity should decrease in embryos lacking essential components of the PcG machinery. We tested this hypothesis by performing Hi-M in homozygous Pc mutant embryos. These embryos showed a loss of 3D proximity both at short-range (within *hox* TADs, Fig. 1D, yellow arrow) and at long-ranges (e.g.

between distant Pc barcodes, Fig 1D, green arrow), indicating that 3D proximity between Pc barcodes requires PcG proteins.

Next, we reasoned that long-range 3D proximity between Pc barcodes should be reduced before the establishment of Polycomb repression programs during development. To test this, we imaged the organization of Pc barcodes in nuclear cycle 14 (NC14/stage 5) embryos. Interestingly, barcodes within *hox* TADs were already proximal in this early developmental stage (Fig. 1E, black boxes). However, long-range proximities between Polycomb barcodes were drastically depleted (Fig. 1E, white dashed squares), consistent with the local organization of Polycomb targets into TADs preceding the establishment of 3D long-range Polycomb contacts.

Polycomb targets display polymer micro-phase separation behavior

To shed light into the chromosome-wide organization of PcG targets, we resorted to a modeling approach that implements a block copolymer (Jost et al. 2014) (Fig. 1F, Fig. S2I, and Methods). In short, the chromosome was modeled by 866 beads with two possible identities: Polycomb or null (i.e. not Polycomb). The size of beads in the simulation (20kb) was slightly larger than the genomic size of Pc barcodes in our experiments (15kb). The genomic distribution of Pc beads mirrored the location of PcG targets in chromosome 3R used in Hi-M experiments (Fig. 1A), with all intervening beads labeled as null. The polymer displays several different regimes depending on the interaction strength between Polycomb monomers (defined as U): random coil ($U < 0.65k_B T$), θ -like polymer ($U \sim 0.65 k_B T$), and an equilibrium globule ($U > 0.65 k_B T$) (Fig. S2I) (Lieberman-Aiden et al. 2009; Mirny 2011; Halverson et al. 2014). In the random coil regime, the proximity frequency P_c between monomers separated by a genomic distance s scales as $P_c \sim s^{-3\nu}$ where $\nu \sim 0.588$ is the Flory exponent of a (non-interacting) self-avoiding polymer (Fig. 1G, grey solid curve). In the globule regime, beads attract each other and the contact probability between monomers scales as $P_c \sim s^{-3/2}$ before reaching a plateau at genomic distances corresponding to the boundary of the globule (Fig. 1G, green curve). The θ -like polymer represents an intermediate regime where the attractive interactions between beads compensate exactly for the swelling due to self-avoidance, leading to Gaussian statistics with contact probability between monomers scaling as $P_c \sim s^{-3/2}$ at all scales (Fig. 1G, grey dashed curve). The θ -like transition (at $U \sim 0.65 k_B T$) has to be considered with caution, due to the inhomogeneous distribution of PcG beads: high density regions of PcG beads are already in the (equilibrium) globule regime while regions of low PcG bead densities are still in the swollen coil regime (see Fig. 1F, θ -like polymer). In the same line, the globule regime is displayed by PcG beads forming a compact object, but null-beads can form loops escaping from it.

To determine the regime that best described the 3D folding of PcG targets in chr. 3R, we calculated the proximity frequency as a function of genomic distance $P(s)$. The experimental $P(s)$ for S15-S16 WT embryos decreases with genomic distances below ~ 1 Mbp, then reaches a plateau at large genomic distances (>1 Mbp). Thus, the experimental data was best represented by an equilibrium globule ($U = 0.9kT$, Fig. 1G). The plateau in the curve is the signature of microphase separation, characteristic in block copolymers (Nuebler et al. 2018; Khokhlov, Grosberg, and Pande 1994; Colby and Rubinstein 2003, Jost et al. 2014). In this regime, distant genomic loci come into contact to form limited-sized microphase-separated domains, and distant PcG targets display a high degree of mixing (at short physical distances, ≤ 250 nm) (Naumova et al. 2013).

We then sought to determine which polymer folding regime best described the experimental $P(s)$ for NC14 embryos. Interestingly, it was also best represented by an equilibrium globule ($U = 0.8 kT$, Fig. S2 K). It should be noted that small differences in interaction energies between monomers between NC14 versus S15-S16 embryos (0.1kT) can lead to a large overall energy difference when integrated over the whole chromosome (containing 75 PcG beads), which can considerably impact the global organization of the chromosome (see green and blue data points, Fig. 1H). This result suggests that

Polycomb proteins might play a role in the formation of microphase separated repressive compartments.

To test this prediction, we examined whether the presence of a plateau in the experimental $P(s)$ curve was abolished in Pc mutant and early stage embryos. Proximity frequencies between PcG targets were notably reduced in the absence of Pc, and declined even more in NC14 embryos, consistent with our previous conclusions (Fig. 1H). However, $P(s)$ curves for Pc depleted and NC14 embryos still exhibited a plateau above $\sim 1\text{Mb}$ and were also well represented by an equilibrium globule (Fig. 1H, Fig. S2K, Fig. S2L). Thus, our results indicate that PcG proteins reinforce the spatial de-mixing of distant chromatin regions leading to micro-phase separated compartments, but that other factors (e.g. HP1, chromatin insulators, active transcription) (Zenk et al. 2021; Hug et al. 2017; Rowley et al. 2017) are likely also involved in this process in *Drosophila*.

Chromosome-wide association of Polycomb targets involves predominantly pairwise interactions

In *Drosophila* Polycomb components assembly into large Polycomb foci (Buchenau et al. 1998; Saurin et al. 1998; Bantignies et al. 2011). These results suggest that Polycomb compartments may involve the spatial clustering of multiple Polycomb targets. To test this hypothesis, we calculated how often a Polycomb target was proximal (at a distance $\leq 250\text{ nm}$) to any other Polycomb target within the same chromosome in single cells. We focused on long-range proximities ($> 1\text{ Mb}$) to avoid any bias introduced by Polycomb target clustering within large Polycomb domains (i.e. ANT-C, BX-C, NK-C). In S15-S16 embryos, two or more distant Polycomb genes were found to spatially co-localize in only $5 \pm 4\%$ of cells (Fig. 2A). This frequency was comparable for all the Polycomb targets investigated, and in all cases lower than 10%. As expected, this frequency of co-localization was even smaller for NC14 embryos ($1 \pm 4\%$) (Fig. 2B), consistent with the loss of long-range Polycomb proximity in early embryos (Figure 1E), and suggesting that PcG architecture is gradually acquired during development. To determine if this behaviour was dependent on the distance cutoff, we calculated the mean colocalization frequency of Polycomb targets for different thresholds (Fig. 2C). The mean proximity frequencies remained lower than 15% in most cases, even for distance cutoffs as large as 400 nm. For early embryos, the mean contact frequency remained lower than 10% for all thresholds tested (Fig. 2D). Interestingly, the co-localization frequency did not depend on the size of the Pc domain within which the Pc barcode was located (Fig. 2E). This result suggests that the size of a Pc domain does not determine how often it will co-localize with other Pc domains. Thus, in single cells Polycomb targets within large and small Pc domains rarely spatially co-localize with other Polycomb targets to form clusters.

To explore whether these infrequent spatial encounters involved multiple Polycomb targets, we calculated the proportion of clusters containing two (i.e. pairwise cluster) or more Polycomb targets (multi-way cluster). Clusters containing only two Polycomb targets were the most common in all cases ($>70\%$) (Fig. 2F). Next, we calculated the frequency of multi-way clusters as a function of the number of targets in a cluster, normalized by the pairwise cluster frequency (Fig. 2G). The frequency of multi-way interactions decreased monotonically with the number of co-localizing targets, inconsistent with nucleation of multiple Polycomb targets. This behaviour was not tissue-specific, as the trend was the same for all segments of the embryo (Fig. S3A). The distribution of multi-way proximities remains similar for different thresholds (Fig. 2I). For NC14 embryos, Polycomb clusters contained almost exclusively two targets, with the frequency of multi-way clusters being almost negligible ($<5\%$, Fig. 2G, Fig.S3B). All in all, these results suggest that microphase separation of Polycomb targets involves the rare formation of Polycomb clusters containing a very limited number of targets.

To test this hypothesis, we calculated the frequencies with which multiple Polycomb targets co-localized in the block copolymer model presented above (Fig. 1F). Pairwise proximity frequencies calculated from the model were low ($\sim 10\%$), and decayed with the number of interacting partners in

a manner similar to the experimental data (Fig. 2H). Thus, our simple polymer model reproduces the experimental frequencies of pairwise and multi-way proximities, suggesting that the polymer behavior of the chromosome largely dominates over the enthalpic contributions provided by attractive interactions between Polycomb targets.

To further validate this hypothesis, we devised a toy polymer model containing two Polycomb targets (one in each end) and studied the behavior of the polymer for different Polycomb interaction energies (U) and polymer lengths (L). We found that the interaction energy required to bring Polycomb targets together increased linearly with polymer length (Fig. S2J). In a first approximation, the entropy of the polymer increases linearly with its length (Fig. S2J), thus the entropy of chromatin acts to counteract the tendency of Polycomb targets to coalesce in space. This interpretation suggests that most often Polycomb targets should be resolvable as individual units and would be unmixed from intervening chromatin regions.

We tested this by designing and imaging an oligopaint library that labeled the 19 Polycomb targets detected in chr. 3R (Fig. 1A, shown in blue in 3G) as well as 39 active regions between them (Fig. 2J, red; see Methods). In most cells, Polycomb and active domains were spatially segregated (Fig. 2J, overlap coefficient: 0.1, Pearson's correlation coefficient: 0.095). From the genomic distribution of Polycomb targets in the oligopaint library, a maximum of 11 Polycomb domains should be resolvable (Fig. S3C). This estimation is lower than the total number of Polycomb targets in our design (19), as targets in close genomic proximity would appear as single diffraction-limited spots. Considering the efficiency of barcode detection (~ 0.6), and a probability of pairwise interactions of ~ 0.1 (Fig. 2A), we estimate that we should be able to visualize ~ 6.8 barcode spots per cell. Remarkably, we observed 7 ± 2 Polycomb spots per cell, consistent with a low degree of spatial clustering. All in all, these data indicate that spatial coalescence of distant Polycomb targets is limited.

Gene repression and expression change the 3D internal organization of Polycomb domains

Our data shows that interactions between distant Polycomb targets are rare and involve primarily two targets. To determine whether these pairwise interactions depend on the transcriptional status of the co-localizing Polycomb targets, we mapped proximity frequencies for different segments of the embryo displaying distinct transcriptional programs. First, we focused on intra-domain interactions within *hox* TADs, that contain the genes responsible for the development of body segments, and display well-defined patterns of expression and repression along the embryo antero-posterior axis (E. B. Lewis 1978; Dessain and McGinnis 1993; Edward B. Lewis et al. 2004; Kaufman, Seeger, and Olsen 1990).

We profited from the ability of Hi-M to maintain spatial information to calculate the intra-TAD proximity frequencies between *hox* target genes within BX-C and ANT-C for each segment of the embryo (Fig. 3A), and relied on existing transcriptional data to identify the segment where each gene was expressed (Fig. S5). Proximity frequencies were normalised with respect to the segment of repression of the anchor to detect whether the expression of a Polycomb target gene changed the frequency with which it co-localized with other *hox* genes within the TAD (Figs. 3A-3C). For BX-C, intra-TAD normalized proximities were negative, indicating that gene repression consistently led to higher colocalization frequencies for *hox* genes within BX-C (Figs. 3A-B). This result is consistent with previous observations (Bantignies et al. 2011; Cheutin and Cavalli 2018). ANTP-C displays a more complex behaviour, with some targets displaying no change (e.g. *lab*, *Scr*, *Antp*) and others exhibiting positive changes (*pb*, *Dfd*, Figs. 3A, 3C, S4B). Thus, we conclude that gene repression does not always lead to the most compact TAD configuration.

To test whether gene expression leads to changes in internal TAD architecture, we calculated the intra-TAD proximity frequencies normalized by the segment of expression for both BX-C and ANT-C (Fig. 3D-F, Fig. S4A). Notably, normalized intra-TAD proximity frequencies were positive for most *Hox* targets, indicating that expression of *hox* genes leads to their spatial segregation from other

repressed targets within their TAD, and generalizing a previous observation on a smaller set of targets (Lanzuolo et al. 2007; Cheutin and Cavalli 2018).

Finally, we tested whether the simple copolymer model proposed above (Fig. 1) was able to qualitatively reproduce these observations. For this, we performed simulations under three scenarios: (1) all three genes within BX-C are repressed (head). In this case, the three genes in BX-C interact with energy U ; (2) *bx-d-Ubx* is expressed and *abd-A/Abd-B* are repressed (segment A1); (3) *Abd-B* is expressed and *bx-d-Ubx/abd-A* are repressed (segments A7-9). In the last two cases, repressed genes interact with energy U , while the region containing the active gene is considered as non-interacting. To compare results of the simulations and experiments, we plotted the proximity matrices for BX-C for the head, segment A1 and segments A7-9 (Fig. 3G). Notably, the simulations were able to reproduce experimental data in the three different segments. In the head, where all genes within BX-C are repressed, proximities between Polycomb targets were high, notably between *bx-d-Ubx* and *abd-A*, and *bx-d-Ubx* and *Abd-B*. In segments A1/A7-9, Polycomb targets in active regions were less often proximal to repressed targets (Fig. 3G, green arrows). In these segments, proximity between repressed genes increased, possibly due to the loss of interactions with an active target within the TAD (Fig. 3G, yellow arrows). This phenomenon can be also seen by plotting the normalized proximity frequencies for each segment using *Ubx* as an anchor (Figs. S3C-D, green arrows). Thus, tuning of the epigenetic state of Polycomb target genes within a TAD in the lattice copolymer model was enough to qualitatively reproduce the trends in the experimental proximity maps of cell types with different TAD configurations.

We previously established that clusters of Polycomb targets involved predominantly two genes (Fig. 2). To determine if this property depended on cell type or epigenetic state, we analyzed the distribution of multi-way interactions in the head, A1, and A7-9 segments (Fig. 3H). In all segments, the frequency of pairwise interactions was predominant, and diminished upon gene activation, consistent with our previous results. The frequency of 3-way interactions was highest for the head, where all genes are repressed. Overall, these results indicate that formation of higher-order complexes involving multiple Polycomb targets (more than two) within a TAD are modulated by epigenetic state, but remain rare, even in segments where all Polycomb targets within the TAD are repressed.

Chromosome-wide 3D physical proximity between Polycomb domains increases in both repressed and co-expressed segments

Next, we investigated whether the co-localization of Polycomb targets located in different TADs also correlated to transcriptional state. For this, we calculated the normalized proximity frequency between Hox genes and all other Polycomb targets in chr3R. Proximities were normalized to segments in which the target genes are expressed. For most Polycomb targets, the normalized proximity displayed positive values (Fig. 4A), thus Hox genes co-localized more often with other Polycomb targets in segments where they were repressed. Overall, these results show that activation of Hox genes leads to their local spatial segregation from other Polycomb genes within their TAD (Fig. 3), but also from most other more distant Polycomb targets (Figs. 4A-C, S6A).

Next, we explored how co-localization frequency changed with the transcriptional status of both anchor and target. For this, we analyzed the changes in proximity maps for different anchors and targets, in all cases normalized by the head, where most of the Hox genes are repressed (Figs. 4D-G). In all cases, we observed that co-localization frequency between two distant Polycomb targets was highest in segments where both genes were repressed, and diminished in segments where one or the other gene was activated (Figs. 4D-G). For instance, proximity between *Abd-B* (anchor) and *Antp* (target) diminished between T2-A1, where *Antp* is active, and increased in A3-A4, where both targets are repressed (Fig. 4D). In the tail (A7-9), expression of *Abd-B* and other genes within BX-C is correlated to an overall loss of proximity between *Abd-B* and *Antp*. Similarly, *Abd-B* and *Scr/Dfd*

displayed the highest proximity frequency in segments where they are both repressed (Fig. 4E-F). A similar behaviour was observed for *Antp* (anchor) and *bxd-Ubx* (target) (Fig. 4G). Thus, spatial colocalization between distant Hox Polycomb targets was highest in segments where both targets are repressed, and was lower in segments where one of the targets was activated.

Finally, we tested whether non-hox Polycomb target genes displayed a similar behavior. For this, we calculated the proximity maps for the non-Hox targets displaying clear antero-posterior expression patterns: *ems*, *hth*, *svp* and *grn* (Figs. 4H and S5A). We normalized proximity maps by the proximity frequencies on the segment where the anchor exhibited maximal expression (Fig. 4H) (Figs. 4F-G). Notably, normalized proximity frequencies were negative for the majority of segments and targets (Fig. 4H and 4I-4L). Thus, and in contrast to Hox polycomb targets, non-Hox Polycomb targets displayed the highest proximity frequencies in regions where they are co-expressed. All in all, our results show that proximity frequencies of distant Polycomb targets are spatially modulated, and can be tuned in different cell types by co-repression and co-expression.

Discussion

Previous evidence suggested that multiple PcG TADs may often associate with each other in single cells to form PcG compartments (bodies) to reinforce gene repression (Isono et al. 2013; Delest, Sexton, and Cavalli 2012; Bantignies and Cavalli 2011). Here, we investigated the nature of these compartments by implementing a multiplexed imaging-based approach that maps the multiscale organization of Polycomb target genes in different presumptive tissues within the *Drosophila* embryo.

Pairs of Polycomb target genes are able to interact in 3D by 'gene kissing', an activity that requires Polycomb components and possibly other factors, such as chromatin insulators (Bantignies et al. 2011; Sexton et al. 2012). The ability of our approach to detect multiple Polycomb target genes in single cells allowed us to shed light into the nature of these kissing interactions. Previous studies determined that interactions between pairs of distant Hox genes were rare (10-20%), and proposed that the existence of multiple accessible Polycomb partners may explain why two Hox genes only interact in a small fraction of nuclei (Bantignies et al. 2011; Sexton et al. 2012). In fact, our analysis shows that spatial colocalization of any two distant intra-chromosomal Polycomb targets is rather infrequent. Moreover, we show that these rare long-range interactions are acquired after the emergence of TADs at NC14 (Hug et al. 2017; Ogiyama et al. 2018), and concomitantly with the enrichment of PcG foci (Cheutin and Cavalli 2012). Notably, our data shows that frequencies of long-range interactions vary widely between targets and do not only depend on genomic distance, suggesting a role for other factors (e.g. insulators) in the modulation of interaction specificity.

Previous genome-wide studies showed extensive interactions between distant Polycomb genes (Bantignies et al. 2011), raising the possibility that Polycomb repressive compartments could involve the coalescence of multiple repressed genomic regions. We tested this hypothesis by directly calculating the frequency of pairwise versus multi-way interactions. Notably, we found that binary interactions are predominant, with the frequency of multi-way contacts drastically decreasing with an increasing number of targets. This finding is consistent with previous studies showing that Polycomb TADs often appear as discrete 3D chromosomal units (Szabo et al. 2018). These results indicate that Polycomb repressive compartments most often contain only two Polycomb target genes.

This result is supported by polymer modelling, which shows that a microphase-separated polymer in the globule regime correctly captures the behaviour of Polycomb domains. This polymer is close to the θ -like transition in the phase space. In this configuration, a small change in the interaction energy between monomers leads to a large change in the overall energy of the polymer, allowing chromatin

to switch conformation easily with a small difference in interaction energies. Microphase separation is consistent with the dynamic occupancy of Pc sites by PRC1 proteins, observed both in *Drosophila* and mammals (Ficz, Heintzmann, and Arndt-Jovin 2005; Fonseca et al. 2012; Steffen et al. 2013; Huseyin and Klose 2021). Furthermore, this behaviour is maintained in Pc mutants, consistent with other factors (HP1, insulators, transcription hubs, or other PcG proteins subunits) are likely also driving long-range PcG domain organization (Zenk et al. 2021; Hug et al. 2017; Rowley et al. 2017). This polymer model correctly captures the behaviour of PcG domains, notably the predominantly pairwise nature of interacting partners, and the correlation between Polycomb architecture and gene expression. Overall, our experiments and simulations suggest that Polycomb repressive compartments form by infrequent associations of Polycomb domains. PRC1 proteins play an important role in the formation of these compartments, however, other factors such as the entropy of the chromatin polymer, specific contacts mediated by other chromatin factors, and attractive interactions between active or repressed regions are also relevant. This suggests that the composition of Polycomb compartments could be regulated by their epigenetic and transcriptional status.

We tested this hypothesis by resorting to the ability of our method to reconstruct chromatin architecture in embryonic segments with different epigenetic and transcriptional states. Remarkably, we found that interaction frequencies between Polycomb targets are modulated by both transcriptional repression and activation. Hox genes colocalized most frequently in segments where they were co-repressed, both for targets located within the same TAD or for very distant genes. This result was consistent with previous observations on a limited number of targets (Lanzuolo et al. 2007; Bantignies et al. 2011; Cheutin and Cavalli 2018). Notably, transcriptional activation of Hox genes led to their spatial segregation, locally from other Polycomb targets within their TAD, and more globally from other repressed distant Polycomb targets. Finally, non-Hox genes more frequently colocalized in regions where they were both expressed, consistent with previous observations on a limited number of targets (Li et al. 2013). These interactions among co-expressed genes might depend on trithorax-group factors that can physically interact with Polycomb components to activate gene expression (Strübbe et al. 2011; Kadoch et al. 2017; Stanton et al. 2017).

In conclusion, our data are inconsistent with repressive Polycomb compartments being formed by the extensive coalescence of multiple distant Polycomb regions, and instead show that interactions between Polycomb genes occur infrequently, and involve mostly pairwise encounters modulated by transcriptional status.

Acknowledgements

This project was funded by the European Union's Horizon 2020 Research and Innovation Program (Grant ID 724429) (M.N.). We acknowledge the Bettencourt-Schueller Foundation for their prize 'Coup d'élan pour la recherche Française', the France-BioImaging infrastructure supported by the French National Research Agency (grant ID ANR-10-INBS-04, "Investments for the Future"), and the Drosophila facility (BioCampus Montpellier, CNRS, INSERM, Univ Montpellier, Montpellier, France).

Methods

Probe selection and library design

A portion of ~15 Mb of chromosome 3R was selected. A 3 node self-organizing map (SOM, 'kohonen' R package) was used to produce a 3-way segmentation of 10 Kb genome wide bins. Each bin was scored based on the average ChIP-seq read counts of H3K27me3, H3K4me3 and H3K36me3 from 14-16 hr embryos (modEncode, 3955 H3K27me3, Embryos-14-16 hr, OregonR, ChIP-seq; modEncode, 5096: H3K4me3, Oregon-R, Embryos 14-16 hr OR, ChIP-seq; 4950: H3K36me3, Oregon-R, Embryos 14-16 hr OR, ChIP-seq). Each SOM node was treated as a discrete cluster and contiguous bins assigned to the same node were merged into one epi-domain. Only epi-domains of a size equal or bigger to 20 kb were selected. For PcG domains, these epi-domains were later re-selected based on the enrichment of H3K27me3 (modEncode, 3955 H3K27me3, Embryos-14-16 hr; OregonR;ChIP-seq), and of PRC1 subunits PC, PH for embryos of 16 - 18 hrs of development (coming from Schuettengruber B, et. al, 2014, accession number GSE60428) and PSC (modEncode, 3960: Psc;Oregon-R;Embryos 14-16 hr OR;ChIP-seq, *D. melanogaster*). Domains having peaks of at least two of these PRC1 subunits were kept. They were also visually inspected using Hi-C maps from (Ogiyama et al. 2018). For active domains, they were re-selected based on the enrichment of H3K4me3 and H3K36me3 (modEncode, 5096: H3K4me3;Oregon-R;Embryos 14-16 hr OR;ChIP-seq; 4950: H3K36me3; Oregon-R; Embryos 14-16 hr OR ;ChIP-seq), and they were also visually inspected using Hi-C maps from (Ogiyama et al. 2018). For inactive domains, they were selected based on the absence of the aforementioned epigenetic marks. Domains between 20 - 100 Kb were labeled by one 15 Kb probe, centered in the middle of the domain, for all domain types. Domains between 100 - 200 Kb were labeled by two 15 kb probes centered at PcG protein peaks for PcG domains, and two 15 Kb domains homogeneously distributed for active and inactive domains. Domains bigger than 200 Kb comprise ANTP-C, BX-C and NK-C, and are labeled by 15 Kb probes targeting the promoters of their genes (5,3 and 3 probes respectively). The selected Polycomb targets correspond to the PcG targets in Chromosome 3R displaying the large majority of interactions (Bantignies, 2011). Polycomb domains located outside the selected ~15 Mb region, or smaller than 20 Kb were not labeled as they interacted with other Polycomb genes very infrequently.

Library synthesis and amplification

The library synthesis method is based on the development by (Beliveau et al. 2012). After selecting the genomic regions of interest, a database of genomically unique, non overlapping sequences was used to generate the Oligopaint primary probes (Oligopaints website, <https://oligopaints.hms.harvard.edu/>). They were mined using OligoArray (Rouillard, Zuker, and Gulari 2003). Each Oligo of the library is made of 148 nucleotides (nt), and consists in (from 5' to 3'): a 22-nt forward universal primer region for library amplification, a 20-nt readout region, unique for each 15 kb targeted region, a 2-nt spacer, a 20-nt readout region, unique for each 15 kb targeted region, a 42-nt region of homology to chromosomal DNA, a 20-nt readout region, unique for each 15 kb targeted region, and a 22-nt unique reverse primer for library amplification. An Oligopool with all the nucleotides used was ordered from Custom Array.

The procedure to amplify the library consists in four main steps: I) PCR amplification of the Oligopaints library using a reverse primer that adds the T7 promoter sequence; II) Conversion of the PCR product to RNA via an in vitro transcription using T7 polymerase; III) Generation of single-stranded DNA (ssDNA) via reverse transcription; IV) Degradation of the RNA template using alkaline hydrolysis. The full protocol can be found at (Cardozo Gizzi et al. 2020).

Primer sequences for library amplification are listed below (5' to 3'):

BB291.fw: CAGGTCGAGCCCTGTAGTACG

BB292.rev: GTGTCCGAGGCTGTCTCCTAG

Imaging oligo sequence:

MER1-SS-A647-32pb: CACACGCTCTCCGTTCTATGCGACGTCGGTG/iThioMC6-D//3AlexF647N/

Adaptor, displacement and imaging oligos

Adaptor oligos were used to bind the fluorescent label to the primary Oligopaint library. They're made of 62 base pairs, and consist in (from 5' to 3'): I) a binding region of 20 bp, complementary to the binding site of the oligos in the primary library; a bridge of 10 bp; and a binding site for the imaging oligo, of 32 bp.

The bridge is used to bind a displacement oligo. A displacement oligo consists in the complementary sequence of the bridge, followed by the complementary sequence of the Binding region on the adaptor oligos. When injected at the proper concentration, they bind the adaptor oligo. The adaptor oligo bound by a displacement oligo can then be washed out, removing with it the fluorophore in the imaging oligo. This technique was first used in Mateo et. al. 2019, and it is used in our work to remove the fluorescent signal from the fiducial mark every 10 cycles, to avoid bleaching and ensure an optimal signal intensity. To remove the fluorescent signal from barcodes, a chemical bleaching step was performed (see image acquisition section).

Imaging oligos consist of a 32-mer complementary to the binding region in the adaptor oligo, followed by a cleavable Alexa-647 fluorophore. Fiducial marker imaging oligo consists of a 32-mer complementary to the binding region of the corresponding adaptor oligo, followed by a non-cleavable Rhodamine Red fluorophore. Adaptors, displacements and imaging oligos were synthesized by Integrated DNA Technologies (IDT; Coralville, USA). Their sequences can be found in Appendix 1.

Embryo collection and fixation

Oregon-R w¹¹¹⁸ flies were used for the WT strain. For the mutant line, the *Pc*^{XT109} strain was used. It consists in a null mutant (Franke, Messmer, and Paro 1995) that was balanced over the KrGFP-TM3 Sb balancer (TKG: obtained from BL#5195 of the Bloomington Drosophila Stock Center). Flies were maintained at room temperature with natural light/dark cycles and were grown on standard cornmeal yeast media at 21°C.

Following a pre-laying period of 16-18 H in cages with yeasted 0.4% acetic acid agar plates, agar plates were changed for new ones so flies can lay eggs during the corresponding time (1.5 H for NC14 embryos, 4 H for S15-16 embryos and mutants) on the new plates. Embryos were then incubated at 25°C for the corresponding time to obtain the desired developmental stage for fixation (1 H for NC14, 12 H for S15-16 and mutants). For fixation, embryos were dechorionated with bleach for 5 min and thoroughly rinsed with water. They were fixed in a fixation buffer (1:1 mixture of 4% methanol-free formaldehyde in PBS and Heptane) by agitating vigorously for 15 s and then letting stand the vial for 25 min at RT. The bottom formaldehyde layer was replaced by 5 mL methanol and embryos were

vortexed for 30 s. Embryos that sank to the bottom of the tube, devitellinized, were rinsed three times with methanol. Embryos were stored in methanol at -20°C until further use.

Hybridization of Hi-M library

Embryos were rehydrated by incubating them sequentially for 5 min at RT on a rotating wheel, using 1 mL of each of the following solutions: I) 90% methanol, 10% PBT; II) 70% methanol, 30% PBT; III) 50% methanol, 50% PBT; IV) 30% methanol, 70% PBT; V) 100% PBT. Then embryos were RNase treated during 2h at RT, and permeabilized in 0,5% Triton/PBS during 1h. Next, embryos are incubated for 20 min at RT on a rotating wheel sequentially in the following Triton/pHM solutions (pHM: 2X SSC, NaH₂PO₄ 0.1M pH = 7, 0.1% Tween-20, 50% formamide (v/v)): I) 80% PBS-Triton, 20% pHM; II) 50% PBS-Triton, 50% pHM; III) 20% PBS-Triton, 80% pHM; IV) 100% pHM. Then 225 pmol of primary probe were diluted in 25 µL of FHB (FHB =50% Formamide, 10% dextran sulfate, 2X SSC, Salmon Sperm DNA 0.5 mg mL). Primary probes and embryos were denatured by incubating them 15 min at 80 °C. Embryos were then transferred to a 500 µL PCR tube, next pHM was removed from embryos and 30 µL of the denatured probes were added. Embryos were then placed into a thermocycler with the following program: Starting from 80°C, 43 cycles of 10 minutes, with a temperature drop of -1°C/cycle, then incubation at 37°C indefinitely. Embryos were then transferred back to a 1.5 mL tube, and sequentially washed for 20 min in the following solutions: I) 50% (vol/vol) formamide, 2× SSC; repeat this wash once; II) 40% (vol/vol) formamide, 2× SSC; III) 30% formamide, 70% PBT; IV) 20% formamide, 80% PBT; V) 10% formamide, 90% PBT; VI) 100% PBT; VII) 100% PBS-Triton. Washes I-IV were performed at 37 °C in a thermal mixer with agitation (900 r.p.m.); washes V–VII were performed at RT on a rotating wheel. An additional crosslink in 4% PFA was performed. Embryos were washed and resuspended in PBS, and stored at 4°C until use.

Microscope setup

Experiments with NC14 embryos were performed on a home-made wide-field epifluorescence microscope built on a RAMM modular microscope system (Applied Scientific Instrumentation) coupled to a microfluidic device as described previously (Cardozo Gizzi et al. 2019; 2020). Samples were imaged using a 60x Plan-Achromat water-immersion objective (NA = 1.2, Nikon, Japan). The objective lens was mounted on a closed-loop piezoelectric stage (Nano-F100, Mad City Labs Inc. - USA). Illumination was provided by 3 lasers (OBIS-405/640 nm and Sapphire-LP-561 nm, Coherent – USA). Images were acquired using a sCMOS camera (ORCA Flash 4.0V3, Hamamatsu – Japan), with a final pixel size calibrated to 106 nm. A custom-built autofocus system was used to correct for axial drift in real-time and maintain the sample in focus as previously described (Cardozo Gizzi et al. 2019). A fluidic system was used for automated sequential hybridizations, by computer-controlling a combination of three eight-way valves (HVXM 8-5, Hamilton) and a negative pressure pump (MFCS-EZ, Fluigent) to deliver buffers and secondary readout probes onto a FCS2 flow chamber (Biopetech). Software-controlled microscope components, including camera, stages, lasers, pump, and valves were run using a custom-made software package developed in LabView 2015 (National Instrument).

Experiments with S15-S16 and Pc del embryos were performed on an AxioObserver microscope coupled to a LSM800 laser-scanning confocal detection (Zeiss, Germany). Samples were imaged using a 63x, NA = 1.2 water-immersion objective (W DICII, Zeiss). Illumination was provided by 3 laser lines (405/561/640 nm). Images were acquired with a pixel size of 100 nm, and 0.5 µm z-slices. A pinhole size of 62 µm was used. ZEN 2.3/6 blue edition (.NET Framework Version: 4.0.30319.42000) was used for acquisition. Focus reproducibility during the experiment was ensured by the built-in autofocus tools available in ZEN.

Sequential hybridizations were performed using a computer-controlled fluidic system. In brief, a peristaltic pump (Instech, P720) coupled to an eight-way valve (HVXM 8-5, Hamilton) delivers the buffers into a FCS2 flow chamber (Bioptechs). Barcodes were injected sequentially using a home-made delivery platform composed of a rotating tray where the tubes are arranged (Physik Instrumente, M-404.4PD). A needle coupled to a linear stage (Physik Instrumente, VT-80) is used to inject the barcodes into the chamber. A second peristaltic pump (Instech, P720) is coupled to the needle and a two-way valve (HVXM 2-5, Hamilton), to wash the residual barcode solution from the needle between cycles. Flow rate is constantly monitored (FRP, flow-rate platform, Fluigent) in order to control the injected volumes and ensure reproducible hybridization conditions for all probes.

Finally, a XY translation stage (MS2000, Applied Scientific Instrumentation) is used to select the positions of the embryos. Pumps, valves, and translation stages were controlled using a custom-made software package developed in LabView 2015 (National Instrument). Synchronization between injections and confocal acquisitions was ensured using a trigger box (SVB-1 Zeiss, Germany) and an analog voltage output device (USB-3104, Measurement computing).

Image acquisition

Embryos labeled with the primary library were attached to a poly-L-lysine coated coverslip, placed into the FCS2 fluidics chamber. Fiducial mark labeling with a Rhodamine labeled readout probe and DAPI staining were performed in the chamber, using the fluidics to inject solutions and perform washes. For image acquisition, the fluidics system contained: 1 tube with 50 mL of washing buffer (WB, 2XSSC, 40% v/v formamide), 1 tube with 50 mL of 2x SSC, 1 tube with 20 mL of imaging buffer (IB, 1xPBS, 5% w/v glucose, 0.5 mg/mL glucose oxidase and 0.05 mg/mL catalase), 1 tube with 50 mL of chemical bleaching buffer (CB, 2X SSC, 50 mM TCEP hydrochloride), and 19 tubes with 2 mL of each readout probe solution (25 nM readout probe, 2XSSC, 40% v/v formamide). To avoid degradation by oxygen, IB was stored under a layer of mineral oil throughout the experiment, and renewed every 12 h.

Several 200 μ m X 200 μ m fields of view (FOV) containing the embryos were selected, using the LabView script. Z stacks of 15 - 20 μ m were selected, with steps of 250nm in the widefield setup and 500nm in the Airyscan.

DAPI was imaged first, together with fiducial marks, using 405, and 561 nm laser lines. For barcode imaging, LabView software controlled the sequential hybridization and imaging procedure. Briefly, the chamber was filled with 1.7 mL barcode probe solution over \sim 17 min to ensure binding of readout probes. Next, the sample was washed with 1.5 mL of wash buffer for 10 min. Then 1.5 mL of 2X SSC were flushed during 10 min and finally 1.2 mL of imaging buffer was injected in \sim 12 min. Flow was stopped, and the FOVs were imaged in two channels by exciting at 561 and 641 nm to image fiducial marks and barcode probes, respectively. After imaging, the fluorescence signal of the barcode probes was cleaved using chemical bleaching by flowing 1.5 mL of CB buffer for 10 min. The Rhodamine-labeled fiducial barcode was insensitive to chemical removal. After chemical bleaching, the chamber was flushed with 1.5 mL of 2XSSC for 10 min and a new hybridization cycle started. All buffers were freshly prepared and filtered for each experiment. Barcodes displayed a labeling efficiency in the 40-65% range (Fig. S2B).

Polymer modelling

A block copolymer of N=866 beads, each of size a=20kb, matching the genomic size and distribution of the experimental probes was implemented and simulated by Monte Carlo simulations (Walter and Barkema 2015) on a Face-Centered Cubic lattice (FCC). This lattice polymer model has proven to be extremely precise up to second order corrections when compared to analytical results for DNA hybridization/melting (Sakaue et al. 2017) and for the unwinding dynamics (Walter et al. 2013).

Beads were divided into two classes in all simulations: Pc beads, that displayed a finite interaction strength U ; and null beads, for which $U=0$. In order to access the behaviour of this polymer versus U , we built the phase diagram in Fig.S2G where the radius of gyration R_g is plotted versus U . To do so, R_g was sampled from $U=0$ over $2 \cdot 10^5$ configurations. N^2 Monte Carlo steps were performed to decorrelate the polymer between two samplings. Subsequently to the completion of the sampling at a given U , the value of U was increased by $0.05kT$, the system was thermalized during 10^7 Monte Carlo steps and the sampling procedure was resumed at this new interaction energy. Different values of U were used, to match experimental data: for all observables presented in the main text (Frequency versus genomic distance; histogram of pairwise interactions and contact map between *ubx*, *abd-A* and *Abd-B*) we have used $U=0.8kT$ for early embryos and $U=0.9kT$ for late embryos.

Data analysis

Airyscan images (.czi format) were converted to TIFF files using Bio-Formats plugin in Fiji (Schneider, Rasband, and Eliceiri 2012; Schindelin et al. 2012, <https://github.com/ome/bioformats>, (Linkert et al. 2010).

Acquired images are deconvolved using Huygens Professional version 20.04 (Scientific Volume Imaging, the Netherlands, <https://svi.nl/>), via the CMLE algorithm (SNR:20, 40 iterations) run with a custom-made script written in Tcl/Tk.

The following analysis steps were performed with a home made script in MATLAB 2019b (The MathWorks, Inc., Natick, United States). First, X-Y drift is corrected for each hybridization cycle. A global X-Y correction is obtained by cross-correlating the images of the fiducial barcodes with that of the first barcode (reference cycle). This produces a single 3D vector for each barcode and represents a 'global' correction applied to the whole FOV. Then, an adaptive thresholding is used to pre-segment the spots of each fiducial barcode in each cell for all FOVs and for all barcodes. The 3D coordinates of each barcode were then found using a 3D Gaussian fitting algorithm on the pre-segmented mask. Fiducial barcodes with sizes larger than the diffraction limit of light (2.2 pixels for our microscope) were filtered out. Third, we obtained 'local' 3D correction vectors for each cell in each FOV. This was done by first using the global X-Y correction vector to pre-align fiducial barcode spots in each cycle to fiducial barcode spots in the reference cycle. Then, image-based cross-correlation of these pre-aligned fiducial barcode images is used to reach sub-pixel accuracy in the correction vector. This approach allowed for 3D, subpixel accuracy drift-correction across the whole FOV (Fig. S2C). Fourth, barcodes were segmented for all hybridization cycles in batch processing mode using optimized adaptive thresholding. 3D coordinates of each barcode were then determined by 3D Gaussian fitting of the segmented regions. These positions were corrected for drift by using the closest fiducial barcode vector obtained from the previous analysis step. Nuclei were segmented from DAPI images by adaptive local thresholding and watershed filtering. Embryo's segments were selected by manually drawing polygons over them. This was used to assign each DAPI-segmented cell to the corresponding segment. Then, barcodes were attributed to each cell by using the DAPI segmentation. For each nuclei we then calculate pairwise distance matrices. All further analysis is done using home made Python 3. The contact probability is obtained as the number of nuclei where the pairwise distances were lower or equal to 250 nm, normalized by the number of nuclei containing both barcodes. Outliers (defined using the interquartile rule) or bins with no reported interactions were filtered out. All image processing was carried out on Linux terminals connected to a server running Linux PopOS 19.10, with 4 GeForce GTX 1080Ti GPU cards (SCAN computers, UK).

Figure legends

Figure 1: Polycomb domains behave as a self-interacting polymer in the globule regime.

- a. **Library design.** Schematic representation of the Oligopaints library used, covering PcG domains over a portion of ~ 12 Mb of chromosome 3R. Triangles represent the three bigger domains: ANTP-C, BX-C and NK-C. Bottom: H3K27me3, PC, PH, PSC Chip-seq data for a portion of ANTP-C
- b. **Experimental setup.** Diagram of the experimental setup. Hi-M allows to image PcG domains sequentially in single cells of full embryos, keeping spatial resolution. Briefly, images are acquired using an Airyscan confocal microscope coupled to a fluidics system. Barcodes are injected using a needle attached to a translation stage. A peristaltic pump delivers solutions into the microfluidics chamber. See supplementary data for a detailed description of the setup.
- c. **Hi-M proximity frequency and pairwise distance maps for WT late embryos.** Hi-M proximity frequency map for selected PcG domains (top) and pairwise distance map for the same region (bottom), for late embryos. Barcode IDs are indicated on the axis of the figure. The colormaps corresponding to the proximity frequency and pairwise distance are shown above and below the plot respectively. Grey bins in the matrix correspond to interactions that did not satisfy our quality control filters (Methods).
- d. **Hi-M proximity frequency and pairwise distance maps for Pc del mutants.** Hi-M proximity frequency maps (top) and pairwise distance map for the same region (bottom) for mutants carrying a deletion of Pc gene. Barcode IDs are indicated on the axis of the figure. The colormaps corresponding to the contact frequency and pairwise distance are shown above and below the plot respectively. Grey bins in the matrix correspond to interactions that did not satisfy our quality control filters (Methods).
- e. **Hi-M proximity frequency and pairwise distance maps for early NC14 embryos.** Hi-M proximity frequency maps (top) and pairwise distance map for the same region (bottom) for early NC14 WT embryos. Barcode IDs are indicated on the axis of the figure. The colormaps corresponding to the contact frequency and pairwise distance are shown above and below the plot respectively. Grey bins in the matrix correspond to interactions that did not satisfy our quality control filters (Methods).
- f. **Polymer modelling of chromosome 3R.** Co-polymer containing interacting beads with energy U (PcG beads, blue), and non interacting beads (pink). Increasing U leads to three different behaviours: swollen (random) Coil, θ -like polymer, and Equilibrium globule.
- g. **Contact probability vs genomic distance for late embryos vs simulation results of a self-interacting polymer in the globule phase (see text for details).** Contact frequency vs genomic distance for WT S15-16 embryos (blue dots), contact frequency from simulation of a self-interacting polymer in the globule regime (green curve, $U=0.9kT$), contact frequency from simulation of a polymer at the theta-like transition (grey dashed curve, $U=0.65 kT$) and contact frequency from simulation of a polymer in the swollen coil regime (grey curve, $U=0 kT$). Experimental data is best described as a polymer in the globule regime.
- h. **Contact probability vs genomic distance for WT S15-S16 embryos, Pc del embryos and NC14 embryos.** Contact probability vs genomic distance, for WT S15-16 embryos, Pc del embryos, and NC14 embryos. Solid and dashed lines represent a guide to the eye for the

three datasets. A plateau in contact probability can be observed at genomic distances higher than 1 Mb.

Figure 2: PcG genes rarely form multi-way interactions with targets outside their TAD

- a. **A - B) The frequency of interaction between PcG genes is low (means < 10%), regardless of the developmental stage.** Median inter-domain proximity frequency for all PcG domains in late S15-S16 embryos (panel A) and NC14 (S5) embryos. White dots represent the median proximity frequency and gray lines represent the mean contact probability.
- b. **C - D) Mean proximity frequencies remain low at different contact thresholds.** Mean proximity frequencies per domain for late (left) and early (right) embryos, for different contact thresholds (between 250nm - 400 nm). In all cases mean contact probabilities remain below 17%.
- c. **E) Proximity frequency does not depend on domain size.** Mean inter-domain proximity frequency as a function of domain size. Domains are separated in Hox and Non Hox
- d. **F - G) Most PcG targets form pairwise interactions.** Left: frequency of pairwise interactions among all multi-way contacts. Right: Histograms in log-scale of the number of interacting partners in single cells, for all genes, normalized by the number of pairwise interactions (1 interacting partner), for late S15-S16 (left) and early NC14 (S5) (right) embryos. Genes are indicated on the left of the figure, the number of interacting partners is indicated on the bottom, and the color-scale for the normalized frequency of interaction is shown on the right.
- e. **H) Multi-way interactions are negligible over 4-way interactions, in agreement with the self interaction polymer model.** Normalized proximity frequencies vs number of interacting partners for experimental data for WT S15-S16 embryos (blue curve), NC14 embryos (red curve) and simulations of a copolymer in the equilibrium globule regime ($U = 0.9kT$, green curve).
- f. **I) Experimental multiway interactions remain negligible for different interaction thresholds.** Experimental proximity frequency vs number of interacting partners for contact thresholds between 250 nm - 400 nm. In all cases, contacts are predominantly pairwise.
- g. **J) Active and PcG domains segregate spatially. PcG domains form discrete foci in agreement with polymer microphase separation.** All active and all Polycomb domains imaged in two consecutive Hi-M cycles. They spatially separate. Pearson's colocalization coefficient $P = 0.095$. Overlap Coefficient = 0.16.

Figure 3: Regulation of gene expression changes chromatin contacts within Hox gene PcG TADs

A-C) Repression of Hox PcG targets leads to the most compact intraTAD configuration for some, but not all Hox target genes. IntraTAD proximity frequencies for Hox target genes, normalized in the repression segment of anchors. For BX-C, intra-TAD normalized proximities are negative, indicating that gene repression led to higher colocalization frequencies for *hox* genes within BX-C. ANTP-C displays a more complex behaviour, with some targets displaying no change (e.g. *lab*, *Scr*, *Antp*) and others exhibiting positive changes (*pb*, *Dfd*). Panels B and C show the intra TAD normalized proximity frequency in different segments for two of the targets, *bx-d-Ubx* and *Antp*, normalized in segments where they're repressed.

D-F) Expression of Hox PcG target genes leads to changes in PcG TAD organization. IntraTAD proximity frequencies for Hox target genes, normalized in the expression segment of

anchors. Normalized intra-TAD proximity frequencies are positive for most Hox targets, indicating that expression of *hox* genes leads to their spatial segregation from other repressed targets within their TAD. Panels E and F show the intra TAD normalized proximity frequency in different segments for two of the targets, *bxd-Ubx* and *Antp*, normalized in segments where they're expressed.

G) Polymer physics simulations recover the segregation of PcG genes upon activation. Experimental and simulated contact probability submatrices for genes in the BX-C in the head (where all genes are repressed), segment A1 (where *bxd/Ubx* is active, and *abd-A* and *Abd-B* are repressed), and segments A7-A9 (where *Abd-B* is active, *bxd/Ubx* and *abd-A* are mostly repressed). Non-activated genes become physically closer when one gene in the complex becomes active (yellow arrows). Bottom: microscopy images for the BX-C in the three regions described.

H) Distribution of intra-TAD multi-way interactions are predominantly pairwise. IntraTAD interaction frequencies for the BX-C in the segments shown on panel G. In all segments, the frequency of pairwise interactions is predominant, and diminishes upon gene activation. The frequency of 3-way interactions is the highest for the head, where all genes are repressed.

Figure 4: Pairwise, long-range chromatin interactions between PcG domains correlate with expression patterns. Co-expressed and co-activated genes display an increase in physical proximity.

A - C) Expression of PcG target genes decreases contacts with other PcG genes at long-range genomic distances. Normalized proximity frequencies for Hox target genes, with all other PcG targets in chr. 3R. Proximity frequencies are normalized in segments where the target genes are expressed. Proximities were normalized to segments in which the target genes are expressed. For most Polycomb targets, the normalized proximity displayed positive values (Fig. 4A), indicating that Hox genes co-localized more often with other Polycomb targets in segments where they were not expressed. Panels B and C show the normalized proximity frequency for long range interactions between *Abd-B* and *lab* anchor genes.

D-G) Repression of PcG target genes leads to higher proximities between PcG TADs. Difference in contact probability for LR interactions between anchors (*Abd-B*, *Dfd*, *Antp*, shown by anchor sign) and selected genes (*Antp*, *Scr*, *Abd-B*, *Ubx(bxd)*), with respect to a normalizing segment. The normalizing segment is highlighted in grey on the embryo scheme. Patterns of expression of the interacting genes are also shown on the embryo scheme, where darker shades represent higher levels of expression. Above the plot, the scheme represents changes in looping interactions in different segments. Below, regions in the embryo where the two partners are co-repressed, or where only one of them is expressed, are depicted in blue and green respectively.

H - L) Expression of PcG non-Hox target genes leads to higher proximity between expressed targets. Normalized proximity frequencies for non-Hox targets, normalized in the segment of maximal expression. Normalized proximity frequencies are negative for the majority of segments and targets, showing that non Hox targets display the highest proximity frequencies in regions where they are co-expressed. In figures 4I-4L, expression patterns of selected targets are shown on the right (orange patterns).

Supplementary figure 1: Selected genomic loci in chromosome 3R. Selected PcG genomic loci in chromosome 3R (blue) and active regions (red). For each PcG loci, the probe position within the loci as well as the Chip-seq profiles for H3K27me3, PC, PH, and PSC are shown.

Supplementary figure 2:

- A) Schematic representation of the experimental setup. Briefly, peristaltic pump 1 delivers buffers and barcodes into the microfluidics chamber. An 8-way valve selects the solution to be injected. A 2-way valve is used to either inject barcodes, or to rinse remaining barcode solution in the needle between cycles, via peristaltic pump 2.
- B) Labelling efficiency for all barcodes, defined as the percentage of nuclei displaying at least one detected barcode per imaging cycle.
- C) Boxplot of residual error in drift correction of fiducial barcodes after global and local drift correction. Global correction is obtained by cross-correlating the fiducial mark images. Local correction is obtained centering subvolumes of 20x20x60 pixels for each segmented object in the first cycle. Then each subvolume i in cycle j is cross-correlated with subvolume i in cycle 1 to obtain a detection-specific local correction vector. The final correction vector is obtained by adding the global correction vector to the local correction vectors.
- D) Comparison between Hi-M contact probability map and Hi-C map, for WT late embryos.
- E) Pairwise distance distributions for all pairs of barcodes, obtained using Hi-M.
- F) Pearson correlation coefficients for different distance thresholds used to define a contact, and different genomic distances. For the threshold used in this work ($T = 250$ nm), the correlation is high (>0.7) for all genomic distances.
- G) Pearson correlation between Hi-M contact probability matrix obtained with a distance threshold of $T = 250$ nm, and matrices obtained with different distance thresholds.
- H) Proximity frequency matrix (top), and pairwise distance matrix (bottom) for WT S15-16 embryos. Two loci with similar mean distances may have different proximity frequencies (blue and red squares), as we can see from the distance distribution.
- I) Phase diagram of a polymer, with the radius of gyration (R_G^2 , in units of monomer length a) as a function of the interaction energy between monomers (U). Three different phases can be observed for PcG beads: Coil regime ($R_G \sim N^{\nu}$), Theta regime ($R_G \sim N^{1/2}$), and Globule regime ($R_G \sim N^{1/2}$, followed by saturation), where N is the number of monomers.
- J) **Rescaled end to end distance of the polymer as a function of the energy of interaction U between two attractively interacting beads separated by a polymeric chain.** The different curves correspond to different polymer lengths. The energy needed to bridge the polymer increases with increasing polymer length (and thus increasing entropy). This illustrates that two distant PcG loci need to compete against the entropy of chromatin separating them, preventing the coalescence of several loci into phase separated droplets. The rescaled end to end distance of the polymer is proportional to the proximity frequency of the end beads, $P_{\text{contact}} = 1 - R_{ee}/L^{2\nu}$
- K) **Contact probability vs genomic distance for late S15-S16 embryos and Pc del embryos vs simulation results of a self-interacting polymer in globule phase.** Contact frequency vs genomic distance for WT S15-16 embryos (blue dots), for Pc del mutant embryos (gray dots), and contact frequency from simulation of a self-interacting polymer in the globule regime

(green curve, $U=0.9kT$). Both WT and mutant data are best described as a polymer in the globule regime.

- L) **Contact probability vs genomic distance for early NC14 embryos vs simulation results of a self-interacting polymer in globule phase.** Contact frequency vs genomic distance for WT S15-16 embryos (blue dots), for Pc del mutant embryos (gray dots), and contact frequency from simulation of a self-interacting polymer in the globule regime (green curve, $U=0.8kT$). Experimental data is best described as a polymer in the globule regime, although with lower interaction energy than S15-S16 embryos.

Supplementary figure 3:

A) Frequency of multi-way clusters as a function of the number of targets in a cluster, normalized by the pairwise cluster frequency, for different segments of WT S15-S16 embryos. The frequency of multi-way interactions decreases with the number of co-localizing targets for all segments of the embryo, indicating that pairwise interactions are prevalent regardless of the tissue.

B) Frequencies of pairwise interactions among all multiway interactions for S15-S16 WT embryos. In all cases, they're high (>50%).

C) Genomic distribution of PcG targets on chr. 3R.

Supplementary figure 4:

A) IntraTAD normalized proximity frequencies in different segments for BX-C gene targets, normalized in segments of expression. In most cases, proximity frequencies are positive, indicating that BX-C targets segregate from other repressed targets within the TAD upon activation.

B) IntraTAD normalized proximity frequencies in different segments for ANT-C gene targets, normalized in segments of repression. Proximity frequencies display high variability, showing that gene repression does not always lead to the most compact TAD configuration.

Supplementary figure 5:

Expression patterns of selected genes. Images come from the Berkeley database (<https://insitu.fruitfly.org/cgi-bin/ex/insitu.pl>).

References

- Andrey, Guillaume, and Stefan Mundlos. 2017. "The Three-Dimensional Genome: Regulating Gene Expression during Pluripotency and Development." *Development* 144 (20): 3646–58. <https://doi.org/10.1242/dev.148304>.
- Bantignies, Frédéric, and Giacomo Cavalli. 2011. "Polycomb Group Proteins: Repression in 3D." *Trends in Genetics* 27 (11): 454–64. <https://doi.org/10.1016/j.tig.2011.06.008>.
- Bantignies, Frédéric, Virginie Roure, Itys Comet, Benjamin Leblanc, Bernd Schuettengruber, Jérôme Bonnet, Vanessa Tixier, André Mas, and Giacomo Cavalli. 2011. "Polycomb-Dependent Regulatory Contacts between Distant Hox Loci in *Drosophila*." *Cell* 144 (2): 214–26. <https://doi.org/10.1016/j.cell.2010.12.026>.
- Beliveau, Brian J., Eric F. Joyce, Nicholas Apostolopoulos, Feyza Yilmaz, Chamith Y. Fonseka, Ruth B. McCole, Yiming Chang, et al. 2012. "Versatile Design and Synthesis Platform for Visualizing Genomes with Oligopaint FISH Probes." *Proceedings of the National Academy of Sciences* 109 (52): 21301–6.
- Bintu, Bogdan, Leslie J. Mateo, Jun-Han Su, Nicholas A. Sinnott-Armstrong, Mirae Parker, Seon Kinrot, Kei Yamaya, Alistair N. Boettiger, and Xiaowei Zhuang. 2018. "Super-Resolution Chromatin Tracing Reveals Domains and Cooperative Interactions in Single Cells." *Science* 362 (6413). <https://doi.org/10.1126/science.aau1783>.
- Boettiger, Alistair N., Bogdan Bintu, Jeffrey R. Moffitt, Siyuan Wang, Brian J. Beliveau, Geoffrey Fudenberg, Maxim Imakaev, Leonid A. Mirny, Chao-ting Wu, and Xiaowei Zhuang. 2016. "Super-Resolution Imaging Reveals Distinct Chromatin Folding for Different Epigenetic States." *Nature* 529 (7586): 418–22. <https://doi.org/10.1038/nature16496>.
- Buchenau, Peter, Jacob Hodgson, Helen Strutt, and Donna J. Arndt-Jovin. 1998. "The Distribution of Polycomb-Group Proteins During Cell Division and Development in *Drosophila* Embryos: Impact on Models for Silencing." *Journal of Cell Biology* 141 (2): 469–81. <https://doi.org/10.1083/jcb.141.2.469>.
- Cardozo Gizzi, Andrés M., Diego I. Cattoni, Jean-Bernard Fiche, Sergio M. Espinola, Julian Gurgo, Olivier Messina, Christophe Houbron, et al. 2019. "Microscopy-Based Chromosome Conformation Capture Enables Simultaneous Visualization of Genome Organization and Transcription in Intact Organisms." *Molecular Cell* 74 (1): 212–222.e5. <https://doi.org/10.1016/j.molcel.2019.01.011>.
- Cardozo Gizzi, Andrés M., Sergio M. Espinola, Julian Gurgo, Christophe Houbron, Jean-Bernard Fiche, Diego I. Cattoni, and Marcelo Nollmann. 2020. "Direct and Simultaneous Observation of Transcription and Chromosome Architecture in Single Cells with Hi-M." *Nature Protocols* 15 (3): 840–76. <https://doi.org/10.1038/s41596-019-0269-9>.
- Cattoni, Diego I., Andrés M. Cardozo Gizzi, Mariya Georgieva, Marco Di Stefano, Alessandro Valeri, Delphine Chamousset, Christophe Houbron, et al. 2017. "Single-Cell Absolute Contact Probability Detection Reveals Chromosomes Are Organized by Multiple Low-Frequency yet Specific Interactions." *Nature Communications* 8 (1): 1753. <https://doi.org/10.1038/s41467-017-01962-x>.
- Cavalli, Giacomo, and Tom Misteli. 2013. "Functional Implications of Genome Topology." *Nature Structural & Molecular Biology* 20 (3): 290–99. <https://doi.org/10.1038/nsmb.2474>.
- Cheutin, Thierry, and Giacomo Cavalli. 2012. "Progressive Polycomb Assembly on H3K27me3 Compartments Generates Polycomb Bodies with Developmentally Regulated Motion." *PLOS Genetics* 8 (1): e1002465. <https://doi.org/10.1371/journal.pgen.1002465>.
- . 2018. "Loss of PRC1 Induces Higher-Order Opening of Hox Loci Independently of Transcription during *Drosophila* Embryogenesis." *Nature Communications* 9 (1): 3898. <https://doi.org/10.1038/s41467-018-05945-4>.
- Delest, Anna, Tom Sexton, and Giacomo Cavalli. 2012. "Polycomb: A Paradigm for Genome Organization from One to Three Dimensions." *Current Opinion in Cell Biology, Nucleus and gene expression*, 24 (3): 405–14. <https://doi.org/10.1016/j.ceb.2012.01.008>.

- Dessain, Scott, and William McGinnis. 1993. "Drosophila Homeobox Genes." In *Advances in Developmental Biochemistry*, edited by Paul M. Wassarman, 2:1–55. Advances in Developmental Biochemistry. Academic Press.
[https://doi.org/10.1016/S1064-2722\(08\)60035-3](https://doi.org/10.1016/S1064-2722(08)60035-3).
- Dixon, Jesse R., Siddarth Selvaraj, Feng Yue, Audrey Kim, Yan Li, Yin Shen, Ming Hu, Jun S. Liu, and Bing Ren. 2012. "Topological Domains in Mammalian Genomes Identified by Analysis of Chromatin Interactions." *Nature* 485 (7398): 376–80. <https://doi.org/10.1038/nature11082>.
- Ficz, Gabriella, Rainer Heintzmann, and Donna J. Arndt-Jovin. 2005. "Polycomb Group Protein Complexes Exchange Rapidly in Living Drosophila." *Development* 132 (17): 3963–76. <https://doi.org/10.1242/dev.01950>.
- Fonseca, João Pedro, Philipp A. Steffen, Stefan Müller, James Lu, Anna Sawicka, Christian Seiser, and Leonie Ringrose. 2012. "In Vivo Polycomb Kinetics and Mitotic Chromatin Binding Distinguish Stem Cells from Differentiated Cells." *Genes & Development* 26 (8): 857–71. <https://doi.org/10.1101/gad.184648.111>.
- Francis, Nicole J., Robert E. Kingston, and Christopher L. Woodcock. 2004. "Chromatin Compaction by a Polycomb Group Protein Complex." *Science* 306 (5701): 1574–77. <https://doi.org/10.1126/science.1100576>.
- Franke, Axel, Sabine Messmer, and Renato Paro. 1995. "Mapping Functional Domains of the Polycomb Protein OfDrosophila Melanogaster." *Chromosome Research* 3 (6): 351–60. <https://doi.org/10.1007/BF00710016>.
- Grau, Daniel J., Brad A. Chapman, Joe D. Garlick, Mark Borowsky, Nicole J. Francis, and Robert E. Kingston. 2011. "Compaction of Chromatin by Diverse Polycomb Group Proteins Requires Localized Regions of High Charge." *Genes & Development* 25 (20): 2210–21. <https://doi.org/10.1101/gad.172882.11>.
- Halverson, Jonathan D., Jan Smrek, Kurt Kremer, and Alexander Y. Grosberg. 2014. "From a Melt of Rings to Chromosome Territories: The Role of Topological Constraints in Genome Folding." *Reports on Progress in Physics* 77 (2): 022601. <https://doi.org/10.1088/0034-4885/77/2/022601>.
- Hou, Chunhui, Li Li, Zhaohui S. Qin, and Victor G. Corces. 2012. "Gene Density, Transcription, and Insulators Contribute to the Partition of the Drosophila Genome into Physical Domains." *Molecular Cell* 48 (3): 471–84. <https://doi.org/10.1016/j.molcel.2012.08.031>.
- Hug, Clemens B., Alexis G. Grimaldi, Kai Kruse, and Juan M. Vaquerizas. 2017. "Chromatin Architecture Emerges during Zygotic Genome Activation Independent of Transcription." *Cell* 169 (2): 216–228.e19. <https://doi.org/10.1016/j.cell.2017.03.024>.
- Huseyin, Miles K., and Robert J. Klose. 2021. "Live-Cell Single Particle Tracking of PRC1 Reveals a Highly Dynamic System with Low Target Site Occupancy." *Nature Communications* 12 (1): 887. <https://doi.org/10.1038/s41467-021-21130-6>.
- Isono, Kyoichi, Takaho A. Endo, Manching Ku, Daisuke Yamada, Rie Suzuki, Jafar Sharif, Tomoyuki Ishikura, Tetsuro Toyoda, Bradley E. Bernstein, and Haruhiko Koseki. 2013. "SAM Domain Polymerization Links Subnuclear Clustering of PRC1 to Gene Silencing." *Developmental Cell* 26 (6): 565–77. <https://doi.org/10.1016/j.devcel.2013.08.016>.
- Jost, Daniel, Pascal Carrivain, Giacomo Cavalli, and Cédric Vaillant. 2014. "Modeling Epigenome Folding: Formation and Dynamics of Topologically Associated Chromatin Domains." *Nucleic Acids Research* 42 (15): 9553–61. <https://doi.org/10.1093/nar/gku698>.
- Kadoch, Cigall, Robert T. Williams, Joseph P. Calarco, Erik L. Miller, Christopher M. Weber, Simon M. G. Braun, John L. Pulice, Emma J. Chory, and Gerald R. Crabtree. 2017. "Dynamics of BAF–Polycomb Complex Opposition on Heterochromatin in Normal and Oncogenic States." *Nature Genetics* 49 (2): 213–22. <https://doi.org/10.1038/ng.3734>.
- Kaufman, Thomas C., Mark A. Seeger, and Gary Olsen. 1990. "Molecular and Genetic Organization of The Antennapedia Gene Complex of Drosophila Melanogaster." In *Advances in Genetics*, edited by Theodore R. F. Wright, 27:309–62. Genetic Regulatory Hierarchies in Development.

- Academic Press. [https://doi.org/10.1016/S0065-2660\(08\)60029-2](https://doi.org/10.1016/S0065-2660(08)60029-2).
- Lanzuolo, Chiara, Virginie Roue, Job Dekker, Frédéric Bantignies, and Valerio Orlando. 2007. "Polycomb Response Elements Mediate the Formation of Chromosome Higher-Order Structures in the Bithorax Complex." *Nature Cell Biology* 9 (10): 1167–74. <https://doi.org/10.1038/ncb1637>.
- Lewis, E. B. 1978. "A Gene Complex Controlling Segmentation in *Drosophila*." *Nature* 276 (5688): 565–70. <https://doi.org/10.1038/276565a0>.
- Lewis, Edward B., Barret D. Pfeiffer, David R. Mathog, and Susan E. Celniker. 2004. "Evolution of the Homeobox Complex in the Diptera." In *Genes, Development and Cancer: The Life and Work of Edward B. Lewis*, edited by Howard D. Lipshitz, 381–85. Boston, MA: Springer US. https://doi.org/10.1007/978-1-4419-8981-9_24.
- Li, Hua-Bing, Katsuhito Ohno, Hongxing Gui, and Vincenzo Pirrotta. 2013. "Insulators Target Active Genes to Transcription Factories and Polycomb-Repressed Genes to Polycomb Bodies." *PLOS Genetics* 9 (4): e1003436. <https://doi.org/10.1371/journal.pgen.1003436>.
- Lieberman-Aiden, Erez, Nynke L. van Berkum, Louise Williams, Maxim Imakaev, Tobias Ragozy, Agnes Telling, Ido Amit, et al. 2009. "Comprehensive Mapping of Long-Range Interactions Reveals Folding Principles of the Human Genome." *Science* 326 (5950): 289–93. <https://doi.org/10.1126/science.1181369>.
- Linkert, Melissa, Curtis T. Rueden, Chris Allan, Jean-Marie Burel, Will Moore, Andrew Patterson, Brian Loranger, et al. 2010. "Metadata Matters: Access to Image Data in the Real World." *Journal of Cell Biology* 189 (5): 777–82. <https://doi.org/10.1083/jcb.201004104>.
- Mateo, Leslie J., Sedona E. Murphy, Antonina Hafner, Isaac S. Cinquini, Carly A. Walker, and Alistair N. Boettiger. 2019. "Visualizing DNA Folding and RNA in Embryos at Single-Cell Resolution." *Nature* 568 (7750): 49–54. <https://doi.org/10.1038/s41586-019-1035-4>.
- Mirny, Leonid A. 2011. "The Fractal Globule as a Model of Chromatin Architecture in the Cell." *Chromosome Research* 19 (1): 37–51. <https://doi.org/10.1007/s10577-010-9177-0>.
- Nègre, Nicolas, Jérôme Hennetin, Ling V. Sun, Sergey Lavrov, Michel Bellis, Kevin P. White, and Giacomo Cavalli. 2006. "Chromosomal Distribution of PcG Proteins during *Drosophila* Development." *PLOS Biology* 4 (6): e170. <https://doi.org/10.1371/journal.pbio.0040170>.
- Nora, Elphège P., Bryan R. Lajoie, Edda G. Schulz, Luca Giorgetti, Ikuhiro Okamoto, Nicolas Servant, Tristan Piolot, et al. 2012. "Spatial Partitioning of the Regulatory Landscape of the X-Inactivation Centre." *Nature* 485 (7398): 381–85. <https://doi.org/10.1038/nature11049>.
- Ogiyama, Yuki, Bernd Schuettengruber, Giorgio L. Papadopoulos, Jia-Ming Chang, and Giacomo Cavalli. 2018. "Polycomb-Dependent Chromatin Looping Contributes to Gene Silencing during *Drosophila* Development." *Molecular Cell* 71 (1): 73–88.e5. <https://doi.org/10.1016/j.molcel.2018.05.032>.
- Plys, Aaron J., Christopher P. Davis, Jongmin Kim, Gizem Rizki, Madeline M. Keenen, Sharon K. Marr, and Robert E. Kingston. 2019. "Phase Separation of Polycomb-Repressive Complex 1 Is Governed by a Charged Disordered Region of CBX2." *Genes & Development* 33 (13–14): 799–813. <https://doi.org/10.1101/gad.326488.119>.
- Rouillard, Jean-Marie, Michael Zuker, and Erdogan Gulari. 2003. "OligoArray 2.0: Design of Oligonucleotide Probes for DNA Microarrays Using a Thermodynamic Approach." *Nucleic Acids Research* 31 (12): 3057–62. <https://doi.org/10.1093/nar/gkg426>.
- Rowley, M. Jordan, Michael H. Nichols, Xiaowen Lyu, Masami Ando-Kuri, I. Sarahi M. Rivera, Karen Hermetz, Ping Wang, Yijun Ruan, and Victor G. Corces. 2017. "Evolutionarily Conserved Principles Predict 3D Chromatin Organization." *Molecular Cell* 67 (5): 837–852.e7. <https://doi.org/10.1016/j.molcel.2017.07.022>.
- Sakaue, T., J.-C. Walter, E. Carlon, and C. Vanderzande. 2017. "Non-Markovian Dynamics of Reaction Coordinate in Polymer Folding." *Soft Matter* 13 (17): 3174–81. <https://doi.org/10.1039/C7SM00395A>.
- Saurin, Andrew J., Carol Shiels, Jill Williamson, David P.E. Satijn, Arie P. Otte, Denise Sheer, and Paul S.

- Freemont. 1998. "The Human Polycomb Group Complex Associates with Pericentromeric Heterochromatin to Form a Novel Nuclear Domain." *Journal of Cell Biology* 142 (4): 887–98. <https://doi.org/10.1083/jcb.142.4.887>.
- Schindelin, Johannes, Ignacio Arganda-Carreras, Erwin Frise, Verena Kaynig, Mark Longair, Tobias Pietzsch, Stephan Preibisch, et al. 2012. "Fiji: An Open-Source Platform for Biological-Image Analysis." *Nature Methods* 9 (7): 676–82. <https://doi.org/10.1038/nmeth.2019>.
- Schneider, Caroline A., Wayne S. Rasband, and Kevin W. Eliceiri. 2012. "NIH Image to ImageJ: 25 Years of Image Analysis." *Nature Methods* 9 (7): 671–75. <https://doi.org/10.1038/nmeth.2089>.
- Sexton, Tom, Eitan Yaffe, Ephraim Kenigsberg, Frédéric Bantignies, Benjamin Leblanc, Michael Hoichman, Hugues Parrinello, Amos Tanay, and Giacomo Cavalli. 2012. "Three-Dimensional Folding and Functional Organization Principles of the Drosophila Genome." *Cell* 148 (3): 458–72. <https://doi.org/10.1016/j.cell.2012.01.010>.
- Stanton, Benjamin Z., Courtney Hodges, Joseph P. Calarco, Simon M. G. Braun, Wai Lim Ku, Cigall Kadoch, Keji Zhao, and Gerald R. Crabtree. 2017. "Smarca4 ATPase Mutations Disrupt Direct Eviction of PRC1 from Chromatin." *Nature Genetics* 49 (2): 282–88. <https://doi.org/10.1038/ng.3735>.
- Steffen, Philipp A., João Pedro Fonseca, Cornelia Gänger, Eva Dworschak, Tobias Kockmann, Christian Beisel, and Leonie Ringrose. 2013. "Quantitative in Vivo Analysis of Chromatin Binding of Polycomb and Trithorax Group Proteins Reveals Retention of ASH1 on Mitotic Chromatin." *Nucleic Acids Research* 41 (10): 5235–50. <https://doi.org/10.1093/nar/gkt217>.
- Strübbe, Gero, Christian Popp, Alexander Schmidt, Andrea Pauli, Leonie Ringrose, Christian Beisel, and Renato Paro. 2011. "Polycomb Purification by in Vivo Biotinylation Tagging Reveals Cohesin and Trithorax Group Proteins as Interaction Partners." *Proceedings of the National Academy of Sciences* 108 (14): 5572–77. <https://doi.org/10.1073/pnas.1007916108>.
- Su, Jun-Han, Pu Zheng, Seon S. Kinrot, Bogdan Bintu, and Xiaowei Zhuang. 2020. "Genome-Scale Imaging of the 3D Organization and Transcriptional Activity of Chromatin." *Cell* 182 (6): 1641–1659.e26. <https://doi.org/10.1016/j.cell.2020.07.032>.
- Szabo, Quentin, Frédéric Bantignies, and Giacomo Cavalli. 2019. "Principles of Genome Folding into Topologically Associating Domains." *Science Advances* 5 (4): eaaw1668. <https://doi.org/10.1126/sciadv.aaw1668>.
- Szabo, Quentin, Daniel Jost, Jia-Ming Chang, Diego I. Cattoni, Giorgio L. Papadopoulos, Boyan Bonev, Tom Sexton, et al. 2018a. "TADs Are 3D Structural Units of Higher-Order Chromosome Organization in *Drosophila*." *Science Advances* 4 (2): eaar8082. <https://doi.org/10.1126/sciadv.aar8082>.
- Takei, Yodai, Jina Yun, Shiwei Zheng, Noah Ollikainen, Nico Pierson, Jonathan White, Sheel Shah, et al. 2021. "Integrated Spatial Genomics Reveals Global Architecture of Single Nuclei." *Nature* 590 (7845): 344–50. <https://doi.org/10.1038/s41586-020-03126-2>.
- Tolhuis, Bas, Marleen Blom, Ron M. Kerkhoven, Ludo Pagie, Hans Teunissen, Marja Nieuwland, Marieke Simonis, Wouter de Laat, Maarten van Lohuizen, and Bas van Steensel. 2011. "Interactions among Polycomb Domains Are Guided by Chromosome Architecture." *PLOS Genetics* 7 (3): e1001343. <https://doi.org/10.1371/journal.pgen.1001343>.
- Walter, J. -C., and G. T. Barkema. 2015. "An Introduction to Monte Carlo Methods." *Physica A: Statistical Mechanics and Its Applications*, Proceedings of the 13th International Summer School on Fundamental Problems in Statistical Physics, 418 (January): 78–87. <https://doi.org/10.1016/j.physa.2014.06.014>.
- Walter, J.-C., M. Baiesi, G. T. Barkema, and E. Carlon. 2013. "Unwinding Relaxation Dynamics of Polymers." *Physical Review Letters* 110 (6): 068301. <https://doi.org/10.1103/PhysRevLett.110.068301>.
- Wang, Liangjun, J. Lesley Brown, Ru Cao, Yi Zhang, Judith A Kassis, and Richard S Jones. 2004. "Hierarchical Recruitment of Polycomb Group Silencing Complexes." *Molecular Cell* 14 (5): 637–46. <https://doi.org/10.1016/j.molcel.2004.05.009>.

Wani, Ajazul H., Alistair N. Boettiger, Patrick Schorderet, Ayla Ergun, Christine Munger, Ruslan I. Sadreyev, Xiaowei Zhuang, Robert E. Kingston, and Nicole J. Francis. 2016. "Chromatin Topology Is Coupled to Polycomb Group Protein Subnuclear Organization." *Nature Communications* 7 (1): 10291. <https://doi.org/10.1038/ncomms10291>.

Zenk, Fides, Yinxiu Zhan, Pavel Kos, Eva Loser, Nazerke Atinbayeva, Melanie Schachtle, Guido Tiana, Luca Giorgetti, and Nicola Iovino. 2021. "HP1 Drives de Novo 3D Genome Reorganization in Early *Drosophila* Embryos." *Nature* 593 (7858): 289–93. <https://doi.org/10.1038/s41586-021-03460-z>.

Figure 1

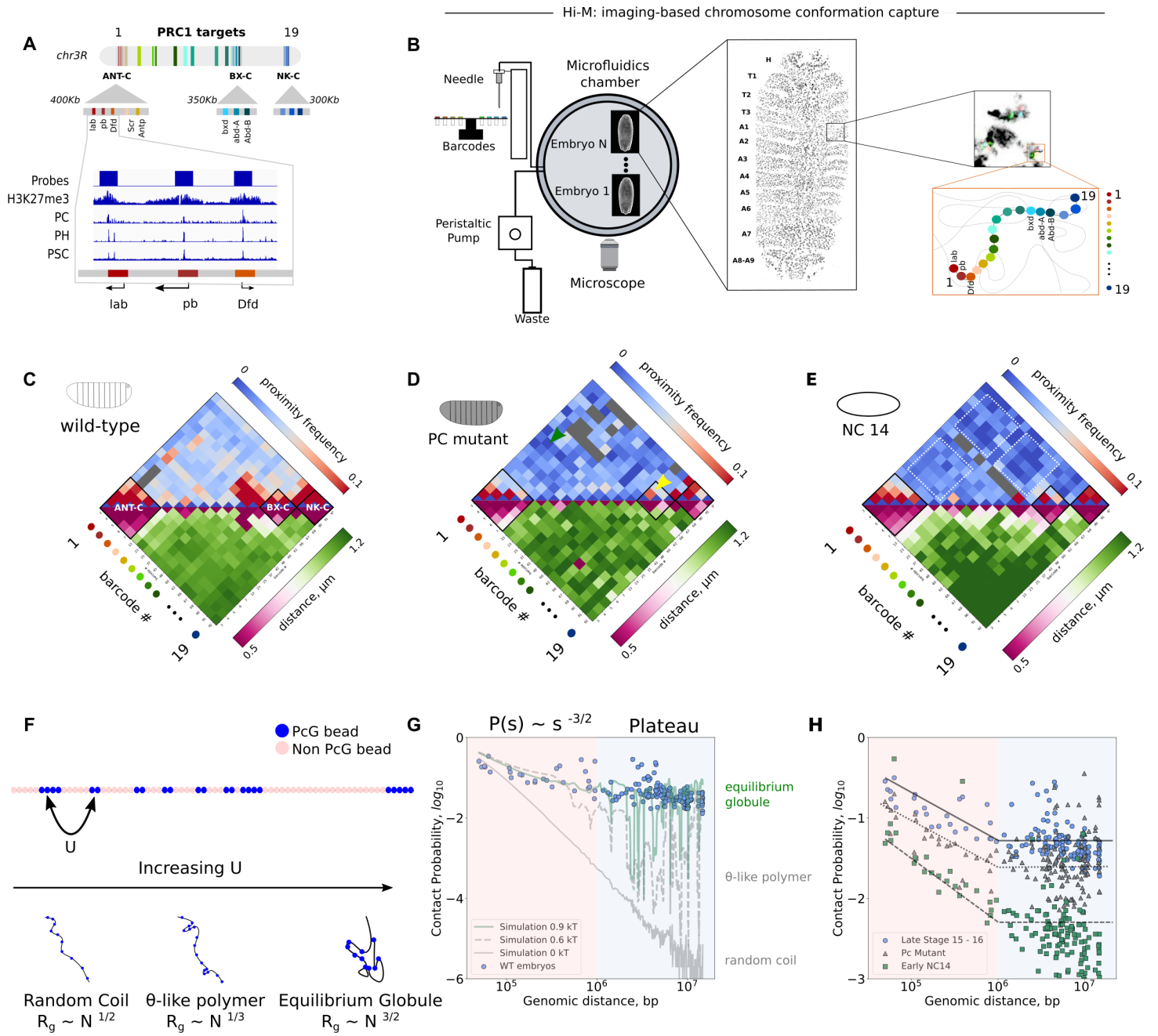


Figure 1 Supplementary

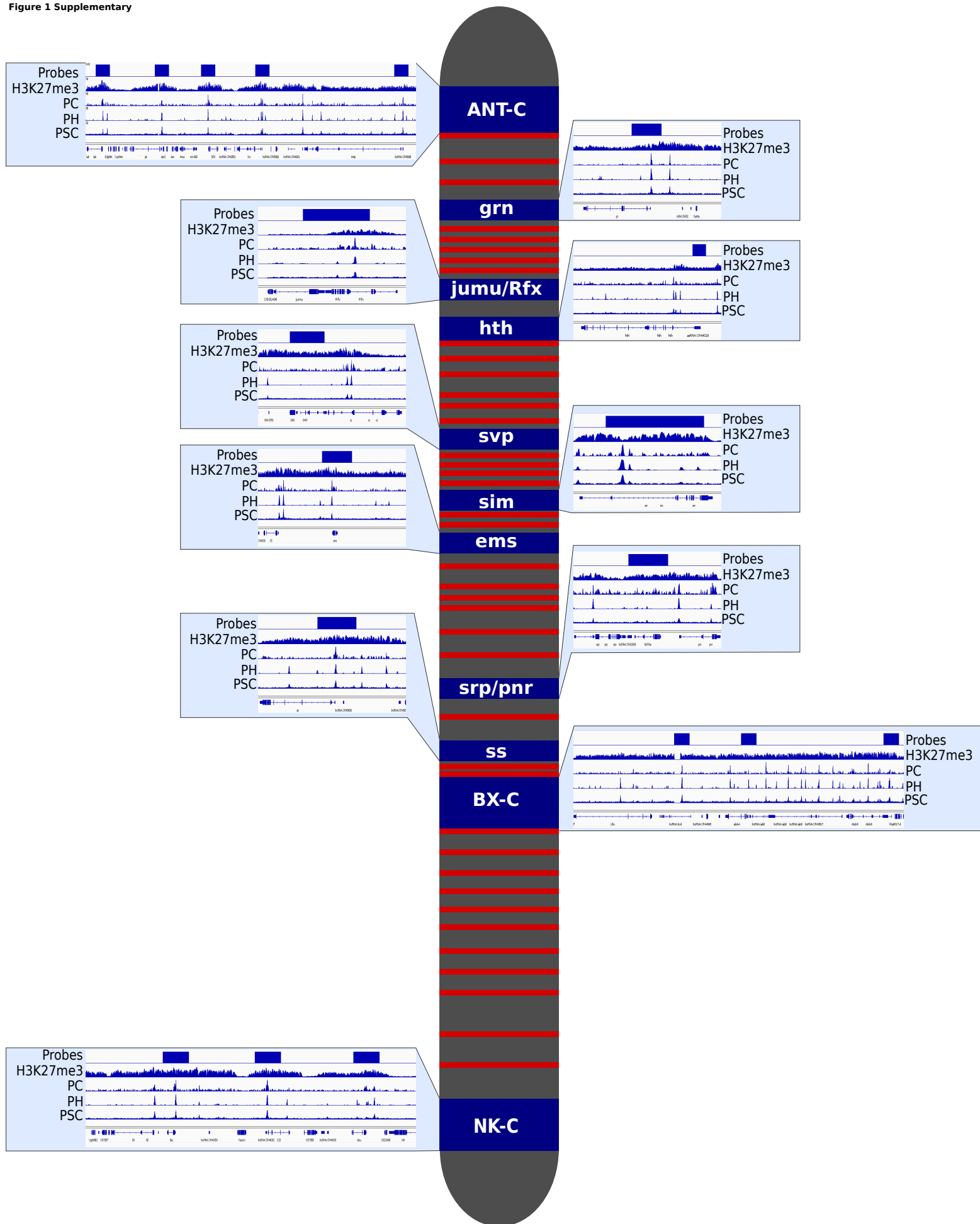


Figure 2 Supplementary

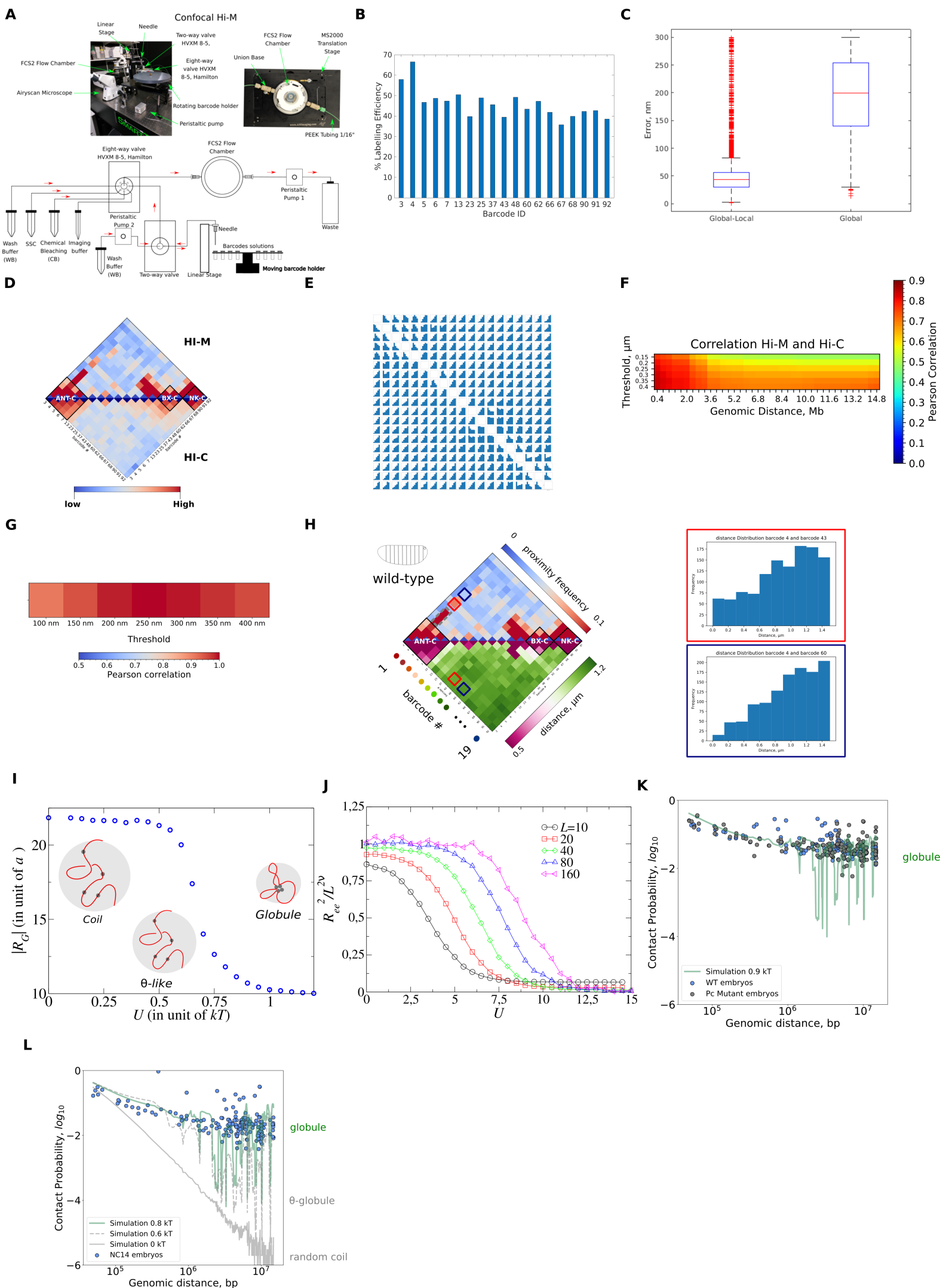


Figure 2

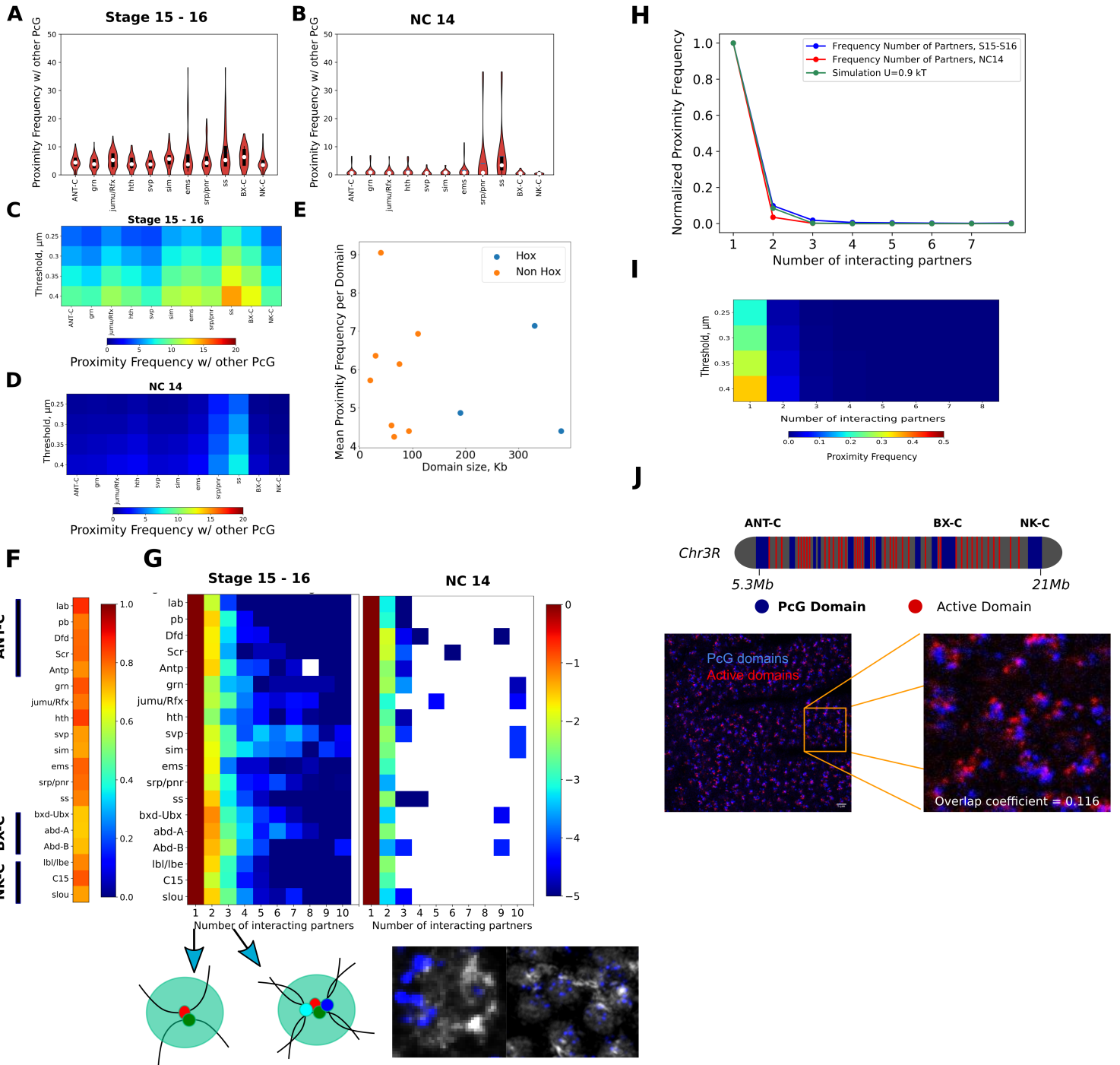


Figure 3 Supplementary

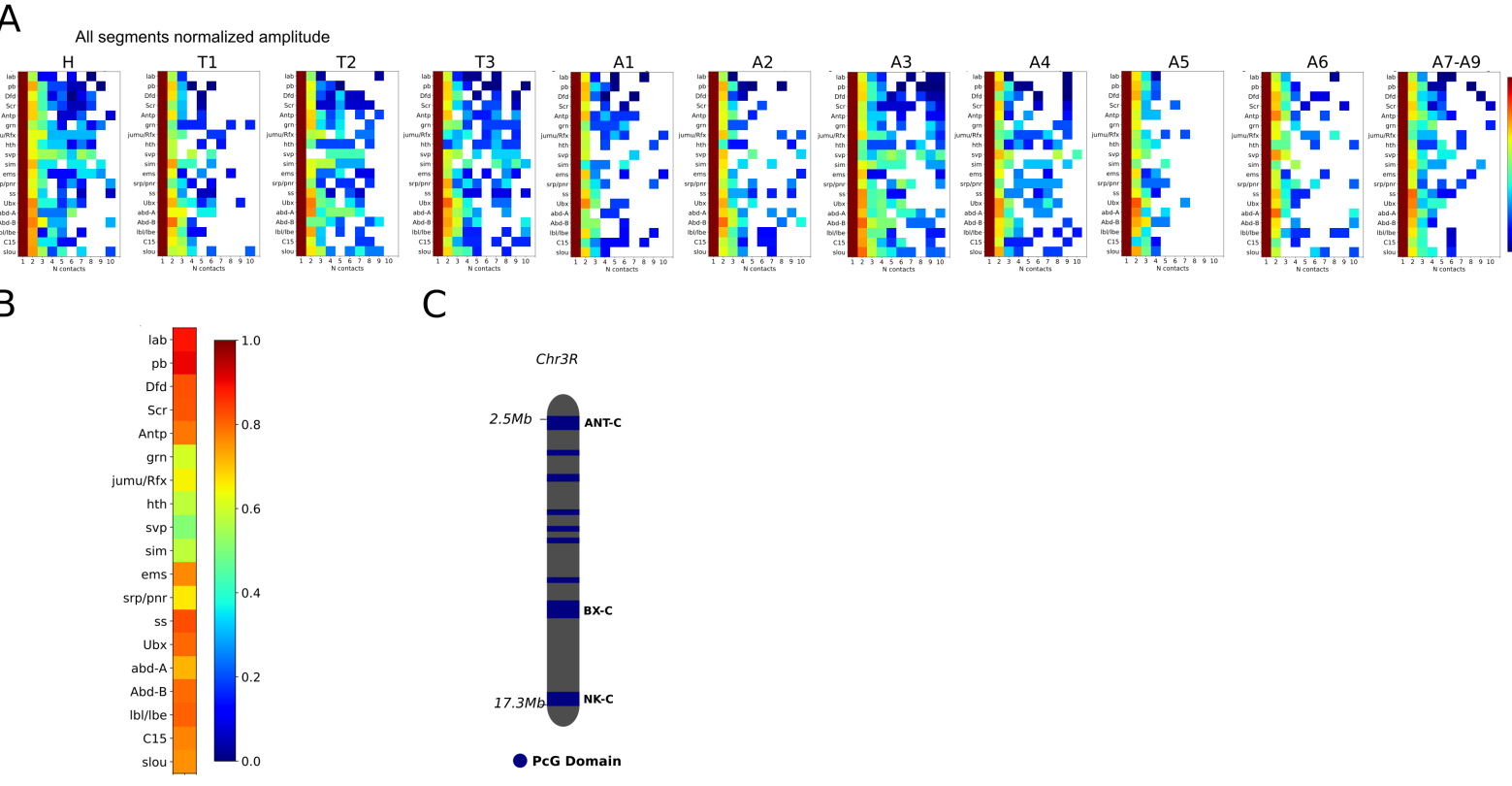


Figure 3

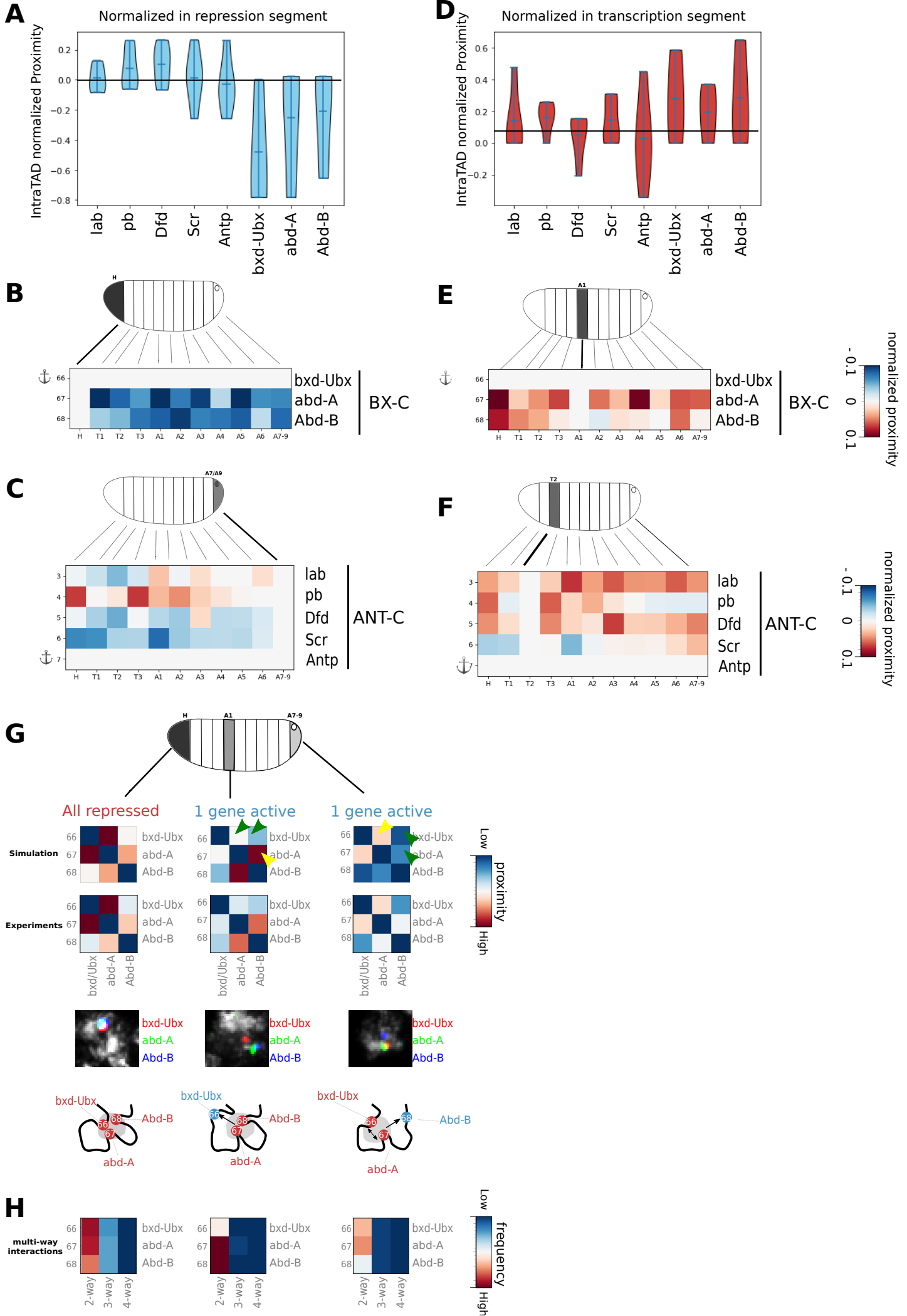
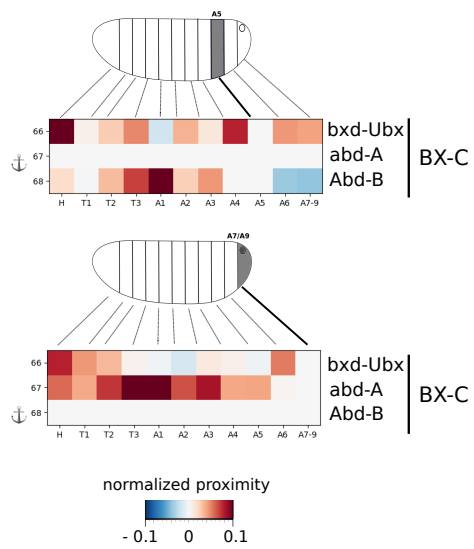


Figure 4 Supplementary

A



B

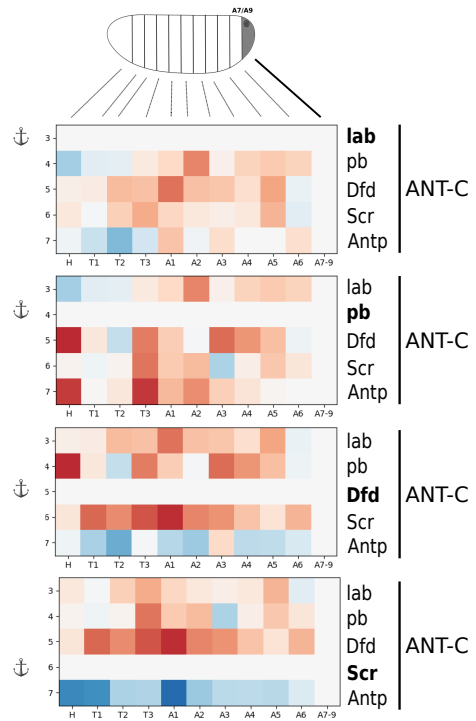


Figure 4

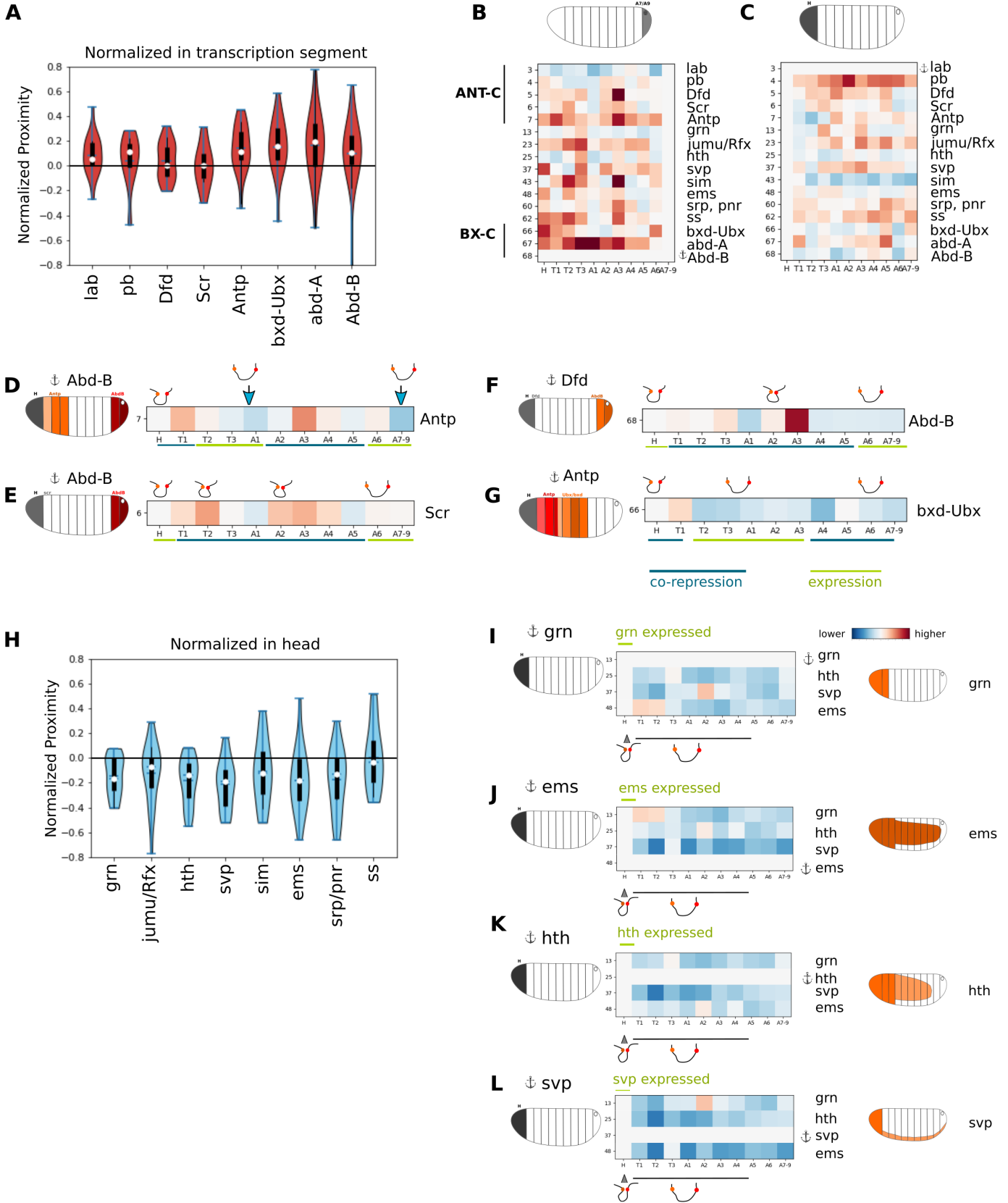


Figure 5 Supplementary

A

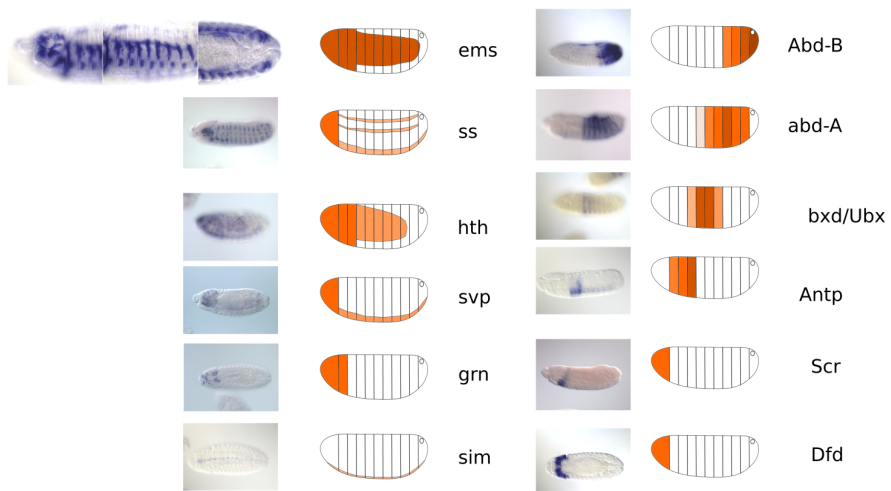
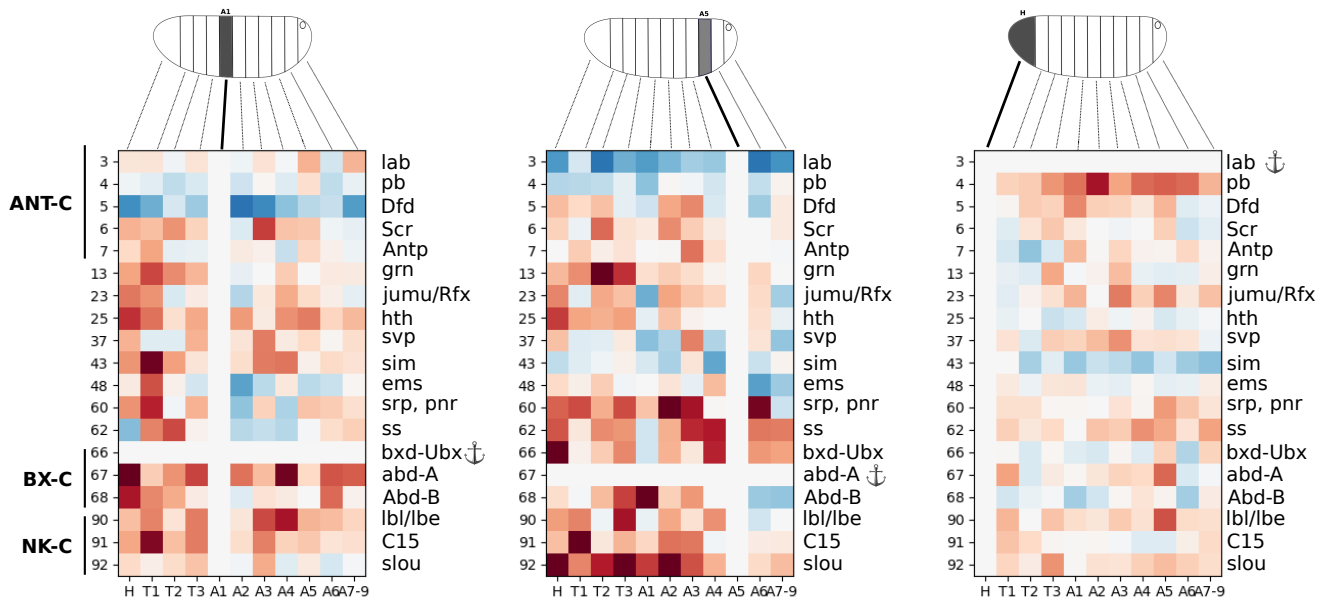


Figure 6 Supplementary

A



3 Discussion

PcG proteins are evolutionarily conserved chromatin modifying factors that regulate repression of key regulatory and developmental genes. They exert their repressive activity both by their histone modifying activity and their role in 3D organization. In *Drosophila*, PRC1 complex proteins cause nucleosome compaction, rendering chromatin inaccessible to the transcriptional machinery or to activating factors such as TrxG proteins [Shao et al., 1999, Francis et al., 2004, Francis et al., 2001, Yuan et al., 2012, Lau et al., 2017]. In addition, regions bound by PcG proteins display a more compact architecture when compared with other chromatin types [Boettiger et al., 2016, Kundu et al., 2017]. PcG components also mediate looping interactions between Polycomb Response Elements (PREs), and cis-regulatory elements (CREs) [Lanzuolo et al., 2007, Comet et al., 2011, Tiwari et al., 2008, Eagen et al., 2017, Ogiyama et al., 2018], PcG proteins both modify the structure and the function of chromatin. At higher orders levels of organization, PcG bound regions can mediate long-range interactions [Bantignies et al., 2011, Schoenfelder et al., 2015, Bonev et al., 2017], even when the interacting loci are separated by several Mb (for example, Hox gene clusters in *Drosophila* [Bantignies et al., 2011]). These interactions are thought to reinforce gene repression, and it has been hypothesized that PcG targets form repressive compartments that appear in single cells as PcG foci (Polycomb bodies) [Delest et al., 2012, Bantignies and Cavalli, 2011, Isono et al., 2013]. These results suggest that multiple PcG domains may associate in single cells to form "repressive environments" with many interacting partners. These hubs may display a tissue specific behaviour that follow the pattern of expression of the genes involved.

In this work, we tested this hypothesis using Hi-M, an imaging-based method that enables the reconstruction of chromatin architecture *in situ*. Hi-M is a well suited technique to investigate PcG architecture because it allows the localization of multiple genomic loci at the same time with genomic specificity, and in addition maintains spatial information so that single-cell conformations can be linked to different tissues within developing embryos. In this way, architecture can be compared with well established gene expression patterns.

Multiple PcG targets on chromosome 3R were imaged using Hi-M, for stage 15-16, nuclear cycle 14, and *PcXT109* null mutant *Drosophila* embryos. It has been observed that PcG target genes interact in 3D, a phenomenon that has been termed 'gene kissing' [Bantignies et al., 2011, Sexton et al., 2012]. These studies determined that interactions between pairs of distant Hox genes were rare (10-20%), and proposed that the existence of multiple Polycomb partners explains why two Hox genes only interact in a small fraction of nuclei. Our work shows that interactions of a PcG target with any other distant PcG targets are indeed infrequent. Moreover, these interactions are acquired after TAD emergence at NC14 [Hug et al., 2017, Ogiyama et al., 2018], concomitantly with the enrichment of PcG foci [Cheutin and Cavalli, 2012]. Furthermore, we show that both intra-TAD and inter-TAD (long range) interactions predominantly involve two PcG target genes. This is consistent with previous works showing that PcG TADs appear as discrete chromosomal units [Szabo et al., 2018]. Thus, our evidence is inconsistent with the hypothesis of cluster formation, and suggests a high degree of diversity and flexibility in the formation of the PcG domains interacting network. PcG bound regions undergo inter-domain interactions with low frequencies, suggesting that most PcG silencing occurs via *in situ* cis regulatory elements. These low-frequency pairwise interactions occur with higher probability in late stage embryos, suggesting that they are established during

development to reinforce repression of their targets. Indeed, PcG long range interactions form a second level of repression, as it has been shown that perturbation of long-range contacts leads to a small but detectable transcriptional de-repression [Bantignies et al., 2011].

DNA is a polymer, and several modelling strategies have been developed to describe and understand the physics of chromatin folding. We combined our data with polymer simulations, using a block copolymer on an FCC lattice [Jost et al., 2014, Jost and Vaillant, 2018]. The simulated polymer consists of Polycomb beads that match the positions of the PcG domains imaged, and active (non interacting) beads in between. Polycomb beads in the model are allowed to interact with an energy of interaction U between monomers defined by the experimental data. Non-Polycomb beads have $U=0$. Phase separation diagrams for these kind of models show that polymers can be either in coil regime, where the chain is in an extended open-configuration and randomly folded; or in globule regime, that represents a more compact phase where different regions of the polymer interact. The separating region between these two phases is known as the θ -line. The modeling approach used in our work shows that PcG domains behave like a polymer in the globule regime, and close to the θ -transition line in the phase diagram. In this configuration, a small change in the interaction energy between monomers leads to a huge change in the overall energy of the polymer, allowing chromatin to switch conformation easily with a small difference in U . Biologically, this allows PcG domains to rapidly switch conformation when needed, for example, when gene activation leads the active gene to avoid repressed partners. PcG simulations show that the experimental data can be well described by a microphase-separated polymer in the globule phase. Strikingly, the model also shows that these interactions are mostly pairwise, in agreement with our experimental results. We sought to determine if the model could reproduce the behaviour of Hox clusters upon the activation of the genes contained. The beads corresponding to BX-C genes were switched from Polycomb to active ($U=0$), following their known behaviour in the zones of the embryo where they become active. The results obtained from modeling show a remarkable similarity with experimental data. Thus, a simple polymer model can describe many experimental observations. Furthermore, the polymer microphase separation phenomenon observed in the model is consistent with PcG TADs forming discrete 3D chromosomal units [Szabo et al., 2018]. Polymer microphase separation is observed both in WT and *PcXT109* null mutant embryos, showing that other factors than Pc are involved in long range PcG interactions. These factors may possibly involve proteins implicated in the formation of heterochromatin, active, or black compartments, such as HP1 [Zenk et al., 2021], chromatin insulators, cohesin, transcription hubs, or other subunits of the Pc- or trithorax-group family. This suggests that the composition of PcG compartments may be regulated by their epigenetic and transcriptional status.

We tested this hypothesis by reconstructing chromatin architecture in different embryonic segments, that display different epigenetic and transcriptional states. We observed that upon activation, PcG genes tend to lose contacts with other PcG domains. To further study the relation between gene activity and architecture, we focused on the Hox gene clusters BX-C and ANTP-C. We observed that PcG domains display the highest contact probabilities with other PcG targets when they are co-repressed. These interactions are predominantly pairwise. Upon activation, PcG target genes display higher physical distances (i.e. lower contact probabilities) with other genes inside the domain. This is consistent with previous observations on a limited number of targets [Lanzuolo et al., 2007, Bantignies et al., 2011, Cheutin and Cavalli, 2018]. Furthermore, we show

that non-Hox PcG domain interactions are also higher when the target genes are co-activated. This is consistent with a previous work using a small number of targets [Li et al., 2013]. Overall, our evidence shows that the spatial proximity of PcG targets is defined by their transcriptional state, both in repressed and active states. A possibility that should be explored in the future is whether Trithorax group proteins (TrxG) may be involved in co-active interactions, since their active role in PcG eviction, and their known molecular interactions with PcG proteins [Kadoch et al., 2017, Stanton et al., 2017, Strübbe et al., 2011]. Indeed, TrxG and PcG proteins may cooperate to fine tune gene expression. Furthermore, other factors like the cohesin complex or the GAGA-factor (GAF) have been also shown to play a role in the formation of Polycomb loops [Ogiyama et al., 2018] or in the interaction with PcG proteins [Strübbe et al., 2011], and have been implicated in gene activation and repression [Dorsett, 2009, Dorsett, 2019]. Their role in shaping PcG architecture should also be explored.

Future experiments that will help us better understand PcG organization include the study of other chromatin types (i.e. active and black) to better understand their role in shaping PcG domain architecture. In particular, it will be interesting to quantify the architecture of those domains in *PcXT109* embryos, to quantify their effect in constraining and shaping PcG organization. Furthermore, perturbations of insulator binding proteins and/or binding sites may help to understand to what extent PcG architecture is solely dependent on PcG proteins.

As mentioned above, we showed that co-expressed genes display a higher physical proximity. This may depend on trithorax-group proteins [Kingston and Tamkun, 2014, Schuettengruber et al., 2017]. An interesting experiment to extend this results would be to image a fly line lacking the trithorax (*trx*) subunit of the TrxG complex, a subunit with chromatin-remodelling and enzymatic activity, to explore whether this mutation leads to a perturbed co-expressed target architecture. Other interesting subunit with similar activity that should be investigated is *brahma* (*brm*). Another interesting open question relates to the correlation between PcG activation state and PcG architecture. Our data only shows that there's a correlation, not being able to discern a cause-effect role. Optogenetic approaches like LADL, where long-range chromatin loops can be generated upon exposure to blue light [Kim et al., 2019], combined with live imaging and post imaging RNA-seq may be a good way to study their relationship. Recently, mammalian PcG-mediated long-range interactions were proposed to involve liquid-liquid phase separation (LLPS), since PcG proteins have been shown to form phase separated condensates *in vitro* and *in vivo* [Seif et al., 2020, Plys et al., 2019, Tatavosian et al., 2019]. An interesting hypothesis to pursue is whether LLPS plays a role on establishing and maintaining PcG domain interactions both in mammals and *Drosophila*. Further experiments are needed to test if PcG proteins form phase separated condensates in *Drosophila*, and if this drives PcG architecture. Future research will be needed to clarify this important question. Approaches like OptoDroplets [Shin et al., 2017] allow to induce phase separation *in vivo*. These methods could be used to induce phase separation of Polycomb Group proteins *in vivo*, to further explore the relation of phase separation of PcG proteins and gene repression.

Finally, another interesting question regards the deposition of PcG proteins during cell division. It could be interesting to study whether and how PcG domain architecture may be passed from one cell generation to the next one. It has been shown that PcG proteins remain bound to DNA during DNA replication *in vitro* [Francis et al., 2009], particularly proteins of the PRC1 group. Interestingly, it has also been shown that PcG

proteins affect physical structure and replication timing [Lo Sardo et al., 2013]. However, it is not known whether this implies conservation of architecture. The monitoring of chromatin state and architecture during cell division using the imaging approaches that we developed may show how architecture and repressed states are passed to daughter cells, and how this affects cell identity.

4 Materials and Methods

4.1 Domain selection and Library design

A portion of 15 Mb of chromosome 3R was selected. A 3 node self-organizing map (SOM, 'kohonen' R package) was used to produce a 3-way segmentation of 10 Kb genome wide bins. Each bin was scored based on the average ChIP-seq read counts of H3K27me3, H3K4me3 and H3K36me3 from 14-16 hr embryos (modEncode, 3955 H3K27me3, Embryos-14-16 hr, OregonR, ChIP-seq; modEncode, 5096: H3K4me3, Oregon-R, Embryos 14-16 hr OR, ChIP-seq; 4950: H3K36me3, Oregon-R, Embryos 14-16 hr OR, ChIP-seq). Each SOM node was treated as a discrete cluster and contiguous bins assigned to the same node were merged into one epi-domain. Only epi-domains of a size equal or bigger to 20 kb were selected.

For PcG domains, these epi-domains were later re-selected based on the enrichment of H3K27me3 (modEncode, 3955 H3K27me3, Embryos-14-16 hr; OregonR;ChIP-seq), and of PRC1 subunits PC, PH for embryos of 16 - 18 hrs of development (coming from Schuettengruber B, et. al, 2014, accession number GSE60428) and PSC (modEncode, 3960: Psc;Oregon-R;Embryos 14-16 hr OR;ChIP-seq, *D. melanogaster*). Domains having peaks of at least two of these PRC1 subunits were kept. They were also visually inspected using Hi-C maps from [Ogiyama et al., 2018].

For active domains, they were re-selected based on the enrichment of H3K4me3 and H3K36me3 (modEncode, 5096: H3K4me3;Oregon-R;Embryos 14-16 hr OR;ChIP-seq; 4950: H3K36me3; Oregon-R; Embryos 14-16 hr OR ;ChIP-seq), and they were also visually inspected using Hi-C maps from [Ogiyama et al., 2018].

For inactive domains, they were selected based on the absence of the aforementioned epigenetic marks.

The criteria used to design the libraries is the following:

- Domains between 20 kb - 100 kb: This domains have one 15 kb probe, centered in the middle of the domain, and not necessarily centered in or covering a PcG protein peak.
- Domains between 100 kb - 200 kb: These domains are covered by two 15 kb probes. They target PcG protein peaks inside the domain.
- Domains bigger than 200 kb: These domains are covered by three 15 kb probes, located in the same way as those 100 kb - 200 kb.

To study the Intra-Domain organization of Hox genes domains (which have a clear and defined pattern of expression), three particular exceptions were made:

- **ANTP-C:** It contains 5 probes targeting the promoters of the ANT-C genes: *lab*, *pb*, *Dfd*, *Scr*, *Antp*.
- **BX-C:** It contains 3 probes targeting the prominent PcG protein peak in *bx*, *abd-A*, *Abd-B*.
- **NK-C:** It contains 3 probes targeting promoters of *lbe/lbl*, *C15* and *slou*.

One extra domain was selected as fiducial mark for drift correction. A total of 89 barcodes is needed to target all libraries (19 PcG, 39 active and 31 inactive, 1 fiducial mark).

4.2 Library synthesis and amplification

The library synthesis method is based on a development by Beliveau et al [Beliveau et al., 2012]. After selecting the genomic regions of interest, a database of genomically unique, non overlapping sequences was used to generate the Oligopaint primary probes (Oligopaints website, <https://oligopaints.hms.harvard.edu/>). They were mined using OligoArray [Rouillard et al., 2003]

Each Oligo of the library is made of 148 nucleotides (nt), and consists of (from 5' to 3'):

- A 22-nt forward universal primer region for library amplification.
- A 20-nt readout region, unique for each 15 kb targeted region.
- A 2-nt spacer.
- A 20-nt readout region, unique for each 15 kb targeted region.
- A 42-nt region of homology to chromosomal DNA.
- A 20-nt readout region, unique for each 15 kb targeted region.
- A 22-nt unique reverse primer for library amplification.

An Oligopool with all the nucleotides used was ordered from Custom Array. The procedure to amplify the library consists in four steps:

1. PCR amplification of the Oligopaints library using a reverse primer that adds the T7 promoter sequence
2. Conversion of the PCR product to RNA via an in-vitro transcription using T7 polymerase.
3. Generation of single-stranded DNA (ssDNA) via reverse transcription.
4. Degradation of the RNA template using alkaline hydrolysis.

The following reagents are needed:

- KAPA Taq Kit with dNTPs (CliniSciences, cat. no. BK1003)
- HiScribe T7 High Yield RNA Synthesis Kit (New England BioLabs, cat. no. E2040S)
- Maxima H Minus reverse transcriptase kit (Fisher Scientific, cat. no. 13243159)
- dNTP set (100 mM) solution (Fisher Scientific, cat. no. 10083252)
- RNasin ribonuclease inhibitor (Promega, cat. no. N2515)
- Oligo Clean & Concentrator Kit (Zymo, cat. no. D4060)
- DNA Clean & Concentrator Kit (Zymo; 25 μ g capacity, cat. no. D4033, 100 μ g capacity, cat. no. D4029)

- SYBR Safe Nucleic Acid Gel Stain (Invitrogen, cat. no. S33102)
- RNA loading dye (2×, New England BioLabs, cat.no. B0363S)
- Low-range ssRNA ladder (New England BioLabs, cat. no. N0364S)
- SYBR Gold Nucleic Acid Gel Stain (Fisher Scientific, cat. no. S11494)
- Agarose (standard DNA grade; Euromedex, cat. no. D5-E)
- GeneRuler 100-bp DNA ladder (Fisher Scientific, cat. no. SM0243)
- Ammonium acetate (5 M, Fisher Scientific, cat. no. 10534645)
- TEMED (Thermo Scientific, cat. no. 17919)
- Acrylamide/bis-acrylamide (19:1, 40% (wt/vol)) solution (Fisher Scientific, cat. no. BP1406-01)
- Cetyl PEG-PPG-10-1 dimethicone (ABIL EM 90; Evonik)
- Diethyl ether (Sigma-Aldrich, cat. no. 296082)
- Ethyl acetate (Sigma-Aldrich, cat. no. 270989)

To perform the amplification, the following solutions should be prepared beforehand:

- **PCR Oil Phase:** The final concentrations is 95.95:4:0.05 v/v/v mineral oil/ABIL EM-90/Triton X-100.
- **Water-saturated diethyl ether:** Mix 3 mL of diethyl ether with 3 mL of ddH₂O and vortex for 30 s. Allow the mixture to settle and use the organic upper phase. Prepare freshly.
- **Water-saturated ethyl acetate:** Mix 2 mL of ethyl acetate with 2 mL of ddH₂O and vortex for 30 s. Allow the mixture to settle and use the organic upper phase. Prepare freshly.
- **1 M NaOH solution:** Weigh 2 g of NaOH, mix it with 30 mL of ddH₂O in a 50-mL Falcon tube and dissolve. Bring the volume to 50 mL with ddH₂O and pass the solution through a 0.22- μ m filter.
- **0.5 M EDTA solution:** To prepare 200 mL, weigh 37.23 g of EDTA and mix it with 150 mL of ddH₂O in a glass beaker. Add a magnetic stir bar and stir while adjusting to pH 8 with 10 M NaOH. Add ddH₂O up to 200 mL. Filter the solution with a 0.22- μ m filter. Store at 4 °C.
- **Gel for urea PAGE:** To make the gel, mix 6 g of urea, 1.25 mL of TBE 10× and 3.5 mL of ddH₂O. Heat the solution at 60 °C in a water bath until the urea dissolves. Add 3.125 mL of crylamide/bisacrylamide, 75 μ L of 10% (w/vol) APS and 15 μ L of TEMED. Cast the polyacrylamide gel in 0.75-mm-thick spacers. Prepare freshly.

The protocol is detailed below:

1. Perform an emulsion PCR, to amplify the starting oligo pool in a non-biased manner. To do this, first prepare a PCR master mix for the library to amplify:

Reagent	Quantity (μ L)
<i>ddH₂O</i>	79
10 \times Kapa Taq buffer A	10
BSA (10 μ g/ μ L)	5
dNTPs (10 mM)	2
Forward Universal primer (200 μ M)	1
Reverse primer with T7 (200 μ M)	1
Kapa polymerase enzyme a (5 U/ μ L)	1
Oligo pool library (10–30 ng/ μ L)	1
Total	100

2. All these steps should be performed at 4°C. Pre-chill a 2mL glass flask in the freezer, then place it on the center of stir plate. Add a pre-cooled stir bar to the flask. Using a positive-displacement pipette, transfer 600 μ L of PCR oil phase to the glass vial. Stir at 1000 r.p.m. for 1 min. While still stirring, add the 100 μ L of PCR master mix in 20- μ L steps. Stir at 1000 r.p.m. for 10 min. At the end the emulsion should appear white and foamy. Using a positive-displacement pipette, transfer the emulsion to a PCR strip tube (8 \times 75- μ L).
3. Perform the PCR, using the following conditions:

Cycle	Denature	Anneal	Extend
1	95 °C, 2 min	-	-
2–31	95 °C, 15 s	60 °C, 15 s	72 °C, 20 s
32	-	-	72 °C, 5 min

4. Small-scale emulsion PCR breaking: Group the emulsion PCR reactions in a 1.5-mL tube. Add 1 μ L of gel loading buffer (to visualize the aqueous phase in the next step). Add 200 μ L of mineral oil and vortex for 30 s. Centrifuge at 16000g for 10 min at RT and discard the upper phase.
5. Add 1 mL of water-saturated diethyl ether and vortex for 1 min. Centrifuge at 16000g for 1 min at RT and discard the upper phase.
6. Add 1 mL of water-saturated ethyl acetate and vortex 1 for min. Centrifuge at 16000g for 1 min at RT and discard the organic upper phase.
7. Repeat Step 5. Incubate the tube at 37 °C for 5 min with the cap open to evaporate residual diethyl ether. The final volume should be 80 μ L.
8. Purify the DNA with the Oligo Clean & Concentrator Kit. Mix 80 μ L of DNA from the preceding step with 160 μ L of Oligo Binding Buffer and 320 μ L of ethanol. Homogenize the solution by pipetting up and down 10 times. Follow the manufacturer’s instructions up to the DNA elution step. Repeat the elution with an extra 15 μ L of water and then add 20 μ L of water directly into the tube to obtain a final volume of 50 μ L (two 15 μ L elutions + 20 μ L water). This is the template emulsion PCR.

9. Quantify the DNA concentration with a spectrophotometer by directly taking 2 μL of purified PCR product. The concentration should be between 20 and 40 $\text{ng}/\mu\text{L}$.
10. Run a gel electrophoresis to check for the presence of a single band, using 200 ng of PCR product in a 1.5% (w/vol) agarose gel with 0.01% (vol/vol) SYBR Safe at 100 V for 45 min.
11. Prepare 8 tubes of the following reaction mix for the small-scale limited-cycle PCR.

Reagent	Quantity per tube (μL)
10 \times Kapa Taq buffer A	5
dNTPs (10 mM)	1
Forward Universal primer (100 μM)	0.5
Reverse primer with T7 (100 μM)	0.5
Template emulsion PCR (1 $\text{ng}/\mu\text{L}$)	2.5
Kapa DNA polymerase a (5 $\text{U}/\mu\text{L}$)	0.5
ddH ₂ O	Bring to a final volume of 50 μL

12. Run the following PCR program:

Cycle	Denature	Anneal	Extend
1	95 $^{\circ}\text{C}$, 5 min	-	-
2–15	95 $^{\circ}\text{C}$, 30 s	60 $^{\circ}\text{C}$, 45 s	72 $^{\circ}\text{C}$, 30 s

Pick the corresponding tube after each of the cycles 8–15, just after the extension phase. This is performed to find the cycle number at which the PCR is still at its exponential phase.

13. To find the number of amplification cycles required to obtain a single band on the expected size and maximum intensity, run 20 μL of each PCR product on a 1.5% (w/vol) agarose gel with 0.01% SYBR Safe at 100 V for 45 min.
14. Perform a large-scale limited-cycle PCR by preparing a reaction mix for 16 tubes as indicated in the table below. This PCR reaction will generate a large quantity of Oligopaints.

Reagent	Quantity (μL)
10 \times Kapa Taq buffer A	80
dNTPs a (10 mM)	16
Forward primer (100 μM)	8
Reverse primer (100 μM)	8
Kapa DNA polymerase a (5 $\text{U}/\mu\text{L}$)	8
ddH ₂ O	640
Template emulsion PCR (1 $\text{ng}/\mu\text{L}$)	40

Split the volume of the PCR mix into 16 PCR tubes (50 μL each) and run the PCR program from step 12, using the optimized number of cycles determined in step 13. Add a last extension cycle of 5 min at 72 $^{\circ}\text{C}$.

15. Collect the 50 μ L aliquots from the preceding step into a 15mL Falcon tube and run 20 μ L of it in an agarose gel as in Step 13 to check that the PCR was successful.
16. Perform a DNA column purification according to the manufacturer's instructions. Elute using 30 μ L of DNase- and RNase-free water. This is the purified PCR product (dsDNA). Prepare 20 μ L of a 1:10 dilution of the stock product, and quantify the concentration. The concentration of the undiluted stock should be between 30 and 50 ng/ μ L.
17. Run the remainder of the 1:10 dilution on a 1.5% agarose gel as in Step 10.
18. In vitro transcription: prepare the reaction mix indicated below. It will be used to convert the DNA template into RNA. It is necessary to ensure RNase-free conditions.

Reagent	Quantity (μ L)
Purified PCR product	6 μ g of template DNA
ATP (100 mM)	6
UTP (100 mM)	6
CTP (100 mM)	6
GTP (100 mM)	6
10 \times T7 buffer	6
RNasin ribonuclease inhibitor (40 U/ μ L)	2.25
HiScribe T7 polymerase	6
ddH ₂ O	Bring to a final volume of 60 μ L

19. Split the in vitro transcription solution into 3 PCR tubes and incubate at 37 °C for 12–16 h in a thermocycler. This is the non purified transcription product.
20. Take 5 μ L of in vitro transcription product and purify it with an Oligo Clean & Concentrator Kit according to manufacturer's instructions. Elute the purified product using 15 μ L of DNase- and RNase-free water.
21. Make a 1:10 dilution to quantify the purified RNA concentration. The concentration should be between 0.5 and 2 μ g/ μ L. The total yield of the in vitro transcription step should be 150–450 μ g from a single transcription step (60 μ L in total).
22. Check for the RNA quality by urea PAGE. Perform a pre-run for 30 min in 1 \times TBE at 190 V to eliminate the excess of persulfate. When finished, wash the wells with the running buffer. Heat the sample at 95 °C for 5 min and put it immediately on ice for 2 min. Load 100 ng of purified RNA per lane. Run the gel for 1 h at 190 V. For gel staining, incubate, protected from light, for 20 min at RT in 30 mL of 1 \times TBE and 3 μ L of SYBR Gold.
23. Prepare the reaction mix indicated below. Perform the reverse transcription reaction according to the Maxima H reverse transcriptase kit instructions.

Product	Quantity (μ L)
Non-purified transcription product	150 μ g
dNTP mix (100 mM)	12
Forward primer (100 μ M)	50
5 \times RT buffer	240
RNasin ribonuclease inhibitor (40 U/ μ L)	30
Maxima H Minus reverse transcriptase b (200 U/ μ L)	30
ddH ₂ O	Bring to a final volume of 1200 μ L

For this step, directly use the non-purified RNA from Step 21. Always keep RNA on ice to prevent degradation.

24. Split the volume obtained in the preceding step into two 1.5-mL tubes and incubate for 3 h at 50 °C in a water bath.
25. Degradate RNA by adding 300 μ L of 0.5 M EDTA and 300 μ L of 1 M NaOH to each tube and incubating the tubes at 95 °C for 15 min in a water bath.
26. Take a 10 μ L aliquot to control for DNA concentration and to perform a gel electrophoresis.
27. DNA probe purification: Mix the two aliquots from Step 25 in a 50mL Falcon tube. Add 4.8 mL of Oligo Binding Buffer and 19.2 mL of ethanol. Homogenize by inverting the tube a few times and spread over two columns. Follow the manufacturer's instructions from this point on.
28. Take a 10 μ L aliquot to measure the DNA concentration and to perform a gel electrophoresis. The concentration should be between 250 and 400 ng/ μ L, that is, 75–120 μ g of ssDNA in total in 300 μ L of DNA elution.
29. Ethanol precipitation: Directly add to the 300- μ L DNA elution from Step 27 (2 \times 150 μ L) 24 μ L of 5 M ammonium acetate, 6 μ L of glycogen and 750 μ L of 100% (vol/vol) ethanol at -20 °C. Vortex and incubate for 1 h at -80 °C. Centrifuge at 13000g for 1 h at 4 °C. Discard the supernatant and wash the pellet with 1 mL of ice-cold 70% ethanol (vol/vol). Centrifuge at 13000g for 15 min at 4 °C. Discard the supernatant, air-dry the pellet for 10 min at 37 °C and add 20 μ L of DNase- and RNase-free water. Let the ssDNA resuspend for 10 min at 37 °C, and then keep on ice.
30. Quantify the oligos ssDNA concentration. The total quantity of ssDNA should be on the order of 80–120 μ g.
31. Check the quality of the ssDNA by urea PAGE. This step enables verification of RNA degradation and the efficacy of the reverse transcription step.

The concentration and quality of the product are monitored during the different steps to ensure the success of the process. Probes are stored at -20 °C for future use.

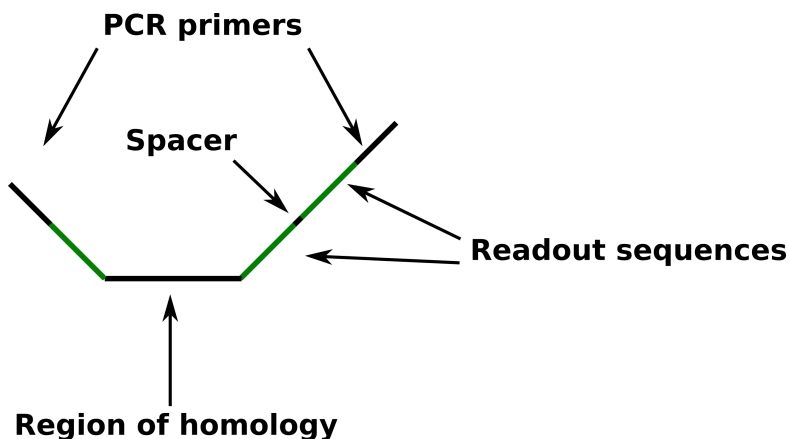


Figure 13: Primary oligos scheme. The region of genomic homology is surrounded by readout sequences (where complementary adaptor oligos bind), and the primers for PCR amplification.

4.3 Adaptor oligos

Adaptor oligos are made of 62 base pairs. They bind on one side to the readout sequences of the primary oligos, and in the other to imaging oligos that carry the fluorophore. They consist in:

- A binding region of 20 bp, that is complementary to the binding site on the primary oligos.
- A bridge of 10 bp.
- A binding site for the imaging oligo, of 32 bp.



Figure 14: Adaptor oligos scheme. Their sequence is complementary to the primary library on one side, and in the other, to the imaging oligos. The region in-between (bridge) is used to bind displacement oligos.

The bridge is used to bind a displacement oligo. A displacement oligo consists in the complementary sequence of the bridge, followed by the complementary sequence of the Binding region on the adaptor oligos. When injected at the proper concentration (in excess), they bind the adaptor oligo. The adaptor oligo bound by a displacement oligo can then be washed out, removing with it the fluorophore in the imaging oligo. This technique was first used in Mateo et. al. [Mateo et al., 2019], and it is used in our work to remove the fluorescent signal from the fiducial mark every 10 cycles, to avoid bleaching and ensure an optimal signal intensity. To remove the fluorescent signal from barcodes, a chemical bleaching step was performed (see DAPI and barcodes acquisition section).

The imaging oligo consists in a 32-mer complementary to the binding region in the adaptor oligo, followed by a cleavable Alexa-647 fluorophore.



Figure 15: Displacement strategy

Fiducial marker imaging oligo consists in a 32-mer complementary to the binding region of the corresponding adaptor oligo, followed by a non-cleavable Rhodamine Red fluorophore. Adaptor, displacements and imaging oligos were synthesized by Integrated DNA Technologies (IDT; Coralville, USA). Their sequences can be found in Appendix X.

4.4 Embryo collection and fixation

For this work, Oregon-R w[1118] flies were used for the WT strain. For the mutant line, the P_C^{XT109} strain was used. It consists in a null mutant [Franke et al., 1995] that was balanced over the KrGFP-TM3 Sb balancer (TKG: obtained from BL#5195 of the Bloomington Drosophila Stock Center).

The full protocol can be found at our Nature Protocols paper [Cardozo Gizzi et al., 2020]

The following reagents are needed:

- Dry yeast, fine (Lab Scientific, cat. no. FLY-8040-20F)
- Dulbecco's phosphate-buffered saline (PBS; Gibco, cat. no. 14190169)
- Paraformaldehyde solution, methanol free (32% (w/vol); Electron Microscopy Sciences, cat. no. 15714)
- Methanol (Fisher Chemical, cat. no. A412-4)
- Clorox Ultra Germicidal Liquid Bleach (Fisher Scientific, cat. no. 50371500)
- Heptane (Fisher Chemical, cat. no. O3008-4)
- Apple juice

The following materials need to be prepared:

- Yeast paste: Dissolve 25 g of fine dry yeast powder in 20 mL of water. Add enough water to achieve a consistency similar to that of peanut butter. Store it at 4 °C for up to 2 weeks.
- Apple juice plates: To make the agar–apple juice plates, fill plastic Petri dishes halfway with agar mixed with apple juice. Apple juice plates can be stored at 4 °C for 1 month.

Flies were grown on standard cornmeal yeast media at 21°C. The protocol for embryo collection and fixation used is described below:

1. Place flies into an egg-collection cage, with an apple juice plate containing a dollop of yeast paste and prewarmed to 25 °C. Perform an O/N pre-laying step.
2. Replace the plate with a new one containing a dollop of yeast paste prewarmed to 25 °C. Perform a laying step and incubation for the time corresponding to the desired developmental stage:
 - For embryos in stage 15 - 16: laying for 4 h at 25 °C. Then remove the plate and incubate it for 12 h at 25 °C. This was done both for WT embryos and *PcXT109* mutant embryos. For *PcXT109* mutant embryos, GFP-minus homozygous mutant Pc embryos were selected on an agar plate under a GFP binocular.
 - For embryos in stage 5: laying for 1:30 h at 25 °C. Then remove the plate and incubate it for 1 h at 25 °C. This was done for WT embryos.
3. Rinse the plate with *ddH₂O*. Detach embryos carefully using a soft brush. Filter the liquid with a Nylon filter. The embryos will remain on the filter.
4. Prepare a six-well plate with one well containing bleach at 2.6% active chlorine, and the other five containing water. Put the filter with the embryos into the bleach-containing well and incubate for 5 min. Then rinse the embryos by sequentially immersing the Nylon filter into each of the water-containing wells. Dry embryos between steps by pressing on a paper tissue.
5. Using 5 mL of 4% (vol/vol) paraformaldehyde in PBS, rinse the filter and displace the embryos into a 20-mL glass vial. Add 5 mL of heptane to the vial, then close and vigorously shake it manually for 30 s. The cap of the vial may be covered with Parafilm to avoid leakage of the paraformaldehyde and heptane solution inside. Incubate the embryos for 20 min at RT into the shaker at 200 rpm.
6. Use a glass Pasteur pipette to aspirate the lower aqueous phase from the bottom of the vial and discard it. Add 5 mL of methanol and vortex the glass vial for 15 s. Use a glass Pasteur pipette to transfer the embryos from the bottom of the glass vial to a 1.5 mL tube.
7. Wash the embryos three times with 1 mL of methanol.

The embryos can then be stored in methanol at -20 °C for several months. The next step is the Hi-M library hybridization, although an immunostaining can be performed before.

4.5 Hybridization of Hi-M library

The following reagents are needed:

- Mineral oil (500 mL; Sigma-Aldrich, cat. no. M5904)
- Triton X-100 (250 mL; Sigma-Aldrich, cat. no. T8787)
- Tween 20 (500 mL; Sigma-Aldrich, cat. no. P2287)
- Dulbecco's phosphate-buffered saline (PBS; Gibco, cat. no. 14190169)

- Saline–sodium citrate buffer (SSC; 3 M NaCl in 0.3 M sodium citrate; 20×; Thermo Fisher Scientific, cat. no. AM 9770)
- Tris base (BM grade; Euromedex, cat. no. 200923-A)
- Sodium chloride (NaCl; 99.5%; Euromedex, cat. no. 1112-A)
- Sodium dihydrogen phosphate, dihydrate ($NaH_2PO_4 - 2H_2O$; Euromedex, cat. no. T879)
- Deionized formamide (100 ml; Amresco, cat. no. 0606)
- RNase A (Sigma-Aldrich, cat. no. R6513)
- Dextran sulfate (Sigma-Aldrich, cat. no. D8906)
- Salmon sperm DNA (Ambion, cat. no. AM9680)

For this step, some solutions need to be prepared in advance. Unless otherwise indicated, they should be prepared freshly:

- **10% Tween 20:** Mix 50 μ L of Tween 20 with 450 μ L of ddH₂O. Homogenize.
- **PBT:** Combine 49.5 mL of PBS with 500 μ L of 10% Tween 20 (vol/vol) solution.
- **PBS-Triton:** Mix 50 μ L of Triton X-100 with 10mL of PBS. Homogenize.
- **Prehybridization mixture (pHM):** This solution consists in 50% formamide, 2× SSC, 100 mM NaH_2O_4 , pH 7, and 0.1% Tween 20 (vol/vol).
- **DNA hybridization solution (DHS):** This solution consists in 2× SSC, 50% (vol/vol) formamide, 10% (vol/vol) dextran sulfate and 0.5 mg/mL salmon sperm. It can be stored at -20 °C for several months. Prewarm at 37 °C before use.

1. Rehydrate the embryos by incubating them sequentially for 5 min at RT on a rotating wheel, using 1 mL of each of the following solutions: (i) 90% methanol, 10% PBT; (ii) 70% methanol, 30% PBT; (iii) 50% methanol, 50% PBT;(iv) 30% methanol, 70% PBT; (v) 100% PBT.
2. Incubate the embryos with 1 mL of PBT, 100 μ g/mL RNase for 2 h at RT on a rotating wheel.
3. Permeabilize the embryos by incubating them with PBS-Triton for 1 h at RT on a rotating wheel.
4. Transfer the embryos to pHM by passing them through 1 mL of each of the following solutions: (i) 80% PBS-Triton, 20% pHM; (ii) 50% PBS-Triton, 50% pHM; (iii) 20% PBS-Triton, 80% pHM; (iv) 100% pHM. Incubate for 20 min at RT on a rotating wheel for each step.
5. Prepare the primary DNA probe by adding 225 pmol of Oligopaints library to 25 μ L of DHS. Keep the mix on ice. Denature the primary DNA probe by incubation for 15 min at 80 °C in the thermal mixer without mixing.

6. Carefully remove the pHM solution from the tube and discard it; then add 1 mL of fresh pHM. Denature the embryonic DNA by incubating embryos for 15 min at 80 °C in a water bath.
7. Transfer embryos to a 500 μ L PCR tube. Carefully remove the pHM solution and discard it; then add 30 μ L of the denatured probes from step 5. Mix by gently flicking the tube with a finger. Place embryos in a thermocycler, and incubate O/N with the following program: 43 cycles of 10 minutes, with a temperature drop of -1°C/cycle, then incubation at 37°C indefinitely. In contrast to other protocols, using a thermocycler allows to avoid covering the embryos with mineral oil to prevent evaporation of the solutions.
8. Transfer embryos back to a 1.5 mL tube. Add 500 μ l of 50% (vol/vol) formamide, 2 \times SSC to the embryos tube. Wait for the embryos to sediment. Carefully remove the supernatant and discard it.
9. Perform post-hybridization washes by passing the embryos through 1mL of each of the following freshly made solutions: (i) 50% (vol/vol) formamide, 2 \times SSC; repeat this wash once; (ii) 40% (vol/vol) formamide, 2 \times SSC; (iii) 30% formamide, 70% PBT; (iv) 20% formamide, 80% PBT; (v) 10% formamide, 90% PBT; (vi) 100% PBT; (vii) 100% PBS-Triton. Perform washes (i–iv) for 20 min at 37 °C in a thermal mixer with agitation (900 r.p.m.); perform washes (v–vii) for 20 min at RT on a rotating wheel.
10. Rinse the embryos with 1 mL of PBT. Crosslink the Oligopaint library by incubating the embryos with 1 mL of 4% (wt/vol) paraformaldehyde in PBT for 30 min at RT on a rotating wheel.
11. Rinse the embryos with 1 mL of PBT, the rinse them 3 times with 1 mL PBS.

DNA-labeled embryos can be stored for several weeks at 4 °C. Once the Oligopaints library has been hybridized, the fiducial mark should be hybridized and the DAPI staining performed. In my experiments I found a higher labeling efficiency when the fiducial mark was hybridized on the microfluidics chamber of the microscope (see experimental design). In order to do so, embryos need to be attached to a coverslip and mounted in the microfluidics chamber.

Before describing the protocol for those steps, I'll describe an optional immunostaining step. In my experiments it was used to perform an immunostaining against Pc protein.

4.5.1 Optional: Immunostaining

The following reagents are needed:

- Dulbecco's phosphate-buffered saline (PBS; Gibco, cat. no. 14190169)
- BSA (Roche, cat. no. 10711454001)

If an immunostaining is to be performed, the following solutions need to be prepared:

- **PBT solution:** To prepare this solution, see the "Hybridization of Hi-M library" section.

- **Blocking Solution:** This solution consists in 1% BSA (weight/vol) in PBT.
- **Primary Antibody solution:** Dilute primary antibody at 1/200 in blocking solution.
- **Secondary Antibody solution:** Dilute the secondary antibody at 1/500 in blocking solution.

For this step, I used the following antibodies:

- Primary Antibody: a PC rabbit polyclonal antibody (described in [Bantignies et al., 2011]).
- Secondary Antibody: Invitrogen, ref. A11070.

The protocol I followed to perform the immunostaining is described below. It is adapted from [Bantignies and Cavalli, 2014]

1. Incubate embryos in 1 mL PBT during 30 min at RT on a rotating wheel.
2. Discard the previous solution and incubate embryos in blocking solution during 2 hours at RT on a rotating wheel.
3. Discard the previous solution and incubate embryos in primary antibody solution O/N on a rotating wheel at 4 °C.
4. Wash embryos 2 times with 1 mL of PBT, then incubate them in PBT for 20 min at RT on a rotating wheel.
5. Incubate embryos in blocking solution for 20 min at RT on a rotating wheel.
6. Discard the previous solution and incubate embryos in secondary antibody solution during 2h at RT on a rotating wheel.
7. Wash the embryos in PBT for 20 min at RT on a rotating wheel. Repeat this step.

4.6 Attachment of embryos to coverslip and mounting into microfluidics chamber

The following reagents are needed:

- Poly- L -lysine solution (Sigma-Aldrich, cat. no. P8920)
- Acetone (Merck, cat. no. 1000122500)
- Ethanol (Fisher Chemical, cat. no. 10680993)
- Microscope coverslips (Bioptechs, cat. no. 40-1313-0319)
- Agarose (standard DNA grade; Euromedex, cat. no. D5-E)

Prepare a 3% agarose gel in a petri dish. It will be used to place embryos before attachment to coverslips.

1. Wash a coverslip sequentially with acetone, ethanol and water and dry it with a flame from a Bunsen burner by smoothly passing the coverslip over the flame three or four times. Place the dry coverslip into a 35-mm plastic dish.
2. Add 1 mL of poly- L -lysine solution (1:10 dilution in *ddH₂O*) to the coverslip and incubate for 20 min at RT. Afterwards, rinse the coverslip with *ddH₂O*, and dry it using compressed air.
3. Cut a piece of agarose and put it under the binocular microscope. Transfer 20–30 embryos to the agarose pad. Align them carefully using metal tweezers, then dry the pad with a paper tissue to absorb the surrounding liquid.
4. Attach the embryos to the coverslip by gently pressing it against the agarose pad.
5. Put the coverslip into a 35-mm plastic dish, with embryos facing up, and fill it with 2X SSC until ready for chamber assembly.

After this step, the microfluidics system of the microscope is washed sequentially with water and 2X SSC, to remove the ethanol solution in which the microfluidics is kept. Then embryos are placed into the microfluidics chamber. Then chamber is then slowly filled with 2X SSC, preventing embryos from drying. The next step is to proceed to fiducial mark staining and DAPI staining.

4.7 Fiducial mark and DAPI staining

For this step, the following solutions need to be prepared:

- **Wash buffer:** it consists in 2× SSC, 40% (vol/vol) formamide. It should be prepared freshly and filtered using a 0.22 μ m filter. Once prepared it can be stored at 4 °C for several weeks.
 - **DAPI solution:** Prepare a 0.5 μ g/mL DAPI solution in 1× PBS by diluting the stock solution.
 - **Fiducial mark mix:** mix 0.6 μ L of the corresponding adaptor, and 0.6 μ L of the corresponding imaging oligo. In my experiments, the imaging oligo carries a Rhodamine Red fluorophore.
 - **Fiducial mark solution:** Add the fiducial mark mix to a 2 mL tube containing 2 mL of wash buffer.
1. Fill the chamber with fiducial mark mix, at a rate of 100 μ L/min. When 1.8 mL passed through the chamber, stop the flux, and incubate for 30 min.
 2. Wash with 1.5 mL of wash buffer at a rate of 150 μ L/min.
 3. Remove the wash buffer by passing 2 mL of 2X SSC at a rate of 150 μ L/min.
 4. Inject 2 mL of DAPI solution at a rate of 150 μ L/min. Incubate for 30 min.
 5. Remove DAPI solution by passing 2 mL of 2X SSC at a rate of 150 μ L/min.

After these steps, we're ready to begin the selection of ROIs and to launch the experiment.

4.8 Microscope setup

Experiments with NC14 embryos were performed on a home-made wide-field epifluorescence microscope built on a RAMM modular microscope system (Applied Scientific Instrumentation) coupled to a microfluidic device as described previously [Cardozo Gizzi et al., 2020, Cardozo Gizzi et al., 2019]. Samples were imaged using a 60x Plan-Achromat water-immersion objective (NA = 1.2, Nikon, Japan). The objective lens was mounted on a closed-loop piezoelectric stage (Nano-F100, Mad City Labs Inc. - USA). Illumination was provided by 3 lasers (OBIS-405/640 nm and Sapphire-LP-561 nm, Coherent – USA). Images were acquired using a sCMOS camera (ORCA Flash 4.0V3, Hamamatsu – Japan), with a final pixel size calibrated to 106 nm. A custom-built autofocus system was used to correct for axial drift in real-time and maintain the sample in focus as previously described ([Cardozo Gizzi et al., 2019]). A fluidic system was used for automated sequential hybridizations, by computer-controlling a combination of three eight-way valves (HVXM 8-5, Hamilton) and a negative pressure pump (MFCS-EZ, Fluigent) to deliver buffers and secondary readout probes onto a FCS2 flow chamber (Biopetechs). Software-controlled microscope components, including camera, stages, lasers, pump, and valves were run using a custom-made software package developed in LabView 2015 (National Instrument).

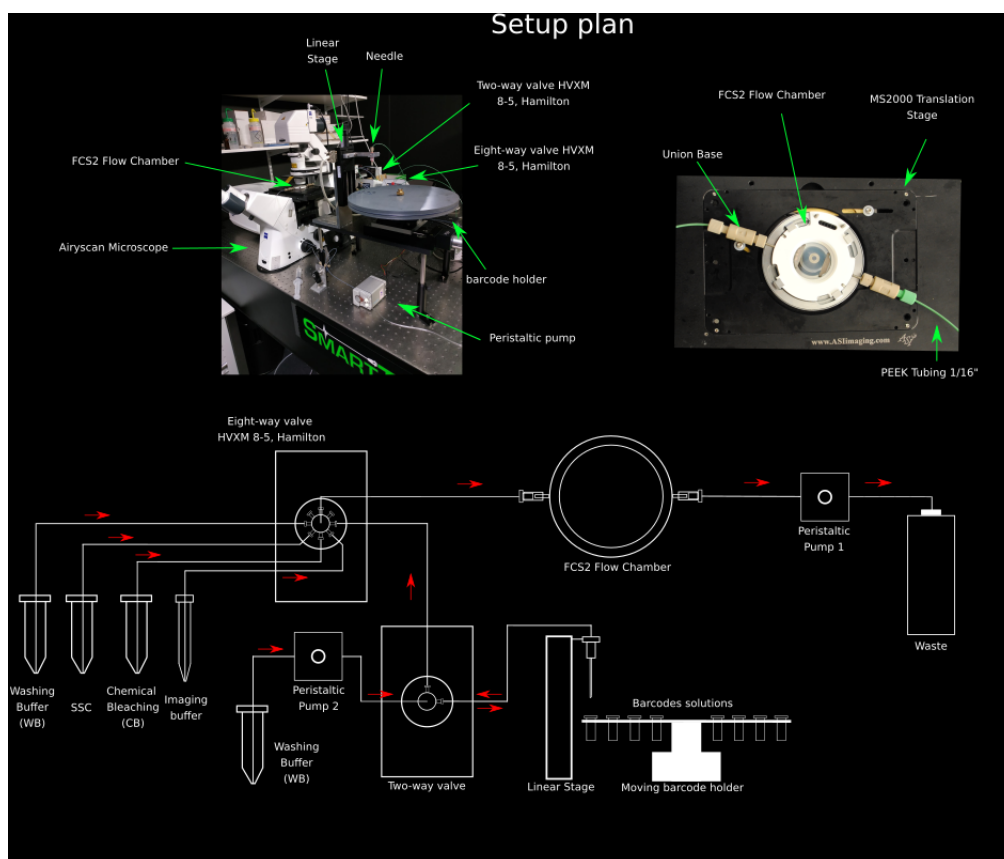


Figure 16: Scheme of the Airyscan experimental setup. A peristaltic pump coupled to Hamilton valves deliver buffers to the microfluidics chamber. The chamber is placed into the microscope.

Experiments with S15-S16 embryos were performed on an Airyscan microscope (Zeiss), coupled to a computer-controlled fluidic system for sequential hybridizations, as shown below. In brief, a peristaltic pump (Instech, P720) coupled to an eight-way valve (HVXM

8-5, Hamilton) delivers the buffers into a FCS2 flow chamber (Bioptechs). Barcodes are fixed onto a home-made rotating holder using a rotating stage (Physik Instrumente, M-404.4PD). A needle coupled to a linear stage (Physik Instrumente, VT-80) and the Hamilton valves is used to deliver the barcodes onto the chamber. A second peristaltic pump (Instech, P720) is coupled to the needle and a two-way valve (HVXM 2-5, Hamilton), to wash residual barcode solution from the needle between cycles. Illumination was provided by 3 laser lines of the Airyscan microscope (405 nm, 561 nm, 640 nm).

Samples were imaged using a 63x, NA = 1.2 water-immersion objective (W DICII, Zeiss). Illumination was provided by 3 laser lines (405/561/640 nm). Images were acquired with a pixel size of 100 nm, and 0.5 μ m z-slices. A pinhole size of 62 μ m was used. ZEN 2.3 blue edition (.NET Framework Version: 4.0.30319.42000) was used for acquisition. Pump, valves, and stage were run using a custom-made software package developed in LabView 2015 (National Instrument).

4.9 Image acquisition

The following reagents are needed:

- Glucose oxidase (Sigma-Aldrich, cat. no. G2133)
- Catalase (Sigma-Aldrich, cat. no. C30)
- D(+) Glucose, anhydrous (Euromedex, cat. no. UG3050)
- Sodium chloride (NaCl; 99.5%; Euromedex, cat. no. 1112-A)
- Alexa 647 readout probes (Integrated DNA Technologies, custom order) Sequences can be found in Appendix XX and are complementary to the readout sequences.
- Rhodamine-labeled DNA oligo for the fiducial barcode readout (Integrated DNA Technologies, custom order). Sequence can be found in Appendix XX.
- Tris(2-carboxyethyl)phosphine hydrochloride (TCEP; Sigma-Aldrich, cat. no. 646547)
- Tris base (BM grade; Euromedex, cat. no. 200923-A)

The following solutions need to be prepared:

- **1 M Tris-HCl solution, pH 8:** To prepare 50 mL of this solution, mix 6 g of Tris base with 30 mL of ddH₂O. Using a pH meter, slowly add HCl with a glass Pasteur pipette to reach the desired pH. Bring the volume to 50 mL with ddH₂O, and pass the solution through a 0.22- μ m filter. The solution can be stored at RT for several months.
- **55 mM NaCl in 11 mM Tris-HCl solution, pH 8:** To prepare 50 mL of this solution, mix 2.75 mL of 1M NaCl solution, 0.55 mL of 1M Tris-HCl solution, pH 8, and 46.7 mL of ddH₂O. Prepare freshly.
- **Gloxy Solution:** To prepare 1 mL of Gloxy solution, mix 50 mg of glucose oxidase, 100 μ L of catalase and 900 μ L of 55 mM NaCl in 11 mM Tris-HCl solution, pH 8. Store at -20 °C. This solution is stable for several months.

- **Imaging Buffer:** To prepare 10 mL of solution, combine 1 mL of 50% (w/vol) glucose with 8.89 mL of PBS and 110 μ L of Gloxy solution. The Gloxy solution should be added just before the imaging buffer is going to be used. Once the tubing is introduced, a layer of mineral oil is added to prevent contact with oxygen from the ambient air. This solution should be replaced every 12–15 h.
- **Chemical bleaching solution:** To prepare 10 mL of chemical bleaching solution, mix one 1-mL ampule of TCEP with 9 mL of 2 \times SSC.
- **Barcodes mix:** mix 0.6 μ L of the corresponding adaptor, and 0.6 μ L of the corresponding imaging oligo. In my experiments, the imaging oligos for barcode carry an A647 fluorophore.
- **Readout probe solution:** Add the barcodes mix to a 2 mL tube containing 2 mL of wash buffer.

Several 200 μ m X 200 μ m fields of view (FOV) in the regions containing embryos were selected, using the LabView script. Z stacks of 15 - 20 μ m were selected, with steps of 250nm in the widefield setup and 500nm in the Airyscan one.

1. Inject 1.2 mL of imaging buffer.
2. Define excitation laser lines (405nm DAPI, 561nm fiducial in Rhodamine Red).
3. Proceed to DAPI acquisition.

After DAPI acquisition, barcodes were acquired. For this, 2 mL tubes containing the corresponding barcodes and the chemical bleaching solution need to be prepared.

4. Prepare as many readout probe solutions as barcodes that are going to be acquired during the experiment.
5. Place the tubes containing the barcodes in the barcodes holder.
6. Place each of the following solutions in an individual valve: 2X SSC, Wash buffer, Chemical bleaching solution, Imaging buffer.

To acquire the barcodes, an injection protocol has to be defined in the LabView program controlling the microscope.

7. Load into the software the list of barcodes in the order that they're going to be injected. Then define the injection protocol as follows:

Image Acquisition		
Buffer	Volume (μ L)	Flow rate (μ L/min)
Readout probe	1700	100
Wash buffer	1500	150
2X SSC	1500	150
Imaging Buffer	1200	100
Bleaching		
Chemical Bleaching	1500	150
2X SSC	1500	150

8. Launch acquisition.

Imaging buffer should be replaced every 12-15h of experiment. The other solutions should be recharged before the tubes empty, to avoid air entering the chamber. The workflow is depicted in the following image.

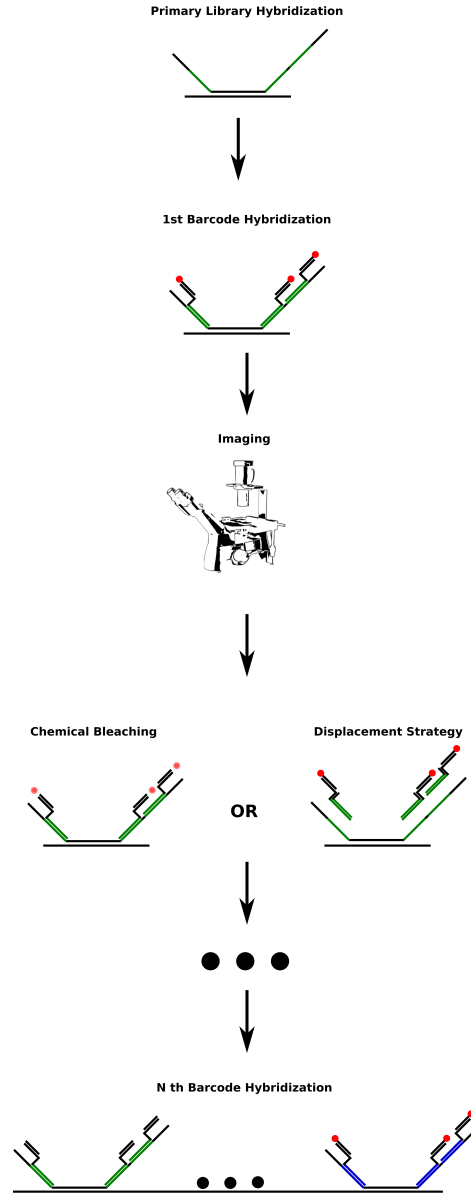


Figure 17: Workflow of the experiment. First primary probes are hybridized to the genomic DNA. Once the sample is placed in the microfluidics chamber, barcodes are hybridized, imaged, and the fluorescent signal is chemically bleached. This is repeated for all the barcodes to be imaged. For the fiducial marker, the imaging and adaptor oligos are replaced using a displacement strategy every 10 cycles.

4.10 Data analysis

Our Airyscan microscope produces images in .czi format, which were converted to TIFF files using Bio-Formats plugin in Fiji (<https://github.com/ome/bioformats>, [Linkert et al., 2010]). Acquired images are deconvolved using Huygens Professional version 20.04 (Scientific Volume Imaging, the Netherlands, <https://svi.nl/>), via the CMLE algorithm (SNR:20,

40 iterations) run with a custom-made script written in Tcl/Tk. The following analysis steps were performed with a home made script in MATLAB 2019b (The MathWorks, Inc., Natick, United States). First, X-Y drift is corrected for each hybridization cycle. A global X-Y correction is obtained by cross-correlating the images of the fiducial barcodes with that of the first barcode (reference cycle). This produces a single 3D vector for each barcode and represents a ‘global’ correction applied to the whole FOV. Then, an adaptive thresholding is used to pre-segment the spots of each fiducial barcode in each cell for all FOVs and for all barcodes. The 3D coordinates of each barcode were then found using a 3D Gaussian fitting algorithm on the pre-segmented mask. Fiducial barcodes with sizes larger than the diffraction limit of light (2.2 pixels for our microscope) were filtered out. Third, we obtained ‘local’ 3D correction vectors for each cell in each FOV. This was done by first using the global X-Y correction vector to pre-align fiducial barcode spots in each cycle to fiducial barcode spots in the reference cycle. Then, image-based cross-correlation of these pre-aligned fiducial barcode images is used to reach sub-pixel accuracy in the correction vector. This approach allowed for 3D, subpixel accuracy drift-correction across the whole FOV. Fourth, barcodes were segmented for all hybridization cycles in batch processing mode using optimized adaptive thresholding. 3D coordinates of each barcode were then determined by 3D Gaussian fitting of the segmented regions. These positions were corrected for drift by using the closest fiducial barcode vector obtained from the previous analysis step. Nuclei were segmented from DAPI images by adaptive local thresholding and watershed filtering. Embryo’s segments were selected by manually drawing polygons over them. This was used to assign each DAPI-segmented cell to the corresponding segment. Then, barcodes were attributed to each cell by using the DAPI segmentation. For each nuclei we then calculate pairwise distance matrices. All further analysis is done using home made Python 3. The contact probability is obtained as the number of nuclei where the pairwise distances were lower or equal to 250 nm, normalized by the number of nuclei containing both barcodes. All image processing was carried out on Linux terminals connected to a server running Linux PopOS 19.10, with 4 GeForce GTX 1080Ti GPU cards (SCAN computers, UK).

5 Appendix

5.1 TADs are 3D structural units of higher-order chromosome organization in *Drosophila*

This work showed that TADs form structural units in *Drosophila*, using a combination of microscopy techniques, Hi-C and polymer modelling. Particularly, we show that repressed TADs form discrete nanocompartments, separated by less condensed active regions. Furthermore, it is shown that TADs engage in inter-TAD interactions. The work performed here was a first step towards the study of repressed domain architecture in *Drosophila*. For this work, images were obtained in a region with two consecutive repressed black TADs. I performed and analysed dSTORM experiments, using probes located either at one of the TADs, or using probes spanning the two domains. I observed that most probes covering a single TAD show a single nanocompartment in the majority of cells, whereas probes that span both TADs are separated into two or more nanocompartments.

My work was done under the supervision of Diego Cattoni and Marcelo Nollmann.

GENETICS

TADs are 3D structural units of higher-order chromosome organization in *Drosophila*

Quentin Szabo,¹ Daniel Jost,² Jia-Ming Chang,^{1*} Diego I. Cattoni,³ Giorgio L. Papadopoulos,¹ Boyan Bonev,¹ Tom Sexton,^{1†} Julian Gurgo,³ Caroline Jacquier,¹ Marcelo Nollmann,³ Frédéric Bantignies,^{1‡} Giacomo Cavalli^{1‡}

Deciphering the rules of genome folding in the cell nucleus is essential to understand its functions. Recent chromosome conformation capture (Hi-C) studies have revealed that the genome is partitioned into topologically associating domains (TADs), which demarcate functional epigenetic domains defined by combinations of specific chromatin marks. However, whether TADs are true physical units in each cell nucleus or whether they reflect statistical frequencies of measured interactions within cell populations is unclear. Using a combination of Hi-C, three-dimensional (3D) fluorescent in situ hybridization, super-resolution microscopy, and polymer modeling, we provide an integrative view of chromatin folding in *Drosophila*. We observed that repressed TADs form a succession of discrete nanocompartments, interspersed by less condensed active regions. Single-cell analysis revealed a consistent TAD-based physical compartmentalization of the chromatin fiber, with some degree of heterogeneity in intra-TAD conformations and in cis and trans inter-TAD contact events. These results indicate that TADs are fundamental 3D genome units that engage in dynamic higher-order inter-TAD connections. This domain-based architecture is likely to play a major role in regulatory transactions during DNA-dependent processes.

INTRODUCTION

The three-dimensional (3D) organization of the genome is closely related to the control of transcriptional programs (1). Recently, high-throughput variants of the chromosome conformation capture method (Hi-C) (2) have been extensively used to molecularly address the 3D spatial organization of genomes [see Bonev and Cavalli (1) for review]. A key architectural feature revealed by Hi-C was the existence of topologically associating domains (TADs) (3–6), corresponding to domains of highly interacting chromatin, with reduced interactions spanning borders between them. In *Drosophila*, TADs correlate well with functional epigenetic domains defined by chromatin marks (4, 6–8). In mammals, an additional level of TAD organization involves dynamic cohesin-dependent loops between CTCF binding sites at convergent orientations (9–13). The correlation of TAD structures with epigenetic marks can be observed in mammals using high-resolution Hi-C maps (7, 11). This compartmentalization, defined by the underlying chromatin state, appears to be reinforced upon removal of CTCF/cohesin loop components (10, 12, 13), suggesting a conserved mode of chromatin organization across species (7). TADs have been proposed to constrain gene regulation (5, 14), for example, by spatially defining the limits of where an enhancer can act (15, 16). However, this model requires TADs to be physical units when they could instead reflect a statistical feature that emerges when populations of nuclei are analyzed. Recent single-cell Hi-C studies (17–19) showed somewhat contrasting results in this respect. Although one study is compatible with the presence of TADs in individual nuclei (18), another suggests that TADs might reflect a statistical property that appears when individual cells are merged (17).

¹Institute of Human Genetics, CNRS, Univ Montpellier, Montpellier, France. ²Univ Grenoble Alpes, CNRS, Grenoble INP, TIMC-IMAG, F-38000 Grenoble, France. ³Centre de Biochimie Structurale, CNRS UMR5048, INSERM U1054, Univ Montpellier, 34090 Montpellier, France.

*Present address: Department of Computer Science, National Chengchi University, 11605 Taipei City, Taiwan.

†Present address: Institut de Génétique et de Biologie Moléculaire et Cellulaire, CNRS UMR 7104, INSERM U964, 67404 Illkirch, France.

‡Corresponding author. Email: frederic.bantignies@igh.cnrs.fr (F.B.); giacomo.cavalli@igh.cnrs.fr (G.C.)

Copyright © 2018
The Authors, some
rights reserved;
exclusive licensee
American Association
for the Advancement
of Science. No claim to
original U.S. Government
Works. Distributed
under a Creative
Commons Attribution
NonCommercial
License 4.0 (CC BY-NC).

Thus, to what extent the compartmentalization of chromatin into TADs is present in each cell nucleus is still unclear. Furthermore, the relation between TADs and higher-order chromosome folding remains to be explored. Recently, super-resolution microscopy has allowed finer-scale chromatin architecture to be analyzed at the single-cell level (20–22), suggesting that different types of chromatin are characterized by distinct degrees of compaction (23) and opening the possibility of studying the structural properties of chromosome domains.

RESULTS

Chromatin is organized in a series of discrete 3D nanocompartments

To investigate the nature of TADs in single cells, we used Oligopaint (24) and fluorescent in situ hybridization (FISH) to homogeneously label an extended 3-million base pair (Mbp) region of *Drosophila* chromosome 2L (table S1) and imaged its nuclear organization using 3D-structured illumination microscopy (3D-SIM) (25, 26). This region comprises three main types of *Drosophila* epigenetic domains: active chromatin (Red) enriched in trimethylation of histone 3 lysine 4 (H3K4me3), H3K36me3, and acetylated histones; Polycomb group (PcG) protein repressed domains (Blue), defined by the presence of PcG proteins and H3K27me3; and inactive domains (Black), which are not enriched in specific epigenetic components (Fig. 1A) (6). Although conventional wide-field (WF) microscopy imaging of this region did not reveal internal structures, 3D-SIM showed that this chromosomal region appears as a semicontinuous sequence of discrete globular structures, defined here as nanocompartments (Fig. 1, B to D, and fig. S1, A and B). These structures are interspersed by less intense gap regions despite uniform probe coverage across the 3 Mb (fig. S1C). In addition, the 3-Mb probe intensity variation displayed correlation with whole nucleus staining [4',6-diamidino-2-phenylindole (DAPI); fig. S1, D to F]. We reasoned that these nanocompartments may reflect the presence of TADs, so we adapted the Oligopaint strategy to two-color chromatin labeling (see Materials and Methods and fig. S2, A and B), simultaneously visualizing the 3-Mb region and single TADs within it (Fig. 1E and table S1). We observed

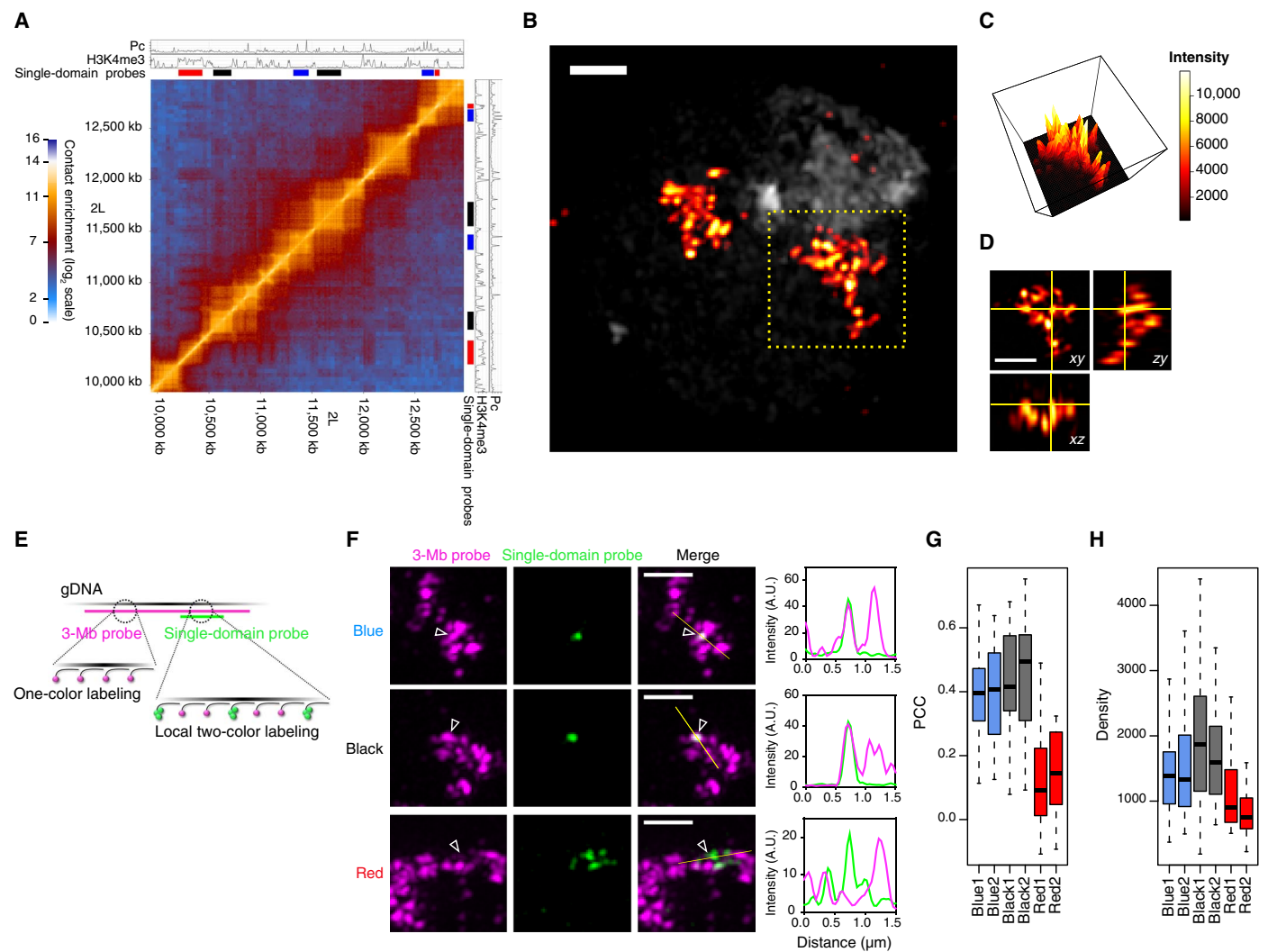


Fig. 1. Super-resolution microscopy reveals chromatin organization into discrete nanocompartments. (A) S2R+ Hi-C map of the labeled 3-Mb region with chromatin immunoprecipitation (ChIP) tracks of Pc and H3K4me3. Colored bars denote the positions of probes designed to label specific epigenetic domains (Blue, Black, and Red). (B) 3D-SIM image of an S2R+ nucleus labeled with the 3-Mb probe (DAPI in gray). (C) Intensity distribution (maximum projection) of the 3-Mb probe in (B). (D) Orthogonal views of the 3-Mb probe labeling in (B). (E) Schematic representation of the dual FISH Oligopaint labeling strategy. gDNA, genomic DNA. (F) Examples of dual FISH labeling (maximum projections) with the 3-Mb probe and a single epigenetic domain (Blue1, Black2, or Red1, indicated with arrowheads). Right: Intensity distributions of the two probes along the yellow line. A.U., arbitrary units. (G) Pearson's correlation coefficient (PCC) between the 3-Mb and the single-domain probe signals. Twenty nuclei were analyzed per conditions, and PCC distributions from all repressed domains were significantly different from those of active domains (at least $P < 0.01$) using Kruskal-Wallis and Dunn's multiple comparisons tests. (H) Oligopaint density (probe genomic size over 3D-segmented volume) of the single-domain probes. At least 57 nuclei were analyzed per condition, and density distributions from all repressed domains were significantly different from those of active domains (at least $P < 0.05$) using Kruskal-Wallis and Dunn's multiple comparisons tests. Scale bars, 1 μm .

that repressed TADs (Blue and Black) form globular structures that coincide with the nanocompartments in the 3-Mb region, suggesting that repressed TADs are true physical chromosomal domains. Conversely, Red active domains were situated in the fluorescence-poor zones of the 3-Mb region (Fig. 1F and fig. S2C), despite a similar probe coverage (fig. S2D). In support of this, the correlation of the fluorescence intensity distribution of the 3-Mb region with that of repressed TADs was much higher than with that of active regions (Fig. 1G). Moreover, active domains had a lower 3D density of Oligopaint signals (Fig. 1H), indicating that they are present in more open chromatin, consistent with the lower number of Hi-C contacts within active compared to repressed domains (fig. S2E) and with a previous report (23).

TAD-based 3D nanocompartments undergo dynamic cis and trans contact events

These data suggest that Hi-C patterns resulting from cell population average studies might reflect the partitioning of chromatin into physical entities in *Drosophila* chromosomes, organized in the cell nucleus as discrete compact chromatin nanocompartments (repressive TADs), interspersed by more open regions (active domains). To test this hypothesis, we asked whether the number of observed nanocompartments corresponds to the number of repressed TADs. Of importance for this study, most nuclei in Dipteran species like *Drosophila* have paired homologous chromosomes in interphase. Chromosome pairing has been shown to be important for appropriate gene regulation (27), but the ultrastructure of paired homologous loci is still unknown. Whereas

conventional WF microscopy often showed single unresolved foci for probes covering a single TAD, 3D-SIM resolved distinct nanocompartments (fig. S3, A and B). To address whether they correspond to the homologous TADs, we compared the numbers of foci observed in tetraploid S2R+ cells versus diploid embryonic (12 to 16 hours) cells, which have conserved TAD structures in Hi-C maps (fig. S4). In addition to single TADs and the 3-Mb probe that contains 12 repressed TADs, we designed additional Oligopaint probes: R2 (195 kb), R3

(805 kb), and R4 (495 kb), covering two, three, and four repressed TADs, respectively (fig. S4). We systematically observed an approximately twofold difference between the number of nanocompartments detected in tetraploid versus diploid cells, consistent with the predominant formation of juxtaposed yet spatially distinct TADs for each homolog in both cell types (Fig. 2, A and B). The distributions of the number of nanocompartments observed per cell indicated some degree of heterogeneity at the single-cell level. We could observe that homologous TADs

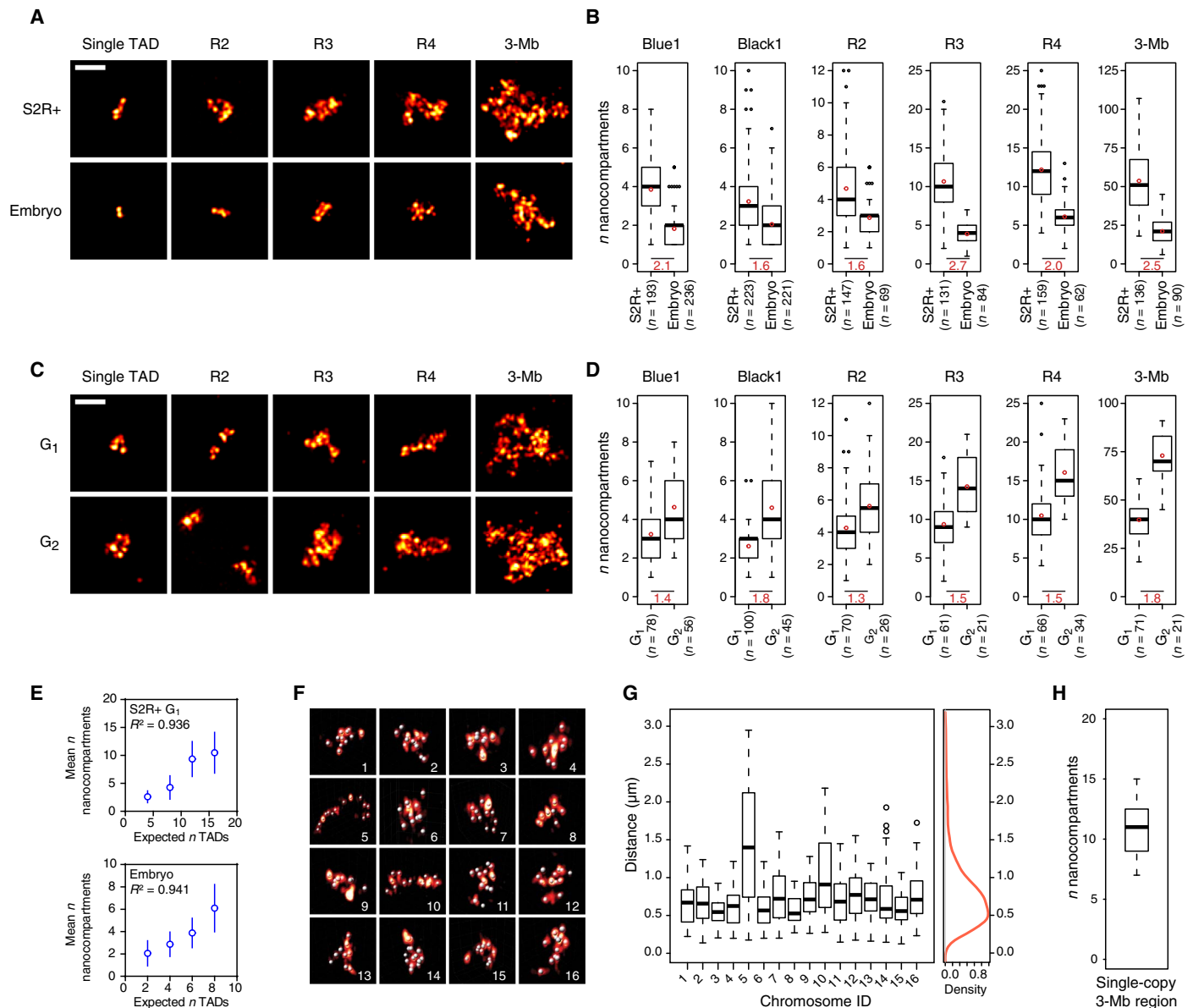


Fig. 2. Repressed TADs form 3D chromosomal units with dynamic contact events. (A) Examples of chromatin labeling (single Black1 TAD, R2, R3, R4, and 3-Mb probe, maximum projections) in (top) tetraploid S2R+ and (bottom) diploid embryonic cells. (B) Number of nanocompartments counted per nucleus in S2R+ and embryonic cells for the different labeling ($P < 0.0001$ in all conditions with two-tailed Mann-Whitney test). Bottom: Ratio of the means (indicated with red circles) between the two conditions. n indicates the number of nuclei analyzed. (C) Examples of chromatin labeling (single Blue1 TAD, R2, R3, R4, and 3-Mb probe, maximum projections) in tetraploid S2R+ cells in (top) G₁ and (bottom) G₂ phases of the cell cycle. (D) Number of nanocompartments counted per nucleus in S2R+ cells in G₁ and G₂ phases for the different labeling ($P < 0.0001$ in all conditions with two-tailed Mann-Whitney test, except for R2, $P < 0.01$). Bottom: Ratio of the means (indicated with red circles) between the two conditions. n indicates the number of nuclei analyzed. (E) Mean (\pm SD) number of nanocompartments counted per S2R+ cells in G₁ phase (top) or in embryonic cells (bottom) as a function of the number of TADs for Black1, R2, R3, and R4 labeling. R^2 values of linear regressions are indicated. (F) 3D view of single chromosome copies labeled with the 3-Mb probe. Nanocompartment positions are represented with 150-nm-diameter beads. (G) Pairwise distances between all nanocompartments identified in the individual chromosomes shown in (F) (one boxplot corresponds to one chromosome). Right: Averaged distance distribution from all the single chromosomes. (H) Number of nanocompartments counted for single chromosomes ($n = 19$). Scale bars, 1 μ m.

can generate well-separated structures but also merge in a subset of the cells (fig. S3, C and D). Thus, chromatin fibers from paired homologous chromosomes do not appear to constantly intermingle, and instead, they form individual homologous TADs that engage in dynamic trans contact events. Some cells displayed more nanocompartments than would be expected based on the number of TADs multiplied by the ploidy (Fig. 2B). This observation was particularly evident for S2R+ cells, which have a sizeable proportion of G₂ cells, compared to embryonic cells, which are highly enriched in the G₀/G₁ phase of the cell cycle (28). To test whether these distributions could reflect differences in cell cycle stage and the fact that G₂ cells have replicated their DNA, we separated S2R+ cells into G₁ and G₂ populations based on DAPI signal (see Materials and Methods and fig. S5) (29). We could count more nanocompartments on average after replication, suggesting that, similar to chromosome homologs, sister chromatids behave largely as non-intermingled series of TADs (Fig. 2, C and D), consistent with the TADs observed by Hi-C in *Drosophila* polytene chromosomes (30). Moreover, there are very strong correlations between the mean number of nanocompartments observed and the number of TADs expected in both G₁ S2R+ cells and G₀/G₁ embryonic cells (Fig. 2E). To assess chromatin folding into TADs independently of pairing events, we also analyzed cells showing distinctly unpaired unique chromosomes, labeled with the 3-Mb probe (fig. S3E). We noticed heterogeneity in the higher-order arrangement of these TADs, ranging from a compact conformation to rarer unfolded chromosomes (Fig. 2, F and G). In this latter state, we

were able to measure an average (\pm SD) nanocompartment diameter of 175 ± 27 nm (fig. S3, F and G). Again, the range of the number of nanocompartments detected in individual chromosomes fitted with the 12 repressed TADs predicted by Hi-C (Fig. 2H), although several cells showed a number of objects different from the expected number, suggesting that individual nanocompartments may contain multiple or split TADs. We thus conclude that the number of nanocompartments corresponds well with the number of repressed TADs, with a degree of cell-to-cell stochasticity due to the dynamics of intra- and inter-TAD contact events.

Repressed TADs form physical and structural chromosomal units

To rigorously quantify the single-cell variability of TAD behavior, we turned our analysis to TADs in a haploid context. We focused on a 400-kb region containing two distinct repressed TADs (Black) separated by an active region on the X chromosome of male embryos (Fig. 3A). We first used three-color FISH to measure intra-TAD (probes 2-1) versus inter-TAD (probes 2-3) 3D distances, with probes 1 and 3 being at the exact same genomic distance from probe 2. Our analysis revealed that intra-TAD distances are considerably shorter than inter-TAD distances (Fig. 3B). Moreover, inter-TAD distance distributions (1-3 and 2-3) were very similar, consistent with TAD structure strongly modulating the interdependence between physical and genomic distances. In support of this, analysis of FISH signal triplets showed that 75% of

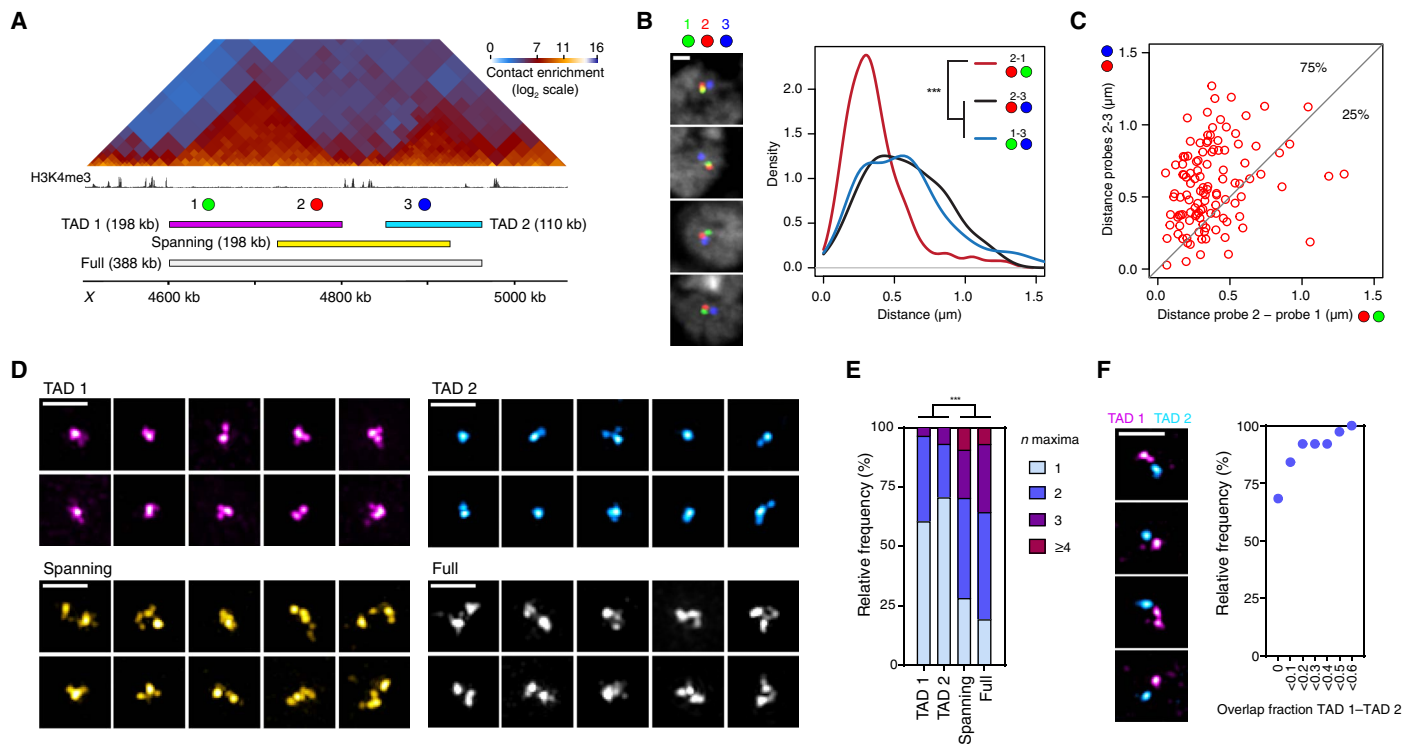


Fig. 3. Single-cell analysis of haploid chromosome reveals consistent TAD-based chromatin compartmentalization. (A) Sixteen- to 18-hour male embryo Hi-C map with H3K4me3 ChIP-seq profile (14- to 16-hour embryos) and FISH probe positions. (B) Representative examples of triple FISH-labeled nuclei (confocal microscopy, z slices) with probes 1 (green), 2 (red), and 3 (blue) and 3D distance distributions (from 115 nuclei) between the probes. (C) Scatter plot of paired distances between probes 2 and 1 (x axis) and probes 2 and 3 (y axis). The proportions of intra-TAD (2-1) distances shorter or larger than inter-TAD (2-3) distances are indicated (75% and 25%, respectively). (D) Representative examples of 3D-SIM images (maximum projections) of TAD 1, TAD 2, spanning, and full probes. (E) Number of FISH local maxima detected per nucleus with the different probes (at least 102 nuclei were analyzed per condition). (F) Representative examples of 3D-SIM images (maximum projections) of TAD 1 and TAD 2 double FISH experiments and quantification of the overlap fraction between TAD 1 and TAD 2 probes (38 nuclei were analyzed). Statistics were performed with Kruskal-Wallis and Dunn’s multiple comparisons tests. ***P < 0.0001. Scale bars, 1 μ m.

the 2-1 intra-TAD distances were shorter than the paired 2-3 inter-TAD distances (78% when considering the paired 1-3 inter-TAD distances; Fig. 3C). Previous studies compared 3D spatial distances between FISH probes corresponding to distinct regions and Hi-C interaction profiles (17, 20, 31), but the relationship between distance distribution and local chromatin conformation still remains unclear. We thus designed Oligopaint probes covering each single TADs independently (TAD 1 and TAD 2 probes), a probe of the same genomic size as TAD 1 but shifted to span the boundary (spanning probe), and a probe covering the entire region (full probe; Fig. 3A). We performed 3D-SIM imaging (Fig. 3D and fig. S6A) and observed that TAD 1 and TAD 2 displayed only one nanocompartment in the majority of cells, whereas most spanning and full probes were split into two or more nanocompartments, providing strong evidence for the physical compartmentalization of chromatin into TADs (Fig. 3E and fig. S6B). We then visualized TAD 1 and spanning probes using direct stochastic optical reconstruction microscopy (dSTORM) (32, 33). Image analysis using this independent method confirmed that TAD 1 appeared as a single nanocompartment in the majority of cells, unlike most spanning probes (fig. S7), despite their same genomic size. Analysis of the sphericity of the 3D-segmented probes also revealed that single TADs have highly globular structures compared to

the spanning and full regions (fig. S6C). Globular single TADs have a similar diameter range as the nanocompartments described above with larger chromosomal regions [mean \pm SD, 192 ± 35 nm (TAD 1) and 182 ± 23 nm (TAD 2); fig. S6D], consistent with nanocompartments corresponding to TADs. We could occasionally resolve numerous substructures in TADs of haploid cells (Fig. 3, D and E, and fig. S6, A and B), arguing for a dynamic behavior of TAD conformations in a subset of the cells. Finally, to further explore whether TADs represent distinct physical units, we labeled the two repressed TADs in different colors. Inter-TAD contacts were not observed in 68% of the nuclei, and less than 10% of volume overlap was detected in 84% of cases (Fig. 3F). This result strongly suggests that inter-TAD contacts reflect restricted chromatin interactions, rather than TAD merging. We thus conclude that, despite variable intra- and inter-TAD contacts in each cell, the physical TAD-based compartmentalization of the chromatin fiber is a general feature of chromosomal domains.

Polymer modeling recapitulates the physical partitioning of chromosomes into TADs

We then tested whether TAD compartmentalization can be predicted by using a self-avoiding and self-interacting polymer model (34, 35).

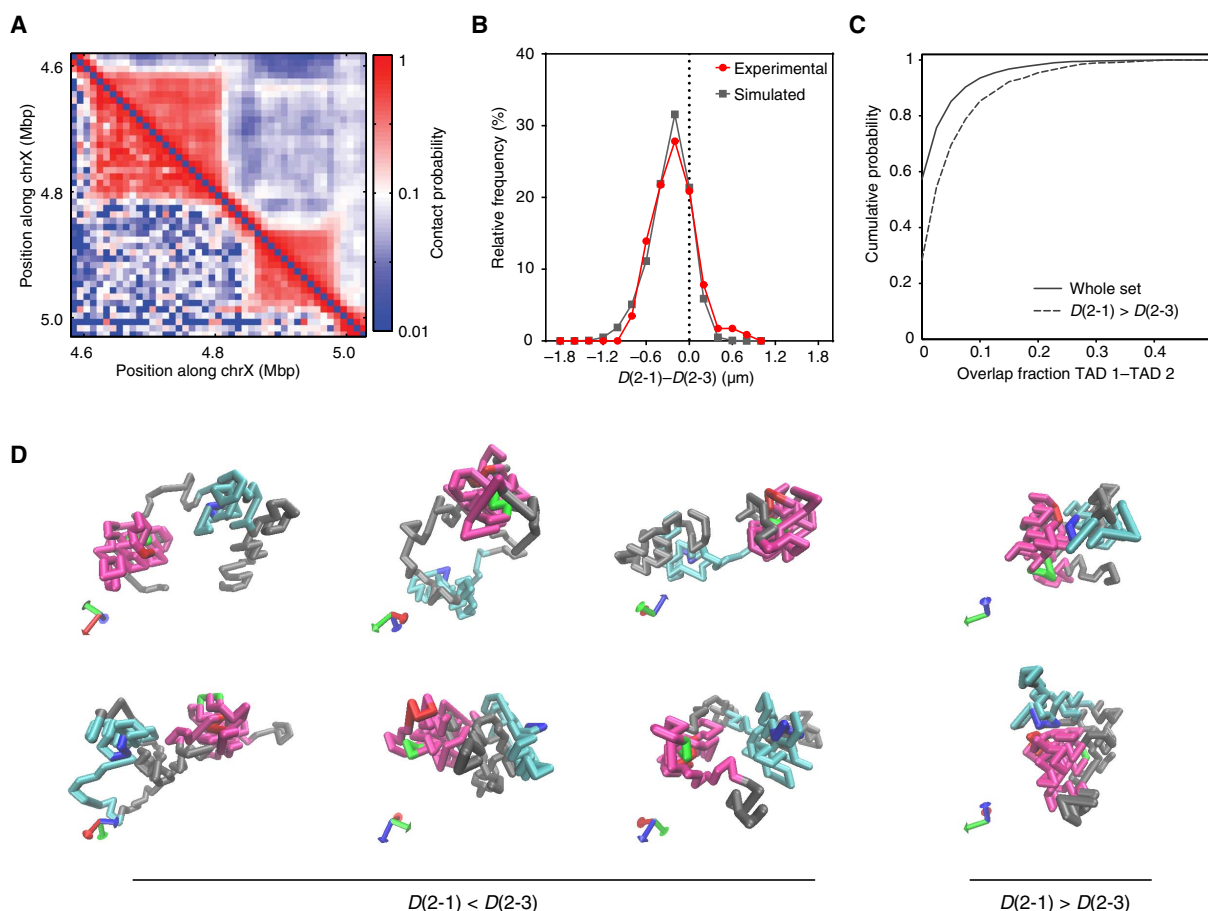


Fig. 4. Integrative view of chromosome conformation with polymer modeling. (A) Inferred (top) and experimental (bottom) contact probability maps. (B) Distributions of the differences between the paired distances (D) (2-1) and (2-3) from FISH experiments (red) and inferred model (gray). Values on the left of the dashed line indicate shorter intra-TAD than inter-TAD distances. (C) Cumulative distribution of the overlap fraction between TAD 1 and TAD 2 obtained from simulated conformations (full line) and from conformations when the inter-TAD distance (2-3) is smaller than the intra-TAD (2-1) distance (dashed line). (D) Representative examples of configurations of the inferred model, with the inter-TAD distance (2-3) larger (left) or smaller (right) than the intra-TAD (2-1) distance. Probe 1, 2, and 3 positions are represented with monomers in green, red, and blue, respectively; TAD 1 and TAD 2 are represented with magenta and cyan monomers, respectively.

First, we built a model of the same region described above, with monomers of 2 kb in which model parameters were fitted to reproduce the Hi-C data available for the same region (see Materials and Methods, Fig. 4A, and fig. S8, A and B). From the inferred ensemble of configurations, we computed distances for monomers corresponding to probes 1, 2, and 3 used

in FISH (see Materials and Methods and Fig. 3A), and the comparison between model and FISH data shows a very good fit of the distance distributions (fig. S8C). The frequency for inter-TAD probe (2-3) distances smaller or equal to intra-TAD probe (2-1) distances is $15 \pm 2\%$, in good agreement with experimental data (Fig. 4B and fig. S8D). To assess how

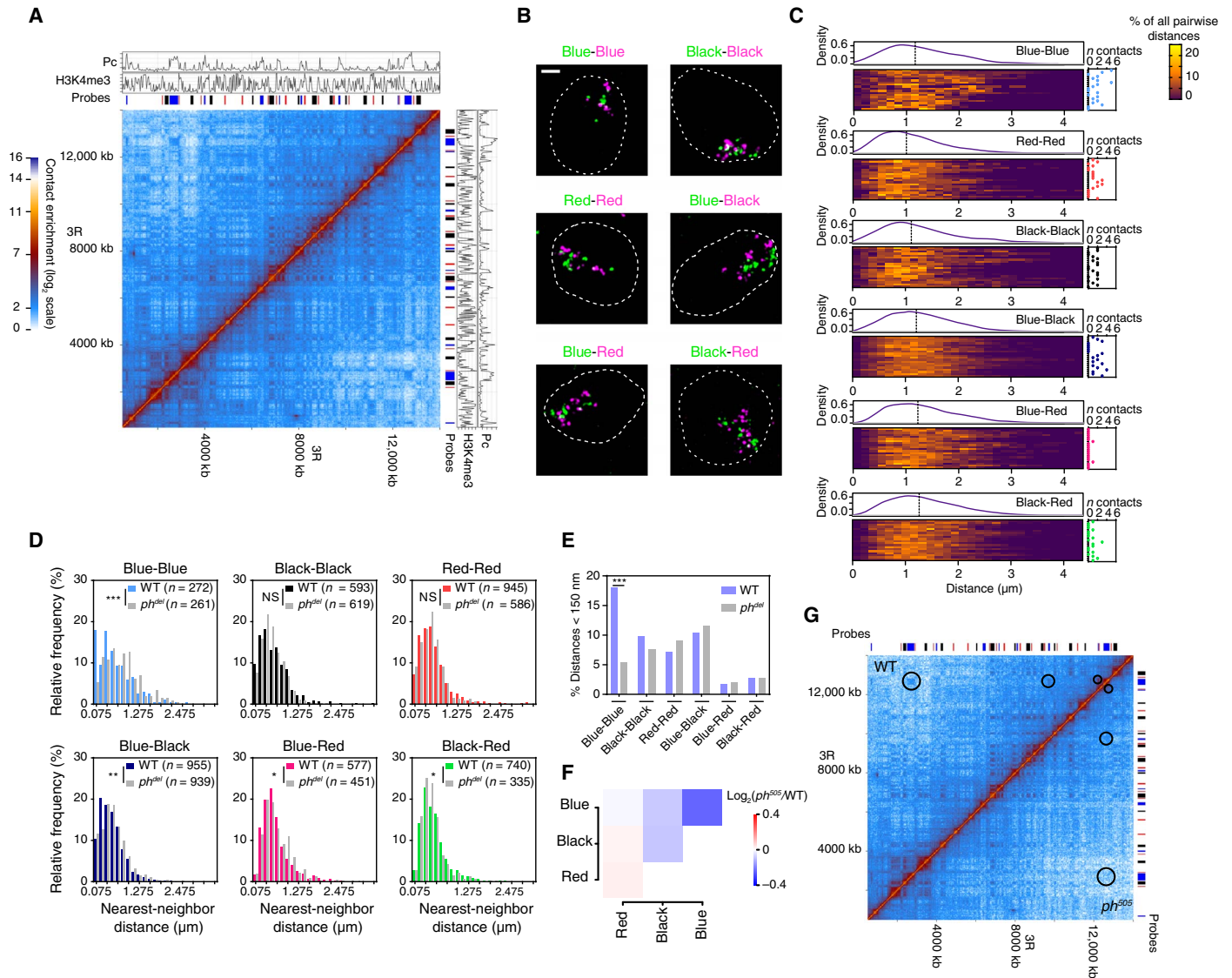


Fig. 5. Large-scale chromatin folding reflects heterogeneous, discrete, and specific interdomain contacts. (A) Sixteen- to 18-hour embryo Hi-C map of a 14-Mb region, along with ChIP-seq profiles of Pc and H3K4me3 (14- to 16-hour embryos). We designed a set of epigenetic state-specific probes (Blue, Black, and Red domains, indicated with colored bars) to perform two-color labeling of domains of the same type that were consecutive along the linear scale of the chromosome (that is, Blue-Blue, Black-Black, and Red-Red) or for different combinations of chromatin type (that is, Blue-Black, Blue-Red, and Black-Red). (B) 3D-SIM images from different two-color FISH labeling combinations in embryonic cells (maximum projections). Scale bar, 1 μ m. (C) Distribution of all the pairwise distances between all differentially labeled domains in the different FISH combinations. Each line of the heat maps represents distance distribution within single-cell (color-coded in the percentage of all the distances within the cell). On top of each heat map, the distribution of the distances for the whole cell population is plotted, and dashed line indicates median. On the right of each heat map, the number of distances is <150 nm per cell (*n* contacts). Twenty nuclei (>1800 distances in total) were analyzed per condition. The broad distributions in all FISH combinations indicate a limited extensive clustering of the domains of the same epigenetic status. (D) Nearest-neighbor distance distributions for each labeling combination in wild-type (WT) and *ph⁵⁰⁵* 12- to 16-hour embryos. The x axis is split into 150-nm bins. *n* indicates the number of distances (measured in at least 30 nuclei) for each condition. Statistics were performed using Kolmogorov-Smirnov tests; ****P* < 0.001, ***P* < 0.01, **P* < 0.05. The depletion of very short range distances in Blue-Red and Black-Red distributions suggests that active chromatin is spatially segregated from inactive chromatin at the nanoscale. NS, not significant. (E) Percentages of nearest-neighbor distances <150 nm in WT embryos versus *ph⁵⁰⁵* embryos, showing the specific loss of contacts between Blue domains. Statistics were performed using two-tailed Fisher's exact tests, ****P* < 0.0001. (F) Genome-wide differential Hi-C contact scores ($\log_2(\text{ph}^{505}/\text{WT})$ normalized scores) between the chromatin domains in WT male versus *ph⁵⁰⁵* male embryos show the specific loss of contacts between Blue domains. (G) Side-by-side Hi-C map of WT male (top) and *ph⁵⁰⁵* male embryos (bottom) showing specific loss of contacts between Blue TADs in *ph⁵⁰⁵* (indicated with circles). The contact enrichment color scale is the same as in (A).

changes in distances influence TAD structure (fig. S8E), we then used the inferred model to measure the overlap fraction (fig. S8F) for all simulated configurations or only for configurations where the inter-TAD probe (2-3) distance was smaller than the intra-TAD probe (2-1) distance. The configurations from the inferred model displayed weak overlap fraction between the TADs ($\leq 10\%$ overlap in 94% of the inferred configurations; Fig. 4C). Strikingly, the small overlap of TADs largely persists for configurations where the intra-TAD distance is higher than the inter-TAD distance ($\leq 10\%$ overlap in 85% of the inferred configurations; Fig. 4C). Therefore, polymer modeling using parameters that fit Hi-C maps supports the frequent folding of the two TADs into well-separated nanocompartments. The fraction of intra-TAD distances larger than the inter-TADs counterparts is thus explained by the dynamic relative positioning of the two TADs, rather than by TAD intermingling (Fig. 4D and fig. S8E). Overall, our microscopy and simulation results are consistent with TADs representing physical units of chromatin folding.

Large-scale chromatin folding reflects highly heterogeneous yet specific, long-range interdomain contacts

Finally, we asked whether large-scale active and repressed compartments (2, 11) also represent physical entities or rather reflect statistical contact preference between highly heterogeneous chromosome configurations. We labeled chromatin domains of different epigenetic states and studied their relative 3D spatial organization (Fig. 5, A and B). This analysis revealed the presence of discrete interdomain contacts, with preference for contacts among TADs of the same epigenetic type (Fig. 5, C and D). These inter-TAD contacts are regulated, as the disruption of the *polyhomeotic* (*ph*) PcG gene specifically affects Pc inter-TAD contacts (36) without affecting contacts between other domains (Fig. 5, E to G). However, they are rare and the overall FISH configurations generated by the probe sets are highly heterogeneous (Fig. 5C). These results, consistent with previous reports (17, 18), suggest that active and repressive compartments reflect stochastic inter-TAD contacts with statistical preference for TADs of the same kind. These findings thus identify a difference between the nature of compartments defined from Hi-C, which is statistical, and that of repressive TADs, which are physical entities.

DISCUSSION

This study demonstrates the partitioning of the chromatin fiber into discrete nanocompartments that correspond to repressed TADs intercalated with active chromatin domains. If individual TAD folding is dynamic and variable, then the meshwork of intra-TAD contacts is sufficient to hold them together to form nanocompartments. We thus propose that the high frequency and cooperativity, rather than the stability and the persistence, of intra-TAD interactions give rise to identifiable structures in single cells. Furthermore, the weak propensity of active chromatin, highly enriched in acetylated histones, to interact with inactive chromatin (7, 8) may be sufficient to shape a chromatin pattern made of a succession of segregated TAD-based discrete domains. These conclusions thus reconcile previous observations using microscopy and Hi-C (5, 6, 14, 17, 31, 34). Our data are consistent with TAD-based nanocompartments persisting through the interphase cell cycle, providing a role for TADs in the spatial segregation of autonomously regulated genomic regions. This chromosome organization is thus maintained in G_2 cells and may be the basis of chromosome pairing in interphase insect cells. Finally, the fact that TAD identity and architecture depend on cell fate regulation (15, 37) calls for further analysis in different cell types and species to generalize these findings and

understand the mechanistic basis of the relation between 3D chromosome organization and chromatin contact patterns.

MATERIALS AND METHODS

Experimental design

Probe design and synthesis

Oligopaint libraries were constructed following the procedures described by Beliveau *et al.* (24) [see the Oligopaints website (<http://genetics.med.harvard.edu/oligopaints>) for further details]. The 3-Mb (chr2L: 9935314-12973080) library, synthesized at the Wyss Institute (Harvard University, Boston, MA), was a gift from the laboratory of C.-T. Wu (Harvard Medical School, Boston, MA). All other libraries were ordered from CustomArray in the 12K Oligo pool format. Coordinates, size, number, and density of probes for the libraries are given in table S1.

All libraries consisted of 42-mer genomic sequences discovered by OligoArray 2.1 run in the laboratory of C.-T. Wu with the following settings: -n 30 -l 42 -L 42 -D 1000 -t 80 -T 99 -s 70 -x 70 -p 35 -P 80 -m 'GGGG;CCCC;TTTTT;AAAAA' -g 44. Each library contains a universal primer pair followed by a specific primer pair hooked to the 42-mer genomic sequences (126-mers in total). Single TAD probe libraries allowing dual labeling (named "1:3") contained one oligonucleotide of three potential genomic targets.

The 3-Mb Oligopaint probe was produced by emulsion polymerase chain reaction (PCR) amplification using universal primers followed by a "one-step PCR" and the lambda exonuclease procedure (24). In this case, each oligonucleotide contained a single fluorochrome. All other Oligopaint libraries were produced by emulsion PCR amplification from oligonucleotide pools followed by a "two-step PCR" procedure and the lambda exonuclease method (24). The two-step PCR leads to secondary oligonucleotide binding sites for signal amplification with a secondary oligonucleotide (Sec1 or Sec6) containing two additional fluorochromes. In this case, each oligonucleotide carried three fluorochromes in total. All oligonucleotides used for Oligopaint production were purchased from Integrated DNA Technologies. All oligonucleotide sequences (5'→3') are listed below:

Emulsion PCR with universal primers

BB297-FWD: GACTGGTACTCGCGTGACTTG

BB299-REV: GTAGGGACACCTCTGGACTGG

3-Mb probe one-step PCR

BB291-FWD: /5Phos/CAGGTCGAGCCCTGTAGTACG

BB292-REV-ATTO565: /5ATTO565N/CTAGGAGACAGCC-TCCGACAC

Two-step PCR

PCR1 with FWD 5' phosphorylation and REV 53-mers:

- A BB82-FWD: /5Phos/GTATCGTGCAAGGGTGAATGC
SecX-BB278-REV: /SecX/GAGCAGTCACAGTCCAGAAGG
- B BB81-FWD: /5Phos/ATCCTAGCCCATACGGCAATG
SecX-BB281-REV: /SecX/GGACATGGGTCAGGTAGGTTG
- C BB287-FWD: /5Phos/CGCTCGGTCTCCGTTTCGTCTC
SecX-BB288-REV: /SecX/GGGCTAGGTACAGGGTTCAGC
- D BB293-FWD: /5Phos/CCGAGTCTAGCGTCTCCTCTG
SecX-BB294-REV: /SecX/AACAGAGCCAGCCTCTACCTG
- E BB298-FWD: /5Phos/CGTCAGTACAGGGTGTGATGC
SecX-BB187-REV: /SecX/TTGATCTTGACCCATCGAAGC
Binding sequence Sec1: CACCGACGTCGCATAGAACGGAA-GAGCGTGTG
Binding sequence Sec6: CACACGCTCTCCGTCTTGCCGT-GGTCGATCA

PCR2 with labeled “back primer”

BB506-Alexa488: /5Alex488N/CACCGACGTCGCATAGAACGG

BB511-Cy3: /5Cy3/CACACGCTCTCCGTCTTGGC

BB511-ATTO565: /5ATTO565N/CACACGCTCTCCGTCTTGGC

Secondary oligos

Sec1-Alexa488-X2: /5Alex488N/CACACGCTCTTCCGTTTC-TATGCGACGTCGGTGagatggtt/3AlexF488N/

Sec6-Cy3-X2: /5Cy3/TGATCGACCACGGCCAAGACGGA-GAGCGTGTGagatggtt/3Cy3Sp/

Sec6-ATTO565-X2: /5ATTO565N/TGATCGACCACGGC-CAAGACGGAGAGCGTGTGagatggtt/3ATTO565N/

Sec6-Alexa488-X2: /5Alex488N/TGATCGACCACGGCCA-GACGGAGAGCGTGTGagatggtt/3AlexF488N/

In Fig. 5, for the labeling of domains of the same chromatin type (that is, Blue-Blue, Black-Black, and Red-Red), domains that were consecutive along the chromosome were alternatively labeled, that is, one in A488 followed by one in Cy3 or ATTO565, etc. For this purpose, the oligopools corresponding to nonconsecutive domains of the same chromatin type were on the same array, which allows their amplification as one library using the same primer set. For the labeling of domains of different chromatin type (that is, Blue-Black, Blue-Red, and Black-Red), all domains of the same chromatin type were labeled using one color.

Small probes 1, 2, and 3 used for triple FISH experiments (Fig. 3) were generated using four consecutive PCR fragments of 1.1 to 1.6 kb from *Drosophila* genomic DNA, each covering approximately 8 kb. The list below shows the amplicon size (bp) and the corresponding primers for each probe fragment.

Probe 1

Fragment 1	1299	1_FWD	AGGTGGAGTTGTGTATGCGA
		1_REV	GAGTGAAAAGGCGTTGGTGT
Fragment 2	1568	2_FWD	TCCACTTCGCCTGATGTCT
		2_REV	GAGGTGTTGTGCCAGGAAG
Fragment 3	1084	3_FWD	TTTCTTACCCCATCCCCC
		3_REV	TATAAGCCCGCCAAGTTGA
Fragment 4	1443	4_FWD	GAGCTGGGACGTAACCTCTT
		4_REV	ATGTTACAGCTTCTCTCGA

Probe 2

Fragment 1	1446	1_FWD	CAGCGTGAGTGTCAAGTGAG
		1_REV	GCTGATGTTTGGCTTCCGA
Fragment 2	1568	2_FWD	TGAAATACGACGAACCGCAG
		2_REV	TGTTTCGACTGTAAAGCCGC
Fragment 3	1310	3_FWD	CTGGGCGACAAGAACAACAA
		3_REV	AAGAAAATTGCCAGCCCCAG
Fragment 4	1305	4_FWD	TAACCAATTGCCGCTTGAA
		4_REV	AAATCGGTGGGTGATGAGGT

Probe 3

Fragment 1	1421	1_FWD	CCACAAGAAAAGCACCCACA
		1_REV	TCTCGCTCTGTCAAGGTGT
Fragment 2	1243	2_FWD	CCTCAGCAGCTTTTCGGATC
		2_REV	GCCCCGGATTGTTGATTCTC
Fragment 3	1481	3_FWD	ACCTTACGCTCCAGATTTCG
		3_REV	AGTGCTTATCAACGACCCCA
Fragment 4	1292	4_FWD	GCTCGCTCATTTGACCCAAT
		4_REV	CTTCCGCTCATCTTGGGTG

Probes were labeled using the FISH Tag DNA Kit (Invitrogen Life Technologies) with Alexa Fluor 488, 555, and 647 dyes. All probe coordinates refer to Dm3/FlyBase R5 reference genome.

Three-dimensional FISH

3D-FISH was adapted from Bantignies and Cavalli (38). For optimal imaging, we used coverslips of 0.170 ± 0.005 mm (Zeiss). Coverslips were rinsed in 96% ethanol before incubation for 5 min in 1:10 poly-L-lysine (P8920, Sigma-Aldrich) diluted in water (final concentration at 0.01%, w/v). Briefly, cells in suspension (about 2×10^6 cells/ml) were deposited on a coverslip for 1-hour sedimentation in a humid chamber, or four to five dechorionated and selected embryos were squeezed directly on a coverslip with a Dumont #55 tweezer. Samples were fixed with phosphate-buffered saline (PBS)/4% paraformaldehyde (PFA), washed in PBS, permeabilized with PBS/0.5% Triton X-100 for 10 min, washed in PBS, and incubated for 30 min in PBS/20% glycerol. After PBS washes, cells were incubated with 0.1 M HCl for 10 min, washed in $2 \times$ SSCT ($2 \times$ SSC/0.1% Tween 20), and incubated for 30 min in 50% formamide, $2 \times$ SSCT. Probe mixture contains 20 pmol of each probe with 20 pmol of their complementary secondary oligonucleotide (except for the 3-Mb region, used without secondary oligo), 0.8 μ l of ribonuclease A (10 mg/ml), and FISH hybridization buffer [FHB; 50% formamide, 10% dextran sulfate, $2 \times$ SSC, and salmon sperm DNA (0.5 mg/ml)], in a total mixture volume of approximately 20 to 25 μ l, keeping at least a 3:4 ratio of FHB/total volume. Probe mixture was added to the coverslip before sealing on a glass slide with rubber cement (Fixogum, Marabu). Cell DNA was denatured at 78°C for 3 min, and hybridization was performed at 37°C overnight in a humid dark chamber. Cells were then washed 3×5 min at 37°C in $2 \times$ SSC, 3×5 min at 45°C in 0.1 \times SSC, and 2×5 min in PBS before DNA counterstaining with DAPI (final concentration at 0.3 mg/ml in PBS). After final washing in PBS, coverslips were mounted on slides with Vectashield (CliniSciences) and sealed with nail polish.

Immunostaining

Cells in suspension (about 2×10^6 cells/ml) were deposited on coverslips for 1-hour sedimentation in a humid chamber. Cells were fixed in PBS/4% PFA, washed in PBS, treated with PBS/0.1% Triton X-100 for 15 min, and washed in PBS/0.02% Tween 20 (PBT) before blocking in PBT/2% bovine serum albumin (BSA) (A7906, Sigma-Aldrich) for 30 min. Cells were then incubated with cyclin B (CycB) antibody (Developmental Studies Hybridoma Bank, product F2F4), diluted in PBT/2% BSA (1:500 dilution) overnight at 4°C in a humid chamber. Cells were then washed with PBT, incubated with secondary antibody (1:200 dilution; A-31570, Life Technologies) for 1 hour at room temperature, washed

with PBT, and incubated in PBS and DAPI (final concentration at 0.5 mg/ml in PBS). Cells were then washed with PBS, and coverslips were mounted on slides with Vectashield (CliniSciences).

Image acquisition

3D-SIM super-resolution imaging was performed with a DeltaVision OMX V3/V4 microscope (GE Healthcare) equipped with a $\times 100/1.4$ numerical aperture (NA) Plan Super Achromat oil immersion objective (Olympus). Electron-multiplying charge-coupled device (EMCCD) (Evolve 512B, Photometrics) cameras for a pixel size of 79 nm at the sample were used. Diode lasers at 405, 488, and 561 nm and the standard corresponding emission filters were used. Z-stacks were acquired with five phases and three angles per image plane, with a z-step of 125 nm. Raw images were reconstructed using SoftWorx (version 6.5, GE Healthcare), using channel-specific optical transfer functions (pixel size of reconstructed images, 39.5 nm). TetraSpeck beads (200 nm) (T7280, Thermo Fisher Scientific) were used to calibrate alignment parameters between the different channels. Quality of reconstructed images was assessed using ImageJ and the SIMcheck plugin (39), and examples of quality controls are shown in fig. S9. Conventional WF images were generated from raw images using SoftWorx by averaging the different angles and phases for each plane. Automatic “Threshold and 16-bit Conversion” (SIMcheck plugin) was applied to the reconstructed images shown.

Confocal microscopy images were acquired with a Leica SP8 microscope (Leica Microsystems) equipped with a $\times 63/1.4$ NA Plan-Apochromat oil immersion objective and photomultiplier tube and hybrid detectors for a pixel size of 59 nm (z-step, 300 nm).

dSTORM super-resolution imaging was carried out with a custom-made inverted microscope using an oil immersion objective (Plan-Apochromat, 100 \times , 1.4 NA oil DIC, Zeiss) mounted on a z-axis piezoelectric stage (P-721.CDQ, PICO, PI). A 1.5 \times telescope was used to obtain a final imaging magnification of 150-fold corresponding to a pixel size of 105 nm. Two lasers were used for excitation/photoactivation: 642 nm (MPB Communications Inc.) and 405 nm (OBIS, LX 405-50, Coherent Inc.). Laser lines were expanded and coupled into a single beam using a dichroic mirror (427-nm LaserMUX, Semrock). An acousto-optic tunable filter (AOTFnc-400.650-TN, AA Opto-Electronics) was used to modulate laser intensity. Light was circularly polarized using an achromatic quarter wave plate. Two achromatic lenses were used to expand the excitation laser and an additional dichroic mirror (zt405/488/561/638rpc, Chroma Technology) to direct it toward the back focal plane of the objective. Fluorescence light was spectrally filtered with emission filters (ET700/75m, Chroma Technology) and imaged on an EMCCD camera (iXon X3 DU-897, Andor Technology). The microscope was equipped with a motorized stage (MS-2000, ASI) to translate the sample perpendicularly to the optical axis. To ensure the stability of the focus during the acquisition, a homemade autofocus system was built. A 785-nm laser beam (OBIS, LX 785-50, Coherent Inc.) was expanded twice and directed toward the objective lens by a dichroic mirror (z1064rdc-sp, Chroma Technology). The reflected infrared beam was redirected following the same path than the incident beam and guided to a CCD detector (Pixelfly, Cooke) by a polarized beam splitter cube. Camera, lasers, and filter wheel were controlled with software written in LabVIEW (40).

For image acquisition, an average of 15,000 frames was recorded at a rate of 10 ms per frame. To induce photoswitching, samples were imaged in a freshly prepared Smart Kit buffer (Abbelight). Continuous excitation and activation was used with output laser powers of 600 mW at 642 nm (for AF647 excitation) and 0 to 2.5 mW at 405 nm (for activation). The intensity of activation was progressively increased through-

out the acquisition to ensure a constant amount of simultaneously emitting fluorophores within the labeled structures. These excitation powers were optimized to ensure single-molecule detection. Imaging data are available upon request.

Image analysis

3D image analysis was performed using Imaris software and its XT module. For all images analyzed in 3D, a background subtraction filter was applied. For fluorescence intensity correlation, the regions of interest were first segmented in 3D (the 3-Mb probe for fig. S1E or the single-domain probes for fig. S2B and Fig. 1G). PCCs were then calculated in single cell using the voxels within the regions of interest. To measure the probe density of the single domains (Fig. 1H), we divided the genomic size of the labeled regions by the volume occupied by the 3D-segmented probes (probes with full Oligopaint coverage) in each single nucleus analyzed. To count the number of nanocompartments in the different FISH experiments (and to identify the 3-Mb maxima in fig. S1F), we used the point-like structure function (spots) of Imaris. Examples of nanocompartment identification with this method are shown in Fig. 2F. Distances between nanocompartments were calculated between the centered voxels of the spots identified. The sizes of nanocompartments (figs. S3, F and G, and S6D) were determined using full width at half maximum of Gaussian curves fitted to the intensity profiles obtained along lines passing through single nanocompartments in z-stacked (maximum projections) images [processed with Threshold and 16-bit Conversion from SIMcheck (39)]. To investigate contact frequency and overlap between TAD 1 and TAD 2 (Fig. 3F), we segmented the probes in 3D and calculated the Jaccard index by dividing the volume of the colocalized voxels (intersection of the two probes) by the sum of the volumes of the segmented probes minus the colocalized volume (union of the volumes of the two probes). This Jaccard index was defined as the overlap fraction. The quantification of segmented objects (fig. S6B) was performed with ImageJ's Otsu automatic thresholding of FISH signals (minimum size of 6 pixels²) in z-stacked (maximum projections) images (processed with Threshold and 16-bit Conversion from SIMcheck). Sphericity scores (fig. S6C) were calculated from probe 3D segmentation in individual nuclei. Specific epigenetic domains on the 3R chromosome (Fig. 5) were identified using the spot function of Imaris, and distances (all pairwise or nearest-neighbor distances) were measured in 3D from the centered voxels of the spots.

To measure the distances between small probes 1, 2, and 3 (Fig. 3, B and C), we applied a Gaussian filter ($\sigma = 1$ pixel) to the image before 3D segmentation of the spot signals and calculation of their center of mass. We then identified mutual nearest neighbors between the centers of mass of probes 2 and 1 and between the centers of mass of probes 2 and 3 and calculated combinatorial 3D distances for these triplets. To assess the experimental error, we used 200-nm TetraSpeck beads (T7280, Thermo Fisher Scientific) coupled with dyes of the same colors than the FISH probes, and we applied the same method for 3D distance measurements. We obtained from the beads a mean (\pm SD) of 164 ± 41 nm between red and green dyes (corresponding to probe 2 and 1 dyes, respectively), 107 ± 46 nm between red and far-red dyes (corresponding to probe 2 and 3 dyes, respectively), and 231 ± 67 nm between green and far-red dyes (corresponding to probe 1 and 3 dyes, respectively). This indicates that the shorter distance distribution between intra-TAD probes (2-1) compared to inter-TAD (2-3) is not due to technical bias.

For dSTORM image after processing and analysis, single-molecule localization was performed using the ImageJ ThunderSTORM plugin. Default values were used for the analysis (B-spline wavelet filter—order 3 and scale 2.0, approximate localization by eight-neighborhood local

maximum, subpixel localization by point spread function (PSF)–integrated Gaussian with the weighted least squares fitting method with a 3-pixel fitting radius and 1.6-pixel initial sigma). Particle coordinates and statistical properties were exported, and further analysis was conducted using MATLAB (MathWorks). Clustering of localizations was performed using an algorithm that was previously described by Cattoni *et al.* (41). A particle density and area threshold was set to define and quantify the number of objects per imaged probe. Automatic detection and quantification were further verified by visual inspection and comparison of conventional fluorescence and super-resolution rendered images using variable intensity thresholds.

Determination of cell cycle stage

We used the method published by Roukos *et al.* (29) to determine cell cycle stages of S2R+ cells. This method is based on DAPI fluorescence intensity after microscopy image acquisition (fig. S5). Briefly, DAPI channels of images were separated and projected along the *z* axis using average intensity, and nuclei were identified with CellProfiler software (<http://cellprofiler.org/>). The DAPI-integrated intensity was calculated for each nucleus, and the distribution for the whole population was plotted. The nuclei were then classified as G₁ or G₂ according to their DAPI-integrated intensity profile relative to the profile obtained for the population (fig. S5). To classify nuclei positive for CycB (fig. S5C), the CycB signal was segmented using CellProfiler software, and overlapped nuclei were counted.

Hi-C library preparation and sequencing

For S2R+ cells, Hi-C and library preparation was performed using the *in situ* method as published by Rao *et al.* (11) with minor modifications. Two biological replicates were done using 5×10^6 cells. Briefly, cells were digested overnight at 37°C using 500 U of Dpn II. After biotin filling, proximity ligation was carried out for 4 hours at 18°C with 2000 U of T4 DNA ligase, and after reverse cross-linking, DNA was purified with ethanol precipitation and sheared to 300- to 400-bp fragments using a Covaris S220 sonicator. Ligation fragments with biotin were pulled down using MyOne Streptavidin T1 beads (catalog no. 65602, Thermo Fisher Scientific), end-repaired, and adenylated as described. Fragments were then ligated with NEXTFlex adaptors (catalog no. 514101, BioScientific) and amplified by PCR using the KAPA HiFi Library Amplification Kit (catalog no. KK2620, Kapa Biosystems) for eight cycles. DNA size selection (300 to 800 bp) was performed using AMPure XP beads (catalog no. A63881, Agencourt). Libraries were validated qualitatively and quantitatively with Fragment Analyzer and by qPCR (Roche Light-Cycler 480). They were sequenced with 2×50 -bp paired-end runs on an Illumina HiSeq 2500.

For embryo Hi-C, embryos were collected in a saline buffer (0.03% Triton X-100, 0.4% NaCl) 16 to 18 hours after egg laying and then dechorionated for 5 min in fresh bleach. About 3000 GFP⁻ (selection of *ph*⁵⁰⁵ null mutant males; see the “*Drosophila*” section for description) and GFP⁺ (selection of WT males from the Y-GFP line) embryos each were sorted with a Union Biometrica COPAS large particle sorter (Union Biometrica Inc.) and then processed for Hi-C as in the study of Sexton *et al.* (6).

Hi-C analysis

Hi-C sequence mapping, read filtering, and normalization were performed as previously published (6). This provided statistics on the number of observed contacts for each pair of restriction fragments and the number of expected contacts from a low-level probabilistic model, which considers local GC content and the Dpn II restriction fragment length. Therefore, technically corrected matrices were generated by calculating ratios between the total observed reads and the

expected reads based on the above model. We visualized contact maps as described by Sexton *et al.* (6). To maximize resolution, we used variable bin sizes from 5 to 160 kb, visualizing each point in the matrix using the ratio as computed for the minimal 2D bin with at least 30 observed contacts. S2R+ Hi-C map (Fig. 1A) was plotted based on merging two replicates for the 3-Mb region 2L:9935314..12973080 and aligned with the ChIP-sequencing (ChIP-seq) profile of Pc (S2 cells, GSM604723) and ChIP-chip of H3K4me3 (S2 cells, modENCODE305). Side-by-side Hi-C comparisons for R2 (2R:10534240..10729120), R3 (3R: 23547420..24352723), R4 (2R: 5203174..5698315), and the 3-Mb Oligopaint-labeled regions (fig. S4) show the contact map in S2R+ cells (merge of replicates) on the top left and embryos [16 to 18 hours, merge of two replicates published by Schuettengruber *et al.* (42)] on the bottom right, alongside with ChIP-seq of H3K4me3 (embryo 14 to 16 hours, modENCODE5096) and ChIP-chip of H3K4me3 (S2 cells, modENCODE305). The male embryo Hi-C map (Fig. 3A) is plotted based on merging two replicates for the region X:4502500..5061200 alongside with ChIP-seq of H3K4me3 (modENCODE5096). The embryo [16 to 18 hours, merge of two replicates published by Schuettengruber *et al.* (42)] Hi-C map (Fig. 5A) is plotted for the region 3R:500000..14000000 and aligned with ChIP-seq of Pc (modENCODE3957) and H3K4me3 (modENCODE5096). The side-by-side Hi-C comparison for the 3R:500000..14000000 region (Fig. 5G) shows the contact map in WT male embryos (merge of two replicates) on the top left and *ph*⁵⁰⁵ male embryos (merge of two replicates) on the bottom right. Data sets are available at GSE99107.

Cis-decay curve analysis

For each single domain (fig. S2E), the observed and expected interaction counts for different bins of genomic separation were computed (from 400 bp to the full TAD size and separated by at least two fragments). The expected scores were taken by computing over all possible pairwise fragment combinations. The observed scores were obtained by counting all interactions within Hi-C data, which correspond to a particular distance. The cis-decay curve was plotted as the observed/expected ratio (the probability of detecting a Hi-C interaction) over a particular genomic separation on a logarithmic scale.

Analysis of domain contacts between different chromatin colors

The boundaries of domains were demarcated using the topmost fifth percentile of 5 kb–smoothed inferred distance-scaling factors (6). Domains were merged when their length was smaller than 10 kb. Then, domains were colored as red, blue, and black according to *k*-means grouping results based on their average enrichments of H3K4me3, H3K27me3, HP1, and H1 marks (6). We generated a domain-level contact map by calculating ratios between observed contacts of associating fragments within each pair of domains and total expected contacts based on the distance-scaling model (factoring out the general tendency of adjacent domains to contact each other). Differential contacts between WT and *ph* null mutant male embryos are expressed as the log₂ ratio of the *ph*⁵⁰⁵ normalized contacts and the WT normalized contacts (Fig. 5F).

Polymer modeling of haploid chromatin regions

We modeled the genomic region of chromosome X located between 4.58 and 5.03 Mbp by a flexible self-avoiding polymer containing $n = 225$ monomers, each monomer, of size a , representing 2 kbp. The chain dynamics was mapped on a face-centered cubic lattice following the kinetic Monte-Carlo scheme described by

Olarte-Plata *et al.* (35) driven by short-range contact interactions following the Hamiltonian

$$H = \sum_{i=1}^n \sum_{j=i+1}^n U_{ij} \delta_{ij}$$

where U_{ij} is the energy of interaction between monomers i and j , and $\delta_{ij} = 1$ if the two monomers are nearest neighbor on the lattice, and $\delta_{ij} = 0$ otherwise.

Parameters $\{U_{ij}\}$ were inferred such that the predicted contact map at equilibrium is consistent with experiments. The corresponding target contact map (Fig. 4A, bottom) was derived from the experimental Hi-C map at 10-kbp resolution: Similar to previous work (43), we transformed the experimental normalized contact frequencies C_{kl} into contact probabilities $P_{k,l}$ (the observable that we can directly compare to simulations) using the following procedure: $P_{k,l} = \min\left(1, \frac{C_{kl}}{\bar{C}_{\pm 1}}\right)$, where $\bar{C}_{\pm 1}$ is the median value of $\{C_{k,k\pm 1}\}$. The underlying assumption is that in a polymer model, adjacent monomers are always in contact. Note that in our polymer model, a 10-kbp region (the experimental resolution we used to avoid too much sampling noise) is represented by five consecutive beads. Therefore, for a given simulated configuration, two 10-kbp regions will be predicted to be in contact if at least one 2-kbp monomer of the first region is closest than a cutoff distance R to a monomer of the second region. R corresponds to the maximal distance between two loci that is captured by Hi-C experiments as a contact. Using this definition, for a given set of parameters $\{U_{ij}\}$ and a given value of R , we estimated the corresponding contact probability map at 10-kbp resolution from the sampling of 10,000 configurations at equilibrium (examples of configurations are given in Fig. 4D). For a fixed R , the values of $\{U_{ij}\}$ were inferred by minimizing the χ^2 score

$$\chi^2 = \sum_{k,l} \frac{[P_{k,l}(\text{sim}) - P_{k,l}(\text{exp})]^2}{\sigma_{kl}^2(\text{exp})}$$

where $\sigma_{kl}^2(\text{exp})$ is the standard error of $P_{k,l}(\text{exp})$ estimated using experimental replicates. We followed the scheme developed by Giorgetti *et al.* (34) that makes use of Boltzmann reweighting to numerically speed up the inference. Using this technique, convergence to a local minimum of χ^2 is fast (fig. S8B). We repeated this operation several times by varying also the values of R and took the realization with the lowest local minimum (Fig. 4A and fig. S8B for $R = 1.4a$). The length unit in the simulation ($a = 102 \pm 4$ nm) was then fixed by comparing the predicted distances between the three loci investigated by FISH to the corresponding experimental data accounting for a random experimental error of ~ 100 nm (fig. S8C; see the “Image analysis” section for the calculation of the experimental error).

For a given simulated configuration, the overlap fraction between TAD 1 and TAD 2 was computed by estimating the 3D convex envelope of each TAD using the MATLAB function `convexhull` and by computing the fraction of TAD 1 and TAD 2 monomers belonging to both envelopes (an illustration in 2D is given in fig. S8F). An overlap fraction of 0 (resp. 1) signifies that both TADs occupy separate (resp. common) volumes.

Cell culture

S2R+ cells (stock #150, Drosophila Genomics Resource Center) were grown at 25°C in Schneider’s S2 medium (S0146, Sigma-Aldrich)

complemented with 10% fetal bovine serum (FBS) (10500064, Gibco) and 1% penicillin-streptomycin (15140122, Gibco).

For S2R+ Hi-C, cells were incubated with enhanced green fluorescent protein (EGFP) double-stranded RNA (dsRNA). For each well (six-well plate), 1×10^6 cells in 1-ml serum-free medium were deposited with 17.5 μg of dsRNA and incubated for 30 min before addition of 2 ml of medium with 15% FBS. Cells were then grown for 5 days at 25°C before harvest. EGFP dsRNAs were obtained from plasmid PCR amplification (sequences given below), followed by *in vitro* transcription using the MEGAscript Kit (Ambion Inc.):

EGFP FWD-primer: 5'-T7-GACGTAACGGCCACAAGTT-3'

EGFP REV-primer: 5'-T7-TGCTCAGGTAGTGGTTGTCG-3'

T7 sequence: 5'-TAATACGACTCACTATAGGG-3'

EGFP amplicon sequence: GACGTAACGGCCACAAGTT-CAGCGTGTCCGGCGAGGGCGAGGGCGATGCCACCTACGG-CAAGCTGACCCCTGAAGTTTCATCTGCACCAACCGG-CAAGCTGCCCGTGCCTGGCCACCCTCGTGACCACCCT-GACCTACGGCGTGCAGTGCTTCAGCCGCTACCCCGACCA-CATGAAGCAGCACGACTTCTTCAAGTCCGCCATGCCC-GAAGGCTACGTCCAGGAGCGCACCATCTTCTTCAAGGAC-GACGGCAACTACAAGACCCGCGCCGAGGTGAAGTTC-GAGGGCGACACCCTGGTGAACCGCATCGAGCTGAAGGG-CATCGACTTCAAGGAGGACGGCAACATCCTGGGGCA-CAAGCTGGAGTACAACACTACAACAGCCACAACGCTCTATAT-CATGGCCGACAAGCAGAAGAACGGCATCAAGGTGAAGTTC-AAGATCCGCCACAACATCGAGGACGGCAGCGTG-CAGCTCGCCGACCACTACCAGCAGAACACCCCATCGGG-GACGGCCCCGTGCTGCTGCCGACAACCACTACCTGAGCA

Drosophila

For the FISH experiments, flies were raised in standard cornmeal yeast extract media at 21°C. Embryos were harvested on agar/vinegar plate at stages 15 to 16 after egg laying, equivalent to a development of 12 to 16 hours at 25°C. Embryos were manually dechorionated on a double-face adhesive tape and displayed on an agar/vinegar plate to avoid drying during manual selection under a GFP binocular. The Oregon-R w[1118] line was used as the WT control line. To analyze haploid regions on chromosome X in male embryos, a Y-GFP reporter line (Y-GFP line: y[1], w[67c23]; Dp(1;Y), y[+] P{ry+11} P{w[+mC]=ActGFP}JMR1) was used for the selection of WT GFP⁺ male embryos. This line was a gift of S. Hayashi and is described by Hayashi (44). The *ph^{del}* stock was balanced over the *KrGFP-FM7c* balancer (obtained from BL#5193 of the Bloomington Drosophila Stock Center) for the selection of hemizygous *ph^{del}* GFP⁻ null mutant male embryos. The *ph^{del}* stock was a gift from the laboratory of J. Wang.

For embryo Hi-C, flies were raised in standard cornmeal yeast extract media at 25°C. The *ph⁵⁰⁵* stock was balanced over the *KrGFP-FM7c* balancer for the selection of hemizygous *ph⁵⁰⁵* GFP⁻ null mutant male embryos. The Y-GFP line described above was used for the selection of WT GFP⁺ male embryos to be compared with the *ph* mutant male embryos.

Statistical analysis

Description of statistical analysis is included in the figure legends.

SUPPLEMENTARY MATERIALS

Supplementary material for this article is available at <http://advances.sciencemag.org/cgi/content/full/4/2/eaar8082/DC1>

fig. S1. Chromatin nanostructure visualization with 3D-SIM imaging.

fig. S2. Dual labeling Oligopaint FISH.

fig. S3. Resolution of homologous TADs with 3D-SIM.

fig. S4. Oligopaint probe-targeted regions in S2R+ cells and embryos.

fig. S5. Cell cycle staging of S2R+ cells.

fig. S6. Super-resolution imaging of haploid chromatin folding.

fig. S7. 2D dSTORM imaging of TAD 1 and spanning probes.

fig. S8. Modeling the X chromatin region.

fig. S9. Quality control of SI acquisitions.

table S1. Libraries for Oligopaint probes.

REFERENCES AND NOTES

- B. Bonev, G. Cavalli, Organization and function of the 3D genome. *Nat. Rev. Genet.* **17**, 661–678 (2016).
- E. Lieberman-Aiden, N. L. van Berkum, L. Williams, M. Imakaev, T. Ragoczy, A. Telling, I. Amit, B. R. Lajoie, P. J. Sabo, M. O. Dorschner, R. Sandstrom, B. Bernstein, M. A. Bender, M. Groudine, A. Gnirke, J. Stamatoyannopoulos, L. A. Mirny, E. S. Lander, J. Dekker, Comprehensive mapping of long-range interactions reveals folding principles of the human genome. *Science* **326**, 289–293 (2009).
- J. R. Dixon, S. Selvaraj, F. Yue, A. Kim, Y. Li, Y. Shen, M. Hu, J. S. Liu, B. Ren, Topological domains in mammalian genomes identified by analysis of chromatin interactions. *Nature* **485**, 376–380 (2012).
- C. Hou, L. Li, Z. S. Qin, V. G. Corces, Gene density, transcription, and insulators contribute to the partition of the *Drosophila* genome into physical domains. *Mol. Cell* **48**, 471–484 (2012).
- E. P. Nora, B. R. Lajoie, E. G. Schulz, L. Giorgetti, I. Okamoto, N. Servant, T. Piolot, N. L. van Berkum, J. Meisig, J. Sedat, J. Gribnau, E. Barillot, N. Blüthgen, J. Dekker, E. Heard, Spatial partitioning of the regulatory landscape of the X-inactivation centre. *Nature* **485**, 381–385 (2012).
- T. Sexton, E. Yaffe, E. Kenigsberg, F. Bantignies, B. Leblanc, M. Hoichman, H. Parrinello, A. Tanay, G. Cavalli, Three-dimensional folding and functional organization principles of the *Drosophila* genome. *Cell* **148**, 458–472 (2012).
- M. J. Rowley, M. H. Nichols, X. Lyu, M. Ando-Kuri, I. S. M. Rivera, K. Hermetz, P. Wang, Y. Ruan, V. G. Corces, Evolutionarily conserved principles predict 3D chromatin organization. *Mol. Cell* **67**, 837–852.e7 (2017).
- S. V. Ulianov, E. E. Khrameeva, A. A. Gavrillov, I. M. Flyamer, P. Kos, E. A. Mikhaleva, A. A. Penin, M. D. Logacheva, M. V. Imakaev, A. Chertovich, M. S. Gelfand, Y. Y. Shevelyov, S. V. Razin, Active chromatin and transcription play a key role in chromosome partitioning into topologically associating domains. *Genome Res.* **26**, 70–84 (2016).
- J. H. I. Haarhuis, R. H. van der Weide, V. A. Blomen, J. O. Yáñez-Cuna, M. Amendola, M. S. van Ruiten, P. H. L. Krijger, H. Teunissen, R. H. Medema, B. van Steensel, T. R. Brummelkamp, E. de Wit, B. D. Rowland, The cohesin release factor WAPL restricts chromatin loop extension. *Cell* **169**, 693–707.e14 (2017).
- E. P. Nora, A. Goloborodko, A. L. Valton, J. H. Gibcus, A. Uebersohn, N. Abdennur, J. Dekker, L. A. Mirny, B. G. Bruneau, Targeted degradation of CTCF decouples local insulation of chromosome domains from genomic compartmentalization. *Cell* **169**, 930–944.e22 (2017).
- S. S. P. Rao, M. H. Huntley, N. C. Durand, E. K. Stamenova, I. D. Bochkov, J. T. Robinson, A. L. Sanborn, I. Machol, A. D. Omer, E. S. Lander, E. L. Aiden, A 3D map of the human genome at kilobase resolution reveals principles of chromatin looping. *Cell* **159**, 1665–1680 (2014).
- S. S. P. Rao, S.-C. Huang, B. Glenn St Hilaire, J. M. Engreitz, E. M. Perez, K.-R. Kieffer-Kwon, A. L. Sanborn, S. E. Johnstone, G. D. Bascom, I. D. Bochkov, X. Huang, M. S. Shamim, J. Shin, D. Turner, Z. Ye, A. D. Omer, J. T. Robinson, T. Schlick, B. E. Bernstein, R. Casellas, E. S. Lander, E. L. Aiden, Cohesin loss eliminates all loop domains. *Cell* **171**, 305–320.e24 (2017).
- W. Schwarzer, N. Abdennur, A. Goloborodko, A. Pekowska, G. Fudenberg, Y. Loe-Mie, N. A. Fonseca, W. Huber, C. H. Haering, L. Mirny, F. Spitz, Two independent modes of chromatin organization revealed by cohesin removal. *Nature* **551**, 51–56 (2017).
- Y. Zhan, L. Mariani, I. Barozzi, E. G. Schulz, N. Blüthgen, M. Stadler, G. Tian, L. Giorgetti, Reciprocal insulation analysis of Hi-C data shows that TADs represent a functionally but not structurally privileged scale in the hierarchical folding of chromosomes. *Genome Res.* **27**, 479–490 (2017).
- B. Bonev, N. Mendelson Cohen, Q. Szabo, L. Fritsch, G. L. Papadopoulos, Y. Lubling, X. Xu, X. Lv, J.-P. Hugnot, A. Tanay, G. Cavalli, Multiscale 3D genome rewiring during mouse neural development. *Cell* **171**, 557–572.e24 (2017).
- D. G. Lupiáñez, K. Kraft, V. Heinrich, P. Krawitz, F. Brancati, E. Klopocki, D. Horn, H. Kayserili, J. M. Opitz, R. Laxova, F. Santos-Simarro, B. Gilbert-Dussardier, L. Wittler, M. Borschiwer, S. A. Haas, M. Osterwalder, M. Franke, B. Timmermann, J. Hecht, M. Spielmann, A. Visel, S. Mundlos, Disruptions of topological chromatin domains cause pathogenic rewiring of gene-enhancer interactions. *Cell* **161**, 1012–1025 (2015).
- I. M. Flyamer, J. Gassler, M. Imakaev, H. B. Brandão, S. V. Ulianov, N. Abdennur, S. V. Razin, L. A. Mirny, K. Tachibana-Konwalski, Single-nucleus Hi-C reveals unique chromatin reorganization at oocyte-to-zygote transition. *Nature* **544**, 110–114 (2017).
- T. Nagano, Y. Lubling, T. J. Stevens, S. Schoenfelder, E. Yaffe, W. Dean, E. D. Laue, A. Tanay, P. Fraser, Single-cell Hi-C reveals cell-to-cell variability in chromosome structure. *Nature* **502**, 59–64 (2013).
- T. Nagano, Y. Lubling, C. Várnai, C. Dudley, W. Leung, Y. Baran, N. Mendelson Cohen, S. Wingett, P. Fraser, A. Tanay, Cell-cycle dynamics of chromosomal organization at single-cell resolution. *Nature* **547**, 61–67 (2017).
- D. I. Cattoni, A. M. Cardozo Gizzi, M. Georgieva, M. Di Stefano, A. Valeri, D. Chamousset, C. Houbroun, S. Déjardin, J. B. Fiche, I. González, J. M. Chang, T. Sexton, M. A. Marti-Renom, F. Bantignies, G. Cavalli, M. Nollmann, Single-cell absolute contact probability detection reveals chromosomes are organized by multiple low-frequency yet specific interactions. *Nat. Commun.* **8**, 1753 (2017).
- Y. Markaki, D. Smeets, S. Fiedler, V. J. Schmid, L. Schermelleh, T. Cremer, M. Cremer, The potential of 3D-FISH and super-resolution structured illumination microscopy for studies of 3D nuclear architecture: 3D structured illumination microscopy of defined chromosomal structures visualized by 3D (immuno)-FISH opens new perspectives for studies of nuclear architecture. *Bioessays* **34**, 412–426 (2012).
- T. Nozaki, R. Imai, M. Tanbo, R. Nagashima, S. Tamura, T. Tani, Y. Joti, M. Tomita, K. Hibino, M. T. Kanemaki, K. S. Wendt, Y. Okada, T. Nagai, K. Maeshima, Dynamic organization of chromatin domains revealed by super-resolution live-cell imaging. *Mol. Cell* **67**, 282–293.e7 (2017).
- A. N. Boettiger, B. Bintu, J. R. Moffitt, S. Wang, B. J. Beliveau, G. Fudenberg, M. Imakaev, L. A. Mirny, C.-t. Wu, X. Zhuang, Super-resolution imaging reveals distinct chromatin folding for different epigenetic states. *Nature* **529**, 418–422 (2016).
- B. J. Beliveau, A. N. Boettiger, M. S. Avendaño, R. Jungmann, R. B. McCole, E. F. Joyce, C. Kim-Kiselak, F. Bantignies, C. Y. Fonseka, J. Erceg, M. A. Hannan, H. G. Hoang, D. Colognori, J. T. Lee, W. M. Shih, P. Yin, X. Zhuang, C.-t. Wu, Single-molecule super-resolution imaging of chromosomes and in situ haplotype visualization using Oligopaint FISH probes. *Nat. Commun.* **6**, 7147 (2015).
- J. Demmerle, C. Innocent, A. J. North, G. Ball, M. Müller, E. Miron, A. Matsuda, I. M. Dobbie, Y. Markaki, L. Schermelleh, Strategic and practical guidelines for successful structured illumination microscopy. *Nat. Protoc.* **12**, 988–1010 (2017).
- M. G. L. Gustafsson, L. Shao, P. M. Carlton, C. J. R. Wang, I. N. Golubovskaya, W. Z. Cande, D. A. Agard, J. W. Sedat, Three-dimensional resolution doubling in wide-field fluorescence microscopy by structured illumination. *Biophys. J.* **94**, 4957–4970 (2008).
- J. A. Kassis, J. L. Brown, Polycomb group response elements in *Drosophila* and vertebrates. *Adv. Genet.* **81**, 83–118 (2013).
- B. A. Edgar, P. H. O'Farrell, The three postblastoderm cell cycles of *Drosophila* embryogenesis are regulated in G2 by *string*. *Cell* **62**, 469–480 (1990).
- V. Roukos, G. Pegoraro, T. C. Voss, T. Misteli, Cell cycle staging of individual cells by fluorescence microscopy. *Nat. Protoc.* **10**, 334–348 (2015).
- K. P. Eagen, T. A. Hartl, R. D. Kornberg, Stable chromosome condensation revealed by chromosome conformation capture. *Cell* **163**, 934–946 (2015).
- I. Williamson, S. Berlivet, R. Eskeland, S. Boyle, R. S. Illingworth, D. Paquette, J. Dostie, W. A. Bickmore, Spatial genome organization: Contrasting views from chromosome conformation capture and fluorescence in situ hybridization. *Genes Dev.* **28**, 2778–2791 (2014).
- M. Heilemann, S. van de Linde, M. Schüttelpelz, R. Kasper, B. Seefeldt, A. Mukherjee, P. Tinnefeld, M. Sauer, Subdiffraction-resolution fluorescence imaging with conventional fluorescent probes. *Angew. Chem. Int. Ed. Engl.* **47**, 6172–6176 (2008).
- M. J. Rust, M. Bates, X. Zhuang, Sub-diffraction-limit imaging by stochastic optical reconstruction microscopy (STORM). *Nat. Methods* **3**, 793–796 (2006).
- L. Giorgetti, R. Galupa, E. P. Nora, T. Piolot, F. Lam, J. Dekker, G. Tian, E. Heard, Predictive polymer modeling reveals coupled fluctuations in chromosome conformation and transcription. *Cell* **157**, 950–963 (2014).
- J. D. Olarte-Plata, N. Haddad, C. Vaillant, D. Jost, The folding landscape of the epigenome. *Phys. Biol.* **13**, 026001 (2016).
- A. H. Wani, A. N. Boettiger, P. Schorderet, A. Ergun, C. Münger, R. I. Sadreyev, X. Zhuang, R. E. Kingston, N. J. Francis, Chromatin topology is coupled to Polycomb group protein subnuclear organization. *Nat. Commun.* **7**, 10291 (2016).
- C. B. Hug, A. G. Grimaldi, K. Kruse, J. M. Vaquerizas, Chromatin architecture emerges during zygotic genome activation independent of transcription. *Cell* **169**, 216–228.e19 (2017).
- F. Bantignies, G. Cavalli, Topological organization of *Drosophila* Hox genes using DNA fluorescent in situ hybridization. *Methods Mol. Biol.* **1196**, 103–120 (2014).
- G. Ball, J. Demmerle, R. Kaufmann, I. Davis, I. M. Dobbie, L. Schermelleh, SIMcheck: A toolbox for successful super-resolution structured illumination microscopy. *Sci. Rep.* **5**, 15915 (2015).
- J.-B. Fiche, D. I. Cattoni, N. Diekmann, J. M. Langerak, C. Clerte, C. A. Royer, E. Margeat, T. Doan, M. Nöllmann, Recruitment, assembly, and molecular architecture of the SpoIIIE DNA pump revealed by superresolution microscopy. *PLoS Biol.* **11**, e1001557 (2013).
- D. I. Cattoni, J.-B. Fiche, A. Valeri, T. Mignot, M. Nöllmann, Super-resolution imaging of bacteria in a microfluidics device. *PLoS ONE* **8**, e76268 (2013).

42. B. Schuettengruber, N. Oded Elkayam, T. Sexton, M. Entrevan, S. Stern, A. Thomas, E. Yaffe, H. Parrinello, A. Tanay, G. Cavalli, Cooperativity, specificity, and evolutionary stability of Polycomb targeting in *Drosophila*. *Cell Rep.* **9**, 219–233 (2014).
43. B. Zhang, P. G. Wolynes, Topology, structures, and energy landscapes of human chromosomes. *Proc. Natl. Acad. Sci. U.S.A.* **112**, 6062–6067 (2015).
44. S. Hayashi, Male-specific GFP marker strain of *Drosophila melanogaster*. *Dros. Inf. Serv.* **93**, 224–225 (2010).

Acknowledgments: We thank H. Hoang, B. Beliveau, M. Hannan, and C.-T. Wu for help in the design of Oligopaints and for the 3-Mb Oligopaint probe. We thank the Montpellier Resources Imagerie facility (BioCampus Montpellier, CNRS, INSERM, Université de Montpellier) for microscopy support, especially J. Mateos-Langerak for help in SIM and J. Cau and A. Sarrazin for image analysis. We thank MGX sequencing and *Drosophila* facilities (BioCampus Montpellier, CNRS, INSERM, Université de Montpellier). We thank the Genotoul bioinformatics facility Toulouse Midi-Pyrenees (Bioinfo Genotoul) for providing computing and storage resources. We thank B. de Massy for critical reading of the manuscript. **Funding:** Q.S. was supported by the French Ministry of Higher Education and Research. J.-M.C. was supported by the Taiwan Ministry of Science and Technology (MOST 105-2218-E-004-003 and MOST 106-2221-E-004-011-MY2). B.B. was supported by Sir Henry Wellcome Postdoctoral Fellowship WT100136MA. Research in the laboratory of M.N. is funded by the European Research Council (ERC) under the European Union's Horizon 2020 research and innovation programme (grant agreement no. 724429) and by France-BioImaging (ANR-10-INBS-04-01). Research in the laboratory of D.J. was supported by the CIMENT infrastructure (supported by the Rhône-Alpes region, grant CPER07 13 CIRA) for computing resources, the Agence Nationale de la Recherche (ANR-15-CE12-0006 EpiDevoMath), the Fondation pour la Recherche Médicale (DEI20151234396), and the CNRS. F.B. was supported by CNRS and the Fulbright Visiting

Program of the French-American Commission. Research in the laboratory of G.C. was supported by grants from the ERC (ERC-2008-AdG No 232947), the CNRS, the FP7 European Network of Excellence EpiGeneSys, the European Union's Horizon 2020 research and innovation programme under grant agreement no. 676556 (MuG), the Agence Nationale de la Recherche (ANR-15-CE12-0006 EpiDevoMath), the Fondation pour la Recherche Médicale (DEI20151234396), the INSERM, the French National Cancer Institute (INCa), and the Laboratory of Excellence EpiGenMed. **Author contributions:** Q.S., F.B., and G.C. initiated and led the project. Q.S. and F.B. designed Oligopaint probes. Q.S. produced FISH probes and performed FISH experiments, 3D-SIM and confocal microscopy acquisition, and image analysis. Q.S. performed Hi-C experiments in S2R+ cells. D.J. performed polymer modeling and analysis. J.-M.C. performed Hi-C bioinformatics analysis. D.I.C., J.G., and M.N. performed dSTORM imaging and analysis. B.B. and G.L.P. provided help analyzing Hi-C. T.S. and C.J. performed WT and *ph* null mutant embryo Hi-C experiments. F.B. performed fly handling. Q.S., F.B., and G.C. interpreted the data. Q.S., F.B., T.S., and G.C. wrote the paper. All the authors reviewed and discussed the data. **Competing interests:** The authors declare that they have no competing interests. **Data and materials availability:** All data needed to evaluate the conclusions in the paper are present in the paper and/or the Supplementary Materials. Additional data related to this paper may be requested from the authors.

Submitted 19 December 2017

Accepted 30 January 2018

Published 28 February 2018

10.1126/sciadv.aar8082

Citation: Q. Szabo, D. Jost, J.-M. Chang, D. I. Cattoni, G. L. Papadopoulos, B. Bonev, T. Sexton, J. Gurgo, C. Jacquier, M. Nollmann, F. Bantignies, G. Cavalli, TADs are 3D structural units of higher-order chromosome organization in *Drosophila*. *Sci. Adv.* **4**, eaar8082 (2018).

TADs are 3D structural units of higher-order chromosome organization in *Drosophila*

Quentin Szabo, Daniel Jost, Jia-Ming Chang, Diego I. Cattoni, Giorgio L. Papadopoulos, Boyan Bonev, Tom Sexton, Julian Gurgo, Caroline Jacquier, Marcelo Nollmann, Frédéric Bantignies and Giacomo Cavalli

Sci Adv 4 (2), eaar8082.
DOI: 10.1126/sciadv.aar8082

ARTICLE TOOLS	http://advances.sciencemag.org/content/4/2/eaar8082
SUPPLEMENTARY MATERIALS	http://advances.sciencemag.org/content/suppl/2018/02/26/4.2.eaar8082.DC1
REFERENCES	This article cites 44 articles, 5 of which you can access for free http://advances.sciencemag.org/content/4/2/eaar8082#BIBL
PERMISSIONS	http://www.sciencemag.org/help/reprints-and-permissions

Use of this article is subject to the [Terms of Service](#)

Science Advances (ISSN 2375-2548) is published by the American Association for the Advancement of Science, 1200 New York Avenue NW, Washington, DC 20005. The title *Science Advances* is a registered trademark of AAAS.

Copyright © 2018 The Authors, some rights reserved; exclusive licensee American Association for the Advancement of Science. No claim to original U.S. Government Works. Distributed under a Creative Commons Attribution NonCommercial License 4.0 (CC BY-NC).

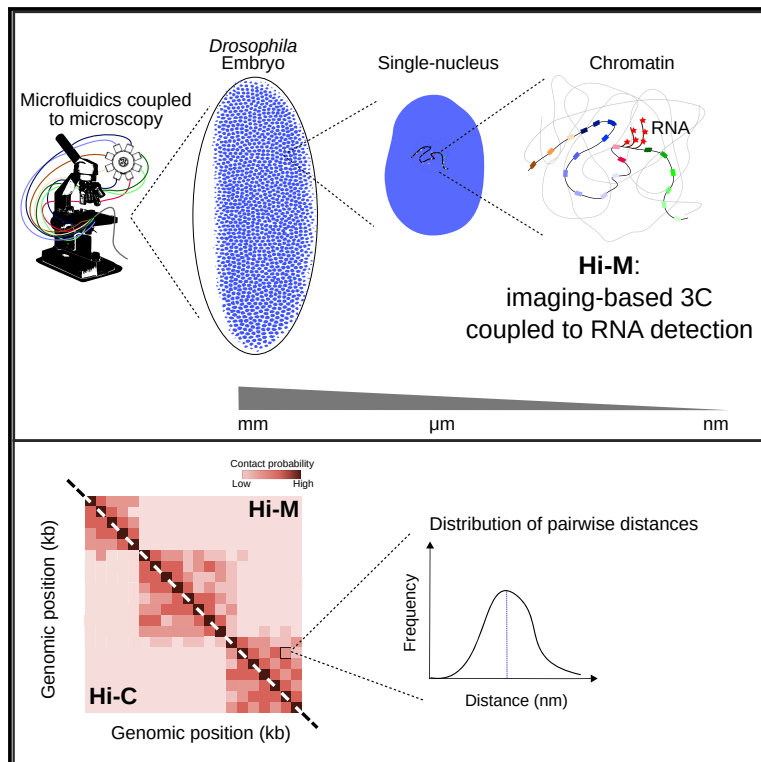
5.2 Microscopy-Based Chromosome Conformation Capture Enables Simultaneous Visualization of Genome Organization and Transcription in Intact Organisms

In this work, we present our recently developed imaging technique, Microscopy-Based Chromosome Conformation Capture (Hi-M). We applied the technique to study the relation between gene expression and TAD architecture, combining sequential hybridization of fluorescent probes and RNA labelling. We show that TADs in cells where the genes are active display a different architecture than those in cells where the genes are not transcribing. We also revealed that paired and unpaired chromosomes have equivalent architectures, but unpaired chromosomes have a more decompacted folding. In this work, I contributed first by performing tests (mainly embryos attachment and drift correction strategies), tuning and modifying protocols (embryos attachment, labeling protocol to improve efficiency) and performing controls (test experiments) that helped to the development of the technique. After this, I contributed to data acquisition, performing embryo labeling and part of the acquisitions in early NC14 embryos. All of this work was done with Andrés Cardozo-Gizzi, Sergio Espinola, Olivier Messina, Christophe Houbron and Jean-Bernard Fiche, under the supervision of Marcelo Nollmann. Then, I analysed the data obtained, together with Andrés Cardozo-Gizzi. I also took care of fly handling and embryo collection, together with Olivier Messina. The work in this paper allowed me to be involved in all stages of Hi-M experiments, from embryo collection to image analysis. My work was done under the supervision of Diego Cattoni and Marcelo Nollmann.

Molecular Cell

Microscopy-Based Chromosome Conformation Capture Enables Simultaneous Visualization of Genome Organization and Transcription in Intact Organisms

Graphical Abstract



Authors

Andrés M. Cardozo Gizzi,
Diego I. Cattoni,
Jean-Bernard Fiche, ...,
Giacomo Cavalli, Mounia Lagha,
Marcelo Nollmann

Correspondence

marcelo.nollmann@cbs.cnrs.fr

In Brief

Cardozo Gizzi et al. developed Hi-M, a multiplexed imaging-based approach to detect 3D chromatin folding in single cells within intact *Drosophila* embryos. The ability of Hi-M to detect the spatial organization of cells enabled measurement of changes in TAD organization during early embryogenesis and upon transcriptional activation.

Highlights

- Hi-M simultaneously reveals 3D chromatin organization and transcriptional activity
- Hi-M and Hi-C maps agree across several orders of magnitude
- Chromatin is spatially compacted into TADs after the midblastula transition
- TAD internal organization dramatically changes upon transcriptional activation



Cardozo Gizzi et al., 2019, *Molecular Cell* 74, 212–222
April 4, 2019 © 2019 Elsevier Inc.
<https://doi.org/10.1016/j.molcel.2019.01.011>

CellPress

Microscopy-Based Chromosome Conformation Capture Enables Simultaneous Visualization of Genome Organization and Transcription in Intact Organisms

Andrés M. Cardozo Gizzi,^{1,4} Diego I. Cattoni,¹ Jean-Bernard Fiche,¹ Sergio M. Espinola,¹ Julian Gurgo,¹ Olivier Messina,¹ Christophe Houbbron,¹ Yuki Ogiyama,² Giorgio L. Papadopoulos,² Giacomo Cavalli,² Mounia Lagha,³ and Marcelo Nollmann^{1,5,*}

¹Centre de Biochimie Structurale, CNRS UMR 5048, INSERM U1054, Université de Montpellier, 60 rue de Navacelles, 34090 Montpellier, France

²Institut de Génétique Humaine, CNRS UMR 9002, Université de Montpellier, 141 rue de la Cardonille, 34396 Montpellier, France

³Institut de Génétique Moléculaire de Montpellier, CNRS UMR 5535, Université de Montpellier, 1919 Route de Mende, 34293 Montpellier, France

⁴Present address: CIQUIBIC (CONICET) – Departamento de Química Biológica Ranwel Caputto, Facultad de Ciencias Químicas, Universidad Nacional de Córdoba, Haya de la Torre y Medina Allende, Ciudad Universitaria, 5000 Córdoba, Argentina

⁵Lead Contact

*Correspondence: marcelo.nollmann@cbs.cnrs.fr

<https://doi.org/10.1016/j.molcel.2019.01.011>

SUMMARY

Eukaryotic chromosomes are organized in multiple scales, from nucleosomes to chromosome territories. Recently, genome-wide methods identified an intermediate level of chromosome organization, topologically associating domains (TADs), that play key roles in transcriptional regulation. However, these methods cannot directly examine the interplay between transcriptional activation and chromosome architecture while maintaining spatial information. Here we present a multiplexed, sequential imaging approach (Hi-M) that permits simultaneous detection of chromosome organization and transcription in single nuclei. This allowed us to unveil the changes in 3D chromatin organization occurring upon transcriptional activation and homologous chromosome unpairing during awakening of the zygotic genome in intact *Drosophila* embryos. Excitingly, the ability of Hi-M to explore the multi-scale chromosome architecture with spatial resolution at different stages of development or during the cell cycle will be key to understanding the mechanisms and consequences of the 4D organization of the genome.

INTRODUCTION

The study of chromosome organization and transcriptional regulation has recently been revolutionized by the advent of genome-wide sequencing methods. In particular, chromosome conformation capture technologies such as Hi-C have revealed that eukaryotic chromosomes are organized into topologically associating domains (Dixon et al., 2012; Nora et al., 2012; Sexton et al., 2012) that can interact to form active or repressed com-

partments (Dixon et al., 2015; Lieberman-Aiden et al., 2009). Importantly, disruption of topologically associating domain (TAD) architecture leads to developmental pathologies and disease because of improper gene regulation (Dixon et al., 2016; Hnisz et al., 2016; Spielmann et al., 2018). Thus, determining the role of chromatin architecture in gene regulation has become a key issue in the fields of chromatin biology and transcription.

Recently, single-cell Hi-C and imaging studies showed that chromosomal contacts within and between TADs are highly stochastic and occur at surprisingly low frequencies (Cattoni et al., 2017; Flyamer et al., 2017; Nagano et al., 2017; Stevens et al., 2017). The origin of these heterogeneities has been unclear and may arise from multiple sources, such as variations in transcriptional and/or epigenetic state between cells in multicellular organisms or in cell cultures. Up until now, it has been difficult to detect the origin of these variations because methods that are able to detect transcriptional output and chromosome organization simultaneously at the single-cell level and in the context of an organism have been lacking. In part, this is due to the loss of spatial information in sequencing-based methods.

The study of chromatin architecture and organization by microscopy is limited by several factors. In conventional fluorescence *in situ* hybridization (FISH), the number of spectrally distinguishable fluorophores in standard microscopes limits the maximum number of genomic loci that can be simultaneously imaged (usually less than 4). In addition, FISH probes are typically large (>10 kb) and difficult to construct, at least in large numbers. These limitations impose an upper limit on the genomic coverage achievable by FISH. Newly developed, low-cost, high-efficiency, on-chip DNA synthesis for high-coverage oligopaint FISH have been used to directly label and image entire TADs (Beliveau et al., 2015; Boettiger et al., 2016; Szabo et al., 2018) and TAD borders (Cattoni et al., 2017). These technologies have recently been combined with multiplexed sequential optical imaging to detect hundreds of individual RNA species while still maintaining spatial information (Chen et al., 2015; Eng et al., 2017; Moffitt et al., 2016; Shah et al., 2018) as well as to visualize



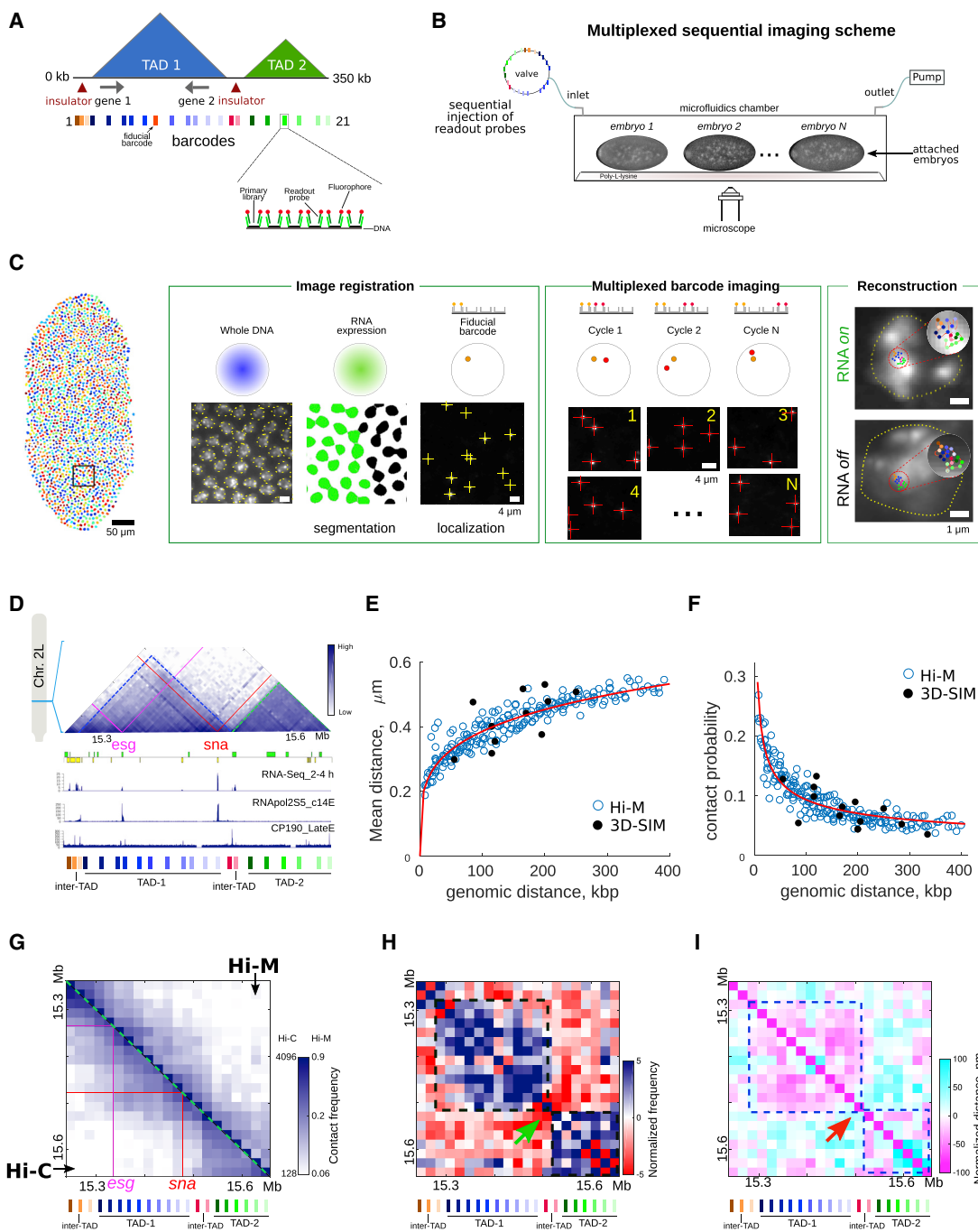


Figure 1. Hi-M Enables Exploration of Chromosome Structure in Single Cells in Intact Organisms with High Genomic Coverage and High Spatial Resolution

(A) Schematic representations of an example locus and the labeling strategy. TADs are depicted as a blue or green triangle, genes as arrows, and insulators as red triangles. Bar codes are indicated as rectangles with a color code following their genomic location. Inset: each bar code is composed of multiple short oligo-nucleotides with a genome homology region (black), a region for secondary oligo binding (light green), and a fluorescent readout probe (dark green and red).

(B) Schematic representation of the Hi-M setup. A robotic multi-color, 3D wide-field imaging system was coupled to an automatic fluid-handling device (see main text and STAR Methods). Multiplexed bar code imaging is achieved by injecting readout probes sequentially (depicted as colored rectangles). Within the microfluidics chamber, *Drosophila* embryos are attached to a poly-lysine-treated coverslip.

(C) Acquisition and analysis Hi-M imaging pipeline (see Figures S1A–S1C for more details). An entire embryo is shown; each nucleus is represented by a different color (left). Image registration phase: each nucleus in a field of view is segmented based on DAPI staining (left). Next, masks were classified according to RNA expression levels as expressing (green) or not expressing (black; middle). Fiducial bar codes are imaged, segmented, and localized (right). Multiplexed bar code

(legend continued on next page)

the segregation of TADs into chromosome territories (Wang et al., 2016). These methods, however, lack the genomic resolution to detect TADs and to correlate them with transcriptional activity in the context of intact tissues or organisms.

DESIGN

To overcome these limitations, we introduce a high-throughput, high-resolution, high-coverage, microscopy-based technology (Hi-M) capable of simultaneously detecting RNA expression and 3D chromatin organization at the single-cell level with nanometer and kilobase resolutions in intact *Drosophila melanogaster* embryos.

Hi-M microscopy relies on the sequential labeling and imaging of multiple DNA loci in genomic regions spanning hundreds of kilobases (kb). DNA was labeled using oligopaint technologies (Beliveau et al., 2012, 2015). A primary library containing thousands of oligonucleotides targeting multiple genomic loci was designed and produced by high-throughput DNA synthesis (STAR Methods). The subset of oligonucleotides targeting each genomic locus (hereafter called bar code) contained unique tails with specific sequences that could be independently read by complementary, fluorescently labeled oligonucleotide probes (hereafter called readout probes; Figures 1A and S1A). An additional bar code (hereafter called fiducial bar code), visible in all rounds of hybridization, was used for image registration and drift correction (STAR Methods).

Bar codes were imaged using a robotic, fully automated, four-color microscope coupled to an automated microfluidics system (Figure S1B). The imaging registration phase involved the acquisition of four-channel, 3D images of each entire embryo in the chamber to identify embryonic morphology (bright field), nuclei by DAPI staining (blue channel), and RNA expression patterns (green channel) and detect the positions of fiducial bar codes (yellow channel) (STAR Methods; Figures 1C and S1C). Next we

performed multiple sequential cycles of hybridization, washing, and imaging of each bar code using a dedicated fluid-handling system (Figures 1B and 1C; STAR Methods). For each hybridization cycle, we performed 3D, two-color imaging of readout probes and fiducial bar codes (Figures 1C and S1A–S1C; STAR Methods). Sample drift during acquisition was corrected using the fiducial bar code (Figures S1D and S1E; STAR Methods). A custom-made analysis pipeline was developed for semi-automated image processing and analysis (STAR Methods).

RESULTS

Hi-M Enables Visualization of Chromosome Structure with High Coverage and High Resolution

We applied Hi-M to study chromosome organization during early *Drosophila* development at the time of zygotic genome activation (ZGA). For this purpose, we initially focused on a genomic locus containing the snail (*sna*) and escargot (*esg*) genes, which are among the ~100 genes expressed during the first wave of ZGA as early as stage 4 (nuclear cycle [nc] 10–13) (Chen et al., 2013). The *Sna* and *esg* genes encode zinc-finger transcription factors, essential for a variety of processes such as gastrulation, neuroblast specification, and stem cell maintenance (Ashraf et al., 1999; Korzelius et al., 2014). In nc 14, the genomic locus encompassing these genes folds into a well-defined TAD (Ogiyama et al., 2018) demarcated by two borders containing class I insulators (CCCTC binding factor [CTCF], Beaf-32, and CP190) (Nègre et al., 2010) and housekeeping genes (Figure 1D). To study the 3D organization of this locus by Hi-M, we designed an oligopaint library covering the whole locus with an average distance between bar codes of 17 kb (Figure 1D). This primary library consisted of ~2,000 different 142-bp oligonucleotides targeting 22 loci around *sna* (21 bar codes and a fiducial bar code).

We performed Hi-M experiments on the *sna-esg* locus in *Drosophila* embryos in nc 14. Dozens of embryos were attached

imaging phase: readout probes are sequentially injected, imaged, segmented, and localized. Reconstruction phase: after drift correction, the 3D positions of all bar codes were retrieved for each nucleus in the embryo. Scale bars are indicated in the figure.

(D) Hi-C map of nc 14 *Drosophila* embryos for the region 2L:15.250–15.650 Mb, indicating normalized contact probability with a scale going from white (low) to blue (high) (Ogiyama et al., 2018). TADs detected by Hi-C (TAD-1 and TAD-2) are delineated with blue and green dotted lines, respectively. *esg* and *sna* are indicated by magenta and red lines, respectively. Normalized counts are color-coded according to scale bar. Bottom: genes, RNA-seq from embryos 2–4 h of development, ChIP-seq from phospho Pol II (S5) from nc 14 embryos, and ChIP-seq against CP190. Genomic positions of bar codes are represented as in (A). (E and F) Mean physical distance (E) and absolute contact probability (F) versus genomic distance from Hi-M (blue circles). Black filled circles are data points from our previous study, where we performed pairwise measurements in *Drosophila* embryo cells in a different locus using 3D-structured illumination microscopy (Cattoni et al., 2017). Solid red lines depict a power-law fit with the scaling exponents. $\beta = 0.23 \pm 0.02$ in (E) and $\alpha = -0.4 \pm 0.02$ in (F). $n = 6,643$.

(G) Hi-M map and interpolated Hi-C matrix from nc 14 wild-type embryos spanning the ~400-kb region encompassing *sna* and *esg*. Bar codes are represented as in (A). *esg* and *sna* are indicated by magenta and red lines, respectively. Features observed in Hi-C at the interpolated resolution and at 5-kb resolution are equivalent (Figure S1J). Relative (Hi-C) and absolute (Hi-M) contact frequencies are color-coded according to the scale bar. We estimate the absolute contact probability, as described previously (Cattoni et al., 2017), by integrating the area of the pairwise distance distribution below 120 nm. This threshold value was chosen from the integration of the pairwise distance distribution of a doubly labeled locus. A good correlation between Hi-M replicates was found (Pearson correlation = 0.92; Figure S1J). $n = 6,643$.

(H) Normalized Hi-M contact maps from nc 14 wild-type *Drosophila* embryos. Normalization is achieved by dividing observed versus expected contact frequencies for equivalent genomic distance. The expected contact frequency is obtained from the fit in (F). The color scale on the right indicates fold enrichment in log scale (positive, blue; negative, red; white, equal). Green arrows indicate chromosomal regions with contact frequencies lower than expected. TADs detected by Hi-C are shown with dotted black lines. Bar codes are represented as in (A). $n = 6,643$.

(I) Normalized mean physical distance map from nc 14 wild-type *Drosophila* embryos. Normalization is achieved by subtracting observed and expected distances. The expected distance was obtained from the fit in (E). The color scale indicates distances lower (magenta) or higher (cyan) than expected. Normalized distances are shown in nanometers. The red arrow indicates regions displaying distances higher than expected. TADs detected by Hi-C are shown with dotted black lines. Bar codes are represented as in (A). $n = 6,643$.

See also Figure S1.

to a poly-L-lysine-coated coverslip and mounted into a microfluidics chamber (STAR Methods; Figure 1B). The overall labeling efficiency was over 60% and did not vary considerably between hybridization cycles (Figure S1G). To validate the method, we first measured the mean physical distances and the absolute probability of interaction between any two loci as a function of their genomic distance (Figures 1E and 1F; STAR Methods). These data overlay well with our recent pairwise distance and absolute contact frequency measurements using super-resolution microscopies (Cattoni et al., 2017). Furthermore, there is a good correspondence between replicates, as reflected by similar chromatin polymer properties, contact probabilities, and pairwise distance distributions (Figures S1H–S1J). It is worth noting that a Hi-M dataset provides much larger coverage for both types of measurements while being much less time-consuming (2 days versus ~1 year for the datasets displayed in Figures 1E and 1F).

Next we constructed a contact probability map from our Hi-M dataset and compared it with published Hi-C data interpolated at the bar code positions (Figures 1D and S1K; STAR Methods) from equivalent *Drosophila* embryonic stages (Ogiyama et al., 2018). Hi-C and Hi-M maps are remarkably similar (Figure 1G). Contact frequencies display a high correlation across several orders of magnitude (Figure S1L; Pearson correlation coefficient = 0.91). This high correlation between results from two different methods provides cross-validation for both technologies at the length scales probed in this study. Two clearly distinguishable TADs are visible in this locus for both matrices (TAD-1 and TAD-2; Figure 1G). TAD-1 contains the *sna* and *esg* genes and is separated from TAD-2 by a barrier containing highly expressed housekeeping genes, RNA polymerase II (Pol II), class I insulator proteins, and *Zelda* (Figures 1D and S4D).

To further characterize chromatin organization, we built normalized contact and distance maps implementing a normalization method similar to that performed for Hi-C data (Lieberman-Aiden et al., 2009). Here we normalized contact frequency and mean spatial distance maps to the expected contact frequencies and spatial distances at each genomic distance as predicted by the power-law scaling fits in Figures 1E and 1F. The normalized contact map showed enriched interactions within each of the two TADs detected by genomic methods (Figure 1H, dashed boxes) and depleted interactions at TAD borders (Figure 1H, green arrow). Interestingly, pairwise distances within TADs were smaller than expected, whereas pairwise distances of loci at TAD borders were higher. Thus, the chromatin fiber appears to be condensed within TADs and decondensed at TAD borders (Figure 1I, dashed boxes and red arrows, respectively).

Chromosome Structure in Paired and Unpaired Chromosomes

Drosophila chromosomes display a high degree of homologous pairing in somatic cells (Fung et al., 1998; Joyce et al., 2012). Thus, an important unanswered question is whether chromosome architecture is influenced by pairing. This question cannot be answered by genome-wide methods because they are unable to distinguish between inter- and intra-chromosomal contacts. We took advantage of the capability of Hi-M to discern paired and unpaired homologous chromosomes to compare

chromatin structure in each configuration. From the bar code coordinates in each nucleus, we classified chromosomes as being “paired” when all bar codes in that nucleus are detected not more than once. Instead, a nucleus contains “unpaired” chromosomes when at least one bar code is detected more than once in that nucleus. Using this definition, partially or completely unpaired chromosomes are classified as unpaired (Figure S2A). In our Hi-M data, the frequency of bar code pairing was ~70% for nc 14 nuclei (Figure S2B), in good agreement with previously published results (Bateman and Wu, 2008; Fung et al., 1998). Normalized distance maps and contact matrices for paired and unpaired chromosomes were qualitatively very similar (Figures 2A, S2C, and S2D). To quantitatively compare these two configurations, we performed a multi-scale correlation analysis of Hi-M distance maps (STAR Methods). This analysis revealed that Hi-M matrices are almost identical (correlation = 1) at low resolution and retained a large, although reduced, similarity even at the highest resolution (correlation = 0.6; Figure 2B). This indicates that the overall organization of chromatin into TADs is partially similar in paired and unpaired chromosomes (see discussion in Figure S2E). Consistently with this picture, mean pairwise distances between paired and unpaired chromosomes were highly correlated (Figure 2C). Remarkably, however, pairwise distances in unpaired chromosomes were, in most cases, larger than the corresponding distance for paired chromosomes (Figure 2C). These results suggest that chromatin folding into TADs is similar in paired and unpaired chromosomes but that there is certainly an overall compaction of chromatin upon pairing or decompaction upon unpairing.

Chromosome Organization Changes during the Cell Cycle and Development

Recent genome-wide studies have shown that chromosome organization into TADs changes during the cell cycle (Hug et al., 2017; Nagano et al., 2017; Naumova et al., 2013). To study whether we could observe such changes by microscopy, we performed Hi-M in embryos undergoing mitosis (Figure 3A). We observed that TADs were no longer discernible at this phase of the cell cycle and that the frequency of genomic contacts was almost independent of genomic distance at short scales (<400 kb; Figures 3B–3D and S3D), reflecting a lack of hierarchical organization during mitosis. Overall, these results are in excellent agreement with published Hi-C data (Hug et al., 2017; Nagano et al., 2017; Naumova et al., 2013; Figures 3B and S3A). Normalized distance maps indicate a low correlation between physical and genomic distances (Figure 3D), consistent with irregular, intermingled loops forming a uniform-density, phase-like structure, as proposed previously (Naumova et al., 2013; Nishino et al., 2012).

Next we used Hi-M to investigate whether chromosome organization changed during the mid-blastula transition (MBT) at the onset of the major wave of zygotic transcription occurring at nc 14. For this, we performed Hi-M in embryos in nc 12–13 (pre-MBT) and nc 14 (MBT) (Figures 3E and 3I). Hi-M maps displayed good correspondence with Hi-C maps (Figures 3F, 3G, 3J, and 3K). Notably, TADs emerged at the onset of ZGA (Figures 3G and 3K), consistent with previous Hi-C studies (Figures 3F, 3J, S3B, and S3C; Hug et al., 2017; Ogiyama et al., 2018). Hi-M contact frequencies decayed more dramatically with

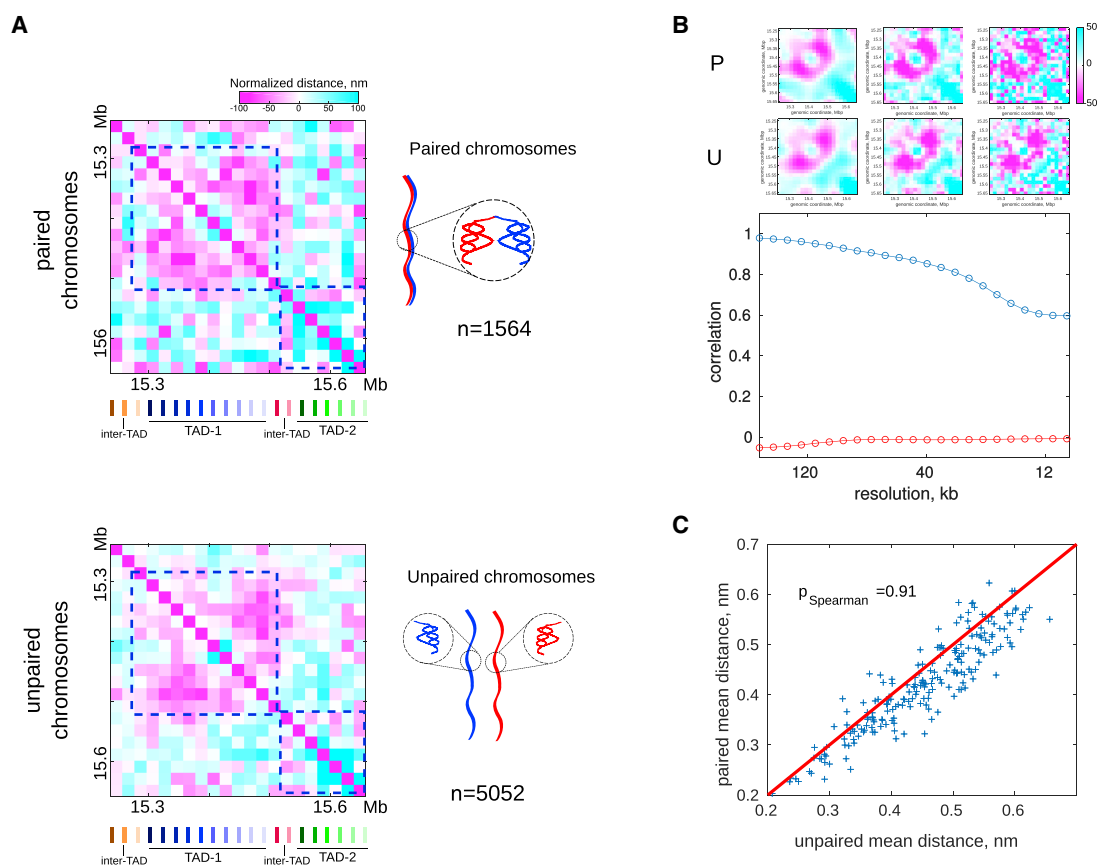


Figure 2. Chromosome Architecture in Unpaired and Paired Homologous Chromosomes

(A) Hi-M normalized distance maps from paired (top) or unpaired (bottom) homologous chromosomes. Normalized distances are color-coded according to scale bar (nm). Bar codes are represented as in Figure 1A. The schematic representation indicates paired and unpaired homologous chromosomes (top and bottom right). Number of examined nuclei: $n = 1,564$ (paired), $n = 5,052$ (unpaired).

(B) Top: Hi-M interpolated normalized distance maps at three different resolutions as examples for paired (P) and unpaired (U) chromosomes. Normalized distances are color-coded according to scale bar (nm). Bottom: multi-scale correlation of Hi-M normalized distance maps for paired and unpaired chromosomes. Blue circles represent the correlation of maps between paired and unpaired chromosomes at different resolutions. Red circles represent the correlation between randomized matrices as a function of resolution. N as in (A).

(C) Paired chromosome mean pairwise distances versus unpaired chromosome mean pairwise distances, represented as blue crosses. The red line represents a slope equal to 1. Note the tendency of unpaired chromosome pairwise distances to be higher than the corresponding ones for paired chromosomes. Pearson correlation coefficient = 0.91. N as in (A).

See also Figure S2.

genomic distance in nc 14 than in previous nuclear cycles, consistent with a change in the overall organization of the chromatin fiber occurring at this stage (Figures S3D–S3F). These local changes in chromatin organization were also clearly seen in normalized mean distance maps, where progressive condensation of chromatin in TADs between nc 12–13 and nc 14 can be observed (Figures 3H and 3L). Next we calculated the coefficient of variation (ratio between SD and mean), a measure of heterogeneity in the cell population. We observed that maps of the coefficient of variation correlate with the emergence of TADs (Figures S3G–S3I). Interestingly, at nc 14 the coefficient of variation was ~ 1 inside TADs, low (~ 0.5) in regions of the map encompassing interactions between TADs, and high (~ 1.5) in gene-rich regions (see the RNA sequencing [RNA-seq] and Pol II profiles in Figure 1D). In contrast, this pattern was disrupted

in early embryos (nc 12–13) or in mitotic cells where TAD architecture was absent (Figures S3G and S3H). Altogether, these results indicate that heterogeneity in chromosome architecture is modulated by structural and functional features of the genome.

Simultaneous Measurement of TAD Organization and Transcriptional Activity in Single Nuclei

Several studies correlating chromosome organization and transcription have suggested that TAD organization changes upon transcriptional activation (Cruz-Molina et al., 2017; Hug et al., 2017; Phanstiel et al., 2017; Stadhouders et al., 2018). However, because of intrinsic limitations in Hi-C technologies, it has been so far impossible to detect chromosome organization and transcriptional state at the same time in single cells. We set out to test whether Hi-M could be adapted to perform this

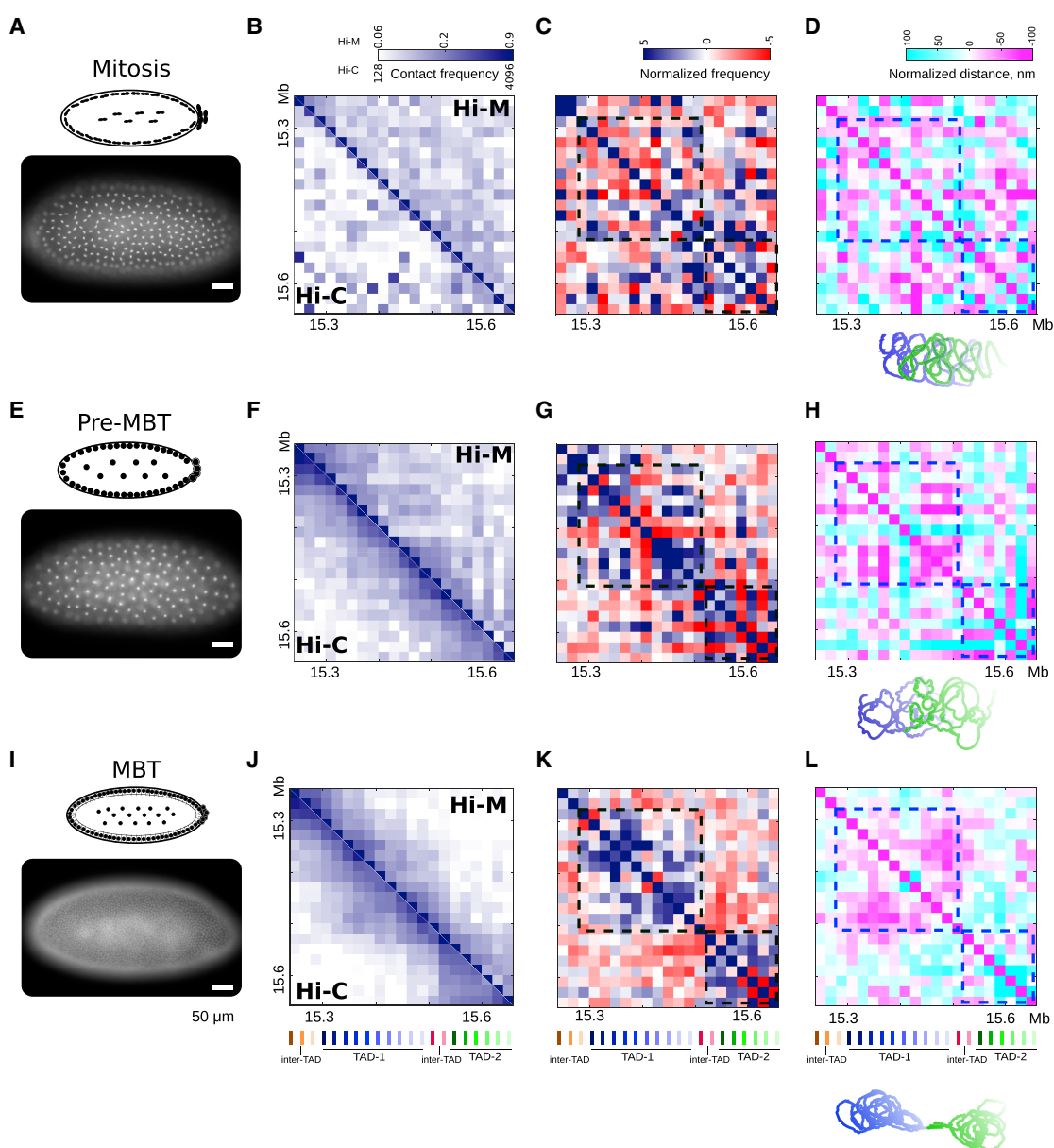


Figure 3. *In Situ* Single-Cell Exploration of Chromosome Conformation during the Cell Cycle and Development

(A, E, and I) Top: schematic representation of an embryo undergoing mitosis (A), nc 9-13 (pre-MBT) (E), and nc 14 (MBT) (I). Bottom: DAPI image of a representative embryo of the corresponding stage. Scale bar, 50 μ m.

(B, F, and J) Hi-M map (top right triangle) and interpolated Hi-C matrix (bottom left triangle) from embryos undergoing mitosis (B), nc 9-13 (pre-MBT) (F), and nc 14 (MBT) (J). Barcodes are represented as in Figure 1A. Features observed in Hi-C at the interpolated resolution and at 5-kb resolution are equivalent (Figure S3A). Relative (Hi-C) and absolute (Hi-M) contact frequencies are color-coded according to the scale bar. Number of examined nuclei: $n = 1,430$ (mitosis), $n = 2,933$ (nc 12-13), $n = 6,643$ (nc 14).

(C, G, and K) Normalized Hi-M contact maps from embryos undergoing mitosis (C), nc 9-13 (pre-MBT) (G), and nc 14 (MBT) (K). The color scale on top is as in Figure 1H. TADs assigned by Hi-C are shown with dotted black lines. Bar codes are represented as in Figure 1A. N as in (B), (F), and (J).

(D, H, and L) Normalized mean physical distance maps from embryos undergoing mitosis (D), nc 9-13 (pre-MBT) (H), and nc 14 (MBT) (L). The color scale on top is as in Figure 1I. TADs observed in nc 14 are delineated with dotted blue lines. Bar codes are represented as in Figure 1A. Schematic representations for each developmental state are shown below the matrices. Blue and green represent the chromatin fiber in each of the two TADs detected by Hi-C. N as in (B), (F), and (J). See also Figure S3.

measurement. For this, we included an RNA labeling step in our imaging pipeline (STAR Methods) that allows us to detect which nuclei in the embryo are transcriptionally active (Figure 4A). Specifically, we labeled and imaged *sna* transcripts in whole embryos and detected their characteristic ventral expression pattern in nc 14 (Alberga et al., 1991; Figure 4A).

Hi-C maps at the *sna* locus contains two TADs (TAD-1 and TAD-2), with TAD-1 displaying looping interactions between regions surrounding *sna* and *esg* (Figure S4A). Surprisingly, TAD-1 could be clearly discerned in nuclei where *sna* was repressed but not in transcriptionally active nuclei (Figures 4B and 4C). These changes are also clearly observed in normalized contact maps (Figure S4B). This observation strongly suggests that chromatin organization into TADs is disrupted by transcriptional activation.

To gain further insight into the structural changes that may underpin this difference in TAD organization, we calculated the normalized median distance maps for *sna*-positive nuclei and for their neighboring inactive nuclei. The patterns of chromatin folding within the largest TAD (containing *sna*) showed clear changes upon *sna* expression (Figures 4D, 4E, and S4C). Strikingly, chromatin structure in the vicinity of *sna* was locally decondensed in nuclei exhibiting active *sna* transcription. In nc 14, the expression patterns of *sna* and *esg* do not overlap in space (Hemavathy et al., 2004). Thus, the local chromatin decondensation in the vicinity of *esg* in nuclei that are not transcribing *sna* is consistent with active *esg* transcription leading to local chromatin decondensation.

Hi-C maps from nc 14 display specific looping interactions between regions surrounding *esg* and *sna* (Figure S4A). However, Hi-C cannot discern whether these contacts depend on the transcriptional status of these genes. Surprisingly, by Hi-M, we observed dramatic changes in the internal organization of TAD-1 upon *sna* activation, with genomic regions around *sna* and *esg* being closer than expected in both active and inactive nuclei (Figures 4D, 4E, and S4B). Exploration of existing chromatin immunoprecipitation sequencing (ChIP-seq) datasets showed that the region surrounding and encompassing these genes is occupied by active (GAF [GAGA-factor], Zelda, CP190) (Blythe and Wieschaus, 2015) as well as inactive marks (polycomb-group proteins, histone 3 lysine 27 tri-methylated [H3K27me3]) (Figure S4D). Thus, we hypothesize that different networks of contacts are responsible for the distinct patterns of interactions visualized by Hi-M in active and inactive nuclei.

DISCUSSION

We developed a new method (Hi-M) based on sequential, multiplexed, high-throughput hybridization and imaging of oligopaint probes to simultaneously visualize chromosome organization and transcriptional activity in single cells while preserving tissue context. We validated our method by comparing our results with existing microscopy and Hi-C datasets and by showing that TADs detected by Hi-M are disrupted during mitosis and emerge at the onset of ZGA during embryonic development. Overall, these experiments strongly support the ability of Hi-M to capture chromosome conformations at the single-cell level under a variety of experimental conditions. In addition, we used Hi-M

to directly show that chromosome pairing leads to general compaction of chromatin without an overall change in TAD organization and that distance distributions within TADs change dramatically upon transcriptional activation.

The degree of pairing between homologous chromosomes in *Drosophila* has been characterized previously (Bateman and Wu, 2008; Cattoni et al., 2017; Fung et al., 1998; Joyce et al., 2012); however, the organization of chromatin within paired or unpaired homologous chromosomes remained inaccessible to conventional microscopy imaging. Hi-M revealed that paired and unpaired chromosomes share equivalent TAD architectural features but that the unpaired chromosomes display less compact folding. Interestingly, during the revision process of this work, a new Hi-C study confirmed our Hi-M predictions for early *Drosophila* embryos, showing the conservation of domains in paired and unpaired chromatin (Erceg et al., 2018).

Upon mitosis, the decrease in insulation at borders leads to loss of chromatin compartmentalization in metazoans (Nagano et al., 2017; Naumova et al., 2013). Hi-M retrieved equivalent results by directly evaluating the absolute frequency of interaction at the single-nucleus level. Moreover, the homogeneous variance distribution of distances (Figure S3G) during mitosis obtained by Hi-M is compatible with the recently proposed model of helical arrangements and nested loops of mitotic chromosomes (Gibcus et al., 2018). Hi-M opens many new possibilities, such as the determination of 3D chromatin architecture at different mitotic stages (prophase, metaphase, and anaphase) to decipher at which of these stages TAD organization is regained and the mechanisms involved in this process.

Early evidence suggesting large-scale chromatin structure changes upon transcriptional activation (Tumbar et al., 1999) has been recently confirmed by genome-wide approaches focusing on genome activation during development (Du et al., 2017; Hug et al., 2017; Ke et al., 2017). Hi-M satisfactorily reproduced previous genome-wide findings of chromosome organization during the zygotic awakening of *Drosophila* and gave additional insight into the organization of chromatin. Particularly, we show that not only changes in the frequency of interaction between loci accompanies gene activation, as suggested previously (Hug et al., 2017), but also full reshaping of the 3D organization of the TAD, compatible with recently proposed models based on kinetic measurements of transcription and local reorganization of chromatin (Chen et al., 2018; Shah et al., 2018).

Excitingly, Hi-M can be widely applied to detecting single-cell chromosome organization and transcription in cultured cells from bacteria to mammals or in multicellular organisms and tissues. We note that a key advantage of our method is that it would also allow the combination of single-nucleus analysis with spatial mapping of the relationship between structure and function (i.e., chromatin architecture and gene expression) in fly embryos and in more complex tissues. Thus, this novel technology has the potential to revolutionize the study of chromosome architecture in many fields and at many different scales.

Limitations

Here we show that Hi-M can simultaneously label ~21 distinct DNA loci. Current developments in liquid-handling technologies are being made to increase this number by about one order of

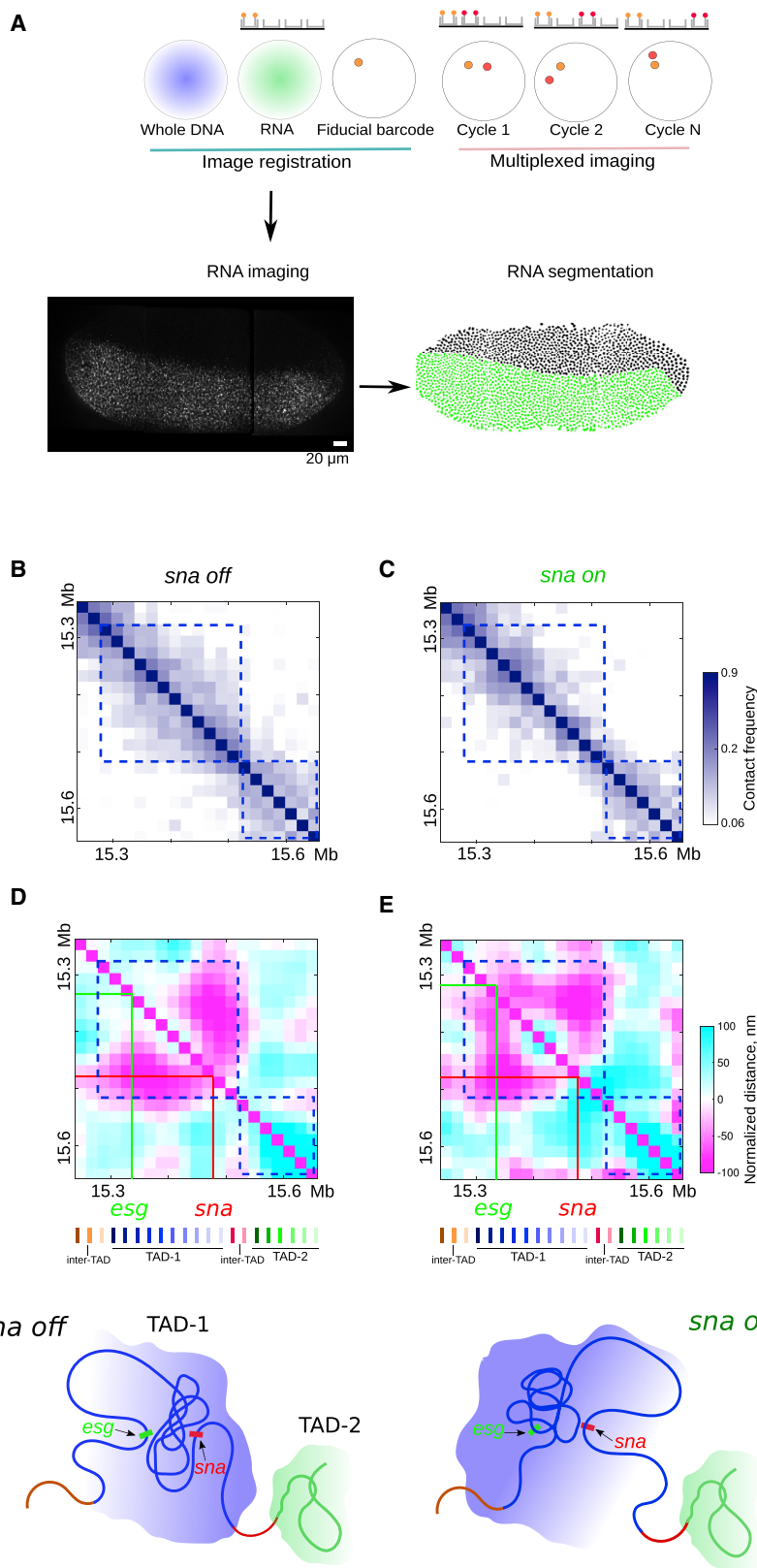


Figure 4. Simultaneous Detection of Chromosome Organization and Transcription by Hi-M

(A) Single-cell RNA expression detection. Top: scheme depicting the Hi-M experimental design. Bottom left: representative full-embryo *sna* RNA image obtained from the image registration step. The image is composed of a mosaic of three fields of view. Scale bar, 20 μ m. Bottom right: result of nucleus segmentation and RNA state assignment for the full embryo. Nuclei expressing *sna* are shown in green, whereas nuclei not expressing *sna* appear in black. For the displayed embryo in the example, 63% of nuclei are expressing *sna*, although this percentage depends on the orientation.

(B and C) Hi-M absolute contact matrices for nuclei expressing (C) or not expressing (B) *sna*. Absolute contact frequency is color-coded according to the scale bar and ranges from 0 to 0.9 (log scale). Bar codes are represented as in Figure 1D. $n = 4,402$ (off nuclei examined) and $n = 2,265$ (on nuclei examined). (D and E) Normalized Hi-M distance maps for nuclei expressing (E) or not expressing (D) *sna*. The color scale indicates distances shorter (magenta) or higher (cyan) than expected (scale in nanometers). Solid lines represent the positions of *sna* and *esg*. Bar codes are colored as in Figure 1A. Bottom: schematic representations of TAD organization in transcriptionally on or off nuclei. TAD-1 is represented in blue and TAD-2 in green. n as in (B) and (C). See also Figure S4.

magnitude, which would allow an overall increase in the size of the region that can be probed by Hi-M in similar timescales. Further optimization of Hi-M will involve simultaneous acquisition of several colors, which would shorten the acquisition time by a factor of 2–3 (Moffitt et al., 2016). Use of combinatorial labeling schemes should make it possible to considerably increase the number of detected DNA loci without increasing the number of hybridization cycles (Chen et al., 2015; Shah et al., 2018).

A second current limitation of Hi-M is that it can detect a single RNA species because it requires the use of digoxigenin-labeled RNA probes. We envision that it should be relatively straightforward to increase the number of RNA species by using orthogonal chemistries (e.g., biotin). This approach, however, will be limited to a few RNA species. To considerably increase the number of detected RNA species will likely require that RNA species are detected prior to DNA detection using adaptations of multiplexed RNA detection protocols (Chen et al., 2015).

A third limitation of Hi-M is the size of probes (currently ~4 kb, 70 primary oligos). We envision that the use of fewer primary oligos (~20–30) should ensure specificity of detection and reduce the size of the probe to ~1.5–2 kb. Further increases in the number of fluorophores per primary oligonucleotide could enable sub-kilobase resolution. It is, however, important to bear in mind that a reduction in probe size will have to be balanced by a reduction in the genomic frequency of probes or by a reduction in the size of the genomic region being probed. The minimal inter-probe distance used in this study was ~10 kb. We note that further reducing the inter-probe distance may require further improvements in localization precision and drift correction. Finally, our current implementation of Hi-M uses wide-field microscopy. This method is ideally suited for detection in early *Drosophila* embryos, where cells are organized in a 2D layer, but not for samples with more complex architectures (such as late-stage embryos). For these architectures, a confocal imaging scheme would be better suited and will be explored in future.

STAR★METHODS

Detailed methods are provided in the online version of this paper and include the following:

- KEY RESOURCES TABLE
- CONTACT FOR REAGENT AND RESOURCE SHARING
- EXPERIMENTAL MODEL AND SUBJECT DETAILS
- METHOD DETAILS
 - *Drosophila* embryo collection
 - Oligopaint libraries
 - RNA-FISH probe preparation
 - RNA-FISH coupled with TSA
 - Hybridization of primary oligopaint library
 - Robotic microscope setup
 - Sequential image acquisition
 - Data processing and image analysis
 - Multiscale correlation of Hi-M distance maps
 - Precision of the method
 - Hi-C and ChIP-Seq data processing
- QUANTIFICATION AND STATISTICAL ANALYSIS
- DATA AND SOFTWARE AVAILABILITY

SUPPLEMENTAL INFORMATION

Supplemental Information includes four figures and four tables and can be found with this article online at <https://doi.org/10.1016/j.molcel.2019.01.011>.

ACKNOWLEDGMENTS

The authors thank Carola Fernandez for providing the *sna* probe and for the help with RNA labeling experiments. This project has received funding from the European Research Council (ERC) under the European Union's Horizon 2020 Research and Innovation Program (grant ID 724429). This work also benefited from support from Labex EpiGenMed, an "Investments for the Future" program (grant ID ANR-10-LABX-12-01). We acknowledge the France-BioImaging infrastructure supported by the French National Research Agency (grant ID ANR-10-INBS-04, "Investments for the Future"). This work was also supported by an ERC SyncDev starting grant (to M.L.).

AUTHOR CONTRIBUTIONS

A.M.C.G., M.L., and M.N. designed the experiments. A.M.C.G., D.I.C., S.M.E., J.G., and O.M. conducted the experiments. J.-B.F. designed and built the microscopy setup and acquisition software. M.N. developed the software for image analysis. A.M.C.G., J.G., and M.N. analyzed the data. A.M.C.G. and M.N. designed the oligopaint probes. J.G. and O.M. performed fly handling. C.H. synthesized and purified the oligopaint libraries. Y.O., G.L.P., and G.C. performed the Hi-C experiments and analysis. A.M.C.G., D.I.C., G.C., M.L., and M.N. wrote the manuscript. All the authors reviewed and commented on the data.

DECLARATION OF INTERESTS

The authors declare no competing financial interests.

Received: October 5, 2018
 Revised: November 27, 2018
 Accepted: January 8, 2019
 Published: February 19, 2019

REFERENCES

- Alberga, A., Boulay, J.L., Kempe, E., Dennefeld, C., and Haenlin, M. (1991). The snail gene required for mesoderm formation in *Drosophila* is expressed dynamically in derivatives of all three germ layers. *Development* **111**, 983–992.
- Ashraf, S.I., Hu, X., Roote, J., and Ip, Y.T. (1999). The mesoderm determinant snail collaborates with related zinc-finger proteins to control *Drosophila* neurogenesis. *EMBO J.* **18**, 6426–6438.
- Bateman, J.R., and Wu, C.-T. (2008). A genomewide survey argues that every zygotic gene product is dispensable for the initiation of somatic homolog pairing in *Drosophila*. *Genetics* **180**, 1329–1342.
- Beliveau, B.J., Joyce, E.F., Apostolopoulos, N., Yilmaz, F., Fonseka, C.Y., McCole, R.B., Chang, Y., Li, J.B., Senaratne, T.N., Williams, B.R., et al. (2012). Versatile design and synthesis platform for visualizing genomes with Oligopaint FISH probes. *Proc. Natl. Acad. Sci. USA* **109**, 21301–21306.
- Beliveau, B.J., Boettiger, A.N., Avendaño, M.S., Jungmann, R., McCole, R.B., Joyce, E.F., Kim-Kiselak, C., Bantignies, F., Fonseka, C.Y., Erceg, J., et al. (2015). Single-molecule super-resolution imaging of chromosomes and in situ haplotype visualization using Oligopaint FISH probes. *Nat. Commun.* **6**, 7147.
- Blythe, S.A., and Wieschaus, E.F. (2015). Zygotic genome activation triggers the DNA replication checkpoint at the midblastula transition. *Cell* **160**, 1169–1181.
- Boettiger, A.N., Bintu, B., Moffitt, J.R., Wang, S., Beliveau, B.J., Fudenberg, G., Imakaev, M., Mirny, L.A., Wu, C.-T., and Zhuang, X. (2016). Super-resolution imaging reveals distinct chromatin folding for different epigenetic states. *Nature* **529**, 418–422.

- Cattoni, D.I., Cardozo Gizzi, A.M., Georgieva, M., Di Stefano, M., Valeri, A., Chamousset, D., Houbbron, C., Déjardin, S., Fiche, J.-B., González, I., et al. (2017). Single-cell absolute contact probability detection reveals chromosomes are organized by multiple low-frequency yet specific interactions. *Nat. Commun.* **8**, 1753.
- Chen, K., Johnston, J., Shao, W., Meier, S., Staber, C., and Zeitlinger, J. (2013). A global change in RNA polymerase II pausing during the *Drosophila* midblastula transition. *eLife* **2**, e00861.
- Chen, K.H., Boettiger, A.N., Moffitt, J.R., Wang, S., and Zhuang, X. (2015). RNA imaging. Spatially resolved, highly multiplexed RNA profiling in single cells. *Science* **348**, aaa6090.
- Chen, H., Levo, M., Barinov, L., Fujioaka, M., Jaynes, J.B., and Gregor, T. (2018). Dynamic interplay between enhancer-promoter topology and gene activity. *Nat. Genet.* **50**, 1296–1303.
- Cohen, E.A.K., Abraham, A.V., and Ober, R.J. (2017). Resolution limit of image analysis algorithms. *bioRxiv*. <https://doi.org/10.1101/240531>.
- Cruz-Molina, S., Respuela, P., Tebartz, C., Kolovos, P., Nikolic, M., Fueyo, R., van Ijcken, W.F.J., Grosveld, F., Frommolt, P., Bazzi, H., and Rada-Iglesias, A. (2017). PRC2 Facilitates the Regulatory Topology Required for Poised Enhancer Function during Pluripotent Stem Cell Differentiation. *Cell Stem Cell* **20**, 689–705.e9.
- Dixon, J.R., Selvaraj, S., Yue, F., Kim, A., Li, Y., Shen, Y., Hu, M., Liu, J.S., and Ren, B. (2012). Topological domains in mammalian genomes identified by analysis of chromatin interactions. *Nature* **485**, 376–380.
- Dixon, J.R., Jung, I., Selvaraj, S., Shen, Y., Antosiewicz-Bourget, J.E., Lee, A.Y., Ye, Z., Kim, A., Rajagopal, N., Xie, W., et al. (2015). Chromatin architecture reorganization during stem cell differentiation. *Nature* **518**, 331–336.
- Dixon, J.R., Gorkin, D.U., and Ren, B. (2016). Chromatin Domains: The Unit of Chromosome Organization. *Mol. Cell* **62**, 668–680.
- Dobin, A., Davis, C.A., Schlesinger, F., Drenkow, J., Zaleski, C., Jha, S., Batut, P., Chaisson, M., and Gingeras, T.R. (2013). STAR: ultrafast universal RNA-seq aligner. *Bioinformatics* **29**, 15–21.
- Du, Z., Zheng, H., Huang, B., Ma, R., Wu, J., Zhang, X., He, J., Xiang, Y., Wang, Q., Li, Y., et al. (2017). Allelic reprogramming of 3D chromatin architecture during early mammalian development. *Nature* **547**, 232–235.
- Eng, C.L., Shah, S., Thomassie, J., and Cai, L. (2017). Profiling the transcriptome with RNA SPOTS. *Nat. Methods* **14**, 1153–1155.
- Erceg, J., Abed, J.A., Goloborodko, A., Lajoie, B.R., Fudenberg, G., Abdennur, N., Imakaev, M., McCole, R.B., Nguyen, S.C., Saylor, W., et al. (2018). The genome-wide, multi-layered architecture of chromosome pairing in early *Drosophila* embryos. *bioRxiv*. <https://doi.org/10.1101/443028>.
- Flyamer, I.M., Gassler, J., Imakaev, M., Brandão, H.B., Ulianov, S.V., Abdennur, N., Razin, S.V., Mirny, L.A., and Tachibana-Konwalski, K. (2017). Single-nucleus Hi-C reveals unique chromatin reorganization at oocyte-to-zygote transition. *Nature* **544**, 110–114.
- Fung, J.C., Marshall, W.F., Dernburg, A., Agard, D.A., and Sedat, J.W. (1998). Homologous chromosome pairing in *Drosophila melanogaster* proceeds through multiple independent initiations. *J. Cell Biol.* **141**, 5–20.
- Gibcus, J.H., Samejima, K., Goloborodko, A., Samejima, I., Naumova, N., Nuebler, J., Kanemaki, M.T., Xie, L., Paulson, J.R., Earnshaw, W.C., et al. (2018). A pathway for mitotic chromosome formation. *Science* **359**, eaao6135.
- Harrison, M.M., Li, X.-Y., Kaplan, T., Botchan, M.R., and Eisen, M.B. (2011). Zelda binding in the early *Drosophila melanogaster* embryo marks regions subsequently activated at the maternal-to-zygotic transition. *PLoS Genet.* **7**, e1002266.
- Hemavathy, K., Hu, X., Ashraf, S.I., Small, S.J., and Ip, Y.T. (2004). The repressor function of snail is required for *Drosophila* gastrulation and is not replaceable by Escargot or Worniu. *Dev. Biol.* **269**, 411–420.
- Hnisz, D., Weintraub, A.S., Day, D.S., Valton, A.-L., Bak, R.O., Li, C.H., Goldmann, J., Lajoie, B.R., Fan, Z.P., Sigova, A.A., et al. (2016). Activation of proto-oncogenes by disruption of chromosome neighborhoods. *Science* **351**, 1454–1458.
- Hug, C.B., Grimaldi, A.G., Kruse, K., and Vaquerizas, J.M. (2017). Chromatin Architecture Emerges during Zygotic Genome Activation Independent of Transcription. *Cell* **169**, 216–228.e19.
- Joyce, E.F., Williams, B.R., Xie, T., and Wu, C.T. (2012). Identification of genes that promote or antagonize somatic homolog pairing using a high-throughput FISH-based screen. *PLoS Genet.* **8**, e1002667.
- Ke, Y., Xu, Y., Chen, X., Feng, S., Liu, Z., Sun, Y., Yao, X., Li, F., Zhu, W., Gao, L., et al. (2017). 3D Chromatin Structures of Mature Gametes and Structural Reprogramming during Mammalian Embryogenesis. *Cell* **170**, 367–381.e20.
- Koenecke, N., Johnston, J., Gaertner, B., Natarajan, M., and Zeitlinger, J. (2016). Genome-wide identification of *Drosophila* dorso-ventral enhancers by differential histone acetylation analysis. *Genome Biol.* **17**, 196.
- Korzelius, J., Naumann, S.K., Loza-Coll, M.A., Chan, J.S., Dutta, D., Oberheim, J., Gläßer, C., Southall, T.D., Brand, A.H., Jones, D.L., and Edgar, B.A. (2014). Escargot maintains stemness and suppresses differentiation in *Drosophila* intestinal stem cells. *EMBO J.* **33**, 2967–2982.
- Kosman, D., Mizutani, C.M., Lemons, D., Cox, W.G., McGinnis, W., and Bier, E. (2004). Multiplex detection of RNA expression in *Drosophila* embryos. *Science* **305**, 846.
- Lagha, M., Bothma, J.P., Esposito, E., Ng, S., Stefanik, L., Tsui, C., Johnston, J., Chen, K., Gilmour, D.S., Zeitlinger, J., and Levine, M.S. (2013). Paused Pol II coordinates tissue morphogenesis in the *Drosophila* embryo. *Cell* **153**, 976–987.
- Li, X.-Y., Harrison, M.M., Villalta, J.E., Kaplan, T., and Eisen, M.B. (2014). Establishment of regions of genomic activity during the *Drosophila* maternal to zygotic transition. *eLife* **3**.
- Lieberman-Aiden, E., van Berkum, N.L., Williams, L., Imakaev, M., Ragozcy, T., Telling, A., Amit, I., Lajoie, B.R., Sabo, P.J., Dorschner, M.O., et al. (2009). Comprehensive mapping of long-range interactions reveals folding principles of the human genome. *Science* **326**, 289–293.
- Moffitt, J.R., Hao, J., Wang, G., Chen, K.H., Babcock, H.P., and Zhuang, X. (2016). High-throughput single-cell gene-expression profiling with multiplexed error-robust fluorescence in situ hybridization. *Proc. Natl. Acad. Sci. USA* **113**, 11046–11051.
- Nagano, T., Lubling, Y., Várnai, C., Dudley, C., Leung, W., Baran, Y., Mendelson Cohen, N., Wingett, S., Fraser, P., and Tanay, A. (2017). Cell-cycle dynamics of chromosomal organization at single-cell resolution. *Nature* **547**, 61–67.
- Naumova, N., Imakaev, M., Fudenberg, G., Zhan, Y., Lajoie, B.R., Mirny, L.A., and Dekker, J. (2013). Organization of the mitotic chromosome. *Science* **342**, 948–953.
- Nègre, N., Brown, C.D., Shah, P.K., Kheradpour, P., Morrison, C.A., Henikoff, J.G., Feng, X., Ahmad, K., Russell, S., White, R.A.H., et al. (2010). A comprehensive map of insulator elements for the *Drosophila* genome. *PLoS Genet.* **6**, e1000814.
- Nishino, Y., Eltsov, M., Joti, Y., Ito, K., Takata, H., Takahashi, Y., Hihara, S., Frangakis, A.S., Imamoto, N., Ishikawa, T., and Maeshima, K. (2012). Human mitotic chromosomes consist predominantly of irregularly folded nucleosome fibres without a 30-nm chromatin structure. *EMBO J.* **31**, 1644–1653.
- Nora, E.P., Lajoie, B.R., Schulz, E.G., Giorgetti, L., Okamoto, I., Servant, N., Piolot, T., van Berkum, N.L., Meisig, J., Sedat, J., et al. (2012). Spatial partitioning of the regulatory landscape of the X-inactivation centre. *Nature* **485**, 381–385.
- Ogizawa, Y., Schuettengruber, B., Papadopoulos, G.L., Chang, J.-M., and Cavalli, G. (2018). Polycomb-Dependent Chromatin Looping Contributes to Gene Silencing during *Drosophila* Development. *Mol. Cell* **71**, 73–88.e5.
- Phanstiel, D.H., Van Bortle, K., Spacek, D., Hess, G.T., Shamim, M.S., Machol, I., Love, M.I., Aiden, E.L., Bassik, M.C., and Snyder, M.P. (2017). Static and Dynamic DNA Loops form AP-1-Bound Activation Hubs during Macrophage Development. *Mol. Cell* **67**, 1037–1048.e6.
- Schuettengruber, B., Oded Elkayam, N., Sexton, T., Entrevan, M., Stern, S., Thomas, A., Yaffe, E., Parrinello, H., Tanay, A., and Cavalli, G. (2014).

- Cooperativity, specificity, and evolutionary stability of Polycomb targeting in *Drosophila*. *Cell Rep.* **9**, 219–233.
- Sexton, T., Yaffe, E., Kenigsberg, E., Bantignies, F., Leblanc, B., Hoichman, M., Parrinello, H., Tanay, A., and Cavalli, G. (2012). Three-dimensional folding and functional organization principles of the *Drosophila* genome. *Cell* **148**, 458–472.
- Shah, S., Takei, Y., Zhou, W., Lubeck, E., Yun, J., Eng, C.L., Koulana, N., Cronin, C., Karp, C., Liaw, E.J., et al. (2018). Dynamics and Spatial Genomics of the Nascent Transcriptome by Intron seqFISH. *Cell* **174**, 363–376.e16.
- Spielmann, M., Lupiáñez, D.G., and Mundlos, S. (2018). Structural variation in the 3D genome. *Nat. Rev. Genet.* **19**, 453–467.
- Stadhouders, R., Vidal, E., Serra, F., Di Stefano, B., Le Dily, F., Quilez, J., Gomez, A., Collombet, S., Berenguer, C., Cuartero, Y., et al. (2018). Transcription factors orchestrate dynamic interplay between genome topology and gene regulation during cell reprogramming. *Nat. Genet.* **50**, 238–249.
- Stevens, T.J., Lando, D., Basu, S., Atkinson, L.P., Cao, Y., Lee, S.F., Leeb, M., Wohlfahrt, K.J., Boucher, W., O’Shaughnessy-Kirwan, A., et al. (2017). 3D structures of individual mammalian genomes studied by single-cell Hi-C. *Nature* **544**, 59–64.
- Szabo, Q., Jost, D., Chang, J.-M., Cattoni, D.I., Papadopoulos, G.L., Bonev, B., Sexton, T., Gurgo, J., Jacquier, C., Nollmann, M., et al. (2018). TADs are 3D structural units of higher-order chromosome organization in *Drosophila*. *Sci. Adv.* **4**, eaar8082.
- Trcek, T., Lionnet, T., Shroff, H., and Lehmann, R. (2017). mRNA quantification using single-molecule FISH in *Drosophila* embryos. *Nat. Protoc.* **12**, 1326–1348.
- Tumbar, T., Sudlow, G., and Belmont, A.S. (1999). Large-scale chromatin unfolding and remodeling induced by VP16 acidic activation domain. *J. Cell Biol.* **145**, 1341–1354.
- Wang, S., Su, J.-H., Beliveau, B.J., Bintu, B., Moffitt, J.R., Wu, C.-T., and Zhuang, X. (2016). Spatial organization of chromatin domains and compartments in single chromosomes. *Science* **353**, 598–602.
- Zhang, Y., Liu, T., Meyer, C.A., Eeckhoute, J., Johnson, D.S., Bernstein, B.E., Nusbaum, C., Myers, R.M., Brown, M., Li, W., and Liu, X.S. (2008). Model-based analysis of ChIP-Seq (MACS). *Genome Biol.* **9**, R137.

STAR★METHODS

KEY RESOURCES TABLE

REAGENT or RESOURCE	SOURCE	IDENTIFIER
Antibodies		
Anti-Digoxigenin-POD, Fab fragments	Sigma-Aldrich	Cat #11207733910; RRID:AB_514500
Chemicals, Peptides, and Recombinant Proteins		
Alexa Fluor 488 Tyramide Reagent	Invitrogen	Cat#B40953
16% Formaldehyde Solution (w/v), Methanol-free	Thermo Fisher	Cat#28908
Tris(2-carboxyethyl)phosphine hydrochloride	Sigma-Aldrich	Cat#646547
Blocking reagent	Sigma-Aldrich	Cat#11096176001
Hydrogen peroxide	Sigma-Aldrich	Cat#H1009
RNase	Sigma-Aldrich	Cat#R6513
Salmon sperm	Ambion	Cat#AM9680
Heparine	Sigma-Aldrich	Cat##H4784
Deposited Data		
Full pairwise distance distributions for all datasets	This paper	https://doi.org/10.17632/5f5hd9yj3z.1#folder-26d1f8c0-fc58-4b87-8c4f-cd8fa294a555
<i>In situ</i> Hi-C from mitotic embryos	Hug et al., 2017	ArrayExpress:E-MTAB-4918
<i>In situ</i> Hi-C from nc 9-13 embryos	Ogiyama et al., 2018	GEO:GSE103625
<i>In situ</i> Hi-C from nc 14 embryos	Ogiyama et al., 2018	GEO:GSE103625
RNA-seq from 2-4 h embryos	ENCODE Project Consortium	Encode:ENCSR086YVX
ChIP-seq against RNA pol II(S5) from early nc 14 embryos	Blythe and Wieschaus, 2015	GEO:GSE62925
ChIP-seq against RNA pol II(S5) from late nc 14 embryos	Blythe and Wieschaus, 2015	GEO:GSE62925
ChIP-seq against H3K27me3 from nc 14c embryos	Li et al., 2014	GEO:GSE58935
ChIP-seq against H3K27me3 from 14-16 h embryos	Modencode consortium	GEO:GSE47230
ChIP-seq against PH from 14-16 h embryos	Schuettengruber et al., 2014.	GEO:GSE60428
ChIP-seq against PC from 2-4 h embryos	Koenecke et al., 2016	GEO:GSE68983
ChIP-seq against CTCF from 14-16 h embryos	Modencode consortium	GEO:GSE47264
ChIP-seq against CP190 from 14-16 h embryos	Modencode consortium	GEO:GSE47234
SNA_2to4h	Koenecke et al., 2016	GEO:GSE68983
ChIP-seq against Zelda from nc 13 embryos	Harrison et al., 2011	GEO:GSE30757
ChIP-seq against Zelda from nc 14 embryos	Harrison et al., 2011	GEO:GSE30757
ChIP-seq against GAF from 14-16 h embryos	Modencode consortium	GEO:GSE47236
ChIP-seq against GAF from 2-4h embryos	Koenecke et al., 2016	GEO:GSE68983
Experimental Models: Organisms/Strains		
Oregon-R w1118		N/A
Oligonucleotides		
Library amplification primers, BB287-FWD: 5' - CGC TCG GTC TCC GTT CGT CTC T7+BB288-REV: 5' -TAA TAC GAC TCA CTA TAG GGT TGG GCT AGG TAC AGG GTT CAG C	IDT DNA	N/A
Fluorescent oligonucleotides, see Table S3	IDT DNA	N/A
Oligopaint library, see Table S4	Twist Bioscience	N/A
Recombinant DNA		
p190 Plasmid: sna gene cloned in pBluescript II SK (+) vector	Lagha et al., 2013	N/A

(Continued on next page)

Continued

REAGENT or RESOURCE	SOURCE	IDENTIFIER
Software and Algorithms		
Huygens Professional version 18.04	Scientific Volume Imaging https://svi.nl/	N/A
MATLAB Release 2017b	The MathWorks, Inc	N/A
Software for processing microscopy images	This paper; Mendeley Data	https://doi.org/10.17632/5f5hd9yj3z.1#folder-26d1f8c0-fc58-4b87-8c4f-cd8fa294a555

CONTACT FOR REAGENT AND RESOURCE SHARING

Further information and requests for resources and reagents should be directed to and will be fulfilled by the Lead Contact, Marcelo Nollmann (marcelo.nollmann@cbs.cnrs.fr).

EXPERIMENTAL MODEL AND SUBJECT DETAILS

Oregon-R w¹¹¹⁸ fly stocks were maintained at room temperature with natural light/dark cycle and raised in standard cornmeal yeast medium. Following a pre-laying period of 16–18 H in cages with yeasted 0.4% acetic acid agar plates, agar plates were changed for new ones so flies can lay eggs during 1.5 H on the new plates. Embryos were then incubated at 25°C for an extra hour with 2.5 h of total developmental time at the time of fixation.

METHOD DETAILS***Drosophila* embryo collection**

Embryos collection were as described (Trcek et al., 2017). Briefly, embryos were dechorionated with bleach for 5 min and thoroughly rinsed with water. They were fixed in fixation buffer (1:1 mixture of 4% methanol-free formaldehyde in PBS and Heptane) by agitating vigorously for 15 s and then letting stand the vial for 25 min at RT. The bottom formaldehyde layer was replaced by 5 mL methanol and embryos were vortexed for 30 s. Embryos that sank to the bottom of the tube, devitelinized, were rinsed three times with methanol. Embryos were stored in methanol at –20°C until further use.

Oligopaint libraries

Oligopaint libraries were obtained from the Oligopaint public database (<http://oligopaints.hms.harvard.edu>) and consisted of unique 42-mer sequences with homology to the genome. Probe density was around 10–15 probes per kb. We selected 22 genomic regions of interest (barcodes from now on) in the *sna* locus (2L:15244500..15630000 *Drosophila* release 6 reference genome), spanning a total of ~400 kb with an average distance between barcodes of 17 kb. For each barcode, we obtained seventy-five probes, covering between 4–6 kb. See Table S1 for the coordinates of all barcodes used. One of the barcodes was selected as the fiducial barcode for image registration and drift correction.

Each oligo in our template primary probe library contained 5 regions: (from 5' to 3') i) a 21-nucleotide (nt) forward universal priming region for library amplification (5'-CGCTCGGTCTCCGTTCGTCTC), ii) a 30/32-nt readout region for binding of a complementary fluorescent secondary probe unique for each barcode (see Table S2 for all of readout region sequences), iii) the 42-nt genome homology region for *in situ* hybridization to the target chromosomal DNA sequence, iv) a duplication of 30/32-nt readout region to allow for the binding of a complementary second secondary probe and v) a 21-nt reverse universal priming region (5'-GCTGAACCCGTGACC TAGCCC). An oligo pool with all the oligonucleotides used in this study (~2000) was ordered from Twist Bioscience (San Francisco, USA). The 4-step procedure used to amplify the oligopaint probes was as described elsewhere (Wang et al., 2016). Briefly, it consists of a i) limited-cycle PCR, with pairs of PCR primers (BB287-FWD: 5'-CGC TCG GTC TCC GTT CGT CTC/ T7+BB288-REV: 5'-TAA TAC GAC TCA CTA TAG GGT TGG GCT AGG TAC AGG GTT CAG C) targeting the 21-nt forward and reverse priming regions. The reverse primer also contained an additional T7 promoter sequence (5'-TAATACGACTCACTATAG). This allows for ii) further amplification via T7 *in vitro* transcription using T7+BB288-REV primer, which were then iii) converted back to single-stranded DNA oligo probes via reverse transcription using BB287-FWD primer. Finally, iv) the intermediate RNA products were removed with alkaline hydrolysis and DNA oligo probes were purified via column purification.

Secondary readout 32-mer fluorescently labeled oligonucleotides (fluorescent readout probes, see Table S3) were synthesized by Integrated DNA Technologies (IDT; Coralville, USA). We employed 22 unique-sequence oligos, 21 of which have a cleavable Alexa-647 attached to the oligo whereas the one used for fiducial barcodes had a non-cleavable Rhodamine fluorophore. The

cleavable bond was a disulfide linkage that was removable with the mild reducing agent Tris(2-carboxyethyl)phosphine (TCEP), and allowed us to eliminate the fluorescence of a particular barcode from one cycle to the next (Moffitt et al., 2016). The whole set of Oligopaints used are in Table S4.

RNA-FISH probe preparation

Sna probe was previously used in Lagha et al. (2013). The full-length sna gene 1.6 kb (Dmel_CG3956, 15476621..15478176 *Drosophila* release 6 reference genome, flanking sequences 5'-ATTTAATTCTTCTCTTTAAGC-3' / 5'-GGGTAAATCGGGAGATCGGCG-3') was cloned into a pBluescript II SK (+) vector, cut by NotI to linearize the vector and *in vitro* transcribed using T7 RNA polymerase in the presence of digoxigenin haptens. RNA probe produced this way was then treated with carbonate buffer at 65°C for 5 min.

RNA-FISH coupled with TSA

The *in situ* hybridization protocol for RNA detection was that of Kosman et al. (2004) with minor modifications. Methanol-stored, fixed embryos were rinsed once with fresh methanol, then passed through 1 mL of 1) 50% methanol, 50% ethanol (once), 2) 100% ethanol (5 times for 3–5 min). Incubations were made in all cases for the indicated times at RT on a rotating wheel for each step unless otherwise specified. After two washes with methanol, embryos were incubated with a 1:1 dilution of methanol with 5% formaldehyde in PBT (PBT = 0.1% Tween-20 PBS) for 5 min and then rinsed with 5% formaldehyde PBT to help remove methanol. Next, embryos were post-fixed with 5% formaldehyde in PBT for 25 min. Embryos were rinsed twice with PBT, incubated 4 times with PBT during 15 min and permeabilized 1 h with 0.3% Triton in PBS. After 3 five-min washes with PBT, embryos were incubated for 10 min with a 1:1 dilution of PBT with RHS (RHS = 50% formamide, 2X SSC, 0.1% Tween-20, 0.05 mg/ml heparin, 0.1 mg/ml salmon sperm). Then, embryos were incubated with RHS at 55°C for 10 min, solution changed and incubated during 45 min and then a final incubation of 1 h 15 min. All incubations at 55°C were made in a Thermomixer with 900 rpm agitation. Next, 2 μ L of digoxigenin-labeled RNA probe was diluted in 250 μ L of RHS, denatured by heating at 85°C for a maximum time of 2.5 min and then placed in ice for at least 5 min. Embryo media at 55°C was removed and the probe-containing RHS was immediately added directly from the ice. Embryos were kept 16–20 h at 55°C for RNA hybridization. The second day, RNA probe was removed, embryos were washed 4 times at 55°C with RHS for 30 min each. After one 10 min wash at RT with a 1:1 dilution of RHS with PBT, 3 incubations with PBT for 20 min were made. Then, a saturation step was performed with 2X blocking solution (10X Blocking solution = 10% (w/v) blocking reagent Sigma #11096176001, 100 mM Maleic acid, 150 mM NaCl, pH = 7.5) for 45 min, and then the activity of endogenous peroxidases eliminated by incubating with 1% H₂O₂ in PBT for 30 min. Finally, after rinsing twice with PBT, embryos were incubated overnight at 4°C with sheep anti-digoxigenin conjugated with POD (Sigma-Aldrich cat #11207733910) with 1:500 working dilution in PBT. The next day, embryos were rinsed twice with PBT and then washed 5 times with PBT for 12 min each time. For the tyramide signal amplification (TSA), embryos were incubated 30 min with a dilution of 5 μ L of Alexa 488 coupled to tyramide dissolved in DMSO (Stock initially dissolved in 150 μ L of DMSO to obtain a 100X solution, Invitrogen cat#B40953) in 500 μ L of PBT. Next, H₂O₂ was directly added to the tube to a final concentration of 0.012% during another 30 min. Embryos were finally washed 3 times with PBT for 5 min.

Hybridization of primary oligopaint library

Embryos were resuspended by sequential dilutions of methanol with 0.1% V/V Tween-20 PBS (PBT). RNA labeled embryos were already in PBT, so this step was omitted. Next, embryos were RNase treated during 2 h, permeabilized 1 h with 0.5% Triton in PBS and rinsed with sequential dilutions (20 min each) of Triton/pHM buffer to 100% pHM (pHM = 2X SSC, NaH₂PO₄ 0.1M pH = 7, 0.1% Tween-20, 50% formamide (v/v)). Then, 225 pmols of the barcode probes were diluted in 30 μ L of FHB (FHB = 50% Formamide, 10% dextran sulfate, 2X SSC, Salmon Sperm DNA 0.5 mg mL⁻¹). Barcodes and embryos were preheated at 80°C during 15 min. The supernatant of pHM buffer was completely removed from embryos and 30 μ L of barcodes-containing solution were rapidly added. Mineral oil was added on top of the mix to avoid evaporation and the sealed tube was deposited in a water bath at 80°C. Immediately, the water bath was set to 37°C and let cooling down overnight. The next day, oil was carefully removed and embryos were washed two times at 37°C during 20 min with 50% formamide, 2X SSC, 0.3% CHAPS. Next, embryos were sequentially washed at 37°C for 20 min with serial dilutions of formamide/PBT to 100% PBT. An additional (optional) crosslink step with PFA 4% was performed and embryos were washed and resuspended in PBS. For the fiducial barcode readout, hybridization was performed in the bench before mounting the sample into the flow chamber. The sample was incubated with Rhodamine-labeled readout probe in hybridization buffer for 30 min at room temperature. Next, the sample was washed and kept in PBT. An additional fixation step could be performed as described before. Finally, embryos were stained with 0.5 μ g mL⁻¹ of DAPI for 20 min, washed with PBT and stored at 4°C until imaging.

Robotic microscope setup

All experiments were performed on a home-made imaging setup built on a RAMM modular microscope system (Applied Scientific Instrumentation - USA). The RAMM module was equipped with a 60x Plan-Achromat water-immersion objective (NA = 1.2, Nikon - Japan). The objective lens was mounted on a closed-loop piezoelectric stage (Nano-F100, Mad City Labs Inc. - USA) allowing for a fine control of the focus and the acquisition of z stacks when imaging embryos. A two-axis translation stage was used to move the sample laterally and select embryos before each experiment (MS2000, Applied Scientific Instrumentation - USA). Four lasers with

excitation wavelengths of 405 nm, 488 nm, 561 nm, and 641 nm were used for fluorescence imaging (OBIS-405/488/640 and Sapphire-LP-561, Coherent – USA). Laser beams were combined by a series of dichroic mirrors (LaserMUX, Semrock – USA), individually controlled by an acousto-optic tunable filter (AOTFnc-400.650, AAopto-electronic – France) and focused onto the back-focal plane of the objective through one of the excitation ports of the RAMM. Excitation and emission wavelengths were separated using a four-band dichroic mirror (zt405/488/561/640rpc-UF2, Chroma – USA) and the fluorescence signal was further filtered using a four-band filter (zet405/488/561/640 m, Chroma – USA) before being imaged on a sCMOS camera (ORCA Flash 4.0V3, Hamamatsu – Japan). The final pixel size was 100 nm. A home-made autofocus system was used to correct for axial drift in real-time and maintain the sample in focus while imaging. This was achieved as follows. Along with a separate path, a 785 nm infrared laser beam (OBIS-785, Coherent – USA) was focused onto the back focal plane of the objective and reached the coverslip-sample interface in total internal reflection conditions. The position of the reflected beam was measured by a position-sensitive detector (OBP-A-4H, Newport – USA) and any variations in the objective-sample distance were corrected through the z-positioning piezo stage using a proportional-integral-differential feedback loop.

For sequential hybridizations, a fluidic system similar to the one described by [Chen et al. \(2015\)](#) was designed. The sample was mounted in a FCS2 flow chamber (Biopetechs – USA). Buffers and probe handling were computer-controlled using a combination of three eight-way valves (HVXM 8-5, Hamilton – USA) and a negative pressure pump (MFCS-EZ, Fluigent – France) ([Figure S1B](#)). The flow rate was monitored in real-time using an online flow unit (FLU_L_D, Fluigent – France), allowing for a precise control of injected volumes.

All instruments, including camera, stages, lasers, pump, and valves were controlled using a custom-made software package developed in LabView 2015 (National Instrument – USA). This software controlled and synchronized multi-color 3D imaging and automated fluid handling.

Sequential image acquisition

Embryos labeled with a primary oligopaint library (see above) were attached to a poly-L-lysine coated coverslip and mounted into the FCS2 flow chamber, connected to the fluidics system and secured to the translation stage (see microscope setup). The fluidics system had 21 tubes connected and distributed as follows: 1 tube with 50 mL of washing buffer (WB, 2 × SSC, 40% v/v formamide), 1 tube with 50 mL of 2× SSC, 1 tube with 20 mL of imaging buffer (IM, 1×PBS, 5% w/v glucose, 0.5 mg/mL glucose oxidase and 0.05 mg/mL catalase), 1 tube with 50 mL of chemical bleaching buffer (CB, 2X SSC, 50 mM TCEP hydrochloride) and 17 tubes with 2.5 mL of each readout probe solution (25 nM readout probe, 2 × SSC, 40% v/v formamide).

Embryos remained firmly attached when confronted with constant flow (~200 μ L/min) for more than 72 hs, largely exceeding the total imaging time required for a single experiment ([Figure S1C](#)). Following embryo selection, embryos were segmented into a mosaic of several fields of view (FOV of size 200 × 200 μ m). First, bright field images were taken for all FOV. Next, DAPI and RNA staining were imaged together with fiducial barcodes by exciting at 405, 488 and 561 nm respectively. Fiducial barcodes hybridized to a Rhodamine-labeled readout probe before mounting the sample. Z stacks of 15 μ m with steps of 250 nm were acquired for all channels. Then, the robotic microscope controlled the sequential hybridization and imaging procedure (see [Figures S1B](#) and [S1C](#)). The flow chamber was initially flushed with 1.7 mL readout hybridization mixture over the span of 15 min to exchange buffers fully and ensure to saturate binding of readout probes. Next, the sample was washed with 2 mL of wash buffer for 18 min. Then 1.5 mL of 2X SSC were flushed during 15 min and finally 0.9 mL of imaging buffer was injected in 5 min. At this stage, flow was stopped, and ~100 FOVs were imaged in two channels by exciting at 561 and 641 nm to image fiducial barcodes and readout probes, respectively (see [Figure S1C](#)). After imaging, the fluorescence of the readout probes was extinguished using chemical bleaching by flowing 2 mL of CB buffer for 15 min. The Rhodamine-labeled fiducial barcode was insensitive to chemical removal. In all cases, the flow speed varied between 0.1 and 0.25 mL/min. After chemical bleaching, the chamber was flushed with 2 mL of 2 × SSC for 5 min and a new hybridization cycle started. A standard experiment required between 30 and 40 h depending on the number of probes and number of imaged FOV.

All buffers were freshly prepared and filtered for each experiment. To avoid degradation by oxygen, the imaging buffer used for a single experiment was stored under a layer of mineral oil throughout the measurement. Imaging buffer was renewed every 12-15 h.

Data processing and image analysis

First, images were deconvolved by Huygens Professional version 18.04 (Scientific Volume Imaging, the Netherlands, <https://svi.nl/>), using the CMLE algorithm (SNR:20, 40 iterations) run with a custom-made script written in Tcl/Tk. All further analysis steps were performed using a homemade analysis pipeline developed using MATLAB Release 2017b (The MathWorks, Inc., Natick, United States). First, we corrected for x-y drift in each cycle of hybridization. For each cycle j , the global x-y correction was obtained by cross-correlating the image of fiducial barcode j with that of the first barcode (reference cycle). This produced a single 3D vector for each barcode j and represented a 'global' correction applied to the whole FOV. Second, we used adaptive thresholding to pre-segment the spots of each fiducial barcode in each cell for all FOVs and for all barcodes. The 3D coordinates of each barcode were then found by using a 3D Gaussian fitting algorithm on the pre-segmented mask. Fiducial barcodes with sizes larger than the diffraction limit of light (~2.2 pixels for our microscope) were then filtered out. Third, we obtained 'local' 3D correction vectors for each cell in each FOV. This was achieved by first using the global x-y correction vector to pre-align fiducial barcode spots in cycle j to fiducial barcode spots in the reference cycle. Then, we used image-based cross-correlation of these pre-aligned fiducial barcode images to reach sub-pixel accuracy in the correction vector. This approach allowed for 3D, subpixel accuracy drift-correction across the whole FOV. Forth,

barcodes were segmented for all hybridization cycles in batch processing mode using optimized adaptive thresholding. 3D coordinates of each barcode were then determined by 3D Gaussian fitting of the segmented regions. These positions were corrected for drift by using the closest fiducial barcode vector obtained from the previous analysis step (local drift 3D correction, see above). Nuclei were segmented from DAPI images by adaptive local thresholding and watershed filtering. RNA images were segmented by manually drawing polygons over the nuclei displaying a pattern of active transcription. This was used to assign an expression status for each DAPI-segmented cell. Then, barcodes were attributed to each cell by using the DAPI segmentation. The efficiency of labeling per cycle for all barcodes was 60–70 percent (Figure S1F). The barcode localizations for each cell were then clustered as follows. First, the mean number of localizations per readout code was found and used as a measure of the maximum number of clusters N (1 cluster for paired chromosomes, 2 clusters for unpaired chromosomes, etc). Then, K-means was used to separate barcode positions into N clusters. Finally, pairwise distances and contact frequencies were calculated for each cluster in each cell.

All image processing was carried out on Linux terminals connected to a server running Linux Ubuntu 16.04 Xenial or CentOS 7, with 32 CPU processors, two GeForce GTX 1080Ti GPU cards, and 128GB of RAM.

Multiscale correlation of Hi-M distance maps

To compare Hi-M matrices at different scales, we did the following steps. First, we convolved maps with a Gaussian kernel of size s (standard deviation). Then, we calculated the correlation between maps and repeated this process for different values of s , ranging from 0.1 to 5. These values correspond to approximate genomic sizes ranging from 5 to 150 kb. As a control, we simulated random matrices with the same sizes and intensity ranges as the experimental matrices and repeated the same procedure. This process was repeated for 200 random matrices and the average correlation curves are shown in Figure 2B.

Precision of the method

The mean localization accuracy after drift correction was 43 ± 21 nm in xy and 51 ± 58 nm in z (Figure S1E). This was obtained by measuring the distance between fiducial barcodes after applying the correction obtained from the previously described image correlation method. To further verify the precision of co-localization, a single locus was simultaneously labeled with encoding probes bearing binding sites for two distinct readout probes. After image registration, two sequential hybridization cycles with readout probes targeting the selected loci were performed. The co-localization precision after drift correction was of 83 ± 60 nm in xyz (Figure S1F). To further challenge the quality of drift correction and co-localization, a similar control experiment was performed but separating the readout hybridization cycles by 10 additional cycles and by letting the sample mounted in the microscope rest more than 24 hs. In these conditions, drift correction accuracy and precision of colocalization were equivalent to the previous control, ensuring that our internal marker drift correction was unaffected by the set-up or sample stability during long acquisitions. As previously described (Cattoni et al., 2017), we calculate the absolute contact probability by integrating the area of the pairwise distance distribution below 120 nm. This threshold value was chosen from the integration of the pairwise distance distribution of a doubly labeled locus.

Hi-C and ChIP-Seq data processing

Raw Hi-C sequencing data were processed using the scHiC2 pipeline (Nagano et al., 2017). Construction of expected models and Hi-C contact scoring was performed using the ‘shaman’ R package (<https://bitbucket.org/tanaylab/shaman>; Cohen et al., 2017). Raw ChIP-seq sequencing data were mapped to the dm3 reference genome using the bowtie.2 algorithm. Linear read density profiles at 10bp resolution were produced using MACS 1.4 (Zhang et al., 2008) after merging replicates. RNaseq RPM (reads per million) profiles were produced by aligning raw, paired-end, sequencing reads to the dm3 reference genome (BDGP R5/dm3 UCSC gene annotation) using STAR (Dobin et al., 2013; <https://github.com/alexdobin/STAR>) with ‘unstranded’ output.

We interpolated Hi-C matrices to make comparisons with Hi-M maps. For this, we extracted the contact frequencies at the genomic positions at which barcodes were located to construct an interpolated Hi-C map. Interpolated and full Hi-C maps displayed very similar features (Figures S1I and S3A).

QUANTIFICATION AND STATISTICAL ANALYSIS

The number of nuclei quantified per experiment (N) is indicated in each of the corresponding figure legends.

DATA AND SOFTWARE AVAILABILITY

Experimental datasets (lists of pairwise distances for nc 14, nc 9–13 mitosis, nc 12–13 interphase) and software package developed to analyze 3D deconvolved images produced by our Hi-M microscope have been uploaded to Mendeley Data: <https://doi.org/10.17632/5f5hd9y3z.1#folder-26d1f8c0-fc58-4b87-8c4f-cd8fa294a555>.

5.3 Direct and simultaneous observation of transcription and chromosome architecture in single cells with Hi-M

In this publication, we detail all the steps to perform a Hi-M experiment, from embryo recollection to image analysis. As mentioned in the previous subsection, I was involved in all of these steps for our previous publication [Cardozo Gizzi et al., 2019]. In this work I contributing first by helping develop the protocol, and then to write the publication, particularly focusing in embryo collection, library hybridization, and analysis.

Direct and simultaneous observation of transcription and chromosome architecture in single cells with Hi-M

Andrés M. Cardozo Gizzi^{1,2}, Sergio M. Espinola¹, Julian Gurgo¹, Christophe Houbron¹, Jean-Bernard Fiche¹, Diego I. Cattoni¹ and Marcelo Nollmann^{1*}

Simultaneous observation of 3D chromatin organization and transcription at the single-cell level and with high spatial resolution may hold the key to unveiling the mechanisms regulating embryonic development, cell differentiation and even disease. We recently developed Hi-M, a technology that enables the sequential labeling, 3D imaging and localization of multiple genomic DNA loci, together with RNA expression, in single cells within whole, intact *Drosophila* embryos. Importantly, Hi-M enables simultaneous detection of RNA expression and chromosome organization without requiring sample unmounting and primary probe rehybridization. Here, we provide a step-by-step protocol describing the design of probes, the preparation of samples, the stable immobilization of embryos in microfluidic chambers, and the complete procedure for image acquisition. The combined RNA/DNA fluorescence in situ hybridization procedure takes 4–5 d, including embryo collection. In addition, we describe image analysis software to segment nuclei, detect genomic spots, correct for drift and produce Hi-M matrices. A typical Hi-M experiment takes 1–2 d to complete all rounds of labeling and imaging and 4 additional days for image analysis. This technology can be easily expanded to investigate cell differentiation in cultured cells or organization of chromatin within complex tissues.

Introduction

Genomes are folded in a hierarchical organization that contributes to the regulation of transcription and other processes¹. However, our current understanding of chromatin architecture and how it is related to transcriptional regulation remains limited. In the past decade, two strategies for studying chromatin folding became mainstream: chromosome conformation capture (3C and derivatives) and microscopy-based methods. 3C-like methods are powerful because they provide genome-wide information with kilobase resolution, but they have several limitations: (i) most often they rely on population averaging, (ii) they retrieve relative frequencies of pairwise interactions, (iii) they have relatively low detection efficiency in single cells (<10% of the total contacts), (iv) they are unable to provide spatial information (within the cell or the organism/tissue), and (v) they do not permit simultaneous measurement of transcription and chromosome structure². Microscopy-based strategies, on the other hand, use fluorescence in situ hybridization (FISH) to target specific loci and can access their 3D positions inside the nucleus, but until very recently, these strategies were limited to the detection of a small number of genomic locations (typically three or four). Following pioneering work from Xiaowei Zhuang's lab, we and others have recently overcome several of these limitations to reconstruct chromatin architecture at high resolution in single cells while retaining spatial information^{3–6}. Our implementation, which we termed 'Hi-M' (high-throughput, high-resolution, high-coverage microscopy-based technology; see 'Principles of the method' section below), combines high-throughput synthesis of short oligonucleotide (oligo) probes with RNA labeling and multiple rounds of hybridization in a sequential-imaging scheme to enable the measurement of transcriptional state and the localization of tens of different genomic loci within intact *Drosophila* embryos³. A similar approach has been used in concurrent work⁶.

¹Centre de Biochimie Structurale, CNRS UMR 5048, INSERM U1054, Université de Montpellier, Montpellier, France. ²Present address: CIQUIBIC (CONICET), Departamento de Química Biológica Ranwel Caputto, Facultad de Ciencias Químicas, Universidad Nacional de Córdoba, Córdoba, Argentina. *e-mail: marcelo.nollmann@cbs.cnrs.fr

Principles of the method

Hi-M builds on recent innovations in FISH probe design based on high-throughput microarray oligo synthesis, namely Oligopaints^{7,8}, and on the pioneering design of multiplexing schemes for detecting hundreds of RNA species by imaging^{9,10}. A microarray library with thousands of oligonucleotides (an oligo pool) is bioinformatically designed and commercially synthesized to target tens of different genomic locations. Each genomic locus (typically spanning 2–10 kb) is targeted by a unique set of 20–70 tiled oligos. We will refer to the genomic regions covered by these unique sets of oligos as ‘barcodes’. Each oligo in a barcode contains three parts: a region of genomic homology, a barcode-specific readout sequence, and a priming region for PCR amplification (see ‘Experimental design’ section). Labeling involves four steps. First, the oligo pool library is enzymatically amplified and purified. Second, embryos are collected and fixed. Third, embryos are labeled by an RNA hybridization and signal amplification step. Fourth, the oligo pool is hybridized to genomic DNA. After labeling, the samples are mounted within a microfluidic chamber connected to a microfluidic pump system and placed under an automated wide-field fluorescence microscope. In an initial round, DAPI and RNA signals are acquired in multiple regions of interest (ROIs). Then the imaging of each barcode requires (i) labeling of the sample with barcode-specific, fluorescently labeled readout oligonucleotides (readout probes); (ii) removal of unbound readout oligos by washing; (iii) acquisition of 3D, two-color images for all ROIs; and (iv) photobleaching to extinguish the fluorescent signal of the readout probes. This process is repeated sequentially for each barcode. In all sequential rounds, a second, spectrally different fluorescent oligo is present and is used as the fiducial barcode (spatial reference point) for the correction of drift between cycles. Next, images are processed to segment nuclei in the embryo, determine the transcriptional status of each cell, retrieve the 3D position of each barcode in each ROI with sub-pixel accuracy, and correct drift during acquisition and between cycles of hybridization. Finally, the 3D coordinates of each barcode detected in each cell are used to reconstruct Hi-M matrices containing mean pairwise distances and absolute contact probabilities.

Applications of the method

We developed Hi-M to explore genome architecture and transcription in intact *Drosophila* embryos. However, Hi-M can be used in a large variety of model systems. For instance, adaptation to cultured cells should be straightforward. Cultured cells can be readily attached to the coverslip by standard procedures (e.g., by growing them in treated coverslips conducive to cell adhesion). In fact, cultured cells exhibit lower autofluorescence than organisms; thus, the application of Hi-M to cultured cells should result in an increased barcode detection and localization precision. Hi-M could also be adapted to thick tissues and organoids by implementing cryo-sectioning¹¹, tissue clearing¹² or optical-sectioning.

The RNA/DNA staining procedures described in this protocol are fully compatible with other imaging modalities, such as 3D structured imaging microscopy (3D-SIM) and stochastic optical reconstruction microscopy (STORM)^{4,5}. The acquisition of super-resolution images is typically slower than for wide-field microscopy images, therefore limiting the throughput of a Hi-M acquisition. Thus, a compromise between resolution and throughput will have to be found depending on the problem under study. In addition, most super-resolution microscopes are not well adapted to thick specimens; thus, their use in Hi-M will be limited to mainly thin samples.

The flexibility afforded by Oligopaints in the design of probes would enable the adaptation of Hi-M to explore chromosome conformation at different length scales (e.g., chromosomal¹³, compartment⁵ or topologically associated domain (TAD) levels^{3,6}). In the present protocol, barcodes contain ~20–90 primary oligos and cover 2–10 kb to produce diffraction-limited spots and ensure excellent signal-to-noise ratios (SNRs, defined as the maximum intensity of a spot divided by the standard deviation of the background). Labeling of smaller genomic regions is possible but only at the cost of reduced SNR levels (i.e., reduced localization precision).

Limitations

A current limitation of Hi-M is the time required for the acquisition of an entire dataset: typically 2–3 d to image 50–70 barcodes in 30 fields of view (representing ~40,000 cells in 10–12 *Drosophila* embryos). Thus, typically a balance between experimental time and the number of barcodes imaged needs to be found. For instance, 70 barcodes could be used to image an extended genomic region (e.g., 3.5 Mb) at low resolution (50 kb between barcodes) or to image a single genomic locus (e.g., 150 kb) at high resolution (~2 kb).

A second limitation is the minimal required number of primary probes per barcode. The values provided in this protocol (see ‘Experimental design’ section) ensure robust detection with high localization precision. A reduction in the number of primary probes could lead to decreased levels of detection and degraded localization precision. A possible future solution to this limitation may be to increase the number of imaging probes by encoding more readout probes per barcode (e.g., using SABER-FISH¹⁴), but ultimately this approach may limit the specificity of labeling.

A third limitation is the efficiency of barcode detection, which is currently close to 60–70% for 1- to 3-kb barcodes. Thus, a barcode is observed in only ~6–7 out of each 10 nuclei, resulting in a small number of nuclei with all barcodes.

A fourth limitation arises from the high cost of purchasing the fluorescently labeled oligos used as readouts (~US\$500 for 250 nmoles of each, which is enough for ~5,000 experiments). Because each barcode is detected by a specific fluorescently labeled readout probe, the price of an experiment increases linearly with the number of barcodes. A new strategy that can considerably reduce the experimental cost was recently described in two publications^{6,15}. Instead of using a fluorescently labeled oligo for each barcode, a combination of two oligos is used: a non-fluorescent oligo specific to each barcode (bridge oligo) and a single fluorescent oligo common to all barcodes (imaging oligo). The bridge oligo contains 20 nt complementary to the barcode sequence, followed by a 10-nt ‘toehold’ spacer sequence and a 20-nt sequence complementary to the imaging oligo¹⁶. With this design, the same fluorescently labeled imaging oligo can be used to read all barcodes, with barcode specificity provided by the bridge oligo. Furthermore, this strategy can also be exploited to remove the fluorescence after each imaging cycle by the use of displacement oligos. Displacement oligos are complementary to the toehold and bridge probe sequences; therefore, they displace the bridge probe from the barcode, and in doing so, they also remove the imaging probe.

A final limitation is the inability of Hi-M to detect several RNA species at once. The Hi-M protocol described here enables the simultaneous detection of chromosome conformation together with a single RNA species. In the future, additional RNA species could be labeled by using a sequential tyramide signal amplification (TSA) reaction with alternative conjugation molecules (e.g., biotin) or by oligonucleotide-derivatized antibodies. It is worth noting that TSA is non-linear; therefore, quantification of RNA levels requires proper calibration.

Comparison with other methods

Compared to traditional FISH, Hi-M has two main advantages: (i) it uses oligo probes, which provide design flexibility and higher efficiency of labeling as compared with double-stranded bacterial artificial chromosome (BAC) or amplicon-based probes^{17,18}; and (ii) it uses a multiplexed approach that does not rely on the use of spectrally different fluorophores (limited to two to four in most applications). The overall strategy of Hi-M is conceptually similar to that used recent work utilizing sequential imaging schemes and Oligopaints labeling^{4–6,19}. The main differences from these studies are (i) Hi-M enables simultaneous detection of RNA status and chromosome organization without sample unmounting and probe rehybridization. Other approaches also enable RNA/DNA detection but require the hybridization and imaging of RNA probes, unmounting of the sample followed by degradation of RNA, hybridization of DNA probes, and then remounting and imaging of the same cryo-sectioned samples⁶. (ii) Hi-M enables, in contrast to other studies^{4–6}, the imaging of entire, intact *Drosophila* embryos.

Multiplexing has also been recently achieved in the single-cell imaging of multiple RNA species^{10,11,20,21}. These studies used combinatorial schemes to target ~140^{10,11} to ~10,000 genes^{20,21} using only ~20 hybridization cycles. RNA is typically present in many copies per cell, and these copies are spatially well separated, making it possible to decode species using combinatorial approaches. Currently, the use of combinatorial approaches to label DNA is limited by the spatial overlap of the barcodes, the small number of DNA molecules detected (typically 1–4, depending on ploidy) and the relatively low efficiency of detection (~60%, see above). Excitingly, combinatorial approaches based on spectral overlap¹⁵ may be usable in the near future to considerably increase the number of detected barcodes without a linear increase in the number of hybridization cycles.

Hi-M and similar approaches based on FISH are carried out in fixed samples; thus they cannot provide information on dynamic changes in RNA expression and localization or DNA folding. Live imaging of single genomic loci has been achieved using a catalytically inactive Cas nuclease targeted to a locus by a single guide RNA (sgRNA; for a review, see ref. ²²). Typically, CRISPR-based imaging records the position of two genomic loci, although targeting of up to six genomic loci has been

achieved for repetitive sequences²³. Imaging of non-repetitive sequences has proven challenging because of the complexity of simultaneously co-expressing multiple sgRNA species in one cell. Furthermore, off-target binding and background fluorescence can further limit the application of current CRISPR-based imaging methods. More recently, a radically different approach successfully followed the 3D position of a single gene in real time while simultaneously monitoring mRNA synthesis in the same cell^{24,25} by combining stem-loop-based labeling (MS2 and/or PP7^{26–28}) and the ParS/ParB system²⁹. This approach was used to study the positions of a genomic locus and a transcription site at the same time in living *Drosophila* embryos²⁵. This approach requires genetic manipulation to introduce ectopic sequences and is limited at present to a maximum of two colors (typically, a transcript and a genomic locus).

Experimental design

The Hi-M protocol presented here (Fig. 1) consists of the design and amplification of Oligopaints probes (Steps 1–39 and Figs. 2–4), collection and fixation of *Drosophila* embryos (Steps 40–50), RNA and DNA labeling in embryos (Steps 51–92), sample mounting (Steps 93–100 and Fig. 5), sequential imaging of multiple genomic locations (Steps 101–116 and Figs. 6–8), and image processing and analysis (Steps 117–149 and Figs. 9 and 10) in order to reveal chromatin organization and its relationship to the transcriptional status of single nuclei (Fig. 11).

Oligopaints probes

The method is based on massively parallel oligonucleotide synthesis to design probes targeting the genomic locations of interest to perform FISH-based labeling³⁰. This protocol describes how to design a library and amplify Oligopaints probes. Oligonucleotide primary probes contain three regions (Fig. 2a): (i) a region of genomic homology composed of 42 nt complementary to the target locus, (ii) a readout region composed of 32 nt complementary to a readout oligo bearing a fluorophore, and (iii) two flanking 20-nt regions containing primers for PCR amplification of the whole Oligopaints library. With this design, it is possible to include two readout sequences per primary oligo, one each in the 5' and 3' ends of the genomic homology region.

The design pipeline implemented in the current protocol is based on a previous development by Beliveau et al.⁸ and requires the user to input the genomic region of interest and either the number of probes per barcode or, alternatively, the genomic size per barcode (Fig. 2b). The databases of genomically unique, non-overlapping sequences with specific hybridization properties used to generate the Oligopaints primary probes were mined using OligoArray³¹. Such databases are available online for a variety of species (Oligopaints website, <https://oligopaints.hms.harvard.edu/>). An alternative to the design of Oligopaints primary probes, although limited to the human genome, is the use of the web interface (<http://ifish4u.org>) that enables the selection of specific sets of oligos in a user-friendly environment that includes ~400 validated probes³². Of note, a recent development, OligoMiner³³, eliminates the use of online databases because it is capable of discovering thousands of oligo probes in minutes, thus allowing researchers to create their own database for any sequenced genome and to optimize mining parameters (e.g., less stringent conditions to increase the number of probes at the expense of binding affinity). A minimal number of primary oligos per barcode is needed for a high enough SNR to detect barcodes with high localization precision. Currently, we use a minimum of 40 primary oligos per barcode (i.e., 80 fluorophores per barcode). This number is comparable to the 48 fluorophores typically used for single-molecule RNA FISH³⁴. Given an average of 12 unique sequences (i.e., primary oligos) per kilobase in the *Drosophila* genome³³, a probe can be as short as ~3 kb. In the human genome, the average number of unique sequences per kilobase is considerably lower (typically ~8 oligos/kb); thus we would recommend using a probe set spanning ~5 kb to ensure robust detection in most systems and conditions. Recently, a different oligo dataset was mined with a higher density of probes/kilobase (ref. ³²), possibly enabling a reduction in the genomic size of the barcode. The design of the fiducial barcode requires additional considerations, because it has all the elements of the other barcodes but will need to be repeatedly imaged in each cycle of hybridization (i.e., it will suffer more from photobleaching than standard barcodes). Therefore, we recommend using a higher number of primary oligos for the fiducial barcode (e.g., 200 oligos spanning ~20 kb). Currently, we fit the position of the fiducial barcode using a 3D Gaussian function, because the image of this barcode is a diffraction-limited spot. It is important to understand that if the genomic region occupied by the fiducial barcode is large (>20–30 kb in our setup), its image in the camera will not be

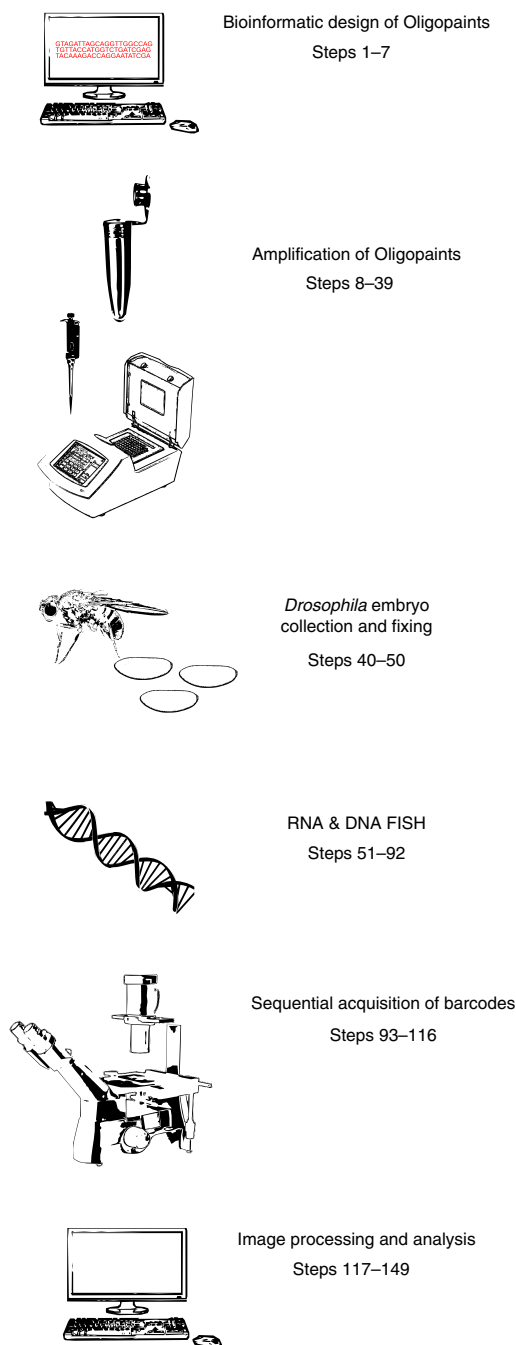


Fig. 1 | Outline of the Hi-M protocol. Schematic description of the main steps in the Hi-M protocol.

diffraction limited. This must be taken into consideration for the fitting of the 3D position of this barcode and adjusted for by appropriate modifications in the analysis pipeline.

For library amplification, the protocol follows a strategy previously introduced by Moffitt and Zhuang for the detection of RNAs using combinatorial approaches³⁵. In short, library amplification consists of four steps: (i) PCR amplification of the Oligopaints library using a reverse primer that adds the T7 promoter sequence, (ii) conversion of the PCR product to RNA via an *in vitro* transcription using T7 polymerase, (iii) generation of single-stranded DNA (ssDNA) via reverse transcription, and (iv) degradation of the RNA template using alkaline hydrolysis (Fig. 3). Quality and concentration are monitored during the different steps to ensure the success of the amplification and purification process (Fig. 4).

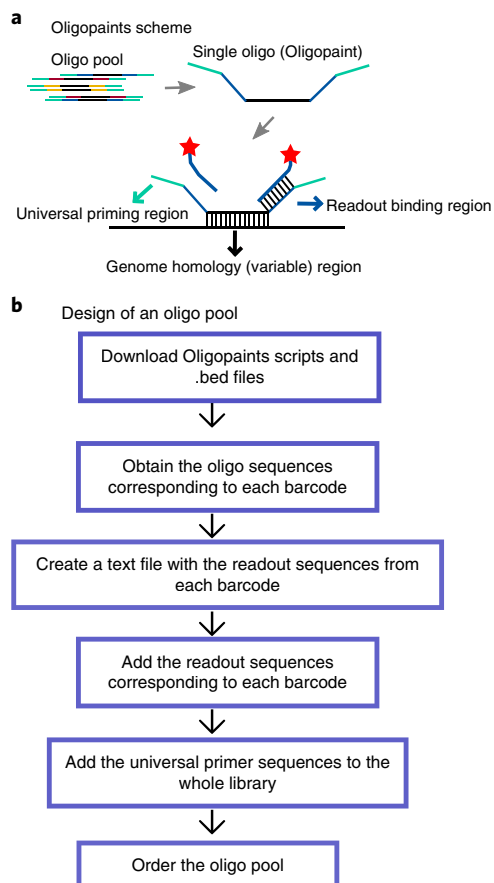


Fig. 2 | Design of Oligopaints. **a**, An oligo pool is composed of thousands of oligo sequences. Each individual oligo shares the following regions: (i) forward and reverse 20-nt universal priming sequences (cyan) to allow for PCR amplification, (ii) 32-nt readout sequences ($\times 2$; blue) complementary to a fluorescent readout oligo (schematized with a red star as the fluorophore) and (iii) a 42-nt genome homology variable region in black, which targets the oligo to a unique genomic site. **b**, Schematic description of the steps involved in designing an oligo pool.

Embryo collection and fixation

The protocol here does not deviate much from a previously published protocol³⁶. Flies lay eggs on yeast agar plates for 1.5 h. The plates are incubated at 25 °C until the embryos reach the desired developmental stage. It is worth noting that after nuclear cycle, 14 multiple layers of cells will appear; therefore, out-of-focus light could compromise readout detection in a wide-field setup. Embryos are then collected, dechorionated by the use of bleach, thoroughly rinsed with water and immediately fixed, using formaldehyde and formaldehyde-saturated heptane. The fixative is then removed, methanol is added and the embryos are vortexed. Embryos that sink to the bottom of the tube are devitellinized, which is critical to enabling penetration of FISH probes into the sample. Devitellinized embryos are washed with methanol and stored at -20 °C until further use.

RNA and DNA FISH

The protocol has two main steps: (i) RNA in situ hybridization and (ii) DNA Oligopaints FISH. To ensure RNA signal preservation after DNA FISH, TSA, adapted from a previous protocol³⁷, is performed. The single-stranded digoxigenin-labeled RNA probe is obtained from an in vitro transcription reaction in the presence of digoxigenin haptens as described elsewhere^{3,38}. RNA probes are targeted with a specific antibody that is coupled to horseradish peroxidase (HRP). HRP then reacts with hydrogen peroxide, creating tyramide free radicals from fluorophore-labeled tyramide that will covalently bind to the vicinity of the RNA probe. It is possible to label a second RNA species by performing a sequential, second antibody–HRP incubation against a biotinylated probe. In any case, controls should be made to ensure specificity of the RNA probe(s). In our previous paper³, we labeled the *snail* gene, which has a distinctive spatial expression pattern that can be used to assert signal specificity. However, we did include a control sample without the RNA probe to establish the

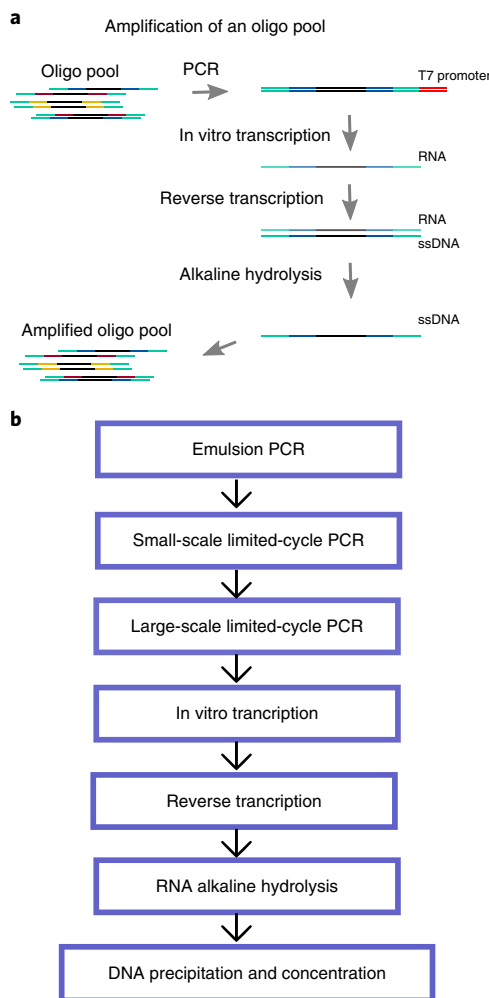


Fig. 3 | Oligo pool amplification. **a**, Oligo pool amplification scheme. Cyan represents the universal priming region common to all barcodes, whereas blue, amber and burgundy represent barcode-specific readout sequences. A complex oligo pool, composed of thousands of oligos, is amplified to double-stranded DNA via a PCR that also adds the T7 promoter sequence (red). An in vitro transcription step leads to the formation of RNA, greatly amplifying the material. Next, the RNA is reverse-transcribed to ssDNA. Finally, the RNA is removed via an alkaline hydrolysis step. **b**, Schematic description of the main steps.

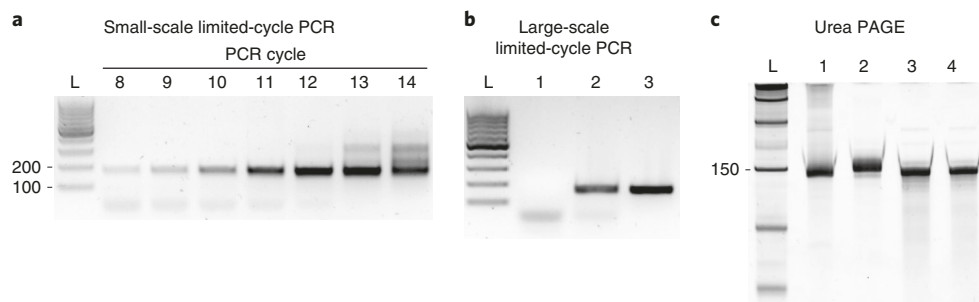


Fig. 4 | Example results. **a**, Example of an agarose gel electrophoresis result for the small-scale limited-cycle PCR step. A band of the expected size (166 nt, in this case) is observed between the 100- and 200-nt bands of the ladder. In cycles 13 and 14, a second, nonspecific band of ~300 nt begins to appear. Therefore, a total of 11 amplification cycles (at PCR cycle 12) was chosen for this specific amplification reaction. **b**, Example of an agarose gel electrophoresis result for the large-scale limited-cycle PCR step. Lanes 1 and 2 correspond to PCRs performed without and with template, respectively. Excess primer-dimers are observed at the bottom. Lane 3 corresponds to column-purified PCR product. **c**, Example of a urea PAGE result. Bands from lanes 1–4 migrate close to the 150-nt band from the ladder. Lane 1 corresponds to 200 ng of emulsion PCR break, lane 2 to 200 ng of RNA product from in vitro transcription (note the larger size due to the presence of the T7-promoter region), and lanes 3 and 4 to 200 ng of ssDNA before and after precipitation, respectively. L, DNA ladder (low-range ssRNA ladder) or molecular weight size marker.

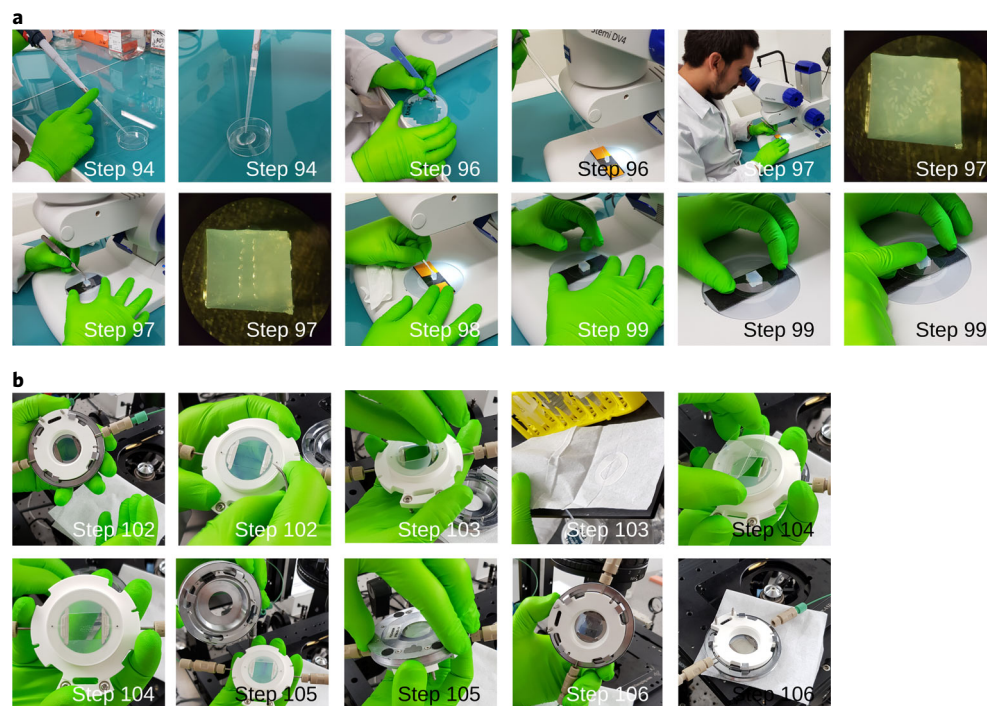


Fig. 5 | Procedure for attaching embryos to the microfluidic chamber. Step numbers are indicated on each subpanel. When a step is represented by multiple subpanels, the events in the procedure are displayed from left to right. **a**, Embryo attachment. (Step 94) Add poly-L-lysine solution to coverslip. (Step 96) Cut an agarose pad and transfer 20–30 embryos to the agarose pad. (Step 97) Use metal tweezers to align the embryos, using a binocular microscope to visualize them. (Step 98) Dry the embryos using a paper tissue. (Step 99) Attach the embryos to a poly-L-lysine-coated coverslip by gently pressing coverslip against the agarose pad. **b**, Embryo mounting within the chamber. (Step 102) Open the microfluidic chamber by unscrewing it. Carefully remove the glass coverslip from the chamber. (Step 103) Remove the plastic spacer and dry it thoroughly with a paper tissue. (Step 104) Put back the dried spacer and mount the coverslip with the attached embryos. (Step 105) Screw the chamber into (mount it on) the microscope stage. (Step 106) Flow 2× SSC buffer through the chamber by slowly applying negative pressure on the outlet with a syringe.

expected background levels. In the case that the expression pattern of the target gene is homogeneous (or unknown), an antisense probe can be used to verify that the sense probe is actually binding to the target RNA.

After the TSA reaction, a DNA FISH step based on a previous method³⁹ that we have optimized for Oligopaints hybridization is performed by changing hybridization and washing conditions.

Embryo attachment

Firm attachment of the embryos to the flow chamber coverslip is essential in order to resist the pressure from non-continuous flow rates during a 2- to 3-d imaging experiment. To this end, 20–30 embryos are deposited and oriented on an agarose pad and then transferred to a glass coverslip previously coated with poly-L-lysine. The microfluidic chamber is then assembled and the system is filled with liquid. The complete procedure is shown in Fig. 5.

For a different type of sample, tests should be performed to ensure stable attachment. This should not be a problem if adherent cells are used. A control with a labeled sample (e.g., using fiducial markers), imaged before and after a certain period of time (~30 min) of continuous flow and at the beginning and at the end of a full experiment, should be performed to assess sample stability and stage drift. The software analysis pipeline corrects for stage drift (see ‘Image analysis’ section), but if the sample become loose or detaches during the experiment, drift correction will not be possible.

Image acquisition

Hi-M requires three acquisition steps. The pre-sequential step involves the acquisition of 3D bright-field and multicolor fluorescence images for each ROI. The channels in the pre-sequential step are as follows: channel 1 = 3D image for DNA masks (DAPI-stained nuclei, excited using the 405-nm laser line); channel 2 = 3D image for RNA (RNA-stained embryos excited using the 488-nm laser line);

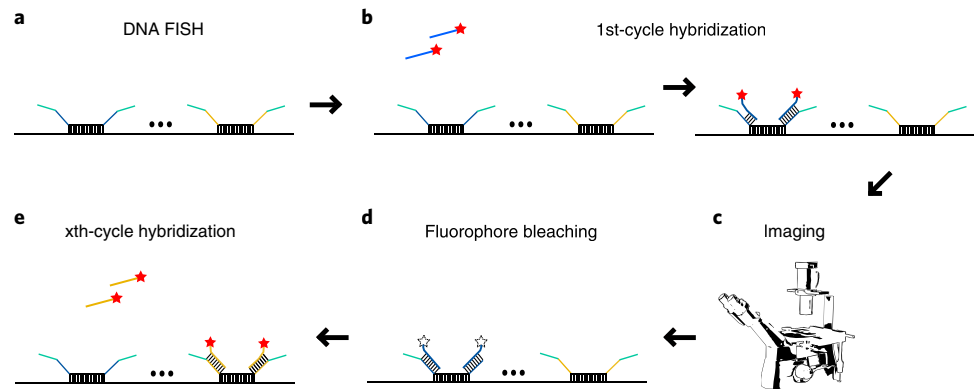


Fig. 6 | Scheme of hybridization/imaging cycles. **a**, Primary oligo pool is hybridized to genomic DNA at the bench. **b**, A readout oligo (blue), bearing a fluorophore (red star), specifically binds to the blue readout barcode. **c**, Once hybridized, images are recorded for all ROIs. **d**, The fluorophore on the readout oligo is chemically cleaved or, alternatively, photobleached. **e**, A new hybridization cycle starts with a different readout oligo, now targeting the amber barcode.

and channel 3 = 3D image of the fiducial barcode used for image registration (obtained using the 561-nm laser line).

The sequential imaging acquisition step involves sequential imaging of barcodes. For each cycle of hybridization (see below), a 3D, two-color fluorescence image is acquired: channel 1 = 3D image of the fiducial barcode (excitation using the 561-nm laser line) and channel 2 = 3D image of the *N*th barcode (acquired using the 641-nm laser line). Thus, for *N* cycles of hybridization and *k* ROIs, one obtains $k(2N + 4)$ 3D images. In a typical experiment with 10 embryos (~30 ROIs) and 22 barcodes, one needs to analyze a total of 1,440 3D images. In our current implementation, the acquisition time for 22 barcodes and ~30 ROIs (i.e., 7–9 embryos) is around 24 h. This time scales linearly with the total number of barcodes and ROIs. *Drosophila* embryos in nuclear cycle 14 have ~6,000 nuclei; therefore, ~25,000 nuclei can be retrieved in a single experiment.

Each cycle of hybridization involves the following steps: (i) using the liquid-handling device to introduce a solution containing the fluorescent readout oligo that will hybridize to the complementary sequence of the primary oligos of a barcode, (ii) washing nonspecifically bound or unbound readout oligos with a formamide-containing solution, (iii) injecting an imaging solution that includes an oxygen scavenger enzymatic reagent to prevent photobleaching during acquisition, (iv) stopping the flow and performing the sequential imaging step described above for all desired ROIs, (v) bleaching of barcodes (see below) (Fig. 6).

The bleaching step can be achieved by either of two means: (i) light-induced photobleaching using a high-power laser. The implementation of this option is straightforward, but the time required for photobleaching all ROIs scales linearly with the number of acquired ROIs. (ii) Chemical bleaching. This option requires the fluorescent molecule in the readout oligo to be attached via a disulfide linkage cleavable by the use of a mild reducing agent such as Tris(2-carboxyethyl)phosphine (TCEP)⁴⁰. The advantage of this option is that all fluorophores are removed at once in a single step, making the bleaching time independent of the number of acquired ROIs. If chemical photobleaching is used, the fluorophore in the fiducial barcode needs to be resistant to the reducing agent (i.e., do not use a disulfide linkage).

In the final acquisition step, a 3D bright-field image for each ROI is acquired for a second time. This image is used later to verify that the embryos did not detach during acquisition (see ‘Controls’ section below).

Image analysis

The first image analysis step involves the deconvolution of images to remove out-of-plane light to increase the SNR and contrast. We have observed that this step greatly increases detection efficiency. We perform this operation using Huygens (<https://svi.nl/HuygensSoftware>), although other software packages will work as well.

The second step involves the manual comparison of bright-field images of embryos before and after sequential imaging. Embryos displaying any apparent movement or morphological distortion are discarded from further analysis.

Next, a custom-made MATLAB program is used to perform the following image analysis steps after deconvolution (Figs. 9 and 10). The workflow starts with the segmentation of nuclei from pre-sequential images with a graphical user interface (GUI). A number of parameters can be pre-tuned (e.g., threshold, *z*-range) (Fig. 10) and manually modified in the GUI. Next, the GUI loads the stack, extracts the usable *z*-range, corrects for inhomogeneous excitation, and flattens the image by maximum-intensity projection. Next, a detection algorithm with tunable parameters (e.g., threshold, intensity range) segments nuclei by using adaptive thresholding and water shedding (using built-in MATLAB functions). The user iteratively changes the parameters until a satisfactory result is reached (i.e., masks reflect the observed nuclei). Once parameters have been optimized and verified, all the ROIs can be analyzed in a batch.

A similar procedure is used to segment the barcodes. This procedure involves loading the image, extracting the *z*-range, correcting for inhomogeneous excitation, and segmentation by local thresholding. An estimate of the 3D positions of the barcodes is obtained from the center of gravity of the masks segmented in this step. These 3D coordinates are next refined using a 3D Gaussian fitting algorithm.

Finally, a registration step is performed by image cross-correlation of the fiducial barcodes. A correction vector is derived and applied for each barcode. Corrected 3D barcode coordinates and nuclei masks are then used to determine which barcodes are associated with which nuclei. These data are used to calculate the mean absolute contact probabilities and normalized mean pairwise distances for each pair of barcodes (see heatmaps in Fig. 11).

Controls

During in situ hybridization, chromatin is denatured by heating in the presence of formamide to enable the binding of the primary probes. First, to ensure that this step did not affect the labeling of the RNA, it is necessary to compare RNA intensities and distributions before and after DNA hybridization.

Second, it is important to take steps to quantify the efficiency of hybridization of the primary probes and the efficiency of binding of the imaging probes. For this, it is useful to measure the distribution, the SNR, and the number of barcode spots per cell. These measurements should be performed for each barcode in several embryos. Barcode spots should appear dense and uniform across the field of view. In *Drosophila*, we typically observe that ~60–70% of nuclei display barcode spots, reflecting the limited labeling efficiency. In these cells, ~80% contain a single barcode, consistent with a high degree of homologous pairing^{41,42}. This contrasts with mammalian cells, for which two barcode spots should be detected in most labeled cells. The typical SNR in our experiments was 50–500 after deconvolution as determined by calculating the average SNR from 20–100 spots. A reduced SNR could indicate incomplete binding of primary or readout oligos.

Third, a bright-field image is acquired before and after the experiment to ensure that the embryos did not move during the experiment. During the analysis phase, it is verified that embryos did not change morphology or position during the experiment. Small-scale changes in embryos may occur during acquisition, such as inhomogeneous expansions/contractions of a few hundred nanometers. To account for these, fiducial marks are used. This enables us to both correct for stage drift and account for any inhomogeneous expansion or contraction.

Fourth, Hi-M matrices should be generated from different regions of interest and for different embryos at the same developmental stage to test whether the data are highly correlated (Pearson test on the Hi-M pairwise distances and contact probabilities). Finally, a consolidated Hi-M contact probability matrix is built and compared with existing Hi-C datasets (Pearson test on contact probabilities). In addition, it can be verified that TAD borders are located at the same genomic positions for both datasets. When available, comparisons of Hi-M matrices with other sources of data (e.g., ChIP-seq, enhancer trapping) is also important to ensure the validity of the results. For example, if a given locus has proven to be an enhancer by a different technique, it would increase the confidence if contacts involving this enhancer and promoters of annotated genes are visible using Hi-M.

Spatial resolution

In our approach, we avoid chromatic shift by using a single channel to record all barcodes. By recording in two channels, the number of hybridization cycles can be reduced by half. However, chromatic aberrations need to be properly corrected, as described elsewhere⁴². Stage drift is inherently present and also needs to be corrected using a fiducial barcode. The reported residual error of fiducial barcodes after drift correction is $\sim 80 \pm 60$ nm in *xyz*³. Ultimately, this will limit the minimal distance that can be resolved between any two barcodes.

Materials

Biological materials

- Wild-type fruit flies

Reagents

- Oligo pool (131–150 nt; CustomArray, custom order) Oligo pool sequences used to generate the example data can be found in Supplementary Table 1.
- KAPA Taq Kit with dNTPs (CliniSciences, cat. no. BK1003)
- HiScribe T7 High Yield RNA Synthesis Kit (New England BioLabs, cat. no. E2040S)
- Maxima H Minus reverse transcriptase kit (Fisher Scientific, cat. no. 13243159)
- dNTP set (100 mM) solution (Fisher Scientific, cat. no. 10083252)
- RNasin ribonuclease inhibitor (Promega, cat. no. N2515)
- Oligo Clean & Concentrator Kit (Zymo, cat. no. D4060)
- DNA Clean & Concentrator Kit (Zymo; 25- μ g capacity, cat. no. D4033; 100- μ g capacity, cat. no. D4029)
- SYBR Safe Nucleic Acid Gel Stain (Invitrogen, cat. no. S33102)
- RNA loading dye (2 \times ; New England BioLabs, cat. no. B0363S)
- Low-range ssRNA ladder (New England BioLabs, cat. no. N0364S)
- SYBR Gold Nucleic Acid Gel Stain (Fisher Scientific, cat. no. S11494)
- Agarose (standard DNA grade; Euromedex, cat. no. D5-E)
- GeneRuler 100-bp DNA ladder (Fisher Scientific, cat. no. SM0243)
- Ammonium acetate (5 M; Fisher Scientific, cat. no. 10534645)
- Glycogen (5 mg/mL; Ambion, cat. no. AM9510)
- TEMED (Thermo Scientific, cat. no. 17919)
- Ammonium persulfate (APS; Fisher Scientific, cat. no. 17874)
- Acrylamide/bis-acrylamide (19:1, 40% (wt/vol)) solution (Fisher Scientific, cat. no. BP1406-01)
- Cetyl PEG-PPG-10-1 dimethicone (ABIL EM 90; Evonik, <https://www.ulprospector.com/en/na/PersonalCare/Detail/1481/51913/ABIL-EM-90>)
- Diethyl ether (Sigma-Aldrich, cat. no. 296082)
- Ethyl acetate (Sigma-Aldrich, cat. no. 270989)
- Mineral oil (500 mL; Sigma-Aldrich, cat. no. M5904)
- Triton X-100 (250 mL; Sigma-Aldrich, cat. no. T8787)
- Tween 20 (500 mL; Sigma-Aldrich, cat. no. P2287)
- CHAPS (Sigma, cat. no. 226947)
- Dulbecco's phosphate-buffered saline (PBS; Gibco, cat. no. 14190169)
- Poly-L-lysine solution (Sigma-Aldrich, cat. no. P8920)
- Saline-sodium citrate buffer (SSC; 3 M NaCl in 0.3 M sodium citrate; 20 \times ; Thermo Fisher Scientific, cat. no. AM 9770)
- Tris base (BM grade; Euromedex, cat. no. 200923-A)
- Sodium chloride (NaCl; 99.5%; Euromedex, cat. no. 1112-A)
- Sodium dihydrogen phosphate, dihydrate (NaH₂PO₄; Euromedex, cat. no. T879)
- Dry yeast, fine (Lab Scientific, cat. no. FLY-8040-20F)
- Clorox Ultra Germicidal Liquid Bleach (Fisher Scientific, cat. no. 50371500)
- Heptane (Fisher Chemical, cat. no. O3008-4)
- Paraformaldehyde (formaldehyde) solution, methanol free (32% (wt/vol); Electron Microscopy Sciences, cat. no. 15714) **! CAUTION** Paraformaldehyde is a toxic cross-linking agent. Wear protective gloves and handle it under a fume hood. Discard according to relevant environmental health and safety instructions **▲ CRITICAL** The use of methanol-free paraformaldehyde to fix embryos can greatly reduce autofluorescence.
- Formaldehyde solution (37% (wt/vol); Sigma-Aldrich, cat. no. 47608)
- Methanol (Fisher Chemical, cat. no. A412-4)
- Acetone (Merck, cat. no. 1000122500)
- Deionized formamide (100 mL; Amresco, cat. no. 0606) **! CAUTION** Formamide is toxic and should be handled with protective gloves under a fume hood and discarded according to relevant environmental health and safety instructions.
- Hydrogen peroxide solution (30% (wt/wt); Sigma-Aldrich, cat. no. H1009) **▲ CRITICAL** The stabilizer included in this reagent warrants a long shelf time.

- Alexa Fluor 488 tyramide reagent (Invitrogen, cat. no. B40953)
- RNA probe: full-length *snail* gene (Dmel_CG3956, dm6 15476621..15478176, flanking sequences ATTTAATTCTTCTCTTTAAGC and GGGTAAATCGGGAGATCGGCG), obtained from in vitro transcription of p190 plasmid⁴³ (Reagent setup)
- Tris(2-carboxyethyl)phosphine hydrochloride (TCEP; Sigma-Aldrich, cat. no. 646547)
- Anti-digoxygenin-POD, Fab fragments (anti-DIG; Roche, cat. no. 11207733910, RRID: AB_514500)
- Blocking reagent (Sigma-Aldrich, cat. no. 11096176001) ▲ **CRITICAL** Commercial blocking reagent warrants reproducibility.
- RNase A (Sigma-Aldrich, cat. no. R6513)
- Dextran sulfate (Sigma-Aldrich, cat. no. D8906)
- Salmon sperm DNA (Ambion, cat. no. AM9680)
- Heparin (Sigma-Aldrich, cat. no. H4784)
- BSA (Roche, cat. no. 10711454001)
- 4',6-Diamidino-2'-phenylindole dihydrochloride (DAPI; Roche, cat. no. 10236276001)
- Glucose oxidase (Sigma-Aldrich, cat. no. G2133)
- Catalase (Sigma-Aldrich, cat. no. C30)
- D(+) Glucose, anhydrous (Euromedex, cat. no. UG3050)
- Alexa 647 readout probes (Integrated DNA Technologies, custom order) Sequences can be found in Supplementary Table 2 and are complementary to the readout sequences.
- Rhodamine-labeled DNA oligo (for the fiducial barcode readout): CATTGCCGTATGGGCTAG-GATGACCTGGCTCG/3RhodRd-XN/ (Integrated DNA Technologies, custom order)
- Sodium hydroxide (NaOH)
- Boric acid
- Agar
- Apple juice
- Maleic acid
- Ethanol
- Dimethyl sulfoxide (DMSO)
- ddH₂O

Equipment

- PCR machine (thermal cycler; Bio-Rad, model no. T100)
- Positive-displacement micropipette (Gilson M250; Fisher Scientific, cat. no. F148505)
- Glass vial (2 mL, 11 mm; VWR, cat. no. 66009-822)
- Magnetic stir bar (BelArt, cat. no. 371191083)
- Magnetic stirrer (10 mm)
- NanoDrop spectrophotometer (Thermo Scientific, model no. ND-1000UV/Vis)
- Vortex (standard mini vortex; VWR)
- Falcon conical centrifuge tubes (15 mL and 50 mL; Fisher Scientific, cat. nos. 14-959-53A and 14-959-49A)
- Tabletop centrifuge (Eppendorf, cat. no. 5424)
- Syringes (30 mL, 20 mL and 10 mL; Terumo, cat. nos. SS-30S and SS-20S2; Dutscher, cat. no. 050008)
- Embryo collection cage (8.75 cm × 14.8 cm; Flystuff, cat. no. 59-101)
- Plastic Petri dishes (for small apple juice plates; 60 × 15 mm; Corning, cat. no. 430166)
- Nylon filter (BD Falcon, cat. no. 352350)
- Water bath (Grant Instruments, model no. JBN5; Fisher Scientific, cat. no. 15177015)
- Thermal mixer (AccuTherm microtube shaking incubator; Labnet, cat. no. I-4001-HCS)
- Gas burner
- Disposable scalpel (Swann-Morton, cat. no. 0516)
- Plastic Petri dishes (60-mm diameter; Greiner Bio-One, cat. no. 628163)
- Disposable glass Pasteur pipette (VWR, cat. no. 612-1702)
- Glass vial for embryo collection (DWK Life Sciences, cat. no. 986562)
- Rotating wheel
- Rapid automated modular microscope system (RAMM; Applied Scientific Instrumentation)
- Water-immersion objective (60×, numerical aperture (NA) = 1.2; Nikon Plan-achromat)
- sCMOS camera (Hamamatsu, model no. Orca Flash 4.0v3)
- Two-axis translation stage (Applied Scientific Instrumentation, model no. MS2000)
- Lasers (405, 488, 561 and 641 nm; Coherent, model nos. obis 405, obis 488, obis 640 and sapphire 561)

- Acousto-optic tunable filter (AA opto-electronics, cat. no. AOTFnC-400.650)
- Four-band dichroic mirror (Chroma, cat. no. zt405/488/561/640rpc-UF2)
- Four-band emission filter (Chroma, cat. no. ZET405/488/561/640m)
- Single-axis piezo stage (Mad City Labs, model no. Nano-F100)
- Laser (785 nm; Coherent, model no. obis 785)
- Position-sensitive detector (Newport, model no. OBP-A-4H)
- Microscope coverslips (Bioptechs, cat. no. 40-1313-0319)
- Microfluidic FCS2 chamber (Bioptechs, cat. no. 03060319-2-NH)
- Negative-pressure pump (Fluigent, model no. MFCS-EZ, cat. no. EZ-80345001)
- Flow unit L (Fluigent, ref. FLU-L-D)
- Online degassing unit (HPLC DegaSi Plus; Cluzeau Info Labo, cat. no. 00036352A)
- Acquisition computer: two Intel processors (model no. Xeon E5-2620), PCIe controller for RAID, two 512-GB SSD drives in RAID0, 32-GB RAM, graphics processing unit (GPU) card, four 2-TB disks for internal storage **▲ CRITICAL** Make sure there is enough space in the computer storage disk. The acquisition of 30 ROIs (~10 embryos) for 20 barcodes can take up to 1–1.5 TB.
- A server running on Linux with 32 CPU processors, 2 GeForce GTX 1080Ti GPU cards, and 128 GB of RAM
- HVXM8-5 injection valves (three) and controller (Hamilton, cat. nos. 36766 and 36798)
- Aluminum foil
- PCR strip tubes
- Parafilm

Software

- Oligopaints script suite (<http://genetics.med.harvard.edu/oligopaints>)
- MATLAB v.2017b (MathWorks: https://www.mathworks.com/products/new_products/release2017b.html)
- LabView 2015 (National Instruments: <https://forums.ni.com/t5/LabVIEW/LabView-2015-download/td-p/3687898?profile.language=en>)
- Huygens deconvolution software (Scientific Volume Imaging: <https://svi.nl/HuygensSoftware>)
- Custom-made software package (<https://github.com/marcnol/HiMacquisitionSoft.git>)

Reagent setup

PCR oil phase

The final concentration is 95.95:4:0.05 (vol/vol/vol) mineral oil/ABIL EM 90/Triton X-100. If available, a positive-displacement pipette can be used to directly pipette 2 mL of ABIL EM 90, 25 μ L of Triton X-100 and 47.975 mL of mineral oil into a 50-mL Falcon tube. Add the mineral oil in two steps, vortexing between them. If a positive-displacement pipette is not available, the volume can be accurately determined by weighing. To prepare 50 mL of PCR oil phase, weigh 20.3 g of mineral oil (around 24 mL) directly into a 50-mL Falcon tube, add 2 mL of ABIL EM 90 and 25 μ L of Triton X-100, vortex thoroughly and all the mixture to rest for 5 min. Then add 20 g of mineral oil and homogenize by inversion of the tube. Make 20-mL aliquots of PCR oil phase and store indefinitely at 4 °C.

1 M NaOH solution

Weigh 2 g of NaOH, mix it with 30 mL of ddH₂O in a 50-mL Falcon tube and dissolve. Bring the volume to 50 mL with ddH₂O and pass the solution through a 0.22- μ m filter. The solution can be stored at room temperature (RT; ~23 °C) for several months.

0.5 M EDTA solution

To prepare 200 mL, weigh 37.23 g of EDTA and mix it with 150 mL of ddH₂O in a glass beaker. Add a magnetic stir bar and stir while adjusting to pH 8 with 10 M NaOH. Add ddH₂O up to 200 mL. Filter the solution with a 0.22- μ m filter. The solution can be stored at 4 °C for several months. **▲ CRITICAL** EDTA will not dissolve until the pH approaches 8. Verify the pH of the final solution because the pH may decrease when EDTA is dissolved.

Water-saturated diethyl ether

Mix 3 mL of diethyl ether with 3 mL of ddH₂O and vortex for 30 s. Allow the mixture to settle and use the organic upper phase. Prepare freshly.

Water-saturated ethyl acetate

Mix 2 mL of ethyl acetate with 2 mL of ddH₂O and vortex for 30 s. Allow the mixture to settle and use the organic upper phase. Prepare freshly.

10% (vol/vol) Tween 20 solution

Mix 50 µL of Tween 20 with 450 µL of ddH₂O and vortex until the solution becomes homogeneous. Store at 4 °C for up to 2 weeks.

PBS–Tween 20 solution

To make PBS–Tween 20 solution (PBT), combine 49.5 mL of PBS with 500 µL of 10% Tween 20 (vol/vol). ▲ **CRITICAL** Prepare freshly.

PBS–Triton X-100 solution

To make PBS–Triton X-100 solution (PBS-Tr), add 50 µL of Triton X-100 to 10 mL of PBS and vortex until the solution becomes homogeneous. ▲ **CRITICAL** Prepare freshly.

4% (wt/vol) paraformaldehyde in PBS

To prepare 8 mL, mix 1 mL of 32% (wt/vol) paraformaldehyde (methanol free) with 7 mL of PBS. ▲ **CRITICAL** Prepare freshly.

5% (wt/vol) formaldehyde in PBT

Mix 1.35 mL of 37% (wt/vol) formaldehyde solution with 9 mL of PBT. ▲ **CRITICAL** Prepare freshly.

10× TBE

10× TBE is 1 M Tris base, 1 M boric acid and 0.02 M EDTA. Dissolve 60.55 g of Tris base, 30.9 g of boric acid and 3.7 g of EDTA. Adjust the volume to 500 mL with ddH₂O. Store at RT indefinitely.

Gel for urea PAGE

To make the gel, mix 6 g of urea, 1.25 mL of TBE 10× and 3.5 mL of ddH₂O. Heat the solution at 60 °C in a water bath until the urea has dissolved. Add 3.125 mL of acrylamide/bisacrylamide, 75 µL of 10% (wt/vol) APS and 15 µL of TEMED. Cast the polyacrylamide gel in 0.75-mm-thick spacers. Prepare freshly.

Yeast paste

Dissolve 25 g of fine dry yeast powder in 20 mL of water. Add enough water to achieve a consistency similar to that of peanut butter. Store it at 4 °C for up to 2 weeks.

Apple juice plates

To make the agar–apple juice plates, fill plastic Petri dishes halfway with agar mixed with apple juice. For a detailed protocol, refer to ref. ⁴⁴. Apple juice plates can be stored at 4 °C for 1 month.

RNA hybridization solution

RNA hybridization solution (RHS) is 5× SSC, 50% (vol/vol) formamide, 0.1% (vol/vol) Tween 20, 0.05 mg/mL heparin and 0.1 mg/mL salmon sperm. To prepare 250 mL of RHS, mix 125 mL of formamide, 62.5 mL of 20× SSC, 1.25 mL of 10 mg/mL heparin, 2.5 mL of 10% Tween 20 (vol/vol), 2.5 mL of 10 mg/mL salmon sperm and 56.25 mL of ddH₂O. Prepare 50-mL aliquots and store at –20 °C for up to several months.

RNA probe preparation

Use 250 ng of linearized p190 plasmid DNA (previously digested with NotI restriction enzyme) to in vitro–transcribe with digoxigenin haptenes using HiScribe T7 RNA polymerase according to the manufacturer's instructions. Treat the probe with carbonate buffer at 65 °C for 5 min to partially hydrolyze it. For a detailed protocol, refer to ref. ⁴⁵. Make 5-µL aliquots and store at –20 °C for a few months. For RNA-FISH, add 2 µL of RNA probe obtained in this way to 250 µL of RHS and incubate at 85 °C in a dry bath incubator for 2.5 min. Then incubate on ice for at least 2 min before adding it to

the embryos. ▲ **CRITICAL** Freshly prepare the RNA probe, keeping it on ice no more than an hour before its use. Check the temperature of the dry bath to avoid probe degradation. Do not exceed 2.5 min of incubation because high temperatures might degrade the probe. Do not denature reused probes.

Maleic acid buffer

Maleic acid buffer is 0.1 M maleic acid, 0.15 M NaCl. To make 200 mL of buffer, add 2.3 g of maleic acid, 1.7 g of NaCl, 1.2 g of NaOH and 100 mL of ddH₂O. Measure the pH and adjust to pH 7.5 with 5 M NaOH. Make up the volume to 200 mL with ddH₂O and filter. The solution can be stored at RT for up to six months.

5× blocking solution

Combine 10 g of blocking reagent with 50 mL of maleic acid buffer, agitate and heat until complete dissolution. Bring the volume to 100 mL with maleic acid buffer. Autoclave and make 10-mL aliquots.

▲ **CRITICAL** 5× blocking solution can be stored at −20 °C for up to several months. Once thawed, keep it on ice at all times.

1× blocking solution

Prepare the solution by mixing 5× blocking solution with PBT in a 1:4 ratio. ▲ **CRITICAL** Freshly prepare solution and keep it on ice. Discard any remaining solution.

RNase A solution

Dissolve the 10-mg vial in 1 mL of ddH₂O (100×). Make 50-μL aliquots and store at −20 °C for up to a year.

50% (wt/vol) dextran sulfate

To prepare the solution, combine 25 g of dextran sulfate with 40 mL of ddH₂O, heat to 37 °C until it fully dissolves and then add ddH₂O to a final volume of 50 mL. The solution can be stored at 4 °C for several months.

100 mM NaH₂PO₄, pH 7

To prepare 50 mL of this solution, mix 0.78 g of NaH₂PO₄ with 30 mL of ddH₂O. Adjust to pH 7, and bring the volume to 50 mL with ddH₂O. Pass the solution through a 0.22-μm filter. The solution can be stored at 4 °C for several months.

Prehybridization mixture

Prehybridization mixture (pHM) is 50% formamide, 4× SSC, 100 mM NaH₂PO₄, pH 7, and 0.1% Tween 20. Prepare freshly.

DNA hybridization solution

DNA hybridization solution (DHS) is 2× SSC, 50% (vol/vol) formamide, 10% (vol/vol) dextran sulfate and 0.5 mg/mL salmon sperm. Combine 5 mL of formamide, 2 mL of 50% (vol/vol) dextran sulfate, 1 mL of 20× SSC, 500 μL of salmon sperm (10 mg/mL) and 1.5 mL of ddH₂O. Store at −20 °C for up to several months. Prewarm at 37 °C before use.

50% (wt/vol) glucose

To prepare 40 mL of 50% (wt/vol) glucose, combine 20 g of glucose with 30 mL of ddH₂O, heat to 60 °C until it dissolves and then add ddH₂O to 40 mL. The solution can be stored at RT for several months.

DAPI solution

Prepare a 0.5 μg/mL DAPI solution in 1× PBS by diluting the stock solution. Store the solution, covered with aluminum foil, at 4 °C. The solution can be used over several weeks.

1 M NaCl solution

To prepare 50 mL of this solution, mix 2.92 g of NaCl with 30 mL of ddH₂O in a 50-mL Falcon tube and dissolve. Bring the volume to 50 mL with ddH₂O and pass the solution through a 0.22-μm filter. The solution can be stored at RT for several months.

1 M Tris-HCl solution, pH 8

To prepare 50 mL of this solution, mix 6 g of Tris base with 30 mL of ddH₂O. Using a pH meter, slowly add HCl with a glass Pasteur pipette to reach the desired pH. Bring the volume to 50 mL with ddH₂O, and pass the solution through a 0.22- μ m filter. The solution can be stored at RT for several months.

55 mM NaCl in 11 mM Tris-HCl solution, pH 8

To prepare 50 mL of this solution, mix 2.75 mL of 1M NaCl solution, 0.55 mL of 1M Tris-HCl solution, pH 8, and 46.7 mL of ddH₂O. Prepare freshly.

Gloxy solution

To prepare 1 mL of Gloxy solution, mix 50 mg of glucose oxidase, 100 μ L of catalase and 900 μ L of 55 mM NaCl in 11 mM Tris-HCl solution, pH 8. **▲ CRITICAL** Make 60- μ L aliquots and store at -20 °C. This solution is stable for several months. Defrost on the day of the experiment and keep on ice until use. If there is a precipitate, spin it down (16,000 g, 3 s at RT) and use the supernatant. Once thawed, an aliquot should be used within 1 week.

Hi-M wash buffer

Hi-M wash buffer is 2 \times SSC, 40% (vol/vol) formamide. To prepare 100 mL, combine 10 mL of 20 \times SSC and 40 mL of formamide and bring the volume to 100 mL with ddH₂O. **▲ CRITICAL** Freshly prepare formamide-containing solutions and pass them through a 0.22- μ m filter.

Hi-M acquisition solution

To prepare 10 mL of solution, combine 1 mL of 50% (wt/vol) glucose with 8.89 mL of PBS and 110 μ L of Gloxy solution. **▲ CRITICAL** Add Gloxy solution just before using the solution and mix. Once the tubing is introduced, add a layer of mineral oil to prevent contact with oxygen from the ambient air. Replace the solution after 12–15 h.

Readout probe solution

This solution contains a 25 nM concentration of the corresponding readout oligo in 40% (vol/vol) formamide, 2 \times SSC. Readout oligo sequences can be found in Supplementary Table 2. **▲ CRITICAL** Prepare freshly and keep the solution protected from light.

Chemical bleaching solution

To prepare 10 mL of chemical bleaching solution, mix one 1-mL ampule of TCEP with 9 mL of 2 \times SSC. **▲ CRITICAL** Prepare the solution immediately before use and discard any remaining solution.

Equipment setup**Wide-field epifluorescence microscope**

We use a RAMM modular microscope system (Fig. 7) equipped with a 60 \times water-immersion objective and a sCMOS camera for Hi-M imaging. With this objective–tube lens combination, we obtained a 108-nm pixel size, leading to a \sim 220 \times 220- μ m field of view. Sample displacement and embryo selection are performed using a two-axis translation stage. Wide-field epifluorescence illumination is achieved using 405-/488-/561- and 641-nm lasers combined with an acousto-optic tunable filter. To avoid the use of a mechanical filter-wheel, separation between excitation and emission light is done using a four-band dichroic mirror combined with a four-band emission filter. Finally, the objective lens is mounted on a single-axis piezo stage, enabling nanometer-precision control of the objective axial position during *z*-scans and focus stabilization.

A homemade focus stabilization system was used to compensate for the axial drift in real time. A 785-nm laser beam is focused on the back focal plane of the objective, reaching the coverslip–sample interface in near-TIRF illumination conditions. The position of the reflected beam is then measured on a position-sensitive detector, and any variation in the objective–sample distance >100 nm is automatically compensated for by repositioning the objective lens.

Hi-M sequential hybridization

Design of the fluid-handling circuits is implemented as described in Cardozo Gizzi et al.³ (Supplementary Fig. 1). Buffers and probes are selected, using a combination of three eight-way valves.

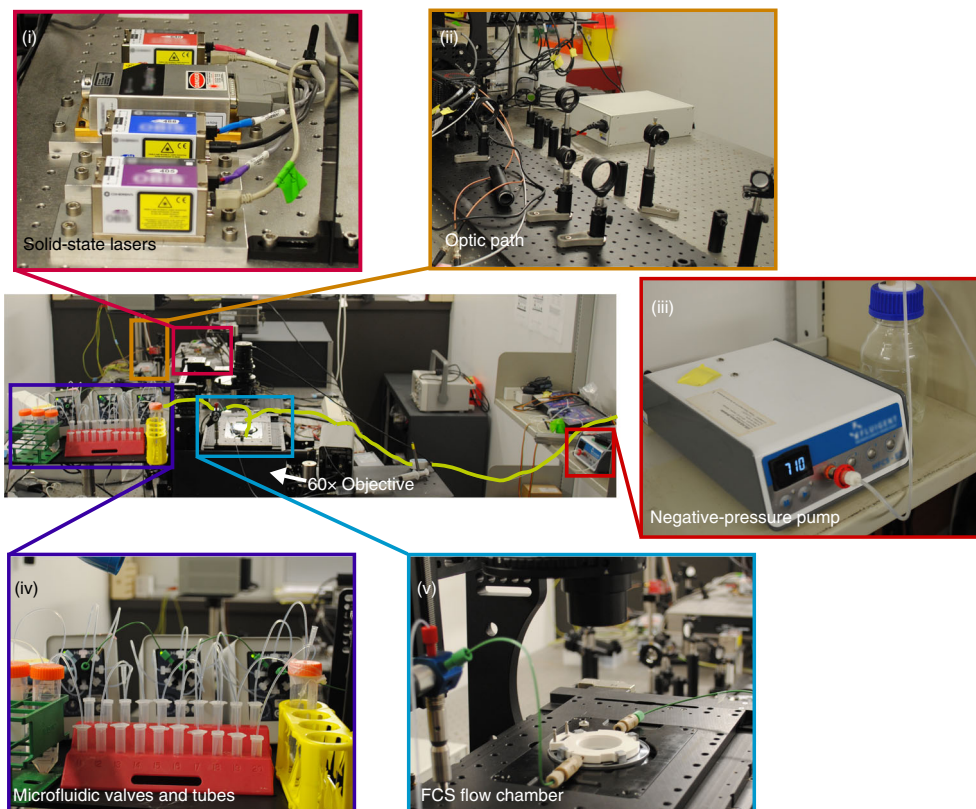


Fig. 7 | Hi-M setup. Center, an image of the Hi-M setup. White arrow indicates the location of the 60× water-immersion objective (not visible). The microfluidic tubing is highlighted in yellow. Colored rectangles correspond to zoomed-in images of key components. (i) The solid-state lasers are combined with dichroic mirrors, and an acousto-optic tunable filter (AOTF) is used to switch the different laser lines on/off and to change intensity. (ii) Beams are expanded by a telescope and focused at the back focal plane of a 60× objective. (iii) Flow is created by a negative-pressure pump at the outlet. Liquid is withdrawn from the inlet of a valve, (iv), passes through the FCS2 flow chamber (v) and the online flow unit, and is then discarded into the bottle in the outlet.

Therefore, the fluid-handling circuit consists of 21 tubes, each connected to one of the valves. The tubes are connected as follows: one tube with 12 mL of Hi-M acquisition solution, one tube with 15 mL of chemical bleaching solution and 17 tubes with 2.5 mL of readout probe solution. One tube with 50 mL of Hi-M wash buffer and another with 50 mL of 2× SSC pass through an online degassing unit before connecting to the corresponding valve to avoid air-bubble nucleation during Hi-M experiments. The sample is mounted within an FCS2 chamber, and flow is created using a negative-pressure pump. An online flow unit is used to continuously monitor flow rate, enabling precise control of injected volumes and maintaining a steady flow in the chamber.

User-microscope interface

Image acquisition, sample positioning and liquid handling are controlled by a custom-made software package developed in LabView 2015. The software package can be accessed at <https://github.com/marcnol/HiMacquisitionSoft.git>.

Procedure

Design of Oligopaints libraries ● Timing 4-5 h

- 1 Download the Oligopaints scripts⁷ (including grabRegion.py and orderFile.py) and .bed files containing all primary oligos by following the instructions in the Scripts Manual found in the ‘Documentation’ tab of <http://genetics.med.harvard.edu/oligopaints>.
▲ CRITICAL STEP .bed files contain the sequences of oligos previously mined using OligoArray³¹ or OligoMiner³³, covering the *Drosophila* non-repetitive genome.
- 2 Define genomic locations of interest (barcodes) and use grabRegion.py to select the oligos corresponding to each barcode. To execute the grabRegion.py script, open a Command Prompt

(Windows) or Terminal (OS X/Linux/UNIX) window in the folder containing the script. Next, type the following command:

```
python grabRegion.py -i data.bed
```

where `data.bed` is the name of the chromosome database file. A dialog box will appear asking the user to enter start and end coordinates. Repeat the process for all barcode coordinates. Record the number of oligos in each barcode because this will be necessary later.

▲ CRITICAL STEP Further instructions on how to use the scripts, including step-by-step examples, can be found on the Scripts Manual.

▲ CRITICAL STEP Include also a fiducial barcode. For this, select a genomic region of ~20 kb (or 200 oligos) that does not overlap with any of the other barcodes.

- An output text file for each barcode is created with a list of oligos. Concatenate all output files using a Command Prompt/Terminal window. For example, in Linux/UNIX, use the following command:

```
cat file1.txt file2.txt file3.txt > mergedfile.txt
```

Use `type` instead of `cat` in a Windows Command Prompt window.

- Create a unique text file with the readout sequences for all barcodes and name it 'primers.txt'. It consists of a line for each barcode. In each line, add (i) the 5' readout sequence, (ii) the 3' readout sequence (repeat the previous sequence) and (iii) and the range of probes that compose the barcodes (i.e., 1–50, 51–96) based on the number of oligos in each barcode obtained in Step 2. The information (i–iii) must be separated with tabs. Use the sequences from Supplementary Table 3. For example, if using readout1 and 50 oligos were found for barcode 1, the first line would be as follows:

```
CACACGCTCTTCCGTTCTATGCGACGTCGGTGACACGCTCTTCCGTTCTATGCGACGTCGGT
G1-50
```

▲ CRITICAL STEP The sequences must be given in the 5' to 3' direction.

▲ CRITICAL STEP For the fiducial barcode, the readout sequence is the reverse complementary of the rhodamine-labeled oligo (Reagents).

- It is necessary to add the universal priming region to the sequences present in the primers.txt file from Step 4. To do so, insert the forward universal priming sequence into the first column and the reverse universal priming sequence into the second column in all rows. Use the sequences from Supplementary Table 4.

▲ CRITICAL STEP Both forward and reverse primers should be input in the 5' to 3' direction.

- Use `orderFile.py` to add the corresponding readout plus universal primer sequences to all the oligos in the library. Open a Command Line/ Terminal window in the folder containing the scripts, where all the output files are located, and type:

```
python orderFile.py -p primers.txt mergedfile.txt
```

This will require the full list of oligos from Step 3 (named 'mergedfile.txt' in this example) and the readout sequences file created in Step 5 (named 'primers.txt' in this example).

▲ CRITICAL STEP It is possible to embed multiple libraries within one oligo pool by using different sets of universal primers.

- Order the library of template oligos from an oligo pool synthesizer company such as CustomArray or Twist Bioscience. Upon receipt, briefly centrifuge the tube (16,000 g, 3 s at RT) and resuspend in nuclease-free 10 mM Tris-HCl solution, pH 8.0, to a concentration of 10–30 ng/μL. Prepare aliquots to limit chances of contamination.

▲ CRITICAL STEP Companies typically require 2 weeks to synthesize a custom-made oligo pool.

■ PAUSE POINT Store at –20 °C for up to a year. For longer (several years) storage, keep at –80 °C.

Amplification of Oligopaints ● Timing 4–5 d

- Emulsion PCR*. This step is performed to amplify the starting oligo pool (which can be limiting) in a non-biased manner. Set up a PCR master mix for each library as indicated below and keep it on ice until needed.

Reagent	Quantity (μL)
ddH ₂ O	79
10× Kapa Taq buffer A ^a	10
BSA (10 μg/μL)	5
dNTPs (10 mM) ^a	2
Forward primer (200 μM)	1
Reverse primer (200 μM)	1
Kapa polymerase enzyme ^a (5 U/μL)	1
Oligo pool library (10–30 ng/μL; from Step 7)	1
Total	100

^aFrom the KAPA Taq Kit with dNTPs.

Pre-chill a 2-mL, 11-mm glass vial in the freezer, place it on the center of a controlled stir plate and then add a pre-cooled stir bar to the vial. Use a positive-displacement pipette to transfer 600 μL of PCR oil phase to the glass vial. Stir at 1,000 r.p.m. for at least 1 min. While the stir bar is still spinning, add 100 μL of PCR master mix in 20-μL increments, using a P20 pipette (i.e., dispense 20 μL five times). Stir at 1,000 r.p.m. for 10 min; the emulsion should appear milky white and foamy. Use a positive-displacement pipette to transfer the emulsion to a PCR strip tube (~8 × 75-μL aliquots).

▲ CRITICAL STEP The forward primer is the 5' to 3' forward universal priming sequence, whereas the reverse primer is the reverse complement of the reverse universal priming sequence listed in Supplementary Table 4.

▲ CRITICAL STEP Emulsion preparation must be performed in a cold room at 4 °C. All the equipment must be put there in advance to cool it down before use.

▲ CRITICAL STEP It is not possible or necessary to transfer the whole emulsion volume to the PCR strip tube.

- 9 Perform the PCR, using the following cycling conditions:

Cycle no.	Denature	Anneal	Extend
1	95 °C, 2 min		
2–31	95 °C, 15 s	60 °C, 15 s	72 °C, 20 s
32			72 °C, 5 min

■ PAUSE POINT PCR product can be stored at 4 °C for a few days.

- 10 *Small-scale emulsion PCR breaking.* Pool the emulsion PCR reactions in a 1.5-mL microcentrifuge tube. Add 1 μL of gel loading buffer (this will enable visualization of the aqueous phase in the next step). Add 200 μL of mineral oil and vortex for 30 s. Centrifuge at 16,000g for 10 min at RT and remove and discard the upper organic phase.
- 11 Add 1 mL of water-saturated diethyl ether and vortex for 1 min. Centrifuge at 16,000g for 1 min at RT and remove and discard the organic upper phase.
- 12 Add 1 mL of water-saturated ethyl acetate and vortex 1 for min. Centrifuge at 16,000g for 1 min at RT and remove and discard the organic upper phase.
- 13 Repeat Step 11. Incubate the tube at 37 °C for 5 min with the cap open to evaporate residual diethyl ether.

▲ CRITICAL STEP The final volume should be ~80 μL.

■ PAUSE POINT The PCR product can be stored at 4 °C for a few days.

- 14 *Purify the DNA with an Oligo Clean & Concentrator Kit.* Mix 80 μL of DNA from the preceding step with 160 μL of Oligo Binding Buffer and 320 μL of ethanol. Homogenize the solution by pipetting up and down 10 times. Follow the manufacturer's instructions up to the DNA elution step. Repeat the elution with an extra 15 μL of water and then add 20 μL of water directly into the tube to obtain a final volume of 50 μL.

- 15 Quantify the DNA concentration with a spectrophotometer by directly taking 2 μL of purified PCR product. The concentration should be between 20 and 40 $\text{ng}/\mu\text{L}$.
- 16 Run a gel electrophoresis to check for the presence of a single band, using 200 ng of PCR product in a 1.5% (wt/vol) agarose gel with 0.01% (vol/vol) SYBR Safe at 100 V for 45 min.

? TROUBLESHOOTING

■ **PAUSE POINT** The purified products can be frozen at $-20\text{ }^{\circ}\text{C}$ for several months.

- 17 Prepare for the small-scale limited-cycle PCR by setting up the following reaction mix for 8 tubes as indicated in the table below.

Reagent	Quantity per tube (μL)
10 \times Kapa Taq buffer A ^a	5
dNTPs (10 mM) ^a	1
Forward primer (100 μM)	0.5
Reverse primer (100 μM)	0.5
Template emulsion PCR (1 $\text{ng}/\mu\text{L}$; from Step 16)	2.5
Kapa DNA polymerase ^a (5 U/ μL)	0.5
ddH ₂ O	Bring to a final volume of 50 μL

^aFrom the KAPA Taq Kit with dNTPs.

▲ **CRITICAL STEP** The T7 promoter sequence (5'-TAATACGACTCACTATAGGGT-3') should be appended 5' to the reverse primer sequence used for the emulsion PCR step to allow for the reverse transcription step.

- 18 Run the following PCR program:

Cycle no.	Denature	Anneal	Extend
1	95 $^{\circ}\text{C}$, 5 min		
2-15	95 $^{\circ}\text{C}$, 30 s	60 $^{\circ}\text{C}$, 45 s	72 $^{\circ}\text{C}$, 30 s

Pick up the corresponding tube after each of cycles 8–15 just after the extension phase. To do so, quickly open the PCR machine, remove the corresponding tube, close the lid and resume the program.

▲ **CRITICAL STEP** The limited number of cycles are performed to find the cycle number at which the PCR is still at its exponential phase (Fig. 4a). Perform this step before proceeding to the large-scale PCR (Step 20).

■ **PAUSE POINT** The PCR product can be left overnight (ON) at 4 $^{\circ}\text{C}$ or frozen for up to a month at $-20\text{ }^{\circ}\text{C}$.

- 19 Run 20 μL of each PCR product on a 1.5% (wt/vol) agarose gel with 0.01% SYBR Safe at 100 V for 45 min. Find the reaction corresponding to the number of amplification cycles resulting in a single band of the expected size and the maximum intensity (PCR cycle 12 in Fig. 4a).
- 20 Perform a large-scale limited-cycle PCR by preparing a reaction mix for 16 tubes as indicated in the table below. This PCR reaction will generate a large quantity of Oligopaints.

Reagent	Quantity (μL)
10 \times Kapa Taq buffer A ^a	80
dNTPs ^a (10 mM)	16
Forward primer (100 μM)	8
Reverse primer (100 μM)	8
Kapa DNA polymerase ^a (5 U/ μL)	8
ddH ₂ O	640
Template emulsion PCR (1 $\text{ng}/\mu\text{L}$; from Step 16)	40

^aFrom the KAPA Taq Kit with dNTPs.

- 21 Split the volume of the PCR mix into 16 PCR tubes (50 μL each) and run the PCR program from Step 18, using the optimized number of cycles determined in Step 19. Add a last extension cycle of 5 min at 72 $^{\circ}\text{C}$.
 - **PAUSE POINT** PCR products can be safely stored for months at -20°C .
- 22 Collect the 50- μL aliquots from the preceding step into a 15-mL Falcon tube and run 20 μL of it in an agarose gel as in Step 16 to check that the PCR was successful.
 - ? **TROUBLESHOOTING**
- 23 Proceed to DNA column purification according to the manufacturer's instructions.
 - ▲ **CRITICAL STEP** Use a Zymo DNA Clean & Concentrator Kit with 25- μg capacity. Elute using 30 μL of DNase- and RNase-free water.
- 24 Quantify the product concentration with a spectrophotometer, using double-stranded DNA parameters. This typically requires a 1:10 dilution of a 2- μL aliquot of the purified product. The concentration of the undiluted stock should be between 30 and 50 $\text{ng}/\mu\text{L}$.
- 25 Run the remainder of the 1:10 stock dilution on a 1.5% agarose gel as in Step 16 (Fig. 4b).
 - ▲ **CRITICAL STEP** Check for a single band of the expected size.
- 26 Perform in vitro transcription by setting up the reaction mix as indicated below:

Reagent	Quantity (μL)
Purified PCR product (from Step 23)	6 μg of template DNA
ATP (100 mM) ^a	6
UTP (100 mM) ^a	6
CTP (100 mM) ^a	6
GTP (100 mM) ^a	6
10 \times T7 buffer ^a	6
RNasin ribonuclease inhibitor (40 U/ μL)	2.25
HiScribe T7 polymerase ^a	6
ddH ₂ O	Bring to a final volume of 60 μL

^aFrom the HiScribe T7 High Yield RNA Synthesis Kit.

- ▲ **CRITICAL STEP** This step is a high-yield reaction that converts the template molecules into RNA and amplifies them further. It is necessary to keep RNase-free conditions at all times.
 - ? **TROUBLESHOOTING**
- 27 Split the volume from the in vitro transcription solution into 3 PCR tubes and incubate at 37 $^{\circ}\text{C}$ for 12–16 h in a thermocycler.
 - **PAUSE POINT** In vitro transcription product can be stored frozen for months at -80°C .
 - 28 Take 5 μL of in vitro transcription product and purify it with an Oligo Clean & Concentrator Kit according to manufacturer's instructions, using 15 μL of DNase- and RNase-free water to elute the purified product.
 - ▲ **CRITICAL STEP** The purification is performed with only a small aliquot to check whether the in vitro transcription was successful and to estimate the RNA concentration in the non-purified RNA solution. Use the Oligo & Concentrator Zymo kit.
 - 29 Make a 1:10 dilution to perform a quantification of the purified RNA on a spectrophotometer using RNA parameters. The concentration should be between 0.5 and 2 $\mu\text{g}/\mu\text{L}$.
 - ▲ **CRITICAL STEP** The concentration obtained enables estimation of the concentration in the remaining non-purified RNA sample. For example, a 2 $\mu\text{g}/\mu\text{L}$ concentration of the purified RNA can be translated to an estimated concentration of 6 $\mu\text{g}/\mu\text{L}$ in the non-purified RNA, taking into account a dilution factor of 3 (from a 5- μL aliquot to a final volume of 15 μL). The total yield of the in vitro transcription step should be ~ 150 –450 μg from a single transcription step (60 μL in total).
 - 30 *Check for the RNA quality by urea PAGE.* Perform a pre-run for 30 min in 1 \times TBE at 190 V to eliminate the excess of persulfate. When finished, wash the wells with the running buffer. Load 100 ng of purified RNA per lane. Heat the sample at 95 $^{\circ}\text{C}$ for 5 min and put it immediately on ice for 2 min. Run the gel for 1 h at 190 V. For gel staining, incubate, protected from light, for 20 min at RT in 30 mL of 1 \times TBE and 3 μL of SYBR Gold (Fig. 4c).
 - 31 Perform the reverse transcription reaction according to the Maxima H reverse transcriptase kit instructions by setting up the reaction mix indicated below.

Product	Quantity (μL)
Non-purified transcription product (from Step 27)	150 μg
dNTP mix ^a (100 mM)	12
Forward primer (100 μM)	50
5 \times RT buffer ^b	240
RNasin ribonuclease inhibitor (40 U/ μL)	30
Maxima H Minus reverse transcriptase ^b (200 U/ μL)	30
ddH ₂ O	Bring to a final volume of 1,200 μL

^aFrom the KAPA Taq Kit with dNTPs. ^bFrom the Maxima H Minus reverse transcriptase kit.

- ▲ CRITICAL STEP** In this step, the non-purified RNA from Step 27 is directly used. RNA should always be kept on ice to prevent degradation.
- ▲ CRITICAL STEP** The primer sequence is the same as for the forward primer used in the emulsion PCR and limited-cycle PCR.
- 32 Split the volume obtained in the preceding step into two 1.5-mL tubes and incubate for 3 h at 50 °C in a water bath.
- PAUSE POINT** The reverse transcription product can be stored frozen for months at -20 °C.
- 33 Perform the RNA degradation by adding 300 μL of 0.5 M EDTA and 300 μL of 1 M NaOH to each tube and incubating the tubes at 95 °C for 15 min in a water bath.
- ▲ CRITICAL STEP** This step enables the selective degradation of the RNA while retaining ssDNA.
- 34 Take a 10- μL aliquot to control for DNA concentration and to perform a gel electrophoresis as in Step 16.
- 35 *DNA probe purification.* Mix the two aliquots from Step 33 in a sterile 50-mL Falcon tube. Add 4.8 mL of Oligo Binding Buffer and 19.2 mL of ethanol. Homogenize by inverting the tube a few times and spread over two columns. Follow the manufacturer's instructions from this point on.
- ▲ CRITICAL STEP** Use the Zymo DNA Clean & Concentrator Kit with 100- μg capacity.
- 36 Take a 10- μL aliquot to measure the DNA concentration using a spectrophotometer and to perform a gel electrophoresis as in Step 16. The concentration should be between 250 and 400 ng/ μL , that is, 75–120 μg of ssDNA in total in 300 μL of DNA elution.
- 37 *Ethanol precipitation.* Directly add to the 300- μL DNA elution from Step 35 (2 \times 150 μL) 24 μL of 5 M ammonium acetate, 6 μL of glycogen and 750 μL of 100% (vol/vol) ethanol at -20 °C. Vortex and incubate for 1 h at -80 °C. Centrifuge at 13,000g for 1 h at 4 °C. Discard the supernatant and wash the pellet with 1 mL of ice-cold 70% ethanol (vol/vol). Centrifuge at 13,000g for 15 min at 4 °C. Discard the supernatant, air-dry the pellet for 10 min at 37 °C and add 20 μL of DNase- and RNase-free water. Let the ssDNA resuspend for 10 min at 37 °C, and then place and keep on ice.
- 38 Quantify the oligo concentration with a spectrophotometer, using ssDNA parameters.
- ▲ CRITICAL STEP** The total quantity of ssDNA should be on the order of 80–120 μg .
- 39 Check the quality of the ssDNA by urea PAGE as described in Step 30 (Fig. 4c).
- ▲ CRITICAL STEP** This step enables verification of RNA degradation and the efficacy of the reverse transcription step.
- PAUSE POINT** Probes can be stored at -20 °C for months.

Embryo collection and fixation ● Timing 2–3 h

- 40 Place 200–400 flies with a 2:1 female/male ratio into an egg-collection cage equipped with an apple juice plate containing a dollop of yeast paste and prewarmed to 25 °C (or the temperature required for the specific experiment). Perform an ON pre-laying step.
- 41 Replace the plate with a new one containing a dollop of yeast paste prewarmed to 25 °C. Perform a laying step for 1.5 h at 25 °C.
- 42 Remove the plate, cover it and incubate for 1 h (or the time required to obtain embryos at the desired developmental stage) at 25 °C.
- 43 Rinse the plates with ddH₂O and carefully detach the embryos using a brush. Filter the liquid with a Nylon filter. The embryos will remain on the filter.
- 44 Prepare a six-well plate with one well containing bleach at 2.6% active chlorine, and the other five containing water. Put the filter with the embryos into the bleach-containing well and incubate for 5 min.

- 45 Rinse the embryos by sequentially immersing the Nylon filter into each of the water-containing wells. Dry embryos between steps by pressing on a paper tissue.
- 46 Use a 1-mL pipette to add 5 mL of 4% (vol/vol) paraformaldehyde in PBS to rinse the filter and displace the embryos into a 20-mL glass vial.
! CAUTION Paraformaldehyde is toxic and should be handled with protective gloves under a fume hood and discarded according to the relevant environmental and safety instructions.
▲ CRITICAL STEP To facilitate the transfer of the embryos, place all of them at the center of the filter. Embryos on the borders of the filter might otherwise be lost.
- 47 Add 5 mL of heptane to the vial, then close and vigorously shake it manually for 30 s. You can cover the cap of the vial with Parafilm to avoid leakage of the paraformaldehyde and heptane solution inside. Incubate the embryos for 20 min at RT.
- 48 Use a glass Pasteur pipette to aspirate the lower aqueous phase from the bottom of the vial and discard it.
! CAUTION Paraformaldehyde is toxic and should be handled with protective gloves under a fume hood and discarded according to the relevant environmental and safety instructions.
- 49 Add 5 mL of methanol and vortex the glass vial for 15 s. Use a glass Pasteur pipette to transfer the embryos from the bottom of the glass vial to a 1.5-mL tube.
! CAUTION Methanol is toxic and highly volatile; it should be handled with protective gloves under a fume hood and discarded according to the relevant environmental and safety instructions.
▲ CRITICAL STEP Avoid using plastic tips to transfer the embryos because a portion of the embryos can remain attached to the plastic.
- 50 Wash the embryos three times with 1 mL of methanol.
■ PAUSE POINT Fixed embryos can be stored in methanol at $-20\text{ }^{\circ}\text{C}$ for months.

(Optional) RNA in situ hybridization ● Timing 2.5 d

▲ CRITICAL This procedure can be omitted if only DNA-labeled embryos are required.

- 51 Transfer 30 μL of fixed embryos from Step 50 to a 1.5-mL tube.
▲ CRITICAL STEP Use a glass Pasteur pipette.
- 52 Rinse the embryos with 1 mL of 100% (vol/vol) methanol. Wash the embryos with 1 mL of a 1:1 mixture of 100% (vol/vol) methanol and 100% (vol/vol) ethanol and incubate for 5 min at RT on a rotating wheel.
▲ CRITICAL STEP Let the embryos settle to the bottom of the tube by gravity (1–2 min) and then carefully remove and discard the washing solution.
- 53 Rinse the embryos twice with 1 mL of 100% (vol/vol) ethanol. Wash the embryos with 1 mL of 100% (vol/vol) ethanol and incubate for 5 min at RT on a rotating wheel.
- 54 Repeat the preceding step.
▲ CRITICAL STEP These steps remove impurities and reduce background.
- 55 Rinse the embryos twice with 1 mL of 100% (vol/vol) methanol. Wash the embryos with 1 mL of 100% (vol/vol) methanol and incubate for 5 min at RT on a rotating wheel.
- 56 Wash the embryos with 1 mL of a 1:1 mixture of 100% (vol/vol) methanol and 5% (vol/vol) formaldehyde in PBT and incubate for 5 min at RT on a rotating wheel. Rinse the embryos with 1 mL of 5% (vol/vol) formaldehyde in PBT.
! CAUTION Formaldehyde is toxic and should be handled with protective gloves under a fume hood and discarded according to the relevant environmental and safety instructions.
- 57 Fix the embryos with 1 mL of 5% (vol/vol) formaldehyde in PBT for 25 min at RT on a rotating wheel.
▲ CRITICAL STEP Post-fixation ensures RNA integrity.
- 58 Rinse the embryos twice with 1 mL of PBT. Wash the embryos four times with 1 mL of PBT and incubate for 15 min at RT on a rotating wheel.
■ PAUSE POINT Once rehydrated, the embryos can be stored in PBT for several hours at RT or for several days at $4\text{ }^{\circ}\text{C}$ before continuing to the next step.
- 59 Permeabilize the embryos by incubation with PBS-Tr for 1 h at RT on a rotating wheel.
- 60 Rinse the embryos with 1 mL of PBT. Wash the embryos three times with 1 mL of PBT and incubate for 5 min at RT on a rotating wheel.
- 61 Wash the embryos with 1 mL of a 1:1 mixture of RHS/PBT and incubate for 10 min at RT on a rotating wheel.
■ PAUSE POINT It is possible to store the embryos in RHS at $-20\text{ }^{\circ}\text{C}$ for several weeks.

- 62 Incubate the embryos with 1 mL of prewarmed (to 55 °C) RHS in a thermal mixer at 800–900 r.p.m. at 55 °C for 10 min.
! CAUTION RHS contains formamide, which is toxic and should be handled with protective gloves under a fume hood and discarded according to the relevant environmental and safety instructions.
- 63 Replace the media with fresh prewarmed (to 55 °C) RHS and incubate the embryos at 55 °C in a thermal mixer at 800–900 r.p.m. for 45 min.
▲ CRITICAL STEP Before changing the media, allow the embryos to settle to the bottom of the tube. Because RHS is highly viscous, this could take several minutes. It is possible to use the thermal mixer at 300 r.p.m. to speed up the process.
- 64 Repeat the preceding step with an incubation time of 1 h 15 min.
- 65 Completely remove the RHS and immediately add the 250 µL of RNA probe (Reagent setup). Incubate the embryos at 55 °C ON in a thermal mixer at 800–900 r.p.m.
▲ CRITICAL STEP Work fast to ensure that the embryos remain at 55 °C when adding the probe directly from the ice.
- 66 Retain the supernatant with the used probe for two more utilizations by carefully aspirating it. The used probe can be stored at –20 °C for up to several months.
▲ CRITICAL STEP Allow the embryos to settle to the bottom of the tube by stopping the thermal mixer agitation for 3–5 min.
- 67 Rinse the embryos twice with 1 mL of RHS prewarmed to 55 °C. Wash the embryos four times with 1 mL of prewarmed RHS in a thermal mixer at 800–900 r.p.m. at 55 °C for 30 min.
- 68 Wash the embryos with 1 mL of a 1:1 mixture of RHS/PBT and incubate for 10 min at RT on a rotating wheel.
- 69 Wash the embryos three times with 1 mL of PBT and incubate for 20 min at RT on a rotating wheel.
- 70 Perform a saturation step by incubating the embryos with 1× blocking solution for 45 min at RT on a rotating wheel.
▲ CRITICAL STEP The use of the commercially available blocking solution greatly reduces unspecific binding of the antibody.
- 71 Remove the 1× blocking solution and incubate the embryos with 1 mL of 1% hydrogen peroxide (vol/vol) in PBT for 30 min at RT on a rotating wheel.
▲ CRITICAL STEP The inactivation of endogenous peroxidases is required to avoid a high fluorescence background.
- 72 Wash the embryos two times with 1 mL of PBT and incubate for 5 min at RT on a rotating wheel.
- 73 Incubate the embryos with the anti-DIG antibody (1:500 dilution in 1× blocking solution) ON at 4 °C on a rotating wheel.
- 74 Rinse the embryos twice with 1 mL of PBT. Wash the embryos five times with 1 mL of PBT and incubate for 12 min at RT on a rotating wheel.
- 75 Incubate the embryos with the tyramide solution (5 µL of Alexa Fluor 488 tyramide reagent in 500 µL of PBT) for 30 min at RT on a rotating wheel.
▲ CRITICAL STEP Use aluminum foil to protect the embryos from the light.
- 76 Prepare a 1.5% hydrogen peroxide (vol/vol) solution. Directly add 4 µL of the solution to the embryos from the preceding step and incubate for 30 min at RT on a rotating wheel.
- 77 Rinse the embryos twice with 1 mL of PBT. Wash the embryos three times with 1 mL of PBT and incubate for 5 min at RT on a rotating wheel.
■ PAUSE POINT RNA-labeled embryos can be stored for weeks at 4 °C before proceeding to DNA labeling or imaging.

DNA in situ hybridization ● Timing 1.5 d

- 78 Transfer ~30 µL of embryos from either Step 50 or Step 77 to a 1.5-mL tube.
▲ CRITICAL STEP Use a glass Pasteur pipette to prevent the embryos from sticking to the pipette.
- 79 Rehydrate the fixed embryos by incubating them sequentially with 1 mL of each of the following solutions: (i) 90% methanol, 10% PBT; (ii) 70% methanol, 30% PBT; (iii) 50% methanol, 50% PBT; (iv) 30% methanol, 70% PBT; (v) 100% PBT. Incubate for 3–5 min at RT on a rotating wheel for each step.
▲ CRITICAL STEP If the embryos are RNA labeled, omit Step 79.
- 80 Incubate the embryos with 1 mL of PBT, 100 µg/mL RNase for 2 h at RT or ON at 4 °C on a rotating wheel.

- 81 Permeabilize the embryos by incubating them with PBS-Tr for 1 h at RT on a rotating wheel.
- 82 Transfer the embryos to pHM by passing them through 1 mL of each of the following freshly made solutions: (i) 80% PBS-Tr, 20% pHM; (ii) 50% PBS-Tr, 50% pHM; (iii) 20% PBS-Tr, 80% pHM; (iv) 100% pHM. Incubate for 20 min at RT on a rotating wheel for each step.
▲ CRITICAL STEP Before exchanging solutions, allow the embryos to settle for 2–3 min.
- 83 Prepare the primary DNA probe by adding 45–225 pmol of Oligopaints probe (barcode oligos) from Step 37 to 25 μ L of DHS. Keep the mix on ice. Denature the primary DNA probe by incubation for 15 min at 80 °C in the thermal mixer without mixing.
▲ CRITICAL STEP The amount of probe used should be tested by quantifying the efficiency of labeling at increasing concentrations of the DNA probe.
- 84 Carefully remove the pHM solution from the embryo tube and discard it; then add 1 mL of fresh pHM. Denature the embryonic DNA by incubation for 15 min at 80 °C in a water bath.
- 85 Carefully remove the pHM solution from the embryo tube and discard it; then add 30 μ L of the denatured probes from Step 83. Mix by gently flicking the tube with a finger. Carefully add 40 μ L of mineral oil. Change the water bath temperature to 37 °C and incubate the embryos ON at 37 °C in the water bath.
▲ CRITICAL STEP Mineral oil layer is added on top to prevent evaporation.
▲ CRITICAL STEP Allowing the embryos to slowly cool from 80 °C to 37 °C in the water bath greatly increases efficiency of labeling.
- 86 Use a P20 pipette to carefully remove as much mineral oil as possible from the tube.
▲ CRITICAL STEP Residual oil markedly affects embryo attachment to coverslips and interferes with image acquisition.
- 87 Add 500 μ L of 50% (vol/vol) formamide, 2 \times SSC, 0.3% (wt/vol) CHAPS to the embryos tube and mix by inverting the tube 3–5 times; wait 30 s for the embryos to reach the bottom of the tube. Carefully remove the supernatant and discard it.
▲ CRITICAL STEP This helps to immediately remove the mineral oil after hybridization. If the quantity of remaining oil is too big, this step will not be enough to prevent subsequent issues of attachment and image acquisition.
- 88 Perform post-hybridization washes by passing the embryos through 1 mL of each of the following freshly made solutions: (i) 50% (vol/vol) formamide, 2 \times SSC, 0.3% (wt/vol) CHAPS; repeat this wash once; (ii) 40% (vol/vol) formamide, 2 \times SSC, 0.3% (wt/vol) CHAPS; (iii) 30% formamide, 70% PBT; (iv) 20% formamide, 80% PBT; (v) 10% formamide, 90% PBT; (vi) 100% PBT; (vii) 100% PBS-Tr. Perform washes (i–iv) for 20 min at 37 °C in a thermal mixer with agitation (800 to 900 r.p.m.); perform washes (v–vii) for 20 min at RT on a rotating wheel.
- 89 (Optional) Rinse the embryos with 1 mL of PBT. Crosslink the barcode oligos by incubating the embryos with 1 mL of 4% (wt/vol) paraformaldehyde in PBT for 30 min at RT on a rotating wheel.
▲ CRITICAL STEP Although optional, in our experience, crosslinking the primary library has improved the labeling efficiency.
- 90 Rinse the embryos with 1 mL of PBT. Incubate the embryos with the rhodamine-labeled DNA oligo (fiducial barcode readout probe) in 1 mL of hybridization buffer (25 nM readout probe solution, 2 \times SSC, 40% vol/vol formamide; Reagent Setup) for 30 min at RT on a rotating wheel.
▲ CRITICAL STEP The rhodamine-labeled probe is used for the fiducial barcode. Protect samples from light exposure from this point onward.
- 91 (Optional) Perform an additional crosslinking step as in Step 89.
- 92 Rinse the embryos with 1 mL of PBT. Incubate the embryos with DAPI for 20 min at RT on a rotating wheel. Afterward, remove and discard the DAPI and rinse the embryos three times with 1 mL of PBS.
▲ CRITICAL STEP Detergent-containing PBT can prevent the embryos from attaching to the coverslip.
■ PAUSE POINT DNA-labeled embryos can be stored for weeks at 4 °C before proceeding to mounting and imaging.

Attachment of embryos to the microfluidic chamber ● Timing 1 h

- 93 Wash a coverslip sequentially with acetone, ethanol and water and dry it with a flame from a Bunsen burner, with the air valve nearly closed, by smoothly passing the coverslip over the flame three or four times. Place the dry coverslip into a 35-mm plastic dish.
▲ CRITICAL STEP Excessive heating of the coverslip with the flame may deform it and may affect imaging and sealing of the sample within the microfluidic chamber.

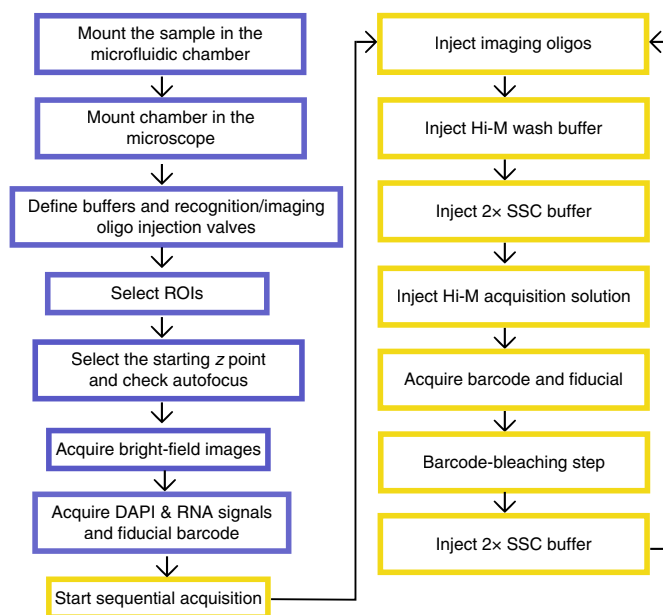


Fig. 8 | Hi-M image acquisition flowchart. Left, sequence of steps required for sample mounting, microscope setup and DAPI/RNA signal acquisition (violet boxes). Right, sequence of steps needed for the sequential barcode acquisition (yellow boxes).

94 Add 1 mL of poly-L-lysine solution (1:10 dilution in ddH₂O) to the coverslip and incubate for 20 min at RT. Steps for embryo attachment are shown in Fig. 5a. Afterward, rinse the coverslip with ddH₂O.

95 Dry the coverslip with a paper tissue. Thoroughly dry the coverslip using compressed air for 10–15 s.

▲ **CRITICAL STEP** The embryos will not attach if coverslip is not completely dry.

96 Cut a piece of agarose and put it under the binocular microscope. Transfer 20–30 embryos to the agarose pad.

▲ **CRITICAL STEP** Use a glass Pasteur pipette for the transfer.

97 Use metal tweezers to align the embryos while looking through the binocular microscope. It might be necessary to wait for a few minutes for the excess PBS to evaporate, which facilitates visualization and the movement of embryos over the agarose pad.

▲ **CRITICAL STEP** Alignment will greatly facilitate finding the embryos in the microscope field of view when defining ROIs. Be gentle when touching and moving the embryos with the tweezers; otherwise, the embryos could break.

98 Dry the embryos with a paper tissue to absorb the surrounding liquid.

▲ **CRITICAL STEP** The embryos will not attach if there is an excess of liquid. If necessary, wait a few minutes for the liquid to evaporate.

99 Attach the embryos to a poly-L-lysine-coated coverslip by gently pressing the coverslip against the agarose pad.

▲ **CRITICAL STEP** Press gently for a few seconds to ensure attachment.

100 Put the coverslip into a 35-mm plastic dish, with embryos facing up, and fill it with PBS until ready for chamber assembly

? **TROUBLESHOOTING**

Hi-M data acquisition ● **Timing** ~1–1.5 h per barcode

▲ **CRITICAL** Experiments are performed on a homemade wide-field epifluorescence microscope coupled to a microfluidic device (Fig. 7) according to the flowchart found in Fig. 8.

101 Wash all the microfluidic tubing with ddH₂O first and then with filtered 2× SCC.

▲ **CRITICAL STEP** The microfluidic tubing should remain filled with 50% (vol/vol) ethanol between experiments, which prevents bacterial growth and, at the same time, facilitates air bubble removal.

▲ **CRITICAL STEP** Check that, by applying a defined pressure in all valves, the obtained flow rate is constant to confirm the absence of clogging. Typical values for the flow rate range between 100 and 150 μL/min at 5-mBar pressure.

- 102 Open the microfluidic chamber by unscrewing it. Carefully remove the glass coverslip from the chamber. Steps for chamber assembly are shown in Fig. 5b.
- 103 Remove the plastic spacer and dry it thoroughly with a paper tissue.
▲ CRITICAL STEP Dry the whole microfluidic chamber as much as possible.
- 104 Put back the dried spacer and mount the coverslip with the attached embryos.
- 105 Screw the chamber into the microscope stage.
- 106 Fill the chamber with 2× SSC by slowly aspirating the buffer with a 10-mL syringe.
▲ CRITICAL STEP If the pressure exerted at this stage is too high, the embryos may detach. At the time of the filling, keep the chamber oriented upward to prevent air retention.
? TROUBLESHOOTING
- 107 Connect all tubing with the corresponding solution and note the respective Hamilton valve numbers.
- 108 Put a small drop of oil onto the 60× objective and focus on the coverslip surface. Locate the embryos using bright-field imaging.
▲ CRITICAL STEP Check whether the embryos are properly attached. Embryo borders will appear out of focus when embryos are detaching.
? TROUBLESHOOTING
- 109 Select the ROIs by checking the DAPI-stained nuclei.
▲ CRITICAL STEP Select embryos on the basis of the developmental stage in which you are interested. Check for RNA expression pattern, because it might depend on the orientation of each particular embryo. Be brief (a few seconds) when checking to avoid photobleaching of RNA signal.
- 110 Check the autofocus and select the starting point for the z stacks. Select the total number of planes to ensure acquisition of the full embryo in the axial direction.
- 111 Acquire bright-field images for all ROIs.
- 112 Acquire DAPI, RNA and fiducial barcode channels. Normally, 3D images of embryos are acquired with a 250-nm z-step size, spanning a 15-μm depth. Typical acquisition parameters are laser power at 15% of output power for the 405-nm (50 mW) and 488-nm lasers (50 mW), and at 60% of output power for the 561-nm laser (50 mW), with exposure time set to 50 ms. These acquisition settings may need to be modified depending on the sample.
? TROUBLESHOOTING
- 113 In the LabView software, set the injection procedure for the sequential imaging steps as follows:

Step	Solution	Volume (mL)	Flow Rate (mL/min)
1	Readout probe	1.8	0.15
2	Hi-M wash	1.5	0.2
3	2× SSC	1.5	0.2
4	Hi-M acquisition solution	0.8	0.15

- ▲ CRITICAL STEP** Keep the flow rate <0.3 mL/min. The embryos can detach from the coverslip with a higher flow rate.
- ▲ CRITICAL STEP** Allow for pressure stabilization before starting imaging.
- 114 Stop the flow by setting the pressure to 0 mBar and switching the position of the two-way valve, closing the fluidics system (this is automatically done by the LabView software). Image the barcode and fiducial channels. Typical acquisition parameters are laser power at 60% of output power for the 561-nm (50 mW) and 640-nm (100 mW) lasers, exposure time set to 50 ms. These acquisition settings may need to be modified depending on the sample.
? TROUBLESHOOTING
- 115 Remove the fluorescence signal by following one of the two alternatives below:
 (A) **Chemical bleaching**
 (i) Inject 1.0 mL of chemical bleaching solution at a flow rate of 0.2 mL/min.
 (ii) Inject 1.5 mL of 2× SSC at a flow rate of 0.2 mL/min.
 (B) **Photobleaching**
 (i) Inject 1.5 mL of 2× SSC at a flow rate of 0.2 mL/min to remove Hi-M acquisition solution.
 (ii) Proceed to photobleaching using 100% of the laser power for 6–10 s in each ROI. See ‘Experimental design’ section for further information.
- 116 Repeat Steps 113–115 for all the barcodes (Fig. 6).

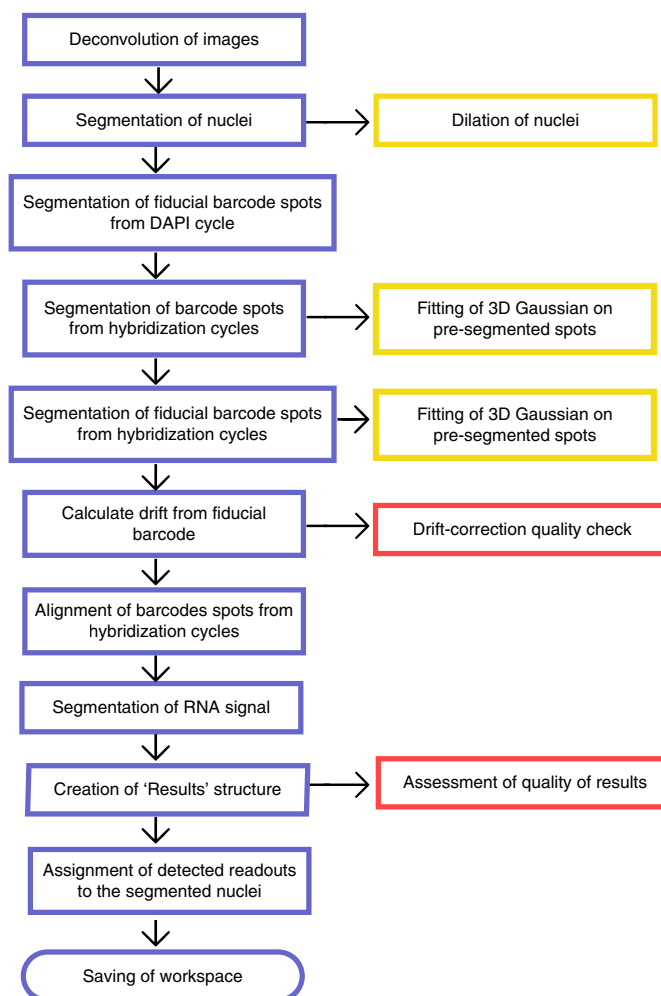


Fig. 9 | Hi-M image analysis flowchart. Sequence of steps required for image analysis (spot detection and registration). Violet boxes indicate key steps; yellow boxes indicate refinement of obtained masks (either by dilating the nuclei mask or by 3D Gaussian fitting of barcode positions); and boxes indicate quality-check steps.

Hi-M data analysis ● Timing 0.5 day per embryo

▲ **CRITICAL** Multiple types of software can be used to implement image segmentation. Here, we provide a typical script in MATLAB format. A flowchart of the procedure can be found on Fig. 9.

117 Deconvolve the 3D-acquired wide-field epifluorescence images using the Huygens deconvolution software.

Parameter	Value
x/y pixel size	0.098 nm
z step	250 nm
Numerical aperture	1.2
Medium refractive index	1.338 (water)
Lens refractive index	1.338

▲ **CRITICAL STEP** Specify the correct parameter values for deconvolution, such as pixel size, numerical aperture of the objective, excitation and emission wavelengths, and refractive index of medium. Typical parameters used are detailed in the following table.

? TROUBLESHOOTING

118 Organize the deconvolved stacks to include in one folder all the ROIs corresponding to one embryo.

- ▲ **CRITICAL STEP** Include in this folder the .inf files that contain the parameters needed for the analysis. They are provided with the analysis pipeline.
- 119 Launch MATLAB and load the provided homemade script, named 'merfish_main.m' (which can be found at <http://dx.doi.org/10.17632/5f5hd9yj3z.1#folder-26d1f8c0-fc58-4b87-8c4f-cd8fa294a555>). The script is written in a modular way; the user must sequentially execute (using 'Control' + 'Enter') the different steps that are described from this point onward. Specify the folder in which the ROIs are located in the `destDir` line.
- 120 Launch the GUI by running the 'GUI to segment DAPI masks' block of code (Fig. 10).
- 121 Click on 'Read new ROI', wait for the program to load the image and then click on 'Process'.
- ▲ **CRITICAL STEP** Select the starting and end planes to be read in the 'ImageSettings' square. If the 'autoPlanes' box in the 'Options' square is marked, it loads only the number of planes above and below the most intense plane, defined by the 'zWindow' box, in the 'ImageSettings' square.
- ▲ **CRITICAL STEP** If you have GPUs available for processing, tick the 'GPU' box in the 'Options' square. This will considerably reduce processing time.
- 122 *Segment the nuclei.* Adjust the 'Segmentation' parameters and click on 'Resegment'. A visual output will be displayed, showing each segmented nucleus as a mask of a different color (Fig. 10).
- ▲ **CRITICAL STEP** Optimize the parameters in an iterative manner by visually inspecting the segmentation output (Fig. 10c) in order to correctly segment the nuclei. For our data, the typical values used are 'Threshold': 0.9–1.1 (with 'relative threshold' box ticked); '# Voxels': 400–5,000; 'extent': 0.2–1, 'equivDiameter': 15–100. Use the histograms on the GUI to discard outliers.
- ▲ **CRITICAL STEP** By ticking on the 'watershed' box, the segmentation is greatly improved.
- ? **TROUBLESHOOTING**
- 123 (Optional) Owing to border effects (e.g., dirty spots outside the embryo or high-intensity regions near the border of the image that are due to deconvolution effects), it may be necessary to define a polygon around the embryo in order to discard regions outside. To do so, tick 'ROI_loc' and click on 'Resegment'. A pop-up window will appear, allowing you to manually select the polygon. Click once to define the vertices of the polygon. You can use the 'backspace' key to delete the last vertex. Double-click once you are done with the selection.
- 124 Repeat Steps 121–123 for all ROIs for the embryo (typically 2–4 ROIs). Change the selected ROI by changing the 'nROI' bar (Fig. 10b). This whole process can also be performed in batch. In this mode, all ROIs are processed without user input, using the set of parameters provided in the GUI.
- ▲ **CRITICAL STEP** Even when performing batch processing, we recommend manually exploring the segmentation results for each ROI after segmentation.
- 125 Click on the 'save data' button and close the GUI window.
- ▲ **CRITICAL STEP** If 'save data' is not clicked, the segmented data will be lost.
- 126 (Optional) Dilate DAPI masks by running the corresponding block named 'Function to dilate DAPI masks'.
- 127 Launch the spot-detection GUI to segment the fiducial barcodes corresponding to the first acquisition cycle. Follow the procedure as in Steps 121–123 for each ROI, only this time execute the 'GUI to segment internal marks DAPI' block. For historical reasons, barcodes are called 'RTs' in the program.
- ▲ **CRITICAL STEP** Change the contrast in the 'ImageSettings' square to correctly visualize the spots. A typical contrast range is between 0.1 and 0.999.
- ▲ **CRITICAL STEP** Optimize the parameters in an iterative manner by visually inspecting the selection of spots (Fig. 10d) to segment all spots. A blue circle will be created around each detected spot in the raw image. Zoom in as needed. For our data, the typical values used are 'Threshold': 1.5–4 (with the 'relative threshold' box unticked); '# Voxels': 5–1,000; 'extent': 0.2–1, and 'equivDiameter': 1–50.
- ? **TROUBLESHOOTING**
- 128 Fit the detections performed in the preceding step using 3D Gaussian fitting, using the 'Refits RTs using 3D gaussian fitting' block.
- 129 Launch the spot-detection GUI to segment the readouts for all cycles. Follow the procedure as in Steps 121–123 for each ROI. It is possible to use 'batch processing' (see next step). For our data, the typical values used are 'Threshold': 1.8–5 (with the 'relative threshold' box unticked); '# Voxels': 5–1,000; 'extent': 0.2–1, and 'equivDiameter': 1–50.
- ? **TROUBLESHOOTING**
- 130 (Optional) Once the parameters are determined for a particular ROI, you can automatically segment all ROIs by clicking on 'batch processing' and unticking the 'batchSingleROI' box in the

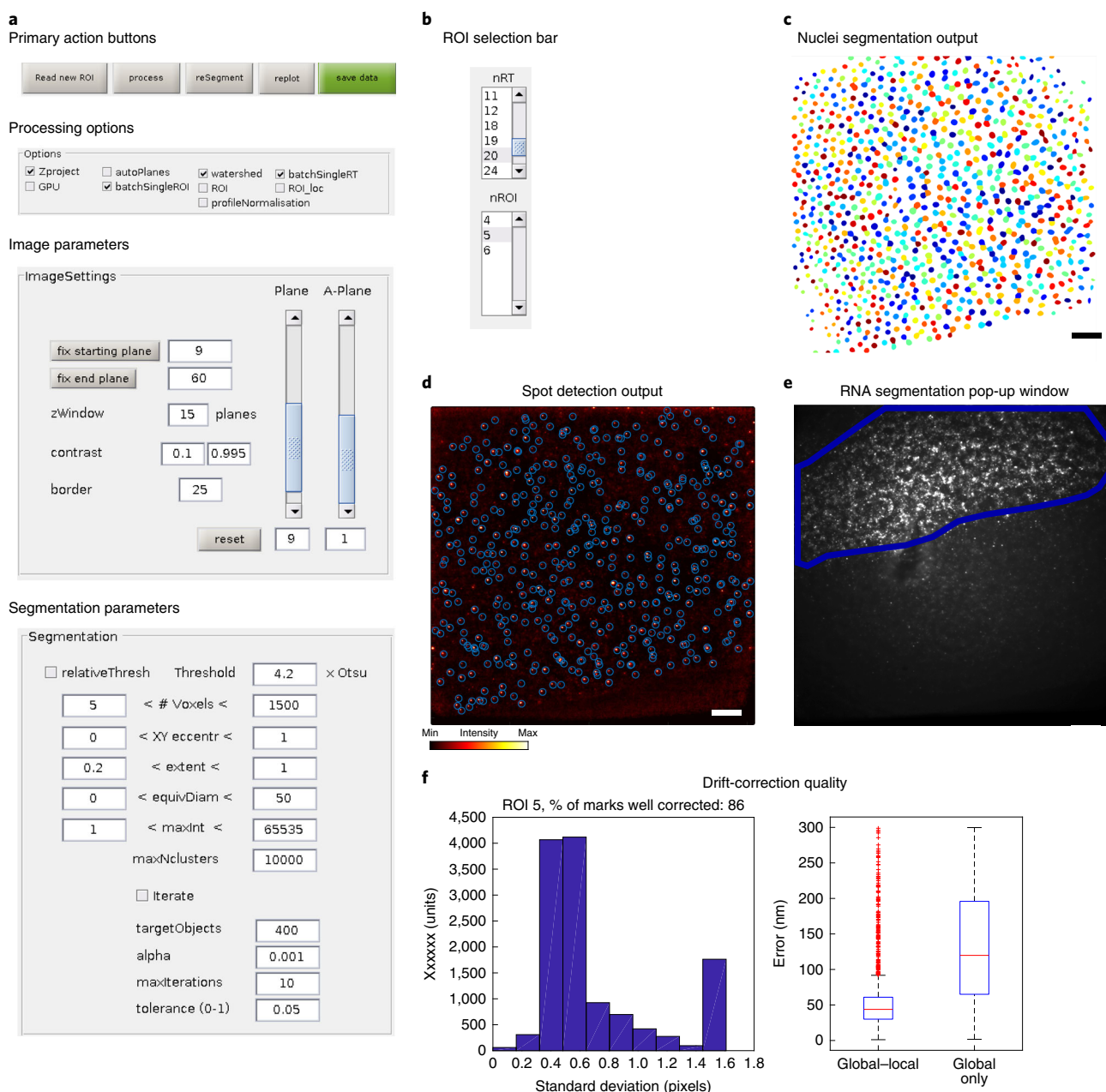


Fig. 10 | Data analysis. **a**, MATLAB GUI for image analysis used in Steps 120–125, 127, 129 and 131. The panels show the primary action buttons ('Read new ROI', 'process', 'reSegment', 'replot' and 'save data'), the processing options, and image and segmentation parameters that are used to segment nuclei or barcodes. **b**, ROI selection bar. nRT is the corresponding barcode, and nROI is the selected ROI. **c**, Typical example of nuclei segmentation. Each nuclei mask is represented by a different color. **d**, Example of a barcode image z-projection after segmentation. The intensity is represented in a color code that ranges from black to orange to white as indicated in the color scale in the bottom-left corner. Identified barcodes are marked with a blue circle. **e**, RNA signal segmentation is performed in a pop-up window. RNA-positive nuclei are manually selected by a blue-line polygon. **c**, **d** and **e** correspond to the same embryo, labeled with DAPI, DNA and RNA (against snail), respectively. Scale bars, 20 μm . **f**, Drift-correction quality. Left, histogram of standard deviations of fiducial barcodes after drift correction, expressed in pixels. Pixel size is 108 nm. Right, boxplots of the residual error in xyz of fiducial barcodes after drift correction, applying only a global (right), or a global and a local correction (left)³.

'options' section of the GUI. Furthermore, by ticking on the 'Iterate' box on the 'segmentation' square before clicking 'batch processing', the program can automatically iterate to find the most suitable parameters for each ROI (Fig. 10a). The 'targetObjects' value is the expected number of spots to detect, with a 'tolerance' indicating the allowed range in percentages. 'Alpha' is a factor by which it will change the threshold in each iteration, considering the difference between the segmented objects and 'targetObjects'. Its standard value is 0.001. 'maxIterations' is the maximal

number of iterations it will perform, even if it does not reach the expected number of objects, before going to the next ROI.

▲ CRITICAL STEP Tick the 'batchSingleROI' box and untick 'bachSingleRT' in the 'options' square to process all readouts for the same ROI.

- 131 Use the spot-detection GUI to segment the fiducial barcodes in all hybridization cycles, following the procedure from Steps 121–123. It is possible to use 'batch processing' as in the preceding step.

? TROUBLESHOOTING

▲ CRITICAL STEP It is necessary to segment each barcode for each ROI. Remember to click on the 'save data' button before closing the GUI window.

- 132 Fit the detections performed in the preceding step using a 3D Gaussian fitting by running the 'Refits RTs using 3D gaussian fitting' block.

- 133 Calculate the drift along the cycles by running the 'Correct drift using internal marker' block. It cross-correlates fiducial barcode spots with the ones from the reference cycle (the first hybridization cycle) to obtain a correction vector.

▲ CRITICAL STEP Select the fiducial barcode of the first cycle as reference, by changing the value of the 'referenceRT' variable. Because the injection sequence is defined by the user, it could be that in the first hybridization cycle, readout probe 8 was injected. In that case, the example code is `referenceRT=8;`.

- 134 Assess the quality of drift correction by running the 'Benchmarks drift correction quality' block (Fig. 10f).

? TROUBLESHOOTING

- 135 Align the barcode spots from all hybridization cycles by running the block named 'Aligns beads from DAPI and MERFISH experiments'. It uses the correction vector from the fiducial barcode spots closest to the barcode to perform alignment.

- 136 Segment the RNA signal by running the 'Segments RNA' block. A pop-up window will appear, allowing you to manually select the polygon. Click once to define the vertices of the polygon. If needed, use the 'backspace' key to delete the last vertex. Double-click once done with the selection.

- 137 Build the results structure by running the block named 'Builds results structure with RTMatrix and other data'.

- 138 Control how successful the clustering of spots in single nuclei was by running the 'Assesses results quality' block. A high percentage (>80%) of clustered barcode spots is expected.

? TROUBLESHOOTING

- 139 Assign detected readouts to the segmented nuclei and build the CellID structure by running the 'Finds RTs for each Cell mask in each ROI' block.

- 140 Save the segmented data by saving the MATLAB workspace.

- 141 Launch the `merfish_cellID_analysis_v4.m` analysis software in MATLAB. The script is provided in the analysis suite and is written in a modular way; a user must sequentially execute ('Control' + 'Enter') the different steps that are described from this point onward. Place the files obtained in the preceding step in a folder and add the folder path to the data path in the program, using the following command as an example:

`datapath='/your-path-to-the-data/data';` Then, in the `dataFiles` variable, choose the files to analyze (obtained in Step 140), for example:

```
dataFiles= {'Matlab_file_name.mat' }
```

- 142 Load the datasets by running the first section, named 'Loads codebook'.

▲ CRITICAL STEP In this section, load the paths that contain the genomic coordinates of the readout probes used in the data acquisition.

- 143 Set the parameters by running the 'Sets parameters' section. They are defined by default but can be adapted for each experiment.

▲ CRITICAL STEP Choose the correct value for the `p.process` variable ('RNAon', 'RNAoff' or 'none'), depending on whether nuclei that contain RNA staining are to be analyzed separately from those that do not ('RNAon' and 'RNAoff', respectively). By choosing the value 'none', the two types of nuclei will be processed together.

- 144 Run the 'Distribution in the number of RTs detected per cell' and 'Loops over cells and detects clusters' sections. These will group barcodes in clusters.
- 145 Order readouts according to their genomic positions, by running the dedicated section named 'orders the list of RTs used in the experiment according to their genomic position'. This will allow you to assign the correct genomic coordinates to each barcode, as well as enabling subsequent construction of distance matrices.
- 146 Run the 'Populates distanceMatrix' section. Then run the 'Calculates mean distance matrix and contact probability matrix from distanceMatrix structure' section.
- 147 Plot genomic distances versus mean physical distances, using the corresponding block named 'Genomic distance versus mean physical distance'.
- 148 Plot contact probability versus genomic distance by running the corresponding block, named 'contact probability versus genomic distance'.
- 149 Plot the normalized distance matrix and normalized contact probability matrix by running 'Plots the normalised distance matrix and normalised contact probability matrices' section.

Troubleshooting

Troubleshooting advice can be found in Table 1.

Table 1 | Troubleshooting table

Step	Problem	Possible reason	Solution
16,22	Nonspecific bands appear during PCR amplification	Mis-priming due to over-amplification	Reduce the number of cycles. Run a small-scale PCR to define the optimal number Increase temperature of annealing Perform a Mg ⁺⁺ curve to find the right concentration. The range of MgCl ₂ usually is from 0.5 to 4 mM in 0.25 mM increments For GC-rich (>65% GC content) samples, adding a final concentration of 5% (vol/vol) DMSO to the mixture might help
26	RNA is degraded or absent	RNA degradation	Maintain RNase-free conditions
100,106,108	Embryos detach from chamber	Embryos have remaining oil	Carefully remove all the oil after the ON incubation with the primary probe. Be sure that embryos are stored in PBS
		Embryos or coverslip were too wet	Dry with paper tissue around the embryos or wait a few minutes until the buffer evaporates
		Coverslip coating is not effective	Keep the coverslip at a distance when drying with the flame. Otherwise, the coverslip can deform and poly-L-lysine will not adhere properly
		Flow rate/pressure was too high	Make sure to check flow rates for all the valves being used before starting the experiment. Wash valves that are not optimal with filtered water to unclog them
112	Autofluorescence is too high (i.e., fluorescence levels are high and homogeneous along the whole field of view)	Paraformaldehyde used for fixation was not methanol free	Collect and fix new embryos using methanol-free paraformaldehyde
		Wash steps were not effective	Label new embryos, carefully following the washing steps
	No RNA signal	RNA degradation	Ensure RNase-free conditions
		RNA probe degradation	Control temperature and time very precisely when denaturing the probe. Do not denature reused probes
		Embryo is not well oriented	Orientation on the coverslip is random, which can be limiting when RNA expression has a spatial pattern. Use more embryos to increase the chance of finding them in the desired position. Alternatively, try to orient them (ventral/dorsal) before attaching them to the coverslip
		RNA is not expressed	Check the developmental time of the selected embryos

Table continued

Table 1 (continued)

Step	Problem	Possible reason	Solution
	Bright spots in the field of view	Coverslip was not properly cleaned	Prepare a new coverslip, cleaning it thoroughly with acetone. Use 70% (vol/vol) ethanol/ddH ₂ O to rinse it before drying it in the flame
	No DAPI signal	Formamide washes away DAPI	Acquire DAPI before incubating with hybridization solution
112,114	Autofocus is lost	Embryos are too far from each other on the coverslip	When defining the ROIs, avoid selecting consecutively very distant embryos.
		Light scattering due to additional reflection of the 785-nm laser (autofocus line) on the embryo	For each embryo, define a nearby reference ROI where the autofocus signal is not affected.
114	No barcode spots	Secondary oligos are degraded or are not the correct ones	Check for the sequences used in both primary and secondary oligos
	Fluorescent signal bleaches (for example, detections in fiducial barcode channel disappear in fewer than 10 cycles)	Exposure time was too long and/or the laser power was too high; the number of planes was too large	Optimize parameters in a control experiment
		Hi-M acquisition solution is no longer active	Hi-M acquisition solution should be stored under a protective layer of mineral oil and changed to a freshly prepared one every 12–15 h
	Pressure is too high (>20 mBar) or flow rate is too low (<100 μ L/min)	Air bubble in the system	Between experiments, wash the system with 50% ethanol. This would facilitate bubble removal and prevent bacterial growth at the same time. Before starting the injection procedure, pass 2 \times SCC through each valve and check that the flow rate is stable
		Dirt or salt deposits in the system	Filter all solutions before injecting them. Wash the system with filtered water to remove anything that may disturb the flow
	Fluorescent spots after bleaching step	The selected bleaching strategy is not effective	Choice of bleaching strategy will depend on factors such as number of ROIs, probes per barcode and experimental model. Optimization is needed
117	Deconvolution artifacts (e.g., spots are elongated in the deconvolved image but not in the original one)	Deconvolution parameters were not optimal	Check the excitation and emission wavelengths. Check pixel size and z step used
122	Nuclei are segmented incorrectly	Threshold parameters are not optimal	Increase threshold value over 1. Extend bounds for number of voxels
127	Detection algorithm under/overcounts barcode spots	Threshold parameters are not optimized	Manually adjust the parameters interactively. Use the zoom to visualize the spots
		Background is too high or SNR is below 3	Deconvolution can greatly increase SNR ratio
		There are several false detections	Increase threshold Change eccentricity upper bound to 0.8–0.9, until spurious detections are filtered
127,129,131	Low spot detection	Efficiency of labeling is low	FISH conditions should be optimized. For example, different probe concentrations, hybridization temperatures or times could be tested
		The z range is too small to capture the entire layer of cells of the embryo	Use DAPI staining to correctly define the stack size
134	Drift correction is not good enough	Fiducial barcode was photobleached during acquisition cycles	Make sure Hi-M acquisition solution is stored under a mineral oil layer and renewed every ~12 h Imaging steps should be optimized, by reducing laser power or acquisition time Fiducial barcode should be designed to have a higher number of oligos (150–300)
		Spot-detection parameters are not well defined, leading to over/undercounting	Resegment the fiducial barcode using optimized parameters. Use visual inspection to ensure parameters are optimized
138	Barcode spot clustering is low (20–70%)	Barcode segmentation was not efficient	Resegment barcodes, using optimized parameters. Use visual inspection to ensure parameters are optimized, and make sure there are no false detections

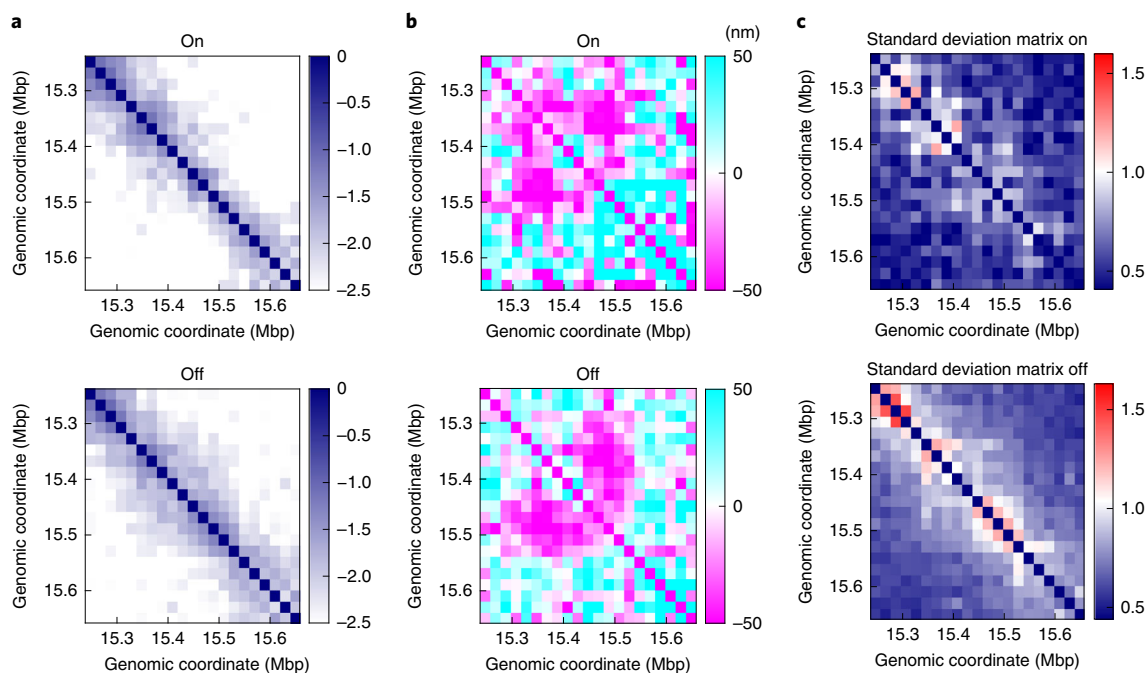


Fig. 11 | Hi-M output. **a**, Hi-M absolute contact probability maps for the region 2L:15.250–15.650 Mb from *Drosophila* embryo nuclei expressing ('On', top) or not expressing ('Off', bottom) snail RNA. The absolute contact probability was estimated as described previously⁴². The colors indicate absolute contact probability as indicated in the scale on the right. **b**, Hi-M normalized mean physical distance map from nuclei expressing ('On', top) or not expressing ('Off', bottom) the target RNA. Normalization is achieved by subtracting expected from observed distances. The expected distance was obtained by fitting a physical versus genomic distance curve³. The color scale indicates distances lower (magenta) or higher (cyan) than expected. Normalized distances are shown in nanometers, as indicated in the scale on the right. **c**, Hi-M ratio between standard deviation and mean pairwise distances from nuclei expressing ('on', top) or not expressing ('off', bottom) the target RNA. The color scale ranges from 0.5 (blue) to 0 (white), to 1.5 (red). **a–c** adapted with permission from ref. ³, Elsevier.

Timing

- Steps 1–7, design of Oligopaints libraries: 4–5 h
- Steps 8–39, amplification of Oligopaints: 4–5 d
- Steps 40–50, embryo collection and fixation: 2–3 h
- Steps 51–77, (optional) RNA in situ hybridization: 2.5 d
- Steps 78–92, DNA in situ hybridization: 1.5 d
- Steps 93–100, attachment of embryos: 1 h
- Steps 101–116, Hi-M data acquisition: ~1–1.5 h per barcode for 25 ROIs
- Steps 117–149, Hi-M data analysis: 0.5 day per embryo (typically 3 or 4 ROIs)

Anticipated results

This protocol provides a detailed description of the steps required to design Oligopaints probes; stain and image RNA and DNA simultaneously; and segment nuclei, RNA and multiple barcodes in thousands of cells in an intact *Drosophila* embryo.

A typical set of results is shown in Fig. 11. It consists of matrices of pairwise absolute contact probability, pairwise distance maps, and ratios between standard deviation and mean pairwise distances. Each matrix provides rich and complementary information regarding chromatin architecture at the TAD level as a function of RNA expression. The absolute contact probability matrix reveals the true probability of interaction between different genomic loci, as well as intra- and inter-TAD contacts for different transcriptional states. By contrast, the normalized distance matrix measures the local changes in spatial organization with respect to what would be expected from the average behavior. These can be used to detect that chromatin is preferentially condensed within TADs and decondensed at TAD borders. Finally, the standard deviation matrix reveals the heterogeneity between cells for each transcriptional state, reflecting the variations in chromatin folding between different cells. Taken together, in the set of results displayed in Fig. 11, one can clearly observe the changes in chromosome organization upon transcriptional activation.

Reporting Summary

Further information on research design is available in the Nature Research Reporting Summary linked to this article.

Data and code availability

The code used and described in this paper and the experimental dataset used to construct Fig. 11 have been uploaded to <https://doi.org/10.17632/5f5hd9yj3z.1#folder-26d1f8c0-fc58-4b87-8c4f-cd8a294a555Software>. Additional advice on how to use these can be obtained from the authors upon reasonable request. Further information and requests for resources, reagents and software should be directed to and will be fulfilled by the lead contact, M.N. (marcelo.nollmann@cbs.cnrs.fr).

References

1. Bonev, B. & Cavalli, G. Organization and function of the 3D genome. *Nat. Rev. Genet.* **17**, 661–678 (2016). erratum **17**, 772 (2016).
2. Giorgetti, L. & Heard, E. Closing the loop: 3C versus DNA FISH. *Genome Biol.* **17**, 215 (2016).
3. Cardozo Gizzi, A. M. et al. Microscopy-based chromosome conformation capture enables simultaneous visualization of genome organization and transcription in intact organisms. *Mol. Cell* **74**, 212–222.e5 (2019).
4. Bintu, B. et al. Super-resolution chromatin tracing reveals domains and cooperative interactions in single cells. *Science* **362**, aau1783 (2018).
5. Nir, G. et al. Walking along chromosomes with super-resolution imaging, contact maps, and integrative modeling. *PLoS Genet.* **14**, e1007872 (2018).
6. Mateo, L. J. et al. Visualizing DNA folding and RNA in embryos at single-cell resolution. *Nature* **568**, 49–54 (2019).
7. Beliveau, B. J. et al. Versatile design and synthesis platform for visualizing genomes with Oligopaint FISH probes. *Proc. Natl Acad. Sci. USA* **109**, 21301–21306 (2012).
8. Beliveau, B. J. et al. Single-molecule super-resolution imaging of chromosomes and in situ haplotype visualization using Oligopaint FISH probes. *Nat. Commun.* **6**, 7147 (2015).
9. Lubeck, E., Coskun, A. F., Zhiyentayev, T., Ahmad, M. & Cai, L. Single-cell in situ RNA profiling by sequential hybridization. *Nat. Methods* **11**, 360–361 (2014).
10. Chen, K. H., Boettiger, A. N., Moffitt, J. R., Wang, S. & Zhuang, X. RNA imaging. Spatially resolved, highly multiplexed RNA profiling in single cells. *Science* **348**, aaa6090 (2015).
11. Moffitt, J. R. et al. Molecular, spatial, and functional single-cell profiling of the hypothalamic preoptic region. *Science* **362**, aau5324 (2018).
12. Moffitt, J. R. et al. High-performance multiplexed fluorescence in situ hybridization in culture and tissue with matrix imprinting and clearing. *Proc. Natl Acad. Sci. USA* **113**, 14456–14461 (2016).
13. Rosin, L. F., Nguyen, S. C. & Joyce, E. F. Condensin II drives large-scale folding and spatial partitioning of interphase chromosomes in *Drosophila* nuclei. *PLoS Genet.* **14**, e1007393 (2018).
14. Kishi, J. Y., Beliveau, B. J., Lapan, S. W., West, E. R. & Zhu, A. SABER enables highly multiplexed and amplified detection of DNA and RNA in cells and tissues. *bioRxiv* (2018).
15. Fields, B. D., Nguyen, S. C., Nir, G. & Kennedy, S. A multiplexed DNA FISH strategy for assessing genome architecture in *Caenorhabditis elegans*. *Elife* **8**, e42823 (2019).
16. Pallikkuth, S. et al. Sequential super-resolution imaging using DNA strand displacement. *PLoS One* **13**, e0203291 (2018).
17. Roohi, J., Cammer, M., Montagna, C. & Hatchwell, E. An improved method for generating BAC DNA suitable for FISH. *Cytogenet. Genome Res.* **121**, 7–9 (2008).
18. Bienko, M. et al. A versatile genome-scale PCR-based pipeline for high-definition DNA FISH. *Nat. Methods* **10**, 122–124 (2013).
19. Wang, S. et al. Spatial organization of chromatin domains and compartments in single chromosomes. *Science* **353**, 598–602 (2016).
20. Shah, S. et al. Dynamics and spatial genomics of the nascent transcriptome by intron seqFISH. *Cell* **174**, 363–376.e16 (2018).
21. Eng, C.-H. L., Shah, S., Thomassie, J. & Cai, L. Profiling the transcriptome with RNA SPOTs. *Nat. Methods* **14**, 1153–1155 (2017).
22. Wu, X., Mao, S., Ying, Y., Krueger, C. J. & Chen, A. K. Progress and challenges for live-cell imaging of genomic loci using CRISPR-based platforms. *Genomics Proteomics Bioinformatics* **17**, 119–128 (2019).
23. Ma, H. et al. Multiplexed labeling of genomic loci with dCas9 and engineered sgRNAs using CRISPRainbow. *Nat. Biotechnol.* **34**, 528–530 (2016).
24. Germier, T. et al. Real-time imaging of a single gene reveals transcription-initiated local confinement. *Biophys. J.* **113**, 1383–1394 (2017).
25. Chen, H. et al. Dynamic interplay between enhancer–promoter topology and gene activity. *Nat. Genet.* **50**, 1296–1303 (2018).

26. Yunger, S., Rosenfeld, L., Garini, Y. & Shav-Tal, Y. Single-allele analysis of transcription kinetics in living mammalian cells. *Nat. Methods* **7**, 631–653 (2010).
27. Larson, D. R., Zenklusen, D., Wu, B., Chao, J. A. & Singer, R. H. Real-time observation of transcription initiation and elongation on an endogenous yeast gene. *Science* **332**, 475–478 (2011).
28. Fukaya, T., Lim, B. & Levine, M. Enhancer control of transcriptional bursting. *Cell* **166**, 358–368 (2016).
29. Saad, H. et al. DNA dynamics during early double-strand break processing revealed by non-intrusive imaging of living cells. *PLoS Genet.* **10**, e1004187 (2014).
30. Boyle, S., Rodesch, M. J., Halvensleben, H. A., Jeddelloh, J. A. & Bickmore, W. A. Fluorescence in situ hybridization with high-complexity repeat-free oligonucleotide probes generated by massively parallel synthesis. *Chromosome Res.* **19**, 901–909 (2011).
31. Rouillard, J.-M., Zuker, M. & Gulari, E. OligoArray 2.0: design of oligonucleotide probes for DNA microarrays using a thermodynamic approach. *Nucleic Acids Res* **31**, 3057–3062 (2003).
32. Gelali, E. et al. iFISH is a publically available resource enabling versatile DNA FISH to study genome architecture. *Nat. Commun.* **10**, 1636 (2019).
33. Beliveau, B. J. et al. OligoMiner provides a rapid, flexible environment for the design of genome-scale oligonucleotide in situ hybridization probes. *Proc. Natl Acad. Sci. USA* **115**, E2183–E2192 (2018).
34. Raj, A., van den Bogaard, P., Rifkin, S. A., van Oudenaarden, A. & Tyagi, S. Imaging individual mRNA molecules using multiple singly labeled probes. *Nat. Methods* **5**, 877–879 (2008).
35. Moffitt, J. R. & Zhuang, X. RNA imaging with multiplexed error-robust fluorescence in situ hybridization (MERFISH). *Methods Enzymol.* **572**, 1–49 (2016).
36. Trcek, T., Lionnet, T., Shroff, H. & Lehmann, R. mRNA quantification using single-molecule FISH in *Drosophila* embryos. *Nat. Protoc.* **12**, 1326–1348 (2017).
37. Shpiz, S., Lavrov, S. & Kalmykova, A. Combined RNA/DNA fluorescence in situ hybridization on whole-mount *Drosophila* ovaries. *Methods Mol. Biol.* **1093**, 161–169 (2014).
38. Boettiger, A. N. & Levine, M. Rapid transcription fosters coordinate snail expression in the *Drosophila* embryo. *Cell Rep.* **3**, 8–15 (2013).
39. Bantignies, F. & Cavalli, G. Topological organization of *Drosophila* Hox genes using DNA fluorescent in situ hybridization. *Methods Mol. Biol.* **1196**, 103–120 (2014).
40. Moffitt, J. R. et al. High-throughput single-cell gene-expression profiling with multiplexed error-robust fluorescence in situ hybridization. *Proc. Natl Acad. Sci. USA* **113**, 11046–11051 (2016).
41. Fung, J. C., Marshall, W. F., Dernburg, A., Agard, D. A. & Sedat, J. W. Homologous chromosome pairing in *Drosophila melanogaster* proceeds through multiple independent initiations. *J. Cell Biol.* **141**, 5–20 (1998).
42. Cattoni, D. I. et al. Single-cell absolute contact probability detection reveals chromosomes are organized by multiple low-frequency yet specific interactions. *Nat. Commun.* **8**, 1753 (2017).
43. Lagha, M. et al. Paused Pol II coordinates tissue morphogenesis in the *Drosophila* embryo. *Cell* **153**, 976–987 (2013).
44. Ashburner, M., Golic, K. G. & Hawley, R. S. *Drosophila: A Laboratory Handbook* (Cold Spring Harbor Laboratory Press, 2011).
45. Ferrandiz, C. & Sessions, A. Preparation and hydrolysis of digoxigenin-labeled probes for in situ hybridization of plant tissues. *CSH Protoc.* <https://doi.org/10.1101/pdb.prot4942> (2008).

Acknowledgements

This project received funding from the European Research Council (ERC) under the European Union's Horizon 2020 Research and Innovation Program (grant 724429). This work also benefited from support from Labex EpiGenMed, an 'Investments for the Future' program (grant ANR-10-LABX-12-01). We acknowledge the France-BioImaging infrastructure supported by the French National Research Agency (grant ANR-10-INBS-04, 'Investments for the Future').

Author contributions

A.M.C.G. and M.N. designed the experiments. A.M.C.G. and M.N. designed the Oligopaints probes. C.H. amplified and purified the Oligopaints libraries. A.M.C.G., C.H., S.M.E. and J.G. developed the RNA/DNA staining protocol; A.M.C.G., S.M.E., J.G. and D.I.C. conducted the experiments. J.-B.F. designed and built the microscopy setup and acquisition software. M.N. developed the software for image analysis. A.M.C.G., and J.G. analyzed the data. A.M.C.G., D.I.C. and M.N. wrote the manuscript. All authors reviewed and commented on the manuscript.

Competing interests

The authors declare no competing interests.

Additional information

Supplementary information is available for this paper at <https://doi.org/10.1038/s41596-019-0269-9>.

Correspondence and requests for materials should be addressed to M.N.

Reprints and permissions information is available at www.nature.com/reprints.

Publisher's note Springer Nature remains neutral with regard to jurisdictional claims in published maps and institutional affiliations.

Received: 28 May 2019; Accepted: 7 November 2019;
Published online: 22 January 2020

Related link**Key reference using this protocol**

Cardozo Gizzi, A. M. et al. *Mol. Cell* **74**, 212–222.e5 (2019): <https://doi.org/10.1016/j.molcel.2019.01.011>

Reporting Summary

Nature Research wishes to improve the reproducibility of the work that we publish. This form provides structure for consistency and transparency in reporting. For further information on Nature Research policies, see [Authors & Referees](#) and the [Editorial Policy Checklist](#).

Statistics

For all statistical analyses, confirm that the following items are present in the figure legend, table legend, main text, or Methods section.

n/a Confirmed

- The exact sample size (n) for each experimental group/condition, given as a discrete number and unit of measurement
- A statement on whether measurements were taken from distinct samples or whether the same sample was measured repeatedly
- The statistical test(s) used AND whether they are one- or two-sided
Only common tests should be described solely by name; describe more complex techniques in the Methods section.
- A description of all covariates tested
- A description of any assumptions or corrections, such as tests of normality and adjustment for multiple comparisons
- A full description of the statistical parameters including central tendency (e.g. means) or other basic estimates (e.g. regression coefficient) AND variation (e.g. standard deviation) or associated estimates of uncertainty (e.g. confidence intervals)
- For null hypothesis testing, the test statistic (e.g. F , t , r) with confidence intervals, effect sizes, degrees of freedom and P value noted
Give P values as exact values whenever suitable.
- For Bayesian analysis, information on the choice of priors and Markov chain Monte Carlo settings
- For hierarchical and complex designs, identification of the appropriate level for tests and full reporting of outcomes
- Estimates of effect sizes (e.g. Cohen's d , Pearson's r), indicating how they were calculated

Our web collection on [statistics for biologists](#) contains articles on many of the points above.

Software and code

Policy information about [availability of computer code](#)

Data collection Image acquisition, sample positioning and fluidics handling during Hi-M experiments were controlled by a custom-made software package developed in LabView 2015.

Data analysis Images were deconvolved using Huygens deconvolution software (Scientific Volume Imaging, <https://svi.nl/HuygensSoftware>) Hi-M data analysis coded in Matlab 2017b (Mathworks) was employed for data analysis

For manuscripts utilizing custom algorithms or software that are central to the research but not yet described in published literature, software must be made available to editors/reviewers. We strongly encourage code deposition in a community repository (e.g. GitHub). See the Nature Research [guidelines for submitting code & software](#) for further information.

Data

Policy information about [availability of data](#)

All manuscripts must include a [data availability statement](#). This statement should provide the following information, where applicable:

- Accession codes, unique identifiers, or web links for publicly available datasets
- A list of figures that have associated raw data
- A description of any restrictions on data availability

Provide your data availability statement here.

Field-specific reporting

Please select the one below that is the best fit for your research. If you are not sure, read the appropriate sections before making your selection.

- Life sciences Behavioural & social sciences Ecological, evolutionary & environmental sciences

Life sciences study design

All studies must disclose on these points even when the disclosure is negative.

Sample size	<input type="text" value="N/A"/>
Data exclusions	<input type="text" value="N/A"/>
Replication	<input type="text" value="N/A"/>
Randomization	<input type="text" value="N/A"/>
Blinding	<input type="text" value="N/A"/>

Reporting for specific materials, systems and methods

We require information from authors about some types of materials, experimental systems and methods used in many studies. Here, indicate whether each material, system or method listed is relevant to your study. If you are not sure if a list item applies to your research, read the appropriate section before selecting a response.

Materials & experimental systems

n/a	Included in the study
<input type="checkbox"/>	<input checked="" type="checkbox"/> Antibodies
<input type="checkbox"/>	<input checked="" type="checkbox"/> Eukaryotic cell lines
<input checked="" type="checkbox"/>	<input type="checkbox"/> Palaeontology
<input checked="" type="checkbox"/>	<input type="checkbox"/> Animals and other organisms
<input checked="" type="checkbox"/>	<input type="checkbox"/> Human research participants
<input checked="" type="checkbox"/>	<input type="checkbox"/> Clinical data

Methods

n/a	Included in the study
<input checked="" type="checkbox"/>	<input type="checkbox"/> ChIP-seq
<input checked="" type="checkbox"/>	<input type="checkbox"/> Flow cytometry
<input checked="" type="checkbox"/>	<input type="checkbox"/> MRI-based neuroimaging

Antibodies

Antibodies used	<input type="text" value="Anti-Digoxigenin-POD, Fab fragments (Sigma, cat. no. 11207733910)"/>
Validation	<input type="text" value="Describe the validation of each primary antibody for the species and application, noting any validation statements on the manufacturer's website, relevant citations, antibody profiles in online databases, or data provided in the manuscript."/>

Eukaryotic cell lines

Policy information about [cell lines](#)

Cell line source(s)	<input type="text" value="Wild-type fruit flies (Bloomington Drosophila Stock Center) embryos"/>
Authentication	<input type="text" value="N/A"/>
Mycoplasma contamination	<input type="text" value="N/A"/>
Commonly misidentified lines (See ICLAC register)	<input type="text" value="N/A"/>

References

- [, 1665] , Robert, H. (1665). Micrographia: or, Some physiological descriptions of minute bodies made by magnifying glasses. The Royal Society.
- [Akgol Oksuz et al., 2021] Akgol Oksuz, B., Yang, L., Abraham, S., Venev, S. V., Krietenstein, N., Parsi, K. M., Ozadam, H., Oomen, M. E., Nand, A., Mao, H., Genga, R. M. J., Maehr, R., Rando, O. J., Mirny, L. A., Gibcus, J. H., and Dekker, J. (2021). Systematic evaluation of chromosome conformation capture assays. Nature Methods, pages 1–10. Bandiera_abtest: a Cg_type: Nature Research Journals Primary_atype: Research Publisher: Nature Publishing Group Subject_term: Genomic analysis;Genomics Subject_term_id: genomic-analysis;genomics.
- [Albiez et al., 2006] Albiez, H., Cremer, M., Tiberi, C., Vecchio, L., Schermelleh, L., Dittrich, S., Küpper, K., Joffe, B., Thormeyer, T., von Hase, J., Yang, S., Rohr, K., Leonhardt, H., Solovei, I., Cremer, C., Fakan, S., and Cremer, T. (2006). Chromatin domains and the interchromatin compartment form structurally defined and functionally interacting nuclear networks. Chromosome Research, 14(7):707–733.
- [Alkema et al., 1997] Alkema, M. J., Bronk, M., Verhoeven, E., Otte, A., Veer, L. J. v. t., Berns, A., and Lohuizen, M. v. (1997). Identification of Bmi1-interacting proteins as constituents of a multimeric mammalian polycomb complex. Genes & Development, 11(2):226–240. Company: Cold Spring Harbor Laboratory Press Distributor: Cold Spring Harbor Laboratory Press Institution: Cold Spring Harbor Laboratory Press Label: Cold Spring Harbor Laboratory Press Publisher: Cold Spring Harbor Lab.
- [Andrey et al., 2013] Andrey, G., Montavon, T., Mascrez, B., Gonzalez, F., Noordermeer, D., Leleu, M., Trono, D., Spitz, F., and Duboule, D. (2013). A Switch Between Topological Domains Underlies HoxD Genes Collinearity in Mouse Limbs. Science, 340(6137). Publisher: American Association for the Advancement of Science Section: Research Article.
- [Baker, 1968] Baker, W. K. (1968). Position-Effect Variegation**The research of the author and his students reported herein has been supported by the U.S. Public Health Service, Grant No. GM 07428. In Caspari, E. W., editor, Advances in Genetics, volume 14, pages 133–169. Academic Press.
- [Bantignies and Cavalli, 2011] Bantignies, F. and Cavalli, G. (2011). Polycomb group proteins: repression in 3D. Trends in Genetics, 27(11):454–464.
- [Bantignies and Cavalli, 2014] Bantignies, F. and Cavalli, G. (2014). Topological Organization of Drosophila Hox Genes Using DNA Fluorescent In Situ Hybridization. In Graba, Y. and Rezsöházy, R., editors, Hox Genes: Methods and Protocols, Methods in Molecular Biology, pages 103–120. Springer, New York, NY.
- [Bantignies et al., 2003] Bantignies, F., Grimaud, C., Lavrov, S., Gabut, M., and Cavalli, G. (2003). Inheritance of Polycomb-dependent chromosomal interactions in Drosophila. Genes & Development, 17(19):2406–2420. Company: Cold Spring Harbor Laboratory Press Distributor: Cold Spring Harbor Laboratory Press Institution: Cold Spring Harbor Laboratory Press Label: Cold Spring Harbor Laboratory Press Publisher: Cold Spring Harbor Lab.

- [Bantignies et al., 2011] Bantignies, F., Roure, V., Comet, I., Leblanc, B., Schuettengruber, B., Bonnet, J., Tixier, V., Mas, A., and Cavalli, G. (2011). Polycomb-Dependent Regulatory Contacts between Distant Hox Loci in *Drosophila*. Cell, 144(2):214–226. Publisher: Elsevier.
- [Baranello et al., 2016] Baranello, L., Kouzine, F., Sanford, S., and Levens, D. (2016). ChIP bias as a function of cross-linking time. Chromosome Research, 24(2):175–181.
- [Barbieri et al., 2012] Barbieri, M., Chotalia, M., Fraser, J., Lavitas, L.-M., Dostie, J., Pombo, A., and Nicodemi, M. (2012). Complexity of chromatin folding is captured by the strings and binders switch model. Proceedings of the National Academy of Sciences, 109(40):16173–16178.
- [Barbieri et al., 2013] Barbieri, M., Scialdone, A., Piccolo, A., Chiariello, A. M., di Lanno, C., Prisco, A., Pombo, A., and Nicodemi, M. (2013). Polymer models of chromatin organization. Frontiers in Genetics, 4. Publisher: Frontiers.
- [Barbieri et al., 2017] Barbieri, M., Xie, S. Q., Torlai Triglia, E., Chiariello, A. M., Bianco, S., de Santiago, I., Branco, M. R., Rueda, D., Nicodemi, M., and Pombo, A. (2017). Active and poised promoter states drive folding of the extended HoxB locus in mouse embryonic stem cells. Nature Structural & Molecular Biology, 24(6):515–524. Bandiera_abtest: a Cg_type: Nature Research Journals Number: 6 Primary_atype: Research Publisher: Nature Publishing Group Subject_term: Chromatin structure;Pluripotent stem cells;Systems biology Subject_term_id: chromatin-structure; pluripotent-stem-cells; systems-biology.
- [Basu et al., 2014] Basu, A., Wilkinson, F. H., Colavita, K., Fennelly, C., and Atchison, M. L. (2014). YY1 DNA binding and interaction with YAF2 is essential for Polycomb recruitment. Nucleic Acids Research, 42(4):2208–2223.
- [Battulin et al., 2015] Battulin, N., Fishman, V. S., Mazur, A. M., Pomaznoy, M., Khabarova, A. A., Afonnikov, D. A., Prokhortchouk, E. B., and Serov, O. L. (2015). Comparison of the three-dimensional organization of sperm and fibroblast genomes using the Hi-C approach. Genome Biology, 16(1):77.
- [Bauman et al., 1980] Bauman, J. G. J., Wiegant, J., Borst, P., and van Duijn, P. (1980). A new method for fluorescence microscopical localization of specific DNA sequences by in situ hybridization of fluorochrome-labelled RNA. Experimental Cell Research, 128(2):485–490.
- [Beagrie et al., 2017] Beagrie, R. A., Scialdone, A., Schueler, M., Kraemer, D. C. A., Chotalia, M., Xie, S. Q., Barbieri, M., de Santiago, I., Lavitas, L.-M., Branco, M. R., Fraser, J., Dostie, J., Game, L., Dillon, N., Edwards, P. A. W., Nicodemi, M., and Pombo, A. (2017). Complex multi-enhancer contacts captured by genome architecture mapping. Nature, 543(7646):519–524. Bandiera_abtest: a Cg_type: Nature Research Journals Number: 7646 Primary_atype: Research Publisher: Nature Publishing Group Subject_term: Chromatin structure;Embryonic stem cells;Epigenomics;Nuclear organization;Transcriptional regulatory elements Subject_term_id: chromatin-structure;embryonic-stem-cells;epigenomics;nuclear-organization;transcriptional-regulatory-elements.

- [Beisel and Paro, 2011] Beisel, C. and Paro, R. (2011). Silencing chromatin: comparing modes and mechanisms. Nature Reviews Genetics, 12(2):123–135. Bandiera_abtest: a Cg_type: Nature Research Journals Number: 2 Primary_atype: Reviews Publisher: Nature Publishing Group Subject_term: Chromatin;Gene silencing;Non-coding RNAs Subject_term_id: chromatin;gene-silencing;non-coding-rnas.
- [Beliveau et al., 2015] Beliveau, B. J., Boettiger, A. N., Avendaño, M. S., Jungmann, R., McCole, R. B., Joyce, E. F., Kim-Kiselak, C., Bantignies, F., Fonseka, C. Y., Erceg, J., Hannan, M. A., Hoang, H. G., Cognori, D., Lee, J. T., Shih, W. M., Yin, P., Zhuang, X., and Wu, C.-t. (2015). Single-molecule super-resolution imaging of chromosomes and in situ haplotype visualization using Oligopaint FISH probes. Nature Communications, 6(1):7147. Number: 1 Publisher: Nature Publishing Group.
- [Beliveau et al., 2012] Beliveau, B. J., Joyce, E. F., Apostolopoulos, N., Yilmaz, F., Fonseka, C. Y., McCole, R. B., Chang, Y., Li, J. B., Senaratne, T. N., Williams, B. R., Rouillard, J.-M., and Wu, C.-t. (2012). Versatile design and synthesis platform for visualizing genomes with Oligopaint FISH probes. Proceedings of the National Academy of Sciences, 109(52):21301–21306.
- [Beliveau et al., 2018] Beliveau, B. J., Kishi, J. Y., Nir, G., Sasaki, H. M., Saka, S. K., Nguyen, S. C., Wu, C.-t., and Yin, P. (2018). OligoMiner provides a rapid, flexible environment for the design of genome-scale oligonucleotide in situ hybridization probes. Proceedings of the National Academy of Sciences, 115(10):E2183–E2192. Publisher: National Academy of Sciences Section: PNAS Plus.
- [Benke and Manley, 2012] Benke, A. and Manley, S. (2012). Live-Cell dSTORM of Cellular DNA Based on Direct DNA Labeling. ChemBioChem, 13(2):298–301. eprint: <https://chemistry-europe.onlinelibrary.wiley.com/doi/pdf/10.1002/cbic.201100679>.
- [Berlivet et al., 2013] Berlivet, S., Paquette, D., Dumouchel, A., Langlais, D., Dostie, J., and Kmita, M. (2013). Clustering of Tissue-Specific Sub-TADs Accompanies the Regulation of HoxA Genes in Developing Limbs. PLOS Genetics, 9(12):e1004018. Publisher: Public Library of Science.
- [Betzig et al., 2006] Betzig, E., Patterson, G. H., Sougrat, R., Lindwasser, O. W., Olenych, S., Bonifacino, J. S., Davidson, M. W., Lippincott-Schwartz, J., and Hess, H. F. (2006). Imaging Intracellular Fluorescent Proteins at Nanometer Resolution. Science, 313(5793):1642–1645. Publisher: American Association for the Advancement of Science Section: Report.
- [Bianco et al., 2018] Bianco, S., Lupiáñez, D. G., Chiariello, A. M., Annunziatella, C., Kraft, K., Schöpflin, R., Wittler, L., Andrey, G., Vingron, M., Pombo, A., Mundlos, S., and Nicodemi, M. (2018). Polymer physics predicts the effects of structural variants on chromatin architecture. Nature Genetics, 50(5):662–667. Number: 5 Publisher: Nature Publishing Group.
- [Bickmore, 2013] Bickmore, W. A. (2013). The Spatial Organization of the Human Genome. Annual Review of Genomics and Human Genetics, 14(1):67–84.
- [Bintu et al., 2018] Bintu, B., Mateo, L. J., Su, J.-H., Sinnott-Armstrong, N. A., Parker, M., Kinrot, S., Yamaya, K., Boettiger, A. N., and Zhuang, X. (2018). Super-resolution

- chromatin tracing reveals domains and cooperative interactions in single cells. Science, 362(6413). Publisher: American Association for the Advancement of Science Section: Research Article.
- [Blackledge et al., 2014] Blackledge, N. P., Farcas, A. M., Kondo, T., King, H. W., McGouran, J. F., Hanssen, L. L. P., Ito, S., Cooper, S., Kondo, K., Koseki, Y., Ishikura, T., Long, H. K., Sheahan, T. W., Brockdorff, N., Kessler, B. M., Koseki, H., and Klose, R. J. (2014). Variant PRC1 Complex-Dependent H2A Ubiquitylation Drives PRC2 Recruitment and Polycomb Domain Formation. Cell, 157(6):1445–1459.
- [Boettiger et al., 2016] Boettiger, A. N., Bintu, B., Moffitt, J. R., Wang, S., Beliveau, B. J., Fudenberg, G., Imakaev, M., Mirny, L. A., Wu, C.-t., and Zhuang, X. (2016). Super-resolution imaging reveals distinct chromatin folding for different epigenetic states. Nature, 529(7586):418–422. Number: 7586 Publisher: Nature Publishing Group.
- [Bohn and Heermann, 2011] Bohn, M. and Heermann, D. W. (2011). Repulsive Forces Between Looping Chromosomes Induce Entropy-Driven Segregation. PLOS ONE, 6(1):e14428. Publisher: Public Library of Science.
- [Bohn et al., 2007] Bohn, M., Heermann, D. W., and van Driel, R. (2007). Random loop model for long polymers. Physical Review E, 76(5):051805. Publisher: American Physical Society.
- [Bolzer et al., 2005] Bolzer, A., Kreth, G., Solovei, I., Koehler, D., Saracoglu, K., Fauth, C., Müller, S., Eils, R., Cremer, C., Speicher, M. R., and Cremer, T. (2005). Three-Dimensional Maps of All Chromosomes in Human Male Fibroblast Nuclei and Prometaphase Rosettes. PLOS Biology, 3(5):e157. Publisher: Public Library of Science.
- [Bonev et al., 2017] Bonev, B., Cohen, N. M., Szabo, Q., Fritsch, L., Papadopoulos, G. L., Lubling, Y., Xu, X., Lv, X., Hugnot, J.-P., Tanay, A., and Cavalli, G. (2017). Multiscale 3D Genome Rewiring during Mouse Neural Development. Cell, 171(3):557–572.e24. Publisher: Elsevier.
- [Boyer et al., 2006] Boyer, L. A., Plath, K., Zeitlinger, J., Brambrink, T., Medeiros, L. A., Lee, T. I., Levine, S. S., Wernig, M., Tajonar, A., Ray, M. K., Bell, G. W., Otte, A. P., Vidal, M., Gifford, D. K., Young, R. A., and Jaenisch, R. (2006). Polycomb complexes repress developmental regulators in murine embryonic stem cells. Nature, 441(7091):349–353. Bandiera_abtest: a Cg_type: Nature Research Journals Number: 7091 Primary_atype: Research Publisher: Nature Publishing Group.
- [Boyle et al., 2001] Boyle, S., Gilchrist, S., Bridger, J. M., Mahy, N. L., Ellis, J. A., and Bickmore, W. A. (2001). The spatial organization of human chromosomes within the nuclei of normal and emerlin-mutant cells. Human Molecular Genetics, 10(3):211–220.
- [Brackley et al., 2016a] Brackley, C. A., Brown, J. M., Waithe, D., Babbs, C., Davies, J., Hughes, J. R., Buckle, V. J., and Marenduzzo, D. (2016a). Predicting the three-dimensional folding of cis-regulatory regions in mammalian genomes using bioinformatic data and polymer models. Genome Biology, 17(1):59.

- [Brackley et al., 2016b] Brackley, C. A., Michieletto, D., Mouvet, F., Johnson, J., Kelly, S., Cook, P. R., and Marenduzzo, D. (2016b). Simulating topological domains in human chromosomes with a fitting-free model. *Nucleus*, 7(5):453–461. Publisher: Taylor & Francis .eprint: <https://doi.org/10.1080/19491034.2016.1239684>.
- [Buchenau et al., 1998] Buchenau, P., Hodgson, J., Strutt, H., and Arndt-Jovin, D. J. (1998). The Distribution of Polycomb-Group Proteins During Cell Division and Development in Drosophila Embryos: Impact on Models for Silencing. *Journal of Cell Biology*, 141(2):469–481.
- [Cannavò et al., 2016] Cannavò, E., Khoueiry, P., Garfield, D. A., Geeleher, P., Zichner, T., Gustafson, E. H., Ciglar, L., Korbil, J. O., and Furlong, E. E. M. (2016). Shadow Enhancers Are Pervasive Features of Developmental Regulatory Networks. *Current biology: CB*, 26(1):38–51.
- [Cao and Zhang, 2004a] Cao, R. and Zhang, Y. (2004a). The functions of E(Z)/EZH2-mediated methylation of lysine 27 in histone H3. *Current Opinion in Genetics & Development*, 14(2):155–164.
- [Cao and Zhang, 2004b] Cao, R. and Zhang, Y. (2004b). SUZ12 Is Required for Both the Histone Methyltransferase Activity and the Silencing Function of the EED-EZH2 Complex. *Molecular Cell*, 15(1):57–67.
- [Cardozo Gizzi et al., 2019] Cardozo Gizzi, A. M., Cattoni, D. I., Fiche, J.-B., Espinola, S. M., Gurgo, J., Messina, O., Houbron, C., Ogiyama, Y., Papadopoulos, G. L., Cavalli, G., Lagha, M., and Nollmann, M. (2019). Microscopy-Based Chromosome Conformation Capture Enables Simultaneous Visualization of Genome Organization and Transcription in Intact Organisms. *Molecular Cell*, 74(1):212–222.e5. Publisher: Elsevier.
- [Cardozo Gizzi et al., 2020] Cardozo Gizzi, A. M., Espinola, S. M., Gurgo, J., Houbron, C., Fiche, J.-B., Cattoni, D. I., and Nollmann, M. (2020). Direct and simultaneous observation of transcription and chromosome architecture in single cells with Hi-M. *Nature Protocols*, 15(3):840–876. Number: 3 Publisher: Nature Publishing Group.
- [Cattoni et al., 2017] Cattoni, D. I., Cardozo Gizzi, A. M., Georgieva, M., Di Stefano, M., Valeri, A., Chamousset, D., Houbron, C., Déjardin, S., Fiche, J.-B., González, I., Chang, J.-M., Sexton, T., Marti-Renom, M. A., Bantignies, F., Cavalli, G., and Nollmann, M. (2017). Single-cell absolute contact probability detection reveals chromosomes are organized by multiple low-frequency yet specific interactions. *Nature Communications*, 8(1):1753. Number: 1 Publisher: Nature Publishing Group.
- [Cesarini et al., 2015] Cesarini, E., Mozzetta, C., Marullo, F., Gregoretti, F., Gargiulo, A., Columbaro, M., Cortesi, A., Antonelli, L., Di Pelino, S., Squarzone, S., Palacios, D., Zippo, A., Bodega, B., Oliva, G., and Lanzaolo, C. (2015). Lamin A/C sustains PcG protein architecture, maintaining transcriptional repression at target genes. *Journal of Cell Biology*, 211(3):533–551.
- [Chen et al., 2015] Chen, K. H., Boettiger, A. N., Moffitt, J. R., Wang, S., and Zhuang, X. (2015). Spatially resolved, highly multiplexed RNA profiling in single cells. *Science*, 348(6233). Publisher: American Association for the Advancement of Science Section: Research Article.

- [Cheutin and Cavalli, 2012] Cheutin, T. and Cavalli, G. (2012). Progressive Polycomb Assembly on H3K27me3 Compartments Generates Polycomb Bodies with Developmentally Regulated Motion. PLOS Genetics, 8(1):e1002465. Publisher: Public Library of Science.
- [Cheutin and Cavalli, 2018] Cheutin, T. and Cavalli, G. (2018). Loss of PRC1 induces higher-order opening of Hox loci independently of transcription during Drosophila embryogenesis. Nature Communications, 9(1):3898.
- [Chiariello et al., 2016] Chiariello, A. M., Annunziatella, C., Bianco, S., Esposito, A., and Nicodemi, M. (2016). Polymer physics of chromosome large-scale 3D organisation. Scientific Reports, 6(1):29775. Number: 1 Publisher: Nature Publishing Group.
- [Chopra et al., 2011] Chopra, V. S., Hendrix, D. A., Core, L. J., Tsui, C., Lis, J. T., and Levine, M. (2011). The Polycomb Group Mutant *esc* Leads to Augmented Levels of Paused Pol II in the Drosophila Embryo. Molecular Cell, 42(6):837–844. Publisher: Elsevier.
- [Ciferri et al., 2012] Ciferri, C., Lander, G. C., Maiolica, A., Herzog, F., Aebersold, R., and Nogales, E. (2012). Molecular architecture of human polycomb repressive complex 2. eLife, 1:e00005. Publisher: eLife Sciences Publications, Ltd.
- [Collombet et al., 2020] Collombet, S., Ranisavljevic, N., Nagano, T., Varnai, C., Shisode, T., Leung, W., Piolot, T., Galupa, R., Borensztein, M., Servant, N., Fraser, P., Ancelin, K., and Heard, E. (2020). Parental-to-embryo switch of chromosome organization in early embryogenesis. Nature, 580(7801):142–146. Bandiera_abtest: a Cg_type: Nature Research Journals Number: 7801 Primary_atype: Research Publisher: Nature Publishing Group Subject_term: Embryogenesis;Epigenetic memory Subject_term_id: embryogenesis;epigenetic-memory.
- [Comet et al., 2011] Comet, I., Schuettengruber, B., Sexton, T., and Cavalli, G. (2011). A chromatin insulator driving three-dimensional Polycomb response element (PRE) contacts and Polycomb association with the chromatin fiber. Proceedings of the National Academy of Sciences, 108(6):2294–2299. Publisher: National Academy of Sciences Section: Biological Sciences.
- [Cooper et al., 2014] Cooper, S., Dienstbier, M., Hassan, R., Schermelleh, L., Sharif, J., Blackledge, N. P., De Marco, V., Elderkin, S., Koseki, H., Klose, R., Heger, A., and Brockdorff, N. (2014). Targeting Polycomb to Pericentric Heterochromatin in Embryonic Stem Cells Reveals a Role for H2AK119u1 in PRC2 Recruitment. Cell Reports, 7(5):1456–1470.
- [Cremer et al., 2003] Cremer, M., Küpper, K., Wagler, B., Wizelman, L., Hase, J. v., Weiland, Y., Kreja, L., Diebold, J., Speicher, M. R., and Cremer, T. (2003). Inheritance of gene density-related higher order chromatin arrangements in normal and tumor cell nuclei. Journal of Cell Biology, 162(5):809–820.
- [Cremer et al., 1982] Cremer, T., Cremer, C., Schneider, T., Baumann, H., Hens, L., and Kirsch-Volders, M. (1982). Analysis of chromosome positions in the interphase nucleus of Chinese hamster cells by laser-UV-microirradiation experiments. Human Genetics, 62(3):201–209.

- [Cremer and Cremer, 2010] Cremer, T. and Cremer, M. (2010). Chromosome Territories. Cold Spring Harbor Perspectives in Biology, 2(3):a003889. Company: Cold Spring Harbor Laboratory Press Distributor: Cold Spring Harbor Laboratory Press Institution: Cold Spring Harbor Laboratory Press Label: Cold Spring Harbor Laboratory Press Publisher: Cold Spring Harbor Lab.
- [Croft et al., 1999] Croft, J. A., Bridger, J. M., Boyle, S., Perry, P., Teague, P., and Bickmore, W. A. (1999). Differences in the Localization and Morphology of Chromosomes in the Human Nucleus. Journal of Cell Biology, 145(6):1119–1131.
- [Dekker et al., 2002] Dekker, J., Rippe, K., Dekker, M., and Kleckner, N. (2002). Capturing Chromosome Conformation. Science, 295(5558):1306–1311. Publisher: American Association for the Advancement of Science Section: Report.
- [Delaval and Feil, 2004] Delaval, K. and Feil, R. (2004). Epigenetic regulation of mammalian genomic imprinting. Current Opinion in Genetics & Development, 14(2):188–195.
- [Delest et al., 2012] Delest, A., Sexton, T., and Cavalli, G. (2012). Polycomb: a paradigm for genome organization from one to three dimensions. Current Opinion in Cell Biology, 24(3):405–414.
- [Denholtz et al., 2013] Denholtz, M., Bonora, G., Chronis, C., Splinter, E., de Laat, W., Ernst, J., Pellegrini, M., and Plath, K. (2013). Long-Range Chromatin Contacts in Embryonic Stem Cells Reveal a Role for Pluripotency Factors and Polycomb Proteins in Genome Organization. Cell Stem Cell, 13(5):602–616. Publisher: Elsevier.
- [Despang et al., 2019] Despang, A., Schöpflin, R., Franke, M., Ali, S., Jerković, I., Paliou, C., Chan, W.-L., Timmermann, B., Wittler, L., Vingron, M., Mundlos, S., and Ibrahim, D. M. (2019). Functional dissection of the Sox9-Kcnj2 locus identifies nonessential and instructive roles of TAD architecture. Nature Genetics, 51(8):1263–1271. Bandiera_abtest: a Cg_type: Nature Research Journals Number: 8 Primary_atype: Research Publisher: Nature Publishing Group Subject_term: Epigenetics;Functional genomics;Gene expression;Gene regulation Subject_term_id: epigenetics;functional-genomics;gene-expression;gene-regulation.
- [de Wit et al., 2015] de Wit, E., Vos, E. S. M., Holwerda, S. J. B., Valdes-Quezada, C., Verstegen, M. J. A. M., Teunissen, H., Splinter, E., Wijchers, P. J., Krijger, P. H. L., and de Laat, W. (2015). CTCF Binding Polarity Determines Chromatin Looping. Molecular Cell, 60(4):676–684. Publisher: Elsevier.
- [Dixon et al., 2015] Dixon, J. R., Jung, I., Selvaraj, S., Shen, Y., Antosiewicz-Bourget, J. E., Lee, A. Y., Ye, Z., Kim, A., Rajagopal, N., Xie, W., Diao, Y., Liang, J., Zhao, H., Lobanenko, V. V., Ecker, J. R., Thomson, J. A., and Ren, B. (2015). Chromatin architecture reorganization during stem cell differentiation. Nature, 518(7539):331–336. Bandiera_abtest: a Cc_license-type: cc_y Cg_type: Nature Research Journals Number: 7539 Primary_atype: Research Publisher: Nature Publishing Group Subject_term: Embryonic stem cells;Epigenomics;Gene regulatory networks Subject_term_id: embryonic-stem-cells;epigenomics;gene-regulatory-networks.

- [Dixon et al., 2012] Dixon, J. R., Selvaraj, S., Yue, F., Kim, A., Li, Y., Shen, Y., Hu, M., Liu, J. S., and Ren, B. (2012). Topological domains in mammalian genomes identified by analysis of chromatin interactions. Nature, 485(7398):376–380. Number: 7398 Publisher: Nature Publishing Group.
- [Dorsett, 2009] Dorsett, D. (2009). Cohesin, gene expression and development: Lessons from *Drosophila*. Chromosome Research, 17(2):185–200.
- [Dorsett, 2019] Dorsett, D. (2019). The Many Roles of Cohesin in *Drosophila* Gene Transcription. Trends in Genetics, 35(7):542–551. Publisher: Elsevier.
- [Dostie et al., 2006] Dostie, J., Richmond, T. A., Arnaout, R. A., Selzer, R. R., Lee, W. L., Honan, T. A., Rubio, E. D., Krumm, A., Lamb, J., Nusbaum, C., Green, R. D., and Dekker, J. (2006). Chromosome Conformation Capture Carbon Copy (5C): A massively parallel solution for mapping interactions between genomic elements. Genome Research, 16(10):1299–1309. Company: Cold Spring Harbor Laboratory Press Distributor: Cold Spring Harbor Laboratory Press Institution: Cold Spring Harbor Laboratory Press Label: Cold Spring Harbor Laboratory Press Publisher: Cold Spring Harbor Lab.
- [Du et al., 2017] Du, Z., Zheng, H., Huang, B., Ma, R., Wu, J., Zhang, X., He, J., Xiang, Y., Wang, Q., Li, Y., Ma, J., Zhang, X., Zhang, K., Wang, Y., Zhang, M. Q., Gao, J., Dixon, J. R., Wang, X., Zeng, J., and Xie, W. (2017). Allelic reprogramming of 3D chromatin architecture during early mammalian development. Nature, 547(7662):232–235. Bandiera_abtest: a Cg.type: Nature Research Journals Number: 7662 Primary_atype: Research Publisher: Nature Publishing Group Subject_term: Chromatin structure;Epigenomics Subject_term_id: chromatin-structure;epigenomics.
- [Eagen et al., 2017] Eagen, K. P., Aiden, E. L., and Kornberg, R. D. (2017). Polycomb-mediated chromatin loops revealed by a subkilobase-resolution chromatin interaction map. Proceedings of the National Academy of Sciences, 114(33):8764–8769.
- [Elgin and Reuter, 2013] Elgin, S. C. and Reuter, G. (2013). Position-Effect Variegation, Heterochromatin Formation, and Gene Silencing in *Drosophila*. Cold Spring Harbor Perspectives in Biology, 5(8):a017780.
- [Entrevan et al., 2016] Entrevan, M., Schuettengruber, B., and Cavalli, G. (2016). Regulation of Genome Architecture and Function by Polycomb Proteins. Trends in Cell Biology, 26(7):511–525. Publisher: Elsevier.
- [Erceg et al., 2019] Erceg, J., AlHaj Abed, J., Goloborodko, A., Lajoie, B. R., Fudenberg, G., Abdennur, N., Imakaev, M., McCole, R. B., Nguyen, S. C., Saylor, W., Joyce, E. F., Senaratne, T. N., Hannan, M. A., Nir, G., Dekker, J., Mirny, L. A., and Wu, C.-t. (2019). The genome-wide multi-layered architecture of chromosome pairing in early *Drosophila* embryos. Nature Communications, 10(1):4486. Number: 1 Publisher: Nature Publishing Group.
- [Espinola et al., 2020] Espinola, S. M., Götz, M., Fiche, J.-B., Bellec, M., Houbbron, C., Cardozo Gizzi, A. M., Lagha, M., and Nollmann, M. (2020). Cis-regulatory chromatin loops arise before TADs and gene activation, and are independent of cell fate during development.

- [Falk et al., 2019] Falk, M., Feodorova, Y., Naumova, N., Imakaev, M., Lajoie, B. R., Leonhardt, H., Joffe, B., Dekker, J., Fudenberg, G., Solovei, I., and Mirny, L. A. (2019). Heterochromatin drives compartmentalization of inverted and conventional nuclei. Nature, 570(7761):395–399. Bandiera_abtest: a Cg_type: Nature Research Journals Number: 7761 Primary_atype: Research Publisher: Nature Publishing Group Subject_term: Biological physics;Chromatin;Chromosomes;Computational biophysics Subject_term_id: biological-physics;chromatin;chromosomes;computational-biophysics.
- [Farcas et al., 2012] Farcas, A. M., Blackledge, N. P., Sudbery, I., Long, H. K., McGouran, J. F., Rose, N. R., Lee, S., Sims, D., Cerase, A., Sheahan, T. W., Koseki, H., Brockdorff, N., Ponting, C. P., Kessler, B. M., and Klose, R. J. (2012). KDM2B links the Polycomb Repressive Complex 1 (PRC1) to recognition of CpG islands. eLife, 1:e00205. Publisher: eLife Sciences Publications, Ltd.
- [Fauvarque and Dura, 1993] Fauvarque, M. O. and Dura, J. M. (1993). polyhomeotic regulatory sequences induce developmental regulator-dependent variegation and targeted P-element insertions in *Drosophila*. Genes & Development, 7(8):1508–1520. Company: Cold Spring Harbor Laboratory Press Distributor: Cold Spring Harbor Laboratory Press Institution: Cold Spring Harbor Laboratory Press Label: Cold Spring Harbor Laboratory Press Publisher: Cold Spring Harbor Lab.
- [Ferraiuolo et al., 2010] Ferraiuolo, M. A., Rousseau, M., Miyamoto, C., Shenker, S., Wang, X. Q. D., Nadler, M., Blanchette, M., and Dostie, J. (2010). The three-dimensional architecture of Hox cluster silencing. Nucleic Acids Research, 38(21):7472–7484.
- [Filion et al., 2010] Filion, G. J., Bommel, J. G. v., Braunschweig, U., Talhout, W., Kind, J., Ward, L. D., Brugman, W., Castro, I. J. d., Kerkhoven, R. M., Bussemaker, H. J., and van Steensel, B. (2010). Systematic Protein Location Mapping Reveals Five Principal Chromatin Types in *Drosophila* Cells. Cell, 143(2):212–224. Publisher: Elsevier.
- [Finlan et al., 2008] Finlan, L. E., Sproul, D., Thomson, I., Boyle, S., Kerr, E., Perry, P., Ylstra, B., Chubb, J. R., and Bickmore, W. A. (2008). Recruitment to the Nuclear Periphery Can Alter Expression of Genes in Human Cells. PLOS Genetics, 4(3):e1000039. Publisher: Public Library of Science.
- [Finn et al., 2019] Finn, E. H., Pegoraro, G., Brandão, H. B., Valton, A.-L., Oomen, M. E., Dekker, J., Mirny, L., and Misteli, T. (2019). Extensive Heterogeneity and Intrinsic Variation in Spatial Genome Organization. Cell, 176(6):1502–1515.e10.
- [Fischle et al., 2003] Fischle, W., Wang, Y., Jacobs, S. A., Kim, Y., Allis, C. D., and Khorasanizadeh, S. (2003). Molecular basis for the discrimination of repressive methyl-lysine marks in histone H3 by Polycomb and HP1 chromodomains. Genes & Development, 17(15):1870–1881. Company: Cold Spring Harbor Laboratory Press Distributor: Cold Spring Harbor Laboratory Press Institution: Cold Spring Harbor Laboratory Press Label: Cold Spring Harbor Laboratory Press Publisher: Cold Spring Harbor Lab.
- [Flavahan et al., 2016] Flavahan, W. A., Drier, Y., Liao, B. B., Gillespie, S. M., Veneticher, A. S., Stemmer-Rachamimov, A. O., Suvà, M. L., and Bernstein, B. E.

- (2016). Insulator dysfunction and oncogene activation in IDH mutant gliomas. Nature, 529(7584):110–114. Bandiera_abtest: a Cg_type: Nature Research Journals Number: 7584 Primary_atype: Research Publisher: Nature Publishing Group Subject_term: Cancer;CNS cancer;DNA methylation;Epigenetics Subject_term_id: cancer;cns-cancer;dna-methylation;epigenetics.
- [Florescu et al., 2016] Florescu, A.-M., Therizols, P., and Rosa, A. (2016). Large Scale Chromosome Folding Is Stable against Local Changes in Chromatin Structure. PLOS Computational Biology, 12(6):e1004987. Publisher: Public Library of Science.
- [Flyamer et al., 2017] Flyamer, I. M., Gassler, J., Imakaev, M., Brandão, H. B., Ulianov, S. V., Abdennur, N., Razin, S. V., Mirny, L. A., and Tachibana-Konwalski, K. (2017). Single-nucleus Hi-C reveals unique chromatin reorganization at oocyte-to-zygote transition. Nature, 544(7648):110–114. Bandiera_abtest: a Cg_type: Nature Research Journals Number: 7648 Primary_atype: Research Publisher: Nature Publishing Group Subject_term: Chromatin analysis;Chromatin structure;Embryology;Nuclear organization;Reprogramming Subject_term_id: chromatin-analysis;chromatin-structure;embryology;nuclear-organization;reprogramming.
- [Francis et al., 2009] Francis, N. J., Follmer, N. E., Simon, M. D., Aghia, G., and Butler, J. D. (2009). Polycomb Proteins Remain Bound to Chromatin and DNA during DNA Replication In Vitro. Cell, 137(1):110–122. Publisher: Elsevier.
- [Francis et al., 2004] Francis, N. J., Kingston, R. E., and Woodcock, C. L. (2004). Chromatin Compaction by a Polycomb Group Protein Complex. Science, 306(5701):1574–1577. Publisher: American Association for the Advancement of Science Section: Report.
- [Francis et al., 2001] Francis, N. J., Saurin, A. J., Shao, Z., and Kingston, R. E. (2001). Reconstitution of a Functional Core Polycomb Repressive Complex. Molecular Cell, 8(3):545–556.
- [Franke et al., 1995] Franke, A., Messmer, S., and Paro, R. (1995). Mapping functional domains of the Polycomb protein of *Drosophila melanogaster*. Chromosome Research, 3(6):351–360.
- [Franke et al., 2016] Franke, M., Ibrahim, D. M., Andrey, G., Schwarzer, W., Heinrich, V., Schöpflin, R., Kraft, K., Kempfer, R., Jerković, I., Chan, W.-L., Spielmann, M., Timmermann, B., Wittler, L., Kurth, I., Cambiaso, P., Zuffardi, O., Houge, G., Lambie, L., Brancati, F., Pombo, A., Vingron, M., Spitz, F., and Mundlos, S. (2016). Formation of new chromatin domains determines pathogenicity of genomic duplications. Nature, 538(7624):265–269. Bandiera_abtest: a Cg_type: Nature Research Journals Number: 7624 Primary_atype: Research Publisher: Nature Publishing Group Subject_term: Chromatin structure;Disease genetics;Disease model;Gene duplication;Gene regulation Subject_term_id: chromatin-structure;disease-genetics;disease-model;gene-duplication;gene-regulation.
- [Franklin and Gosling, 1953] Franklin, R. E. and Gosling, R. G. (1953). Molecular Configuration in Sodium Thymonucleate. Nature, 171(4356):740–741. Number: 4356 Publisher: Nature Publishing Group.

- [Fraser et al., 2015a] Fraser, J., Ferrai, C., Chiariello, A. M., Schueler, M., Rito, T., Laudanno, G., Barbieri, M., Moore, B. L., Kraemer, D. C. A., Aitken, S., Xie, S. Q., Morris, K. J., Itoh, M., Kawaji, H., Jaeger, I., Hayashizaki, Y., Carninci, P., Forrest, A. R. R., FANTOM Consortium, Semple, C. A., Dostie, J., Pombo, A., and Nicodemi, M. (2015a). Hierarchical folding and reorganization of chromosomes are linked to transcriptional changes in cellular differentiation. Molecular Systems Biology, 11(12):852.
- [Fraser et al., 2009] Fraser, J., Rousseau, M., Shenker, S., Ferraiuolo, M. A., Hayashizaki, Y., Blanchette, M., and Dostie, J. (2009). Chromatin conformation signatures of cellular differentiation. Genome Biology, 10(4):R37.
- [Fraser et al., 2015b] Fraser, J., Williamson, I., Bickmore, W. A., and Dostie, J. (2015b). An Overview of Genome Organization and How We Got There: from FISH to Hi-C. Microbiology and Molecular Biology Reviews, 79(3):347–372. Publisher: American Society for Microbiology Section: Review.
- [Fudenberg et al., 2017] Fudenberg, G., Abdennur, N., Imakaev, M., Goloborodko, A., and Mirny, L. A. (2017). Emerging Evidence of Chromosome Folding by Loop Extrusion. Cold Spring Harbor Symposia on Quantitative Biology, 82:45–55. Publisher: Cold Spring Harbor Laboratory Press.
- [Fudenberg et al., 2016] Fudenberg, G., Imakaev, M., Lu, C., Goloborodko, A., Abdennur, N., and Mirny, L. A. (2016). Formation of Chromosomal Domains by Loop Extrusion. Cell Reports, 15(9):2038–2049. Publisher: Elsevier.
- [Gall and Pardue, 1969] Gall, J. G. and Pardue, M. L. (1969). Formation and Detection of Rna-Dna Hybrid Molecules in Cytological Preparations. Proceedings of the National Academy of Sciences, 63(2):378–383. Publisher: National Academy of Sciences Section: Biological Sciences: Genetics.
- [Gambetta et al., 2009] Gambetta, M. C., Oktaba, K., and Müller, J. (2009). Essential Role of the Glycosyltransferase Sxc/Ogt in Polycomb Repression. Science, 325(5936):93–96. Publisher: American Association for the Advancement of Science.
- [Ganai et al., 2014] Ganai, N., Sengupta, S., and Menon, G. I. (2014). Chromosome positioning from activity-based segregation. Nucleic Acids Research, 42(7):4145–4159.
- [Gao et al., 2012] Gao, Z., Zhang, J., Bonasio, R., Strino, F., Sawai, A., Parisi, F., Kluger, Y., and Reinberg, D. (2012). PCGF Homologs, CBX Proteins, and RYBP Define Functionally Distinct PRC1 Family Complexes. Molecular Cell, 45(3):344–356. Publisher: Elsevier.
- [Gavrilov et al., 2015] Gavrilov, A., Razin, S. V., and Cavalli, G. (2015). In vivo formaldehyde cross-linking: it is time for black box analysis. Briefings in Functional Genomics, 14(2):163–165.
- [Ghavi-Helm et al., 2019] Ghavi-Helm, Y., Jankowski, A., Meiers, S., Viales, R. R., Korb, J. O., and Furlong, E. E. M. (2019). Highly rearranged chromosomes reveal uncoupling between genome topology and gene expression. Nature Genetics, 51(8):1272–1282. Bandiera_abtest: a Cg-type: Nature Research Journals Number: 8 Primary_atype: Research Publisher: Nature Publishing Group Subject_term: Functional genomics;Gene expression;Gene expression profiling;Gene regulation;Genomics

Subject_term_id: functional-genomics;gene-expression;gene-expression-profiling;gene-regulation;genomics.

- [Ghavi-Helm et al., 2014] Ghavi-Helm, Y., Klein, F. A., Pakozdi, T., Ciglar, L., Noordermeer, D., Huber, W., and Furlong, E. E. M. (2014). Enhancer loops appear stable during development and are associated with paused polymerase. Nature, 512(7512):96–100. Number: 7512 Publisher: Nature Publishing Group.
- [Ghosh and Jost, 2018] Ghosh, S. K. and Jost, D. (2018). How epigenome drives chromatin folding and dynamics, insights from efficient coarse-grained models of chromosomes. PLOS Computational Biology, 14(5):e1006159. Publisher: Public Library of Science.
- [Goetze et al., 2007] Goetze, S., Mateos-Langerak, J., Gierman, H. J., de Leeuw, W., Giromus, O., Indemans, M. H. G., Koster, J., Ondrej, V., Versteeg, R., and van Driel, R. (2007). The Three-Dimensional Structure of Human Interphase Chromosomes Is Related to the Transcriptome Map. Molecular and Cellular Biology, 27(12):4475–4487. Publisher: American Society for Microbiology.
- [Grasser et al., 2008] Grasser, F., Neusser, M., Fiegler, H., Thormeyer, T., Cremer, M., Carter, N. P., Cremer, T., and Müller, S. (2008). Replication-timing-correlated spatial chromatin arrangements in cancer and in primate interphase nuclei. Journal of Cell Science, 121(11):1876–1886.
- [Grewal and Jia, 2007] Grewal, S. I. S. and Jia, S. (2007). Heterochromatin revisited. Nature Reviews Genetics, 8(1):35–46. Number: 1 Publisher: Nature Publishing Group.
- [Grosberg et al., 1993] Grosberg, A., Rabin, Y., Havlin, S., and Neer, A. (1993). Crumpled Globule Model of the Three-Dimensional Structure of DNA. Europhysics Letters (EPL), 23(5):373–378. Publisher: IOP Publishing.
- [Guelen et al., 2008] Guelen, L., Pagie, L., Brasset, E., Meuleman, W., Faza, M. B., Talhout, W., Eussen, B. H., de Klein, A., Wessels, L., de Laat, W., and van Steensel, B. (2008). Domain organization of human chromosomes revealed by mapping of nuclear lamina interactions. Nature, 453(7197):948–951. Bandiera_abtest: a Cg_type: Nature Research Journals Number: 7197 Primary_atype: Research Publisher: Nature Publishing Group.
- [Guo et al., 2015] Guo, Y., Xu, Q., Canzio, D., Shou, J., Li, J., Gorkin, D. U., Jung, I., Wu, H., Zhai, Y., Tang, Y., Lu, Y., Wu, Y., Jia, Z., Li, W., Zhang, M. Q., Ren, B., Krainer, A. R., Maniatis, T., and Wu, Q. (2015). CRISPR Inversion of CTCF Sites Alters Genome Topology and Enhancer/Promoter Function. Cell, 162(4):900–910.
- [Gustafsson, 2000] Gustafsson, M. G. L. (2000). Surpassing the lateral resolution limit by a factor of two using structured illumination microscopy. Journal of Microscopy, 198(2):82–87. _eprint: <https://onlinelibrary.wiley.com/doi/pdf/10.1046/j.1365-2818.2000.00710.x>.
- [Gustafsson, 2005] Gustafsson, M. G. L. (2005). Nonlinear structured-illumination microscopy: Wide-field fluorescence imaging with theoretically unlimited resolution. Proceedings of the National Academy of Sciences, 102(37):13081–13086.

- [Gustafsson et al., 2008] Gustafsson, M. G. L., Shao, L., Carlton, P. M., Wang, C. J. R., Golubovskaya, I. N., Cande, W. Z., Agard, D. A., and Sedat, J. W. (2008). Three-Dimensional Resolution Doubling in Wide-Field Fluorescence Microscopy by Structured Illumination. Biophysical Journal, 94(12):4957–4970.
- [Hagège et al., 2007] Hagège, H., Klous, P., Braem, C., Splinter, E., Dekker, J., Cathala, G., de Laat, W., and Forné, T. (2007). Quantitative analysis of chromosome conformation capture assays (3C-qPCR). Nature Protocols, 2(7):1722–1733. Number: 7 Publisher: Nature Publishing Group.
- [Heard, 2005] Heard, E. (2005). Delving into the diversity of facultative heterochromatin: the epigenetics of the inactive X chromosome. Current Opinion in Genetics & Development, 15(5):482–489.
- [Heintzman et al., 2007] Heintzman, N. D., Stuart, R. K., Hon, G., Fu, Y., Ching, C. W., Hawkins, R. D., Barrera, L. O., Van Calcar, S., Qu, C., Ching, K. A., Wang, W., Weng, Z., Green, R. D., Crawford, G. E., and Ren, B. (2007). Distinct and predictive chromatin signatures of transcriptional promoters and enhancers in the human genome. Nature Genetics, 39(3):311–318. Bandiera_abtest: a Cg_type: Nature Research Journals Number: 3 Primary_atype: Research Publisher: Nature Publishing Group.
- [Herz et al., 2012] Herz, H.-M., Mohan, M., Garrett, A. S., Miller, C., Casto, D., Zhang, Y., Seidel, C., Haug, J. S., Florens, L., Washburn, M. P., Yamaguchi, M., Shiekhattar, R., and Shilatifard, A. (2012). Polycomb Repressive Complex 2-Dependent and -Independent Functions of Jarid2 in Transcriptional Regulation in *Drosophila*. Molecular and Cellular Biology, 32(9):1683–1693. Publisher: American Society for Microbiology.
- [Hnisz et al., 2016] Hnisz, D., Weintraub, A. S., Day, D. S., Valton, A.-L., Bak, R. O., Li, C. H., Goldmann, J., Lajoie, B. R., Fan, Z. P., Sigova, A. A., Reddy, J., Borges-Rivera, D., Lee, T. I., Jaenisch, R., Porteus, M. H., Dekker, J., and Young, R. A. (2016). Activation of proto-oncogenes by disruption of chromosome neighborhoods. Science, 351(6280):1454–1458. Publisher: American Association for the Advancement of Science Section: Report.
- [Ho et al., 2014] Ho, J. W. K., Jung, Y. L., Liu, T., Alver, B. H., Lee, S., Ikegami, K., Sohn, K.-A., Minoda, A., Tolstorukov, M. Y., Appert, A., Parker, S. C. J., Gu, T., Kundaje, A., Riddle, N. C., Bishop, E., Egelhofer, T. A., Hu, S. S., Alekseyenko, A. A., Rechtsteiner, A., Asker, D., Belsky, J. A., Bowman, S. K., Chen, Q. B., Chen, R. A.-J., Day, D. S., Dong, Y., Dose, A. C., Duan, X., Epstein, C. B., Ercan, S., Feingold, E. A., Ferrari, F., Garrigues, J. M., Gehlenborg, N., Good, P. J., Haseley, P., He, D., Herrmann, M., Hoffman, M. M., Jeffers, T. E., Kharchenko, P. V., Kolasinska-Zwierz, P., Kotwaliwale, C. V., Kumar, N., Langley, S. A., Larschan, E. N., Latorre, I., Libbrecht, M. W., Lin, X., Park, R., Pazin, M. J., Pham, H. N., Plachetka, A., Qin, B., Schwartz, Y. B., Shoresh, N., Stempor, P., Vielle, A., Wang, C., Whittle, C. M., Xue, H., Kingston, R. E., Kim, J. H., Bernstein, B. E., Dernburg, A. F., Pirrotta, V., Kuroda, M. I., Noble, W. S., Tullius, T. D., Kellis, M., MacAlpine, D. M., Strome, S., Elgin, S. C. R., Liu, X. S., Lieb, J. D., Ahringer, J., Karpen, G. H., and Park, P. J. (2014). Comparative analysis of metazoan chromatin organization. Nature, 512(7515):449–452. Bandiera_abtest: a Cc_license_type: cc_y Cg_type: Nature Research Journals Number: 7515 Primary_atype: Research Publisher: Nature Publishing Group

Subject_term: Chromatin;Chromatin analysis;Computational biology and bioinformatics;Epigenomics Subject_term_id: chromatin;chromatin-analysis;computational-biology-and-bioinformatics;epigenomics.

- [Hochstrasser et al., 1986] Hochstrasser, M., Mathog, D., Gruenbaum, Y., Saumweber, H., and Sedat, J. W. (1986). Spatial organization of chromosomes in the salivary gland nuclei of *Drosophila melanogaster*. Journal of Cell Biology, 102(1):112–123.
- [Hou et al., 2012] Hou, C., Li, L., Qin, Z. S., and Corces, V. G. (2012). Gene Density, Transcription, and Insulators Contribute to the Partition of the *Drosophila* Genome into Physical Domains. Molecular Cell, 48(3):471–484.
- [Hozák et al., 1995] Hozák, P., Sasseville, A. M., Raymond, Y., and Cook, P. R. (1995). Lamin proteins form an internal nucleoskeleton as well as a peripheral lamina in human cells. Journal of Cell Science, 108 (Pt 2):635–644.
- [Hsieh et al., 2020] Hsieh, T.-H. S., Cattoglio, C., Slobodyanyuk, E., Hansen, A. S., Rando, O. J., Tjian, R., and Darzacq, X. (2020). Resolving the 3D Landscape of Transcription-Linked Mammalian Chromatin Folding. Molecular Cell, 78(3):539–553.e8. Publisher: Elsevier.
- [Hsieh et al., 2015] Hsieh, T.-H. S., Weiner, A., Lajoie, B., Dekker, J., Friedman, N., and Rando, O. J. (2015). Mapping Nucleosome Resolution Chromosome Folding in Yeast by Micro-C. Cell, 162(1):108–119. Publisher: Elsevier.
- [Hug et al., 2017] Hug, C. B., Grimaldi, A. G., Kruse, K., and Vaquerizas, J. M. (2017). Chromatin Architecture Emerges during Zygotic Genome Activation Independent of Transcription. Cell, 169(2):216–228.e19.
- [Iborra et al., 1996] Iborra, F., Pombo, A., Jackson, D., and Cook, P. (1996). Active RNA polymerases are localized within discrete transcription “factories” in human nuclei. Journal of Cell Science, 109(6):1427–1436.
- [Ingham, 1983] Ingham, P. W. (1983). Differential expression of bithorax complex genes in the absence of the extra sex combs and trithorax genes. Nature, 306(5943):591–593. Bandiera_abtest: a Cg_type: Nature Research Journals Number: 5943 Primary_atype: Research Publisher: Nature Publishing Group.
- [Ingham, 1985] Ingham, P. W. (1985). Genetic Control of the Spatial Pattern of Selector Gene Expression in *Drosophila*. Cold Spring Harbor Symposia on Quantitative Biology, 50:201–208. Publisher: Cold Spring Harbor Laboratory Press.
- [Isono et al., 2013] Isono, K., Endo, T. A., Ku, M., Yamada, D., Suzuki, R., Sharif, J., Ishikura, T., Toyoda, T., Bernstein, B. E., and Koseki, H. (2013). SAM Domain Polymerization Links Subnuclear Clustering of PRC1 to Gene Silencing. Developmental Cell, 26(6):565–577. Publisher: Elsevier.
- [Jackson et al., 1993] Jackson, D., Hassan, A., Errington, R., and Cook, P. (1993). Visualization of focal sites of transcription within human nuclei. The EMBO Journal, 12(3):1059–1065. Publisher: John Wiley & Sons, Ltd.

- [Jerkovic´ and Cavalli, 2021] Jerkovic´, I. and Cavalli, G. (2021). Understanding 3D genome organization by multidisciplinary methods. Nature Reviews Molecular Cell Biology, 22(8):511–528. Bandiera_abtest: a Cg_type: Nature Research Journals Number: 8 Primary_atype: Reviews Publisher: Nature Publishing Group Subject_term: Chromatin;Imaging;Next-generation sequencing Subject_term_id: chromatin;imaging;next-generation-sequencing.
- [Jost et al., 2014] Jost, D., Carrivain, P., Cavalli, G., and Vaillant, C. (2014). Modeling epigenome folding: formation and dynamics of topologically associated chromatin domains. Nucleic Acids Research, 42(15):9553–9561.
- [Jost and Vaillant, 2018] Jost, D. and Vaillant, C. (2018). Epigenomics in 3D: importance of long-range spreading and specific interactions in epigenomic maintenance. Nucleic Acids Research, 46(5):2252–2264.
- [Jost et al., 2017] Jost, D., Vaillant, C., and Meister, P. (2017). Coupling 1D modifications and 3D nuclear organization: data, models and function. Current Opinion in Cell Biology, 44:20–27.
- [Joyce et al., 2012] Joyce, E. F., Williams, B. R., Xie, T., and Wu, C.-t. (2012). Identification of Genes That Promote or Antagonize Somatic Homolog Pairing Using a High-Throughput FISH-Based Screen. PLOS Genetics, 8(5):e1002667. Publisher: Public Library of Science.
- [Jung et al., 2017] Jung, Y. H., Sauria, M. E. G., Lyu, X., Cheema, M. S., Ausio, J., Taylor, J., and Corces, V. G. (2017). Chromatin States in Mouse Sperm Correlate with Embryonic and Adult Regulatory Landscapes. Cell Reports, 18(6):1366–1382. Publisher: Elsevier.
- [Kadoch et al., 2017] Kadoch, C., Williams, R. T., Calarco, J. P., Miller, E. L., Weber, C. M., Braun, S. M. G., Pulice, J. L., Chory, E. J., and Crabtree, G. R. (2017). Dynamics of BAF–Polycomb complex opposition on heterochromatin in normal and oncogenic states. Nature Genetics, 49(2):213–222. Bandiera_abtest: a Cg_type: Nature Research Journals Number: 2 Primary_atype: Research Publisher: Nature Publishing Group Subject_term: Cancer;Epigenetics Subject_term_id: cancer;epigenetics.
- [Kahn et al., 2016] Kahn, T. G., Dorafshan, E., Schultheis, D., Zare, A., Stenberg, P., Reim, I., Pirrotta, V., and Schwartz, Y. B. (2016). Interdependence of PRC1 and PRC2 for recruitment to Polycomb Response Elements. Nucleic Acids Research, 44(21):10132–10149.
- [Kalb et al., 2014] Kalb, R., Latwiel, S., Baymaz, H. I., Jansen, P. W. T. C., Müller, C. W., Vermeulen, M., and Müller, J. (2014). Histone H2A monoubiquitination promotes histone H3 methylation in Polycomb repression. Nature Structural & Molecular Biology, 21(6):569–571. Bandiera_abtest: a Cg_type: Nature Research Journals Number: 6 Primary_atype: Research Publisher: Nature Publishing Group Subject_term: Epigenetics;Gene regulation;Structural biology;Ubiquitylation Subject_term_id: epigenetics;gene-regulation;structural-biology;ubiquitylation.
- [Kassis and Brown, 2013] Kassis, J. A. and Brown, J. L. (2013). Chapter Three - Polycomb Group Response Elements in *Drosophila* and Vertebrates. In Friedmann, T.,

- Dunlap, J. C., and Goodwin, S. F., editors, Advances in Genetics, volume 81, pages 83–118. Academic Press.
- [Kassis and Kennison, 2010] Kassis, J. A. and Kennison, J. A. (2010). Recruitment of Polycomb Complexes: a Role for SCM. Molecular and Cellular Biology, 30(11):2581–2583. Publisher: American Society for Microbiology.
- [Ke et al., 2017] Ke, Y., Xu, Y., Chen, X., Feng, S., Liu, Z., Sun, Y., Yao, X., Li, F., Zhu, W., Gao, L., Chen, H., Du, Z., Xie, W., Xu, X., Huang, X., and Liu, J. (2017). 3D Chromatin Structures of Mature Gametes and Structural Reprogramming during Mammalian Embryogenesis. Cell, 170(2):367–381.e20.
- [Kennison and Tamkun, 1988] Kennison, J. A. and Tamkun, J. W. (1988). Dosage-dependent modifiers of polycomb and antennapedia mutations in *Drosophila*. Proceedings of the National Academy of Sciences, 85(21):8136–8140.
- [Khalil et al., 2007] Khalil, A., Grant, J. L., Caddle, L. B., Atzema, E., Mills, K. D., and Arneodo, A. (2007). Chromosome territories have a highly nonspherical morphology and nonrandom positioning. Chromosome Research, 15(7):899–916.
- [Kharchenko et al., 2011] Kharchenko, P. V., Alekseyenko, A. A., Schwartz, Y. B., Minoda, A., Riddle, N. C., Ernst, J., Sabo, P. J., Larschan, E., Gorchakov, A. A., Gu, T., Linder-Basso, D., Plachetka, A., Shanower, G., Tolstorukov, M. Y., Luquette, L. J., Xi, R., Jung, Y. L., Park, R. W., Bishop, E. P., Canfield, T. K., Sandstrom, R., Thurman, R. E., MacAlpine, D. M., Stamatoyannopoulos, J. A., Kellis, M., Elgin, S. C. R., Kuroda, M. I., Pirrotta, V., Karpen, G. H., and Park, P. J. (2011). Comprehensive analysis of the chromatin landscape in *Drosophila melanogaster*. Nature, 471(7339):480–485. Number: 7339 Publisher: Nature Publishing Group.
- [Khater et al., 2020] Khater, I. M., Nabi, I. R., and Hamarneh, G. (2020). A Review of Super-Resolution Single-Molecule Localization Microscopy Cluster Analysis and Quantification Methods. Patterns, 1(3):100038.
- [Kim et al., 2019] Kim, J. H., Rege, M., Valeri, J., Dunagin, M. C., Metzger, A., Titus, K. R., Gilgenast, T. G., Gong, W., Beagan, J. A., Raj, A., and Phillips-Cremins, J. E. (2019). LADL: light-activated dynamic looping for endogenous gene expression control. Nature Methods, 16(7):633–639. Bandiera_abtest: a Cg_type: Nature Research Journals Number: 7 Primary_atype: Research Publisher: Nature Publishing Group Subject_term: Epigenetics;Functional genomics;Genetic engineering Subject_term_id: epigenetics;functional-genomics;genetic-engineering.
- [Kim et al., 2011] Kim, J. S., Backman, V., and Szleifer, I. (2011). Crowding-Induced Structural Alterations of Random-Loop Chromosome Model. Physical Review Letters, 106(16):168102. Publisher: American Physical Society.
- [King et al., 2005] King, I. F. G., Emmons, R. B., Francis, N. J., Wild, B., Müller, J., Kingston, R. E., and Wu, C.-t. (2005). Analysis of a Polycomb Group Protein Defines Regions That Link Repressive Activity on Nucleosomal Templates to In Vivo Function. Molecular and Cellular Biology, 25(15):6578–6591. Publisher: American Society for Microbiology.

- [Kingston and Tamkun, 2014] Kingston, R. E. and Tamkun, J. W. (2014). Transcriptional Regulation by Trithorax-Group Proteins. Cold Spring Harbor Perspectives in Biology, 6(10):a019349. Company: Cold Spring Harbor Laboratory Press Distributor: Cold Spring Harbor Laboratory Press Institution: Cold Spring Harbor Laboratory Press Label: Cold Spring Harbor Laboratory Press Publisher: Cold Spring Harbor Lab.
- [Klemm et al., 2019] Klemm, S. L., Shipony, Z., and Greenleaf, W. J. (2019). Chromatin accessibility and the regulatory epigenome. Nature Reviews Genetics, 20(4):207–220. Number: 4 Publisher: Nature Publishing Group.
- [Klymenko et al., 2006] Klymenko, T., Papp, B., Fischle, W., Köcher, T., Schelder, M., Fritsch, C., Wild, B., Wilm, M., and Müller, J. (2006). A Polycomb group protein complex with sequence-specific DNA-binding and selective methyl-lysine-binding activities. Genes & Development, 20(9):1110–1122. Company: Cold Spring Harbor Laboratory Press Distributor: Cold Spring Harbor Laboratory Press Institution: Cold Spring Harbor Laboratory Press Label: Cold Spring Harbor Laboratory Press Publisher: Cold Spring Harbor Lab.
- [Kolb et al., 2011] Kolb, T., Maaß, K., Hergt, M., Aebi, U., and Herrmann, H. (2011). Lamin A and lamin C form homodimers and coexist in higher complex forms both in the nucleoplasmic fraction and in the lamina of cultured human cells. Nucleus, 2(5):425–433. Publisher: Taylor & Francis eprint: <https://doi.org/10.4161/nucl.2.5.17765>.
- [Kornberg, 1974] Kornberg, R. D. (1974). Chromatin Structure: A Repeating Unit of Histones and DNA. Science, 184(4139):868–871. Publisher: American Association for the Advancement of Science Section: Articles.
- [Kouzarides, 2007] Kouzarides, T. (2007). Chromatin Modifications and Their Function. Cell, 128(4):693–705. Publisher: Elsevier.
- [Krietenstein et al., 2020] Krietenstein, N., Abraham, S., Venev, S. V., Abdennur, N., Gibcus, J., Hsieh, T.-H. S., Parsi, K. M., Yang, L., Maehr, R., Mirny, L. A., Dekker, J., and Rando, O. J. (2020). Ultrastructural Details of Mammalian Chromosome Architecture. Molecular Cell, 78(3):554–565.e7. Publisher: Elsevier.
- [Kundu et al., 2017] Kundu, S., Ji, F., Sunwoo, H., Jain, G., Lee, J. T., Sadreyev, R. I., Dekker, J., and Kingston, R. E. (2017). Polycomb Repressive Complex 1 Generates Discrete Compacted Domains that Change during Differentiation. Molecular Cell, 65(3):432–446.e5.
- [Küpper et al., 2007] Küpper, K., Kölbl, A., Biener, D., Dittrich, S., von Hase, J., Thormeyer, T., Fiegler, H., Carter, N. P., Speicher, M. R., Cremer, T., and Cremer, M. (2007). Radial chromatin positioning is shaped by local gene density, not by gene expression. Chromosoma, 116(3):285–306.
- [Lagarou et al., 2008] Lagarou, A., Mohd-Sarip, A., Moshkin, Y. M., Chalkley, G. E., Bezstarosti, K., Demmers, J. A. A., and Verrijzer, C. P. (2008). dKDM2 couples histone H2A ubiquitylation to histone H3 demethylation during Polycomb group silencing. Genes & Development, 22(20):2799–2810. Company: Cold Spring Harbor Laboratory Press Distributor: Cold Spring Harbor Laboratory Press Institution: Cold Spring

Harbor Laboratory Press Label: Cold Spring Harbor Laboratory Press Publisher: Cold Spring Harbor Lab.

- [Langer-Safer et al., 1982] Langer-Safer, P. R., Levine, M., and Ward, D. C. (1982). Immunological method for mapping genes on *Drosophila* polytene chromosomes. Proceedings of the National Academy of Sciences, 79(14):4381–4385. Publisher: National Academy of Sciences Section: Research Article.
- [Lanzuolo et al., 2007] Lanzuolo, C., Roure, V., Dekker, J., Bantignies, F., and Orlando, V. (2007). Polycomb response elements mediate the formation of chromosome higher-order structures in the bithorax complex. Nature Cell Biology, 9(10):1167–1174. Number: 10 Publisher: Nature Publishing Group.
- [Lau et al., 2017] Lau, M. S., Schwartz, M. G., Kundu, S., Savol, A. J., Wang, P. I., Marr, S. K., Grau, D. J., Schorderet, P., Sadreyev, R. I., Tabin, C. J., and Kingston, R. E. (2017). Mutation of a nucleosome compaction region disrupts Polycomb-mediated axial patterning. Science, 355(6329):1081–1084. Publisher: American Association for the Advancement of Science.
- [Lee et al., 2006] Lee, T. I., Jenner, R. G., Boyer, L. A., Guenther, M. G., Levine, S. S., Kumar, R. M., Chevalier, B., Johnstone, S. E., Cole, M. F., Isono, K.-i., Koseki, H., Fuchikami, T., Abe, K., Murray, H. L., Zucker, J. P., Yuan, B., Bell, G. W., Herbolsheimer, E., Hannett, N. M., Sun, K., Odom, D. T., Otte, A. P., Volkert, T. L., Bartel, D. P., Melton, D. A., Gifford, D. K., Jaenisch, R., and Young, R. A. (2006). Control of Developmental Regulators by Polycomb in Human Embryonic Stem Cells. Cell, 125(2):301–313. Publisher: Elsevier.
- [Li et al., 2013] Li, H.-B., Ohno, K., Gui, H., and Pirrotta, V. (2013). Insulators Target Active Genes to Transcription Factories and Polycomb-Repressed Genes to Polycomb Bodies. PLOS Genetics, 9(4):e1003436. Publisher: Public Library of Science.
- [Lieberman-Aiden et al., 2009] Lieberman-Aiden, E., Berkum, N. L. v., Williams, L., Imakaev, M., Ragozy, T., Telling, A., Amit, I., Lajoie, B. R., Sabo, P. J., Dorschner, M. O., Sandstrom, R., Bernstein, B., Bender, M. A., Groudine, M., Gnirke, A., Stamatoyannopoulos, J., Mirny, L. A., Lander, E. S., and Dekker, J. (2009). Comprehensive Mapping of Long-Range Interactions Reveals Folding Principles of the Human Genome. Science, 326(5950):289–293. Publisher: American Association for the Advancement of Science Section: Report.
- [Linkert et al., 2010] Linkert, M., Rueden, C. T., Allan, C., Burel, J.-M., Moore, W., Patterson, A., Loranger, B., Moore, J., Neves, C., MacDonald, D., Tarkowska, A., Sticco, C., Hill, E., Rossner, M., Eliceiri, K. W., and Swedlow, J. R. (2010). Metadata matters: access to image data in the real world. Journal of Cell Biology, 189(5):777–782.
- [Lo Sardo et al., 2013] Lo Sardo, F., Lanzuolo, C., Comoglio, F., Bardi, M. D., Paro, R., and Orlando, V. (2013). PcG-Mediated Higher-Order Chromatin Structures Modulate Replication Programs at the *Drosophila* BX-C. PLOS Genetics, 9(2):e1003283. Publisher: Public Library of Science.
- [Lomberk et al., 2006] Lomberk, G., Wallrath, L., and Urrutia, R. (2006). The Heterochromatin Protein 1 family. Genome Biology, 7(7):228.

- [Lomvardas et al., 2006] Lomvardas, S., Barnea, G., Pisapia, D. J., Mendelsohn, M., Kirkland, J., and Axel, R. (2006). Interchromosomal Interactions and Olfactory Receptor Choice. *Cell*, 126(2):403–413. Publisher: Elsevier.
- [Loubiere et al., 2016] Loubiere, V., Delest, A., Thomas, A., Bonev, B., Schuettengruber, B., Sati, S., Martinez, A.-M., and Cavalli, G. (2016). Coordinate redeployment of PRC1 proteins suppresses tumor formation during *Drosophila* development. *Nature Genetics*, 48(11):1436–1442. Bandiera_abtest: a Cg_type: Nature Research Journals Number: 11 Primary_atype: Research Publisher: Nature Publishing Group Subject_term: Cancer;Embryology;Epigenomics Subject_term.id: cancer;embryology;epigenomics.
- [Luger et al., 1997] Luger, K., Mäder, A. W., Richmond, R. K., Sargent, D. F., and Richmond, T. J. (1997). Crystal structure of the nucleosome core particle at 2.8 Å resolution. *Nature*, 389(6648):251–260. Number: 6648 Publisher: Nature Publishing Group.
- [Lupiáñez et al., 2015] Lupiáñez, D. G., Kraft, K., Heinrich, V., Krawitz, P., Brancati, F., Klopocki, E., Horn, D., Kayserili, H., Opitz, J. M., Laxova, R., Santos-Simarro, F., Gilbert-Dussardier, B., Wittler, L., Borschiwer, M., Haas, S. A., Osterwalder, M., Franke, M., Timmermann, B., Hecht, J., Spielmann, M., Visel, A., and Mundlos, S. (2015). Disruptions of Topological Chromatin Domains Cause Pathogenic Rewiring of Gene-Enhancer Interactions. *Cell*, 161(5):1012–1025. Publisher: Elsevier.
- [Luzhin et al., 2019] Luzhin, A. V., Flyamer, I. M., Khrameeva, E. E., Ulianov, S. V., Razin, S. V., and Gavrilov, A. A. (2019). Quantitative differences in TAD border strength underly the TAD hierarchy in *Drosophila* chromosomes. *Journal of Cellular Biochemistry*, 120(3):4494–4503. _eprint: <https://onlinelibrary.wiley.com/doi/pdf/10.1002/jcb.27737>.
- [Maeshima et al., 2014] Maeshima, K., Imai, R., Tamura, S., and Nozaki, T. (2014). Chromatin as dynamic 10-nm fibers. *Chromosoma*, 123(3):225–237.
- [Maison and Almouzni, 2004] Maison, C. and Almouzni, G. (2004). HP1 and the dynamics of heterochromatin maintenance. *Nature Reviews Molecular Cell Biology*, 5(4):296–305. Number: 4 Publisher: Nature Publishing Group.
- [Malyavantham et al., 2008] Malyavantham, K. S., Bhattacharya, S., Alonso, W. D., Acharya, R., and Berezney, R. (2008). Spatio-temporal dynamics of replication and transcription sites in the mammalian cell nucleus. *Chromosoma*, 117(6):553–567.
- [Manuelidis, 1985] Manuelidis, L. (1985). Individual interphase chromosome domains revealed by in situ hybridization. *Human Genetics*, 71(4):288–293.
- [Margueron et al., 2009] Margueron, R., Justin, N., Ohno, K., Sharpe, M. L., Son, J., Drury III, W. J., Voigt, P., Martin, S. R., Taylor, W. R., De Marco, V., Pirrotta, V., Reinberg, D., and Gamblin, S. J. (2009). Role of the polycomb protein EED in the propagation of repressive histone marks. *Nature*, 461(7265):762–767. Bandiera_abtest: a Cg_type: Nature Research Journals Number: 7265 Primary_atype: Research Publisher: Nature Publishing Group.

- [Margueron et al., 2008] Margueron, R., Li, G., Sarma, K., Blais, A., Zavadil, J., Woodcock, C. L., Dynlacht, B. D., and Reinberg, D. (2008). Ezh1 and Ezh2 maintain repressive chromatin through different mechanisms. Molecular Cell, 32(4):503–518.
- [Marshall et al., 1996] Marshall, W. F., Dernburg, A. F., Harmon, B., Agard, D. A., and Sedat, J. W. (1996). Specific interactions of chromatin with the nuclear envelope: positional determination within the nucleus in *Drosophila melanogaster*. Molecular Biology of the Cell, 7(5):825–842. Publisher: American Society for Cell Biology (mboc).
- [Mateo et al., 2019] Mateo, L. J., Murphy, S. E., Hafner, A., Cinquini, I. S., Walker, C. A., and Boettiger, A. N. (2019). Visualizing DNA folding and RNA in embryos at single-cell resolution. Nature, 568(7750):49–54. Number: 7750 Publisher: Nature Publishing Group.
- [Mateos-Langerak et al., 2009] Mateos-Langerak, J., Bohn, M., de Leeuw, W., Giromus, O., Manders, E. M. M., Verschure, P. J., Indemans, M. H. G., Gierman, H. J., Heermann, D. W., van Driel, R., and Goetze, S. (2009). Spatially confined folding of chromatin in the interphase nucleus. Proceedings of the National Academy of Sciences, 106(10):3812–3817.
- [Mayer et al., 2005] Mayer, R., Brero, A., von Hase, J., Schroeder, T., Cremer, T., and Dietzel, S. (2005). Common themes and cell type specific variations of higher order chromatin arrangements in the mouse. BMC Cell Biology, 6(1):44.
- [Meadows et al., 2010] Meadows, L. A., Chan, Y. S., Roote, J., and Russell, S. (2010). Neighbourhood Continuity Is Not Required for Correct Testis Gene Expression in *Drosophila*. PLOS Biology, 8(11):e1000552. Publisher: Public Library of Science.
- [Mendenhall et al., 2010] Mendenhall, E. M., Koche, R. P., Truong, T., Zhou, V. W., Issac, B., Chi, A. S., Ku, M., and Bernstein, B. E. (2010). GC-Rich Sequence Elements Recruit PRC2 in Mammalian ES Cells. PLOS Genetics, 6(12):e1001244. Publisher: Public Library of Science.
- [Mikkelsen et al., 2007] Mikkelsen, T. S., Ku, M., Jaffe, D. B., Issac, B., Lieberman, E., Giannoukos, G., Alvarez, P., Brockman, W., Kim, T.-K., Koche, R. P., Lee, W., Mendenhall, E., O’Donovan, A., Presser, A., Russ, C., Xie, X., Meissner, A., Wernig, M., Jaenisch, R., Nusbaum, C., Lander, E. S., and Bernstein, B. E. (2007). Genome-wide maps of chromatin state in pluripotent and lineage-committed cells. Nature, 448(7153):553–560. Bandiera_abtest: a Cg_type: Nature Research Journals Number: 7153 Primary_atype: Research Publisher: Nature Publishing Group.
- [Mills, 2010] Mills, A. A. (2010). Throwing the cancer switch: reciprocal roles of polycomb and trithorax proteins. Nature Reviews Cancer, 10(10):669–682. Bandiera_abtest: a Cg_type: Nature Research Journals Number: 10 Primary_atype: Reviews Publisher: Nature Publishing Group Subject_term: Cancer epigenetics;Oncogenesis Subject_term_id: cancer-epigenetics;oncogenesis.
- [Min et al., 2003] Min, J., Zhang, Y., and Xu, R.-M. (2003). Structural basis for specific binding of Polycomb chromodomain to histone H3 methylated at Lys 27. Genes & Development, 17(15):1823–1828. Company: Cold Spring Harbor Laboratory Press Distributor: Cold Spring Harbor Laboratory Press Institution: Cold Spring Harbor

Laboratory Press Label: Cold Spring Harbor Laboratory Press Publisher: Cold Spring Harbor Lab.

- [Mirny, 2011] Mirny, L. A. (2011). The fractal globule as a model of chromatin architecture in the cell. Chromosome Research, 19(1):37–51.
- [Miron et al., 2020] Miron, E., Oldenkamp, R., Brown, J. M., Pinto, D. M. S., Xu, C. S., Faria, A. R., Shaban, H. A., Rhodes, J. D. P., Innocent, C., de Ornellas, S., Hess, H. F., Buckle, V., and Schermelleh, L. (2020). Chromatin arranges in chains of mesoscale domains with nanoscale functional topography independent of cohesin. Science Advances, 6(39):eaba8811.
- [Montavon et al., 2011] Montavon, T., Soshnikova, N., Mascrez, B., Joye, E., Thevenet, L., Splinter, E., de Laat, W., Spitz, F., and Duboule, D. (2011). A Regulatory Archipelago Controls Hox Genes Transcription in Digits. Cell, 147(5):1132–1145. Publisher: Elsevier.
- [Muller, 1930] Muller, H. J. (1930). Types of visible variations induced by X-rays in *Drosophila*. Journal of Genetics, 22(3):299–334.
- [Murmam et al., 2005] Murmann, A. E., Gao, J., Encinosa, M., Gautier, M., Peter, M. E., Eils, R., Lichter, P., and Rowley, J. D. (2005). Local gene density predicts the spatial position of genetic loci in the interphase nucleus. Experimental Cell Research, 311(1):14–26.
- [Müller and Bienz, 1991] Müller, J. and Bienz, M. (1991). Long range repression conferring boundaries of Ultrabithorax expression in the *Drosophila* embryo. The EMBO Journal, 10(11):3147–3155. Publisher: John Wiley & Sons, Ltd.
- [Müller et al., 2002] Müller, J., Hart, C. M., Francis, N. J., Vargas, M. L., Sengupta, A., Wild, B., Miller, E. L., O’Connor, M. B., Kingston, R. E., and Simon, J. A. (2002). Histone Methyltransferase Activity of a *Drosophila* Polycomb Group Repressor Complex. Cell, 111(2):197–208. Publisher: Elsevier.
- [Münkel et al., 1999] Münkel, C., Eils, R., Dietzel, S., Zink, D., Mehring, C., Wedemann, G., Cremer, T., and Langowski, J. (1999). Compartmentalization of Interphase Chromosomes Observed in Simulation and Experiment. Journal of Molecular Biology, 285(3):1053–1065.
- [Münkel and Langowski, 1998] Münkel, C. and Langowski, J. (1998). Chromosome structure predicted by a polymer model. Physical Review E, 57(5):5888–5896. Publisher: American Physical Society.
- [Nagano et al., 2013] Nagano, T., Lubling, Y., Stevens, T. J., Schoenfelder, S., Yaffe, E., Dean, W., Laue, E. D., Tanay, A., and Fraser, P. (2013). Single-cell Hi-C reveals cell-to-cell variability in chromosome structure. Nature, 502(7469):59–64. Bandiera_abtest: a Cg_type: Nature Research Journals Number: 7469 Primary_atype: Research Publisher: Nature Publishing Group Subject_term: Chromosomes;Epigenomics Subject_term_id: chromosomes;epigenomics.

- [Nagano et al., 2017] Nagano, T., Lubling, Y., Várnai, C., Dudley, C., Leung, W., Baran, Y., Mendelson Cohen, N., Wingett, S., Fraser, P., and Tanay, A. (2017). Cell-cycle dynamics of chromosomal organization at single-cell resolution. *Nature*, 547(7661):61–67. Bandiera_abtest: a Cg_type: Nature Research Journals Number: 7661 Primary_atype: Research Publisher: Nature Publishing Group Subject_term: Chromosomes;Nuclear organization Subject_term.id: chromosomes;nuclear-organization.
- [Napoles et al., 2004] Napoles, M. d., Mermoud, J. E., Wakao, R., Tang, Y. A., Endoh, M., Appanah, R., Nesterova, T. B., Silva, J., Otte, A. P., Vidal, M., Koseki, H., and Brockdorff, N. (2004). Polycomb Group Proteins Ring1A/B Link Ubiquitylation of Histone H2A to Heritable Gene Silencing and X Inactivation. *Developmental Cell*, 7(5):663–676. Publisher: Elsevier.
- [Nekrasov et al., 2007] Nekrasov, M., Klymenko, T., Fraterman, S., Papp, B., Oktaba, K., Köcher, T., Cohen, A., Stunnenberg, H., Wilm, M., and Müller, J. (2007). Pcl-PRC2 is needed to generate high levels of H3-K27 trimethylation at Polycomb target genes. *The EMBO Journal*, 26(18):4078–4088. Publisher: John Wiley & Sons, Ltd.
- [Nicodemi and Prisco, 2009] Nicodemi, M. and Prisco, A. (2009). Thermodynamic Pathways to Genome Spatial Organization in the Cell Nucleus. *Biophysical Journal*, 96(6):2168–2177.
- [Nir et al., 2018] Nir, G., Farabella, I., Estrada, C. P., Ebeling, C. G., Beliveau, B. J., Sasaki, H. M., Lee, S. D., Nguyen, S. C., McCole, R. B., Chattoraj, S., Erceg, J., Abed, J. A., Martins, N. M. C., Nguyen, H. Q., Hannan, M. A., Russell, S., Durand, N. C., Rao, S. S. P., Kishi, J. Y., Soler-Vila, P., Pierro, M. D., Onuchic, J. N., Callahan, S. P., Schreiner, J. M., Stuckey, J. A., Yin, P., Aiden, E. L., Marti-Renom, M. A., and Wu, C.-t. (2018). Walking along chromosomes with super-resolution imaging, contact maps, and integrative modeling. *PLOS Genetics*, 14(12):e1007872. Publisher: Public Library of Science.
- [Noordermeer et al., 2011] Noordermeer, D., Leleu, M., Splinter, E., Rougemont, J., Laat, W. D., and Duboule, D. (2011). The Dynamic Architecture of Hox Gene Clusters. *Science*, 334(6053):222–225. Publisher: American Association for the Advancement of Science Section: Report.
- [Nora et al., 2012] Nora, E. P., Lajoie, B. R., Schulz, E. G., Giorgetti, L., Okamoto, I., Servant, N., Piolot, T., van Berkum, N. L., Meisig, J., Sedat, J., Gribnau, J., Barillot, E., Blüthgen, N., Dekker, J., and Heard, E. (2012). Spatial partitioning of the regulatory landscape of the X-inactivation centre. *Nature*, 485(7398):381–385. Number: 7398 Publisher: Nature Publishing Group.
- [Nozaki et al., 2017] Nozaki, T., Imai, R., Tanbo, M., Nagashima, R., Tamura, S., Tani, T., Joti, Y., Tomita, M., Hibino, K., Kanemaki, M. T., Wendt, K. S., Okada, Y., Nagai, T., and Maeshima, K. (2017). Dynamic Organization of Chromatin Domains Revealed by Super-Resolution Live-Cell Imaging. *Molecular Cell*, 67(2):282–293.e7.
- [Ogiyama et al., 2018] Ogiyama, Y., Schuettengruber, B., Papadopoulos, G. L., Chang, J.-M., and Cavalli, G. (2018). Polycomb-Dependent Chromatin Looping Contributes to Gene Silencing during Drosophila Development. *Molecular Cell*, 71(1):73–88.e5.

- [Olins and Olins, 1974] Olins, A. L. and Olins, D. E. (1974). Spheroid Chromatin Units (ν Bodies). Science, 183(4122):330–332. Publisher: American Association for the Advancement of Science Section: Reports.
- [Olins and Olins, 2003] Olins, D. E. and Olins, A. L. (2003). Chromatin history: our view from the bridge. Nature Reviews Molecular Cell Biology, 4(10):809–814. Number: 10 Publisher: Nature Publishing Group.
- [Osborne et al., 2004] Osborne, C. S., Chakalova, L., Brown, K. E., Carter, D., Horton, A., Debrand, E., Goyenechea, B., Mitchell, J. A., Lopes, S., Reik, W., and Fraser, P. (2004). Active genes dynamically colocalize to shared sites of ongoing transcription. Nature Genetics, 36(10):1065–1071. Number: 10 Publisher: Nature Publishing Group.
- [Ou et al., 2017] Ou, H. D., Phan, S., Deerinck, T. J., Thor, A., Ellisman, M. H., and O’Shea, C. C. (2017). ChromEMT: Visualizing 3D chromatin structure and compaction in interphase and mitotic cells. Science, 357(6349). Publisher: American Association for the Advancement of Science Section: Research Article.
- [Pandey et al., 2008] Pandey, R. R., Mondal, T., Mohammad, F., Enroth, S., Redrup, L., Komorowski, J., Nagano, T., Mancini-DiNardo, D., and Kanduri, C. (2008). Kcnq1ot1 Antisense Noncoding RNA Mediates Lineage-Specific Transcriptional Silencing through Chromatin-Level Regulation. Molecular Cell, 32(2):232–246. Publisher: Elsevier.
- [Pasini et al., 2008] Pasini, D., Bracken, A. P., Agger, K., Christensen, J., Hansen, K., Cloos, P. a. C., and Helin, K. (2008). Regulation of Stem Cell Differentiation by Histone Methyltransferases and Demethylases. Cold Spring Harbor Symposia on Quantitative Biology, 73:253–263. Publisher: Cold Spring Harbor Laboratory Press.
- [Passarge, 1979] Passarge, E. (1979). Emil Heitz and the concept of heterochromatin: longitudinal chromosome differentiation was recognized fifty years ago. American Journal of Human Genetics, 31(2):106–115.
- [Phillips-Cremins et al., 2013] Phillips-Cremins, J. E., Sauria, M. E. G., Sanyal, A., Gerasimova, T. I., Lajoie, B. R., Bell, J. S. K., Ong, C.-T., Hookway, T. A., Guo, C., Sun, Y., Bland, M. J., Wagstaff, W., Dalton, S., McDevitt, T. C., Sen, R., Dekker, J., Taylor, J., and Corces, V. G. (2013). Architectural Protein Subclasses Shape 3D Organization of Genomes during Lineage Commitment. Cell, 153(6):1281–1295. Publisher: Elsevier.
- [Pickersgill et al., 2006] Pickersgill, H., Kalverda, B., de Wit, E., Talhout, W., Fornerod, M., and van Steensel, B. (2006). Characterization of the *Drosophila melanogaster* genome at the nuclear lamina. Nature Genetics, 38(9):1005–1014. Bandiera_abtest: a Cg_type: Nature Research Journals Number: 9 Primary_atype: Research Publisher: Nature Publishing Group.
- [Piunti and Shilatifard, 2016] Piunti, A. and Shilatifard, A. (2016). Epigenetic balance of gene expression by Polycomb and COMPASS families. Science, 352(6290). Publisher: American Association for the Advancement of Science Section: Review.

- [Plath et al., 2003] Plath, K., Fang, J., Mlynarczyk-Evans, S. K., Cao, R., Worringer, K. A., Wang, H., Cruz, C. C. d. l., Otte, A. P., Panning, B., and Zhang, Y. (2003). Role of Histone H3 Lysine 27 Methylation in X Inactivation. Science. Publisher: American Association for the Advancement of Science.
- [Plys et al., 2019] Plys, A. J., Davis, C. P., Kim, J., Rizki, G., Keenen, M. M., Marr, S. K., and Kingston, R. E. (2019). Phase separation of Polycomb-repressive complex 1 is governed by a charged disordered region of CBX2. Genes & Development, 33(13-14):799–813. Company: Cold Spring Harbor Laboratory Press Distributor: Cold Spring Harbor Laboratory Press Institution: Cold Spring Harbor Laboratory Press Label: Cold Spring Harbor Laboratory Press Publisher: Cold Spring Harbor Lab.
- [Pope et al., 2014] Pope, B. D., Ryba, T., Dileep, V., Yue, F., Wu, W., Denas, O., Vera, D. L., Wang, Y., Hansen, R. S., Canfield, T. K., Thurman, R. E., Cheng, Y., Gülsoy, G., Dennis, J. H., Snyder, M. P., Stamatoyannopoulos, J. A., Taylor, J., Hardison, R. C., Kahveci, T., Ren, B., and Gilbert, D. M. (2014). Topologically associating domains are stable units of replication-timing regulation. Nature, 515(7527):402–405. Bandiera_abtest: a Cc_license_type: cc_y Cg_type: Nature Research Journals Number: 7527 Primary_atype: Research Publisher: Nature Publishing Group Subject_term: Chromosomes;Data integration;DNA replication;Nuclear organization Subject_term_id: chromosomes;data-integration;dna-replication;nuclear-organization.
- [Quinodoz et al., 2018] Quinodoz, S. A., Ollikainen, N., Tabak, B., Palla, A., Schmidt, J. M., Detmar, E., Lai, M. M., Shishkin, A. A., Bhat, P., Takei, Y., Trinh, V., Aznauryan, E., Russell, P., Cheng, C., Jovanovic, M., Chow, A., Cai, L., McDonel, P., Garber, M., and Guttman, M. (2018). Higher-Order Inter-chromosomal Hubs Shape 3D Genome Organization in the Nucleus. Cell, 174(3):744–757.e24.
- [Rao et al., 2014] Rao, S. S. P., Huntley, M. H., Durand, N. C., Stamenova, E. K., Bochkov, I. D., Robinson, J. T., Sanborn, A. L., Machol, I., Omer, A. D., Lander, E. S., and Aiden, E. L. (2014). A 3D Map of the Human Genome at Kilobase Resolution Reveals Principles of Chromatin Looping. Cell, 159(7):1665–1680. Publisher: Elsevier.
- [Reddy et al., 2008] Reddy, K. L., Zullo, J. M., Bertolino, E., and Singh, H. (2008). Transcriptional repression mediated by repositioning of genes to the nuclear lamina. Nature, 452(7184):243–247. Bandiera_abtest: a Cg_type: Nature Research Journals Number: 7184 Primary_atype: Research Publisher: Nature Publishing Group.
- [Ricci et al., 2015] Ricci, M., Manzo, C., García-Parajo, M. F., Lakadamyali, M., and Cosma, M. (2015). Chromatin Fibers Are Formed by Heterogeneous Groups of Nucleosomes In Vivo. Cell, 160(6):1145–1158.
- [Richmond and Davey, 2003] Richmond, T. J. and Davey, C. A. (2003). The structure of DNA in the nucleosome core. Nature, 423(6936):145–150. Number: 6936 Publisher: Nature Publishing Group.
- [Riising et al., 2014] Riising, E. M., Comet, I., Leblanc, B., Wu, X., Johansen, J. V., and Helin, K. (2014). Gene Silencing Triggers Polycomb Repressive Complex 2 Recruitment to CpG Islands Genome Wide. Molecular Cell, 55(3):347–360. Publisher: Elsevier.

- [Rinn et al., 2007] Rinn, J. L., Kertesz, M., Wang, J. K., Squazzo, S. L., Xu, X., Bruggmann, S. A., Goodnough, L. H., Helms, J. A., Farnham, P. J., Segal, E., and Chang, H. Y. (2007). Functional Demarcation of Active and Silent Chromatin Domains in Human HOX Loci by Noncoding RNAs. Cell, 129(7):1311–1323. Publisher: Elsevier.
- [Robinson et al., 2012] Robinson, A. K., Leal, B. Z., Chadwell, L. V., Wang, R., Ilangoan, U., Kaur, Y., Junco, S. E., Schirf, V., Osmulski, P. A., Gaczynska, M., Hinck, A. P., Demeler, B., McEwen, D. G., and Kim, C. A. (2012). The Growth-Suppressive Function of the Polycomb Group Protein Polyhomeotic Is Mediated by Polymerization of Its Sterile Alpha Motif (SAM) Domain *. Journal of Biological Chemistry, 287(12):8702–8713. Publisher: Elsevier.
- [Rodríguez-Carballo et al., 2017] Rodríguez-Carballo, E., Lopez-Delisle, L., Zhan, Y., Fabre, P. J., Beccari, L., El-Idrissi, I., Huynh, T. H. N., Ozadam, H., Dekker, J., and Duboule, D. (2017). The HoxD cluster is a dynamic and resilient TAD boundary controlling the segregation of antagonistic regulatory landscapes. Genes & Development, 31(22):2264–2281. Company: Cold Spring Harbor Laboratory Press Distributor: Cold Spring Harbor Laboratory Press Institution: Cold Spring Harbor Laboratory Press Label: Cold Spring Harbor Laboratory Press Publisher: Cold Spring Harbor Lab.
- [Rose et al., 2016] Rose, N. R., King, H. W., Blackledge, N. P., Fursova, N. A., Ember, K. J., Fischer, R., Kessler, B. M., and Klose, R. J. (2016). RYBP stimulates PRC1 to shape chromatin-based communication between Polycomb repressive complexes. eLife, 5:e18591. Publisher: eLife Sciences Publications, Ltd.
- [Rouillard et al., 2003] Rouillard, J., Zuker, M., and Gulari, E. (2003). OligoArray 2.0: design of oligonucleotide probes for DNA microarrays using a thermodynamic approach. Nucleic Acids Research, 31(12):3057–3062.
- [Rousseau et al., 2014a] Rousseau, M., Crutchley, J. L., Miura, H., Suderman, M., Blanchette, M., and Dostie, J. (2014a). Hox in motion: tracking HoxA cluster conformation during differentiation. Nucleic Acids Research, 42(3):1524–1540.
- [Rousseau et al., 2014b] Rousseau, M., Ferraiuolo, M. A., Crutchley, J. L., Wang, X. Q. D., Miura, H., Blanchette, M., and Dostie, J. (2014b). Classifying leukemia types with chromatin conformation data. Genome Biology, 15(4):R60.
- [Rowley et al., 2017] Rowley, M. J., Nichols, M. H., Lyu, X., Ando-Kuri, M., Rivera, I. S. M., Hermetz, K., Wang, P., Ruan, Y., and Corces, V. G. (2017). Evolutionarily Conserved Principles Predict 3D Chromatin Organization. Molecular Cell, 67(5):837–852.e7. Publisher: Elsevier.
- [Rudkin and Stollar, 1977] Rudkin, G. T. and Stollar, B. D. (1977). High resolution detection of DNA–RNA hybrids in situ by indirect immunofluorescence. Nature, 265(5593):472–473. Number: 5593 Publisher: Nature Publishing Group.
- [Rust et al., 2006] Rust, M. J., Bates, M., and Zhuang, X. (2006). Sub-diffraction-limit imaging by stochastic optical reconstruction microscopy (STORM). Nature Methods, 3(10):793–796. Number: 10 Publisher: Nature Publishing Group.

- [Sanborn et al., 2015] Sanborn, A. L., Rao, S. S. P., Huang, S.-C., Durand, N. C., Huntley, M. H., Jewett, A. I., Bochkov, I. D., Chinnappan, D., Cutkosky, A., Li, J., Geeting, K. P., Gnirke, A., Melnikov, A., McKenna, D., Stamenova, E. K., Lander, E. S., and Aiden, E. L. (2015). Chromatin extrusion explains key features of loop and domain formation in wild-type and engineered genomes. Proceedings of the National Academy of Sciences, 112(47):E6456–E6465.
- [Sarma et al., 2008] Sarma, K., Margueron, R., Ivanov, A., Pirrotta, V., and Reinberg, D. (2008). Ezh2 Requires PHF1 To Efficiently Catalyze H3 Lysine 27 Trimethylation In Vivo. Molecular and Cellular Biology, 28(8):2718–2731. Publisher: American Society for Microbiology.
- [Satrimafitrah et al., 2016] Satrimafitrah, P., Barman, H. K., Ahmad, A., Nishitoh, H., Nakayama, T., Fukagawa, T., and Takami, Y. (2016). RbAp48 is essential for viability of vertebrate cells and plays a role in chromosome stability. Chromosome Research, 24(2):161–173.
- [Saurin et al., 1998] Saurin, A. J., Shiels, C., Williamson, J., Satijn, D. P., Otte, A. P., Sheer, D., and Freemont, P. S. (1998). The Human Polycomb Group Complex Associates with Pericentromeric Heterochromatin to Form a Novel Nuclear Domain. Journal of Cell Biology, 142(4):887–898.
- [Schaaf et al., 2013] Schaaf, C. A., Misulovin, Z., Gause, M., Koenig, A., Gohara, D. W., Watson, A., and Dorsett, D. (2013). Cohesin and Polycomb Proteins Functionally Interact to Control Transcription at Silenced and Active Genes. PLOS Genetics, 9(6):e1003560. Publisher: Public Library of Science.
- [Schardin et al., 1985] Schardin, M., Cremer, T., Hager, H. D., and Lang, M. (1985). Specific staining of human chromosomes in Chinese hamster x man hybrid cell lines demonstrates interphase chromosome territories. Human Genetics, 71(4):281–287.
- [Schermelleh et al., 2008] Schermelleh, L., Carlton, P. M., Haase, S., Shao, L., Winoto, L., Kner, P., Burke, B., Cardoso, M. C., Agard, D. A., Gustafsson, M. G. L., Leonhardt, H., and Sedat, J. W. (2008). Subdiffraction Multicolor Imaging of the Nuclear Periphery with 3D Structured Illumination Microscopy. Science, 320(5881):1332–1336. Publisher: American Association for the Advancement of Science Section: Report.
- [Schermelleh et al., 2001] Schermelleh, L., Solovei, I., Zink, D., and Cremer, T. (2001). Two-color fluorescence labeling of early and mid-to-late replicating chromatin in living cells. Chromosome Research, 9(1):77–80.
- [Scheuermann et al., 2010] Scheuermann, J. C., de Ayala Alonso, A. G., Oktaba, K., Ly-Hartig, N., McGinty, R. K., Fraterman, S., Wilm, M., Muir, T. W., and Müller, J. (2010). Histone H2A deubiquitinase activity of the Polycomb repressive complex PR-DUB. Nature, 465(7295):243–247. Bandiera_abtest: a Cg_type: Nature Research Journals Number: 7295 Primary_atype: Research Publisher: Nature Publishing Group Subject_term: Gene silencing;Hydrolases;Molecular biology Subject_term_id: gene-silencing;hydrolases;molecular-biology.
- [Schoenfelder et al., 2010] Schoenfelder, S., Sexton, T., Chakalova, L., Cope, N. F., Horton, A., Andrews, S., Kurukuti, S., Mitchell, J. A., Umlauf, D., Dimitrova, D. S.,

- Eskiw, C. H., Luo, Y., Wei, C.-L., Ruan, Y., Bieker, J. J., and Fraser, P. (2010). Preferential associations between co-regulated genes reveal a transcriptional interactome in erythroid cells. *Nature Genetics*, 42(1):53–61. Number: 1 Publisher: Nature Publishing Group.
- [Schoenfelder et al., 2015] Schoenfelder, S., Sugar, R., Dimond, A., Javierre, B.-M., Armstrong, H., Mifsud, B., Dimitrova, E., Matheson, L., Tavares-Cadete, F., Furlan-Magaril, M., Segonds-Pichon, A., Jurkowski, W., Wingett, S. W., Tabbada, K., Andrews, S., Herman, B., LeProust, E., Osborne, C. S., Koseki, H., Fraser, P., Luscombe, N. M., and Elderkin, S. (2015). Polycomb repressive complex PRC1 spatially constrains the mouse embryonic stem cell genome. *Nature Genetics*, 47(10):1179–1186. Bandiera_abtest: a Cg_type: Nature Research Journals Number: 10 Primary_atype: Research Publisher: Nature Publishing Group Subject_term: Epigenetics;Gene regulation;Stem cells Subject_term_id: epigenetics;gene-regulation;stem-cells.
- [Schuettengruber et al., 2017] Schuettengruber, B., Bourbon, H.-M., Di Croce, L., and Cavalli, G. (2017). Genome Regulation by Polycomb and Trithorax: 70 Years and Counting. *Cell*, 171(1):34–57.
- [Schuettengruber et al., 2007] Schuettengruber, B., Chourrout, D., Vervoort, M., Leblanc, B., and Cavalli, G. (2007). Genome Regulation by Polycomb and Trithorax Proteins. *Cell*, 128(4):735–745. Publisher: Elsevier.
- [Seif et al., 2020] Seif, E., Kang, J. J., Sasseville, C., Senkovich, O., Kaltashov, A., Boulter, E. L., Kapur, I., Kim, C. A., and Francis, N. J. (2020). Phase separation by the polyhomeotic sterile alpha motif compartmentalizes Polycomb Group proteins and enhances their activity. *Nature Communications*, 11(1):5609. Bandiera_abtest: a Cc_license_type: cc_by Cg_type: Nature Research Journals Number: 1 Primary_atype: Research Publisher: Nature Publishing Group Subject_term: Enzyme mechanisms;Histone post-translational modifications;Ligases;Ubiquitylated proteins;Ubiquitylation Subject_term_id: enzyme-mechanisms;histone-post-translational-modifications;ligases;ubiquitylated-proteins;ubiquitylation.
- [Sexton et al., 2012] Sexton, T., Yaffe, E., Kenigsberg, E., Bantignies, F., Leblanc, B., Hoichman, M., Parrinello, H., Tanay, A., and Cavalli, G. (2012). Three-Dimensional Folding and Functional Organization Principles of the Drosophila Genome. *Cell*, 148(3):458–472. Publisher: Elsevier.
- [Shao et al., 1999] Shao, Z., Raible, F., Mollaaghababa, R., Guyon, J. R., Wu, C.-t., Bender, W., and Kingston, R. E. (1999). Stabilization of Chromatin Structure by PRC1, a Polycomb Complex. *Cell*, 98(1):37–46.
- [Shen et al., 2009] Shen, X., Kim, W., Fujiwara, Y., Simon, M. D., Liu, Y., Mysliwiec, M. R., Yuan, G.-C., Lee, Y., and Orkin, S. H. (2009). Jumonji Modulates Polycomb Activity and Self-Renewal versus Differentiation of Stem Cells. *Cell*, 139(7):1303–1314.
- [Shen et al., 2012] Shen, Y., Yue, F., McCleary, D. F., Ye, Z., Edsall, L., Kuan, S., Wagner, U., Dixon, J., Lee, L., Lobanenko, V. V., and Ren, B. (2012). A map of the cis-regulatory sequences in the mouse genome. *Nature*, 488(7409):116–120. Bandiera_abtest: a Cg_type: Nature Research Journals Number: 7409 Primary_atype: Research Publisher: Nature Publishing Group Subject_term: Gene

expression;Gene regulation;Genomics;Mouse Subject_term_id: gene-expression;gene-regulation;genomics;mouse.

- [Shin et al., 2017] Shin, Y., Berry, J., Pannucci, N., Haataja, M. P., Toettcher, J. E., and Brangwynne, C. P. (2017). Spatiotemporal Control of Intracellular Phase Transitions Using Light-Activated optoDroplets. Cell, 168(1):159–171.e14.
- [Simon et al., 1993] Simon, J., Chiang, A., Bender, W., Shimell, M. J., and O'Connor, M. (1993). Elements of the Drosophila Bithorax Complex That Mediate Repression by Polycomb Group Products. Developmental Biology, 158(1):131–144.
- [Simonis et al., 2006] Simonis, M., Klous, P., Splinter, E., Moshkin, Y., Willemsen, R., de Wit, E., van Steensel, B., and de Laat, W. (2006). Nuclear organization of active and inactive chromatin domains uncovered by chromosome conformation capture–on-chip (4C). Nature Genetics, 38(11):1348–1354. Bandiera_abtest: a Cg_type: Nature Research Journals Number: 11 Primary_atype: Research Publisher: Nature Publishing Group.
- [Smrek and Grosberg, 2015] Smrek, J. and Grosberg, A. Y. (2015). Facilitated diffusion of proteins through crumpled fractal DNA globules. Physical Review E, 92(1):012702. Publisher: American Physical Society.
- [Sparmann and van Lohuizen, 2006] Sparmann, A. and van Lohuizen, M. (2006). Polycomb silencers control cell fate, development and cancer. Nature Reviews Cancer, 6(11):846–856. Bandiera_abtest: a Cg_type: Nature Research Journals Number: 11 Primary_atype: Reviews Publisher: Nature Publishing Group.
- [Stack et al., 1977] Stack, S., Brown, D., and Dewey, W. (1977). Visualization of interphase chromosomes. Journal of Cell Science, 26(1):281–299.
- [Stanton et al., 2017] Stanton, B. Z., Hodges, C., Calarco, J. P., Braun, S. M. G., Ku, W. L., Kadoch, C., Zhao, K., and Crabtree, G. R. (2017). Smarca4 ATPase mutations disrupt direct eviction of PRC1 from chromatin. Nature Genetics, 49(2):282–288. Bandiera_abtest: a Cg_type: Nature Research Journals Number: 2 Primary_atype: Research Publisher: Nature Publishing Group Subject_term: Cancer;Epigenomics;Gene regulation Subject_term_id: cancer;epigenomics;gene-regulation.
- [Stevens et al., 2017] Stevens, T. J., Lando, D., Basu, S., Atkinson, L. P., Cao, Y., Lee, S. F., Leeb, M., Wohlfahrt, K. J., Boucher, W., O'Shaughnessy-Kirwan, A., Cramard, J., Faure, A. J., Ralser, M., Blanco, E., Morey, L., Sansó, M., Palayret, M. G. S., Lehner, B., Di Croce, L., Wutz, A., Hendrich, B., Klenerman, D., and Laue, E. D. (2017). 3D structures of individual mammalian genomes studied by single-cell Hi-C. Nature, 544(7648):59–64. Bandiera_abtest: a Cg_type: Nature Research Journals Number: 7648 Primary_atype: Research Publisher: Nature Publishing Group Subject_term: Cellular imaging;Chromatin structure;Chromosomes;Nuclear organization;Structural biology Subject_term_id: cellular-imaging;chromatin-structure;chromosomes;nuclear-organization;structural-biology.
- [Struhl and Akam, 1985] Struhl, G. and Akam, M. (1985). Altered distributions of Ultrabithorax transcripts in extra sex combs mutant embryos of Drosophila. The EMBO Journal, 4(12):3259–3264. Publisher: John Wiley & Sons, Ltd.

- [Strübbe et al., 2011] Strübbe, G., Popp, C., Schmidt, A., Pauli, A., Ringrose, L., Beisel, C., and Paro, R. (2011). Polycomb purification by in vivo biotinylation tagging reveals cohesin and Trithorax group proteins as interaction partners. Proceedings of the National Academy of Sciences, 108(14):5572–5577. Publisher: National Academy of Sciences Section: Biological Sciences.
- [Su et al., 2020] Su, J.-H., Zheng, P., Kinrot, S. S., Bintu, B., and Zhuang, X. (2020). Genome-Scale Imaging of the 3D Organization and Transcriptional Activity of Chromatin. Cell, 182(6):1641–1659.e26.
- [Sun et al., 2019] Sun, F., Chronis, C., Kronenberg, M., Chen, X.-F., Su, T., Lay, F. D., Plath, K., Kurdistani, S. K., and Carey, M. F. (2019). Promoter-Enhancer Communication Occurs Primarily within Insulated Neighborhoods. Molecular Cell, 73(2):250–263.e5.
- [Sydor et al., 2015] Sydor, A. M., Czymmek, K. J., Puchner, E. M., and Mennella, V. (2015). Super-Resolution Microscopy: From Single Molecules to Supramolecular Assemblies. Trends in Cell Biology, 25(12):730–748. Publisher: Elsevier.
- [Symmons et al., 2014] Symmons, O., Uslu, V. V., Tsujimura, T., Ruf, S., Nassari, S., Schwarzer, W., Ettwiller, L., and Spitz, F. (2014). Functional and topological characteristics of mammalian regulatory domains. Genome Research, 24(3):390–400. Company: Cold Spring Harbor Laboratory Press Distributor: Cold Spring Harbor Laboratory Press Institution: Cold Spring Harbor Laboratory Press Label: Cold Spring Harbor Laboratory Press Publisher: Cold Spring Harbor Lab.
- [Szabo et al., 2019] Szabo, Q., Bantignies, F., and Cavalli, G. (2019). Principles of genome folding into topologically associating domains. Science Advances, 5(4):eaaw1668. Publisher: American Association for the Advancement of Science Section: Review.
- [Szabo et al., 2020] Szabo, Q., Donjon, A., Jerković, I., Papadopoulos, G. L., Cheutin, T., Bonev, B., Nora, E. P., Bruneau, B. G., Bantignies, F., and Cavalli, G. (2020). Regulation of single-cell genome organization into TADs and chromatin nanodomains. Nature Genetics, 52(11):1151–1157. Bandiera_abtest: a Cg_type: Nature Research Journals Number: 11 Primary_atype: Research Publisher: Nature Publishing Group Subject_term: Epigenetics Subject_term_id: epigenetics.
- [Szabo et al., 2018] Szabo, Q., Jost, D., Chang, J.-M., Cattoni, D. I., Papadopoulos, G. L., Bonev, B., Sexton, T., Gurgo, J., Jacquier, C., Nollmann, M., Bantignies, F., and Cavalli, G. (2018). TADs are 3D structural units of higher-order chromosome organization in Drosophila. Science Advances, 4(2):eaar8082. Publisher: American Association for the Advancement of Science Section: Research Article.
- [Takei et al., 2021] Takei, Y., Yun, J., Zheng, S., Ollikainen, N., Pierson, N., White, J., Shah, S., Thomassie, J., Suo, S., Eng, C.-H. L., Guttman, M., Yuan, G.-C., and Cai, L. (2021). Integrated spatial genomics reveals global architecture of single nuclei. Nature, 590(7845):344–350. Number: 7845 Publisher: Nature Publishing Group.
- [Tan et al., 2018] Tan, L., Xing, D., Chang, C.-H., Li, H., and Xie, X. S. (2018). Three-dimensional genome structures of single diploid human cells. Science, 361(6405):924–928. Publisher: American Association for the Advancement of Science Section: Report.

- [Tanabe et al., 2002] Tanabe, H., Müller, S., Neusser, M., Hase, J. v., Calcagno, E., Cremer, M., Solovei, I., Cremer, C., and Cremer, T. (2002). Evolutionary conservation of chromosome territory arrangements in cell nuclei from higher primates. Proceedings of the National Academy of Sciences, 99(7):4424–4429. Publisher: National Academy of Sciences Section: Biological Sciences.
- [Tanay et al., 2007] Tanay, A., O’Donnell, A. H., Damelin, M., and Bestor, T. H. (2007). Hyperconserved CpG domains underlie Polycomb-binding sites. Proceedings of the National Academy of Sciences, 104(13):5521–5526. Publisher: National Academy of Sciences Section: Biological Sciences.
- [Tatavosian et al., 2019] Tatavosian, R., Kent, S., Brown, K., Yao, T., Duc, H. N., Huynh, T. N., Zhen, C. Y., Ma, B., Wang, H., and Ren, X. (2019). Nuclear condensates of the Polycomb protein chromobox 2 (CBX2) assemble through phase separation. Journal of Biological Chemistry, 294(5):1451–1463. Publisher: Elsevier.
- [Tavares et al., 2012] Tavares, L., Dimitrova, E., Oxley, D., Webster, J., Poot, R., Demmers, J., Bezstarosti, K., Taylor, S., Ura, H., Koide, H., Wutz, A., Vidal, M., Elderkin, S., and Brockdorff, N. (2012). RYBP-PRC1 Complexes Mediate H2A Ubiquitylation at Polycomb Target Sites Independently of PRC2 and H3K27me3. Cell, 148(4):664–678.
- [Terranova et al., 2008] Terranova, R., Yokobayashi, S., Stadler, M. B., Otte, A. P., Lohuizen, M. v., Orkin, S. H., and Peters, A. H. F. M. (2008). Polycomb Group Proteins Ezh2 and Rnf2 Direct Genomic Contraction and Imprinted Repression in Early Mouse Embryos. Developmental Cell, 15(5):668–679. Publisher: Elsevier.
- [Tie et al., 2016] Tie, F., Banerjee, R., Fu, C., Stratton, C. A., Fang, M., and Harte, P. J. (2016). Polycomb inhibits histone acetylation by CBP by binding directly to its catalytic domain. Proceedings of the National Academy of Sciences, 113(6):E744–E753.
- [Tiwari et al., 2008] Tiwari, V. K., McGarvey, K. M., Licchesi, J. D. F., Ohm, J. E., Herman, J. G., Schübeler, D., and Baylin, S. B. (2008). PcG Proteins, DNA Methylation, and Gene Repression by Chromatin Looping. PLOS Biology, 6(12):e306. Publisher: Public Library of Science.
- [Tolhuis et al., 2011] Tolhuis, B., Blom, M., Kerkhoven, R. M., Pagie, L., Teunissen, H., Nieuwland, M., Simonis, M., Laat, W. d., Lohuizen, M. v., and Steensel, B. v. (2011). Interactions among Polycomb Domains Are Guided by Chromosome Architecture. PLOS Genetics, 7(3):e1001343. Publisher: Public Library of Science.
- [Tolhuis et al., 2002] Tolhuis, B., Palstra, R.-J., Splinter, E., Grosveld, F., and Laat, W. d. (2002). Looping and Interaction between Hypersensitive Sites in the Active β -globin Locus. Molecular Cell, 10(6):1453–1465. Publisher: Elsevier.
- [Ulianov et al., 2016] Ulianov, S. V., Khrameeva, E. E., Gavrillov, A. A., Flyamer, I. M., Kos, P., Mikhaleva, E. A., Penin, A. A., Logacheva, M. D., Imakaev, M. V., Chertovich, A., Gelfand, M. S., Shevelyov, Y. Y., and Razin, S. V. (2016). Active chromatin and transcription play a key role in chromosome partitioning into topologically associating domains. Genome Research, 26(1):70–84. Company: Cold Spring Harbor Laboratory Press Distributor: Cold Spring Harbor Laboratory Press Institution: Cold Spring Harbor Laboratory Press Label: Cold Spring Harbor Laboratory Press Publisher: Cold Spring Harbor Lab.

- [Van Bortle et al., 2014] Van Bortle, K., Nichols, M. H., Li, L., Ong, C.-T., Takenaka, N., Qin, Z. S., and Corces, V. G. (2014). Insulator function and topological domain border strength scale with architectural protein occupancy. Genome Biology, 15(5):R82.
- [Vazquez et al., 2006] Vazquez, J., Müller, M., Pirrotta, V., and Sedat, J. W. (2006). The Mcp Element Mediates Stable Long-Range Chromosome–Chromosome Interactions in *Drosophila*. Molecular Biology of the Cell, 17(5):2158–2165. Publisher: American Society for Cell Biology (mboc).
- [Vernimmen et al., 2007] Vernimmen, D., Gobbi, M. D., Sloane-Stanley, J. A., Wood, W. G., and Higgs, D. R. (2007). Long-range chromosomal interactions regulate the timing of the transition between poised and active gene expression. The EMBO Journal, 26(8):2041–2051. Publisher: John Wiley & Sons, Ltd.
- [Vian et al., 2018] Vian, L., Pekowska, A., Rao, S. S. P., Kieffer-Kwon, K.-R., Jung, S., Baranello, L., Huang, S.-C., El Khattabi, L., Dose, M., Pruett, N., Sanborn, A. L., Canela, A., Maman, Y., Oksanen, A., Resch, W., Li, X., Lee, B., Kovalchuk, A. L., Tang, Z., Nelson, S., Di Pierro, M., Cheng, R. R., Machol, I., St Hilaire, B. G., Durand, N. C., Shamim, M. S., Stamenova, E. K., Onuchic, J. N., Ruan, Y., Nussenzweig, A., Levens, D., Aiden, E. L., and Casellas, R. (2018). The Energetics and Physiological Impact of Cohesin Extrusion. Cell, 173(5):1165–1178.e20.
- [Vietri Rudan et al., 2015] Vietri Rudan, M., Barrington, C., Henderson, S., Ernst, C., Odom, D. T., Tanay, A., and Hadjur, S. (2015). Comparative Hi-C Reveals that CTCF Underlies Evolution of Chromosomal Domain Architecture. Cell Reports, 10(8):1297–1309. Publisher: Elsevier.
- [Vieux-Rochas et al., 2015] Vieux-Rochas, M., Fabre, P. J., Leleu, M., Duboule, D., and Noordermeer, D. (2015). Clustering of mammalian Hox genes with other H3K27me3 targets within an active nuclear domain. Proceedings of the National Academy of Sciences, 112(15):4672–4677.
- [Wang et al., 2011] Wang, K. C., Yang, Y. W., Liu, B., Sanyal, A., Corces-Zimmerman, R., Chen, Y., Lajoie, B. R., Protacio, A., Flynn, R. A., Gupta, R. A., Wysocka, J., Lei, M., Dekker, J., Helms, J. A., and Chang, H. Y. (2011). A long noncoding RNA maintains active chromatin to coordinate homeotic gene expression. Nature, 472(7341):120–124. Bandiera_abtest: a Cg_type: Nature Research Journals Number: 7341 Primary_atype: Research Publisher: Nature Publishing Group Subject_term: Chromatin;Gene regulation;Long non-coding RNAs Subject_term_id: chromatin;gene-regulation;long-non-coding-rnas.
- [Wang et al., 2004] Wang, L., Brown, J. L., Cao, R., Zhang, Y., Kassis, J. A., and Jones, R. S. (2004). Hierarchical Recruitment of Polycomb Group Silencing Complexes. Molecular Cell, 14(5):637–646.
- [Wang et al., 2016] Wang, S., Su, J.-H., Beliveau, B. J., Bintu, B., Moffitt, J. R., Wu, C.-t., and Zhuang, X. (2016). Spatial organization of chromatin domains and compartments in single chromosomes. Science, 353(6299):598–602. Publisher: American Association for the Advancement of Science Section: Report.

- [Wani et al., 2016] Wani, A. H., Boettiger, A. N., Schorderet, P., Ergun, A., Münger, C., Sadreyev, R. I., Zhuang, X., Kingston, R. E., and Francis, N. J. (2016). Chromatin topology is coupled to Polycomb group protein subnuclear organization. Nature Communications, 7(1):10291. Bandiera.abtest: a Cc_license_type: cc_by Cg_type: Nature Research Journals Number: 1 Primary_atype: Research Publisher: Nature Publishing Group Subject_term: Cell signalling;Chromatin structure Subject_term.id: cell-signalling;chromatin-structure.
- [Watson and Crick, 1953] Watson, J. D. and Crick, F. H. C. (1953). Molecular Structure of Nucleic Acids: A Structure for Deoxyribose Nucleic Acid. Nature, 171(4356):737–738. Number: 4356 Publisher: Nature Publishing Group.
- [Wiegant et al., 1991] Wiegant, J., Ried, T., Nederlof, P. M., Ploeg, M. V. d., Tanke, H. J., and Raap, A. K. (1991). In situ hybridisation with fluoresceinated DNA. Nucleic Acids Research, 19(12):3237–3241.
- [Wilkins et al., 1953] Wilkins, M. H. F., Stokes, A. R., and Wilson, H. R. (1953). Molecular Structure of Nucleic Acids: Molecular Structure of Deoxyribose Nucleic Acids. Nature, 171(4356):738–740. Number: 4356 Publisher: Nature Publishing Group.
- [Wilkinson et al., 2010] Wilkinson, F., Pratt, H., and Atchison, M. L. (2010). PcG recruitment by the YY1 REPO domain can be mediated by Yaf2. Journal of Cellular Biochemistry, 109(3):478–486. eprint: <https://onlinelibrary.wiley.com/doi/pdf/10.1002/jcb.22424>.
- [Williamson et al., 2019] Williamson, I., Kane, L., Devenney, P. S., Flyamer, I. M., Anderson, E., Kilanowski, F., Hill, R. E., Bickmore, W. A., and Lettice, L. A. (2019). Developmentally regulated Shh expression is robust to TAD perturbations. Development, 146(19).
- [Wit and Laatz, 2012] Wit, E. d. and Laatz, W. d. (2012). A decade of 3C technologies: insights into nuclear organization. Genes & Development, 26(1):11–24. Company: Cold Spring Harbor Laboratory Press Distributor: Cold Spring Harbor Laboratory Press Institution: Cold Spring Harbor Laboratory Press Label: Cold Spring Harbor Laboratory Press Publisher: Cold Spring Harbor Lab.
- [Woodcock et al., 1976] Woodcock, C. L., Safer, J. P., and Stanchfield, J. E. (1976). Structural repeating units in chromatin. I. Evidence for their general occurrence. Experimental Cell Research, 97:101–110.
- [Würtele and Chartrand, 2006] Würtele, H. and Chartrand, P. (2006). Genome-wide scanning of HoxB1-associated loci in mouse ES cells using an open-ended Chromosome Conformation Capture methodology. Chromosome Research, 14(5):477–495.
- [Yildiz et al., 2003] Yildiz, A., Forkey, J. N., McKinney, S. A., Ha, T., Goldman, Y. E., and Selvin, P. R. (2003). Myosin V Walks Hand-Over-Hand: Single Fluorophore Imaging with 1.5-nm Localization. Science, 300(5628):2061–2065. Publisher: American Association for the Advancement of Science Section: Research Article.
- [Yuan et al., 2012] Yuan, W., Wu, T., Fu, H., Dai, C., Wu, H., Liu, N., Li, X., Xu, M., Zhang, Z., Niu, T., Han, Z., Chai, J., Zhou, X. J., Gao, S., and Zhu, B. (2012).

Dense Chromatin Activates Polycomb Repressive Complex 2 to Regulate H3 Lysine 27 Methylation. *Science*, 337(6097):971–975. Publisher: American Association for the Advancement of Science Section: Report.

[Zenk et al., 2021] Zenk, F., Zhan, Y., Kos, P., Löser, E., Atinbayeva, N., Schächtle, M., Tiana, G., Giorgetti, L., and Iovino, N. (2021). HP1 drives de novo 3D genome reorganization in early *Drosophila* embryos. *Nature*, 593(7858):289–293. Bandiera_abtest: a Cc_license_type: cc_by Cg_type: Nature Research Journals Number: 7858 Primary_atype: Research Publisher: Nature Publishing Group Subject_term: Chromatin;Embryogenesis;Epigenetic memory;Epigenetics;Nuclear organization Subject_term_id: chromatin;embryogenesis;epigenetic-memory;epigenetics;nuclear-organization.

[Zhan et al., 2017] Zhan, Y., Mariani, L., Barozzi, I., Schulz, E. G., Blüthgen, N., Stadler, M., Tiana, G., and Giorgetti, L. (2017). Reciprocal insulation analysis of Hi-C data shows that TADs represent a functionally but not structurally privileged scale in the hierarchical folding of chromosomes. *Genome Research*. Company: Cold Spring Harbor Laboratory Press Distributor: Cold Spring Harbor Laboratory Press Institution: Cold Spring Harbor Laboratory Press Label: Cold Spring Harbor Laboratory Press Publisher: Cold Spring Harbor Lab.